EMBODYING AUTONOMY IN SOFT MACHINES VIA MECHANO-FLUIDIC NONLINEARITIES

ALBERTO COMORETTO

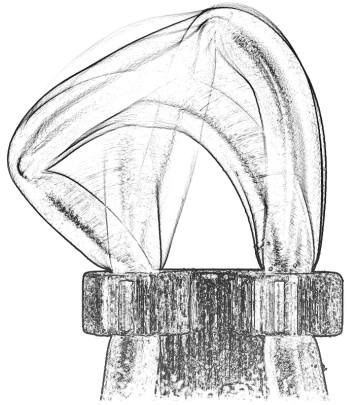

Ph.D. Thesis, Eindhoven University of Technology, October 2025

Embodying autonomy in soft machines via mechano-fluidic nonlinearities
Alberto Comoretto

Cover design: Alberto Comoretto.

ISBN: 978-90-386-6497-2
A catalog record is available from the Eindhoven University of Technology Library. A digital version of this thesis can be downloaded from:
https://amolf.nl and https://research.tue.nl

The work described in this thesis was performed at AMOLF, Science Park 104, 1098 XG Amsterdam, The Netherlands, and partially at Massachusetts Institute of Technology, 77 Massachusetts Ave, Cambridge, MA 02139, United States.

This work is part of the Dutch Research Council (NWO).
This project receives funding from the European Union's 2020 ERC-STG under grant agreement No. 948132.

Embodying autonomy in soft machines via mechano-fluidic nonlinearities

PROEFSCHRIFT

ter verkrijging van de graad van doctor aan de Technische Universiteit Eindhoven, op gezag van de rector magnificus prof. dr. S.K. Lenaerts, voor een commissie aangewezen door het College voor Promoties, in het openbaar te verdedigen op 30 oktober 2025 om 11:00 uur

door

Alberto Comoretto

geboren te Brescia, Italië

Dit proefschrift is goedgekeurd door de promotoren en de samenstelling van de promotiecommissie is als volgt:

Voorzitter:	prof. dr. ir. D. Smeulders
Promotor:	dr. ir. J.T.B. Overvelde
Copromotor:	dr. ir. E. Steur
Promotiecommissieleden:	prof. dr. ir. M.J.G. van de Molengraft
	prof. dr. A.J. Ijspeert (École Polytechnique Fédérale de Lausanne)
	prof. dr. M.M.G. Kamperman (Rijksuniversiteit Groningen)
Adviseurs:	dr. D. Liu
	dr. V. Cacucciolo (Politecnico di Bari)

Het onderzoek of ontwerp dat in dit proefschrift wordt beschreven is uitgevoerd in overeenstemming met de TU/e Gedragscode Wetenschapsbeoefening.

'The mystery of life isn't a problem to solve, but a reality to experience. A process that cannot be understood by stopping it. We must move with the flow of the process. We must join it. We must flow with it.'

Dune, Frank Herbert (1965)

SUMMARY

Animals display mesmerizing autonomous behaviors through complex interplays of physical interactions within their soft bodies and with the environment in which they live, often even bypassing their central brain. Contrarily, artificial robots typically perform tasks by relying on centralized computers that send sequential control signals to actuators. Here, we ask how we can embody autonomous behaviors directly in the physical structure of soft machines, beyond processors and control signals, similar to how natural systems often behave. Through this largely explorative study, we investigate soft machines with mechanical elements, such as elastic shells and tubes, coupled with the fluidic domain of airflow and pressure. We propose that the richness of nonlinear mechano-fluidic phenomena can set the basis for autonomy without a brain, by enabling complex behaviors to emerge directly from the physics of the soft machines rather than being forced from upstream by hardware and software.

We start by embodying memory effects directly in the machines' structure. This allows soft machines, which usually respond passively to interactions, to remember past interactions even after they occur. We harness the highly nonlinear behavior of elastic shells to provide bistability to the fluidic properties of an enclosed cavity. This bistability allows a locomoting soft machine to switch between stable behaviors when tubes in its fluidic circuits kink or unkink upon touch interactions. We implement both long- and short-term memory in a machine that programs its behaviors in response to a human user and that autonomously changes direction after detecting a wall. Via purely geometry and elasticity, embodying memory enables passive physical structures to exhibit programmability features typically reserved for computer-based systems.

We then explore a peculiar behavior of a specific device in our soft machines: a self-oscillating valve where two distinct modes, pressure regulation and oscillation, coexist given the same operating conditions. We explain this coexistence phenomenon through a lumped-parameter model that couples the mechanical and the fluidic domains, capturing the highly nonlinear characteristics of the valve. Using analytical tools from dynamical systems theory, we learn the mechanical and fluidic conditions under which the coexistence holds. In addition, our analytical model informs an updated design for the valve that inhibits the regulation regime, thereby proving useful for applications such as the cyclic activation of a soft artificial heart that should not stop beating once implanted.

Following these designer approaches, we next study autonomous behaviors that emerge from the physics of body-environment dynamics. We observe a self-oscillating phenomenon peculiar to soft tubes with flowing air, where kink instabilities form, travel, and disappear along the tube itself. As this behavior is periodic and asymmetric, we find it equivalent to the motion of animals' limbs. As such, the tube represents a fundamental building block for autonomous locomotion by co-localizing multiple functionalities such as oscillation, actuation, and motion sequencing within the same physical phenomenon. We experimentally show that multiple of these self-oscillating limbs synchronize at relatively high frequencies through internal fluidic coupling and external mechanical coupling with the environment, leading to rapid locomotion. As the synchronization patterns are responsive to external interactions, these seemingly simple machines, composed of only tubes as limbs and lacking a brain, exhibit emergent autonomous behaviors, including obstacle avoidance, amphibious gait transitions, and phototaxis.

Lastly, we aim to overcome the need for bulky external energy sources, such as electric pumps and batteries, by instilling activity directly in the physical composition of soft fluidic machines. In particular, we study active oscillations emerging from the coupling between elastic membranes and a catalytic reaction of an energy-dense fuel. We devise a system where a catalyst embedded in an elastomeric membrane is suspended over a tank filled with liquid hydrogen peroxide as fuel. With both experiments and a basic lumped-parameter model, we show that separate timescales intrinsic to the catalytic reaction lead to active oscillations where the reaction activates and deactivates spontaneously, cyclically inflating and deflating the membrane. As such, we demonstrate a soft device that harnesses the nonlinear physical characteristic of a catalytic reaction to self-sustain oscillations, drawing power from within the system itself.

In conclusion, through this explorative journey we show how mechano-fluidic nonlinearities represent a powerful tool to instill complex autonomous behaviors directly in the structure of seemingly simple machines. From our exploration, we conclude that nonlinearities enable the co-localization of multiple qualitatively distinct functionalities within the same device for increased behavioral complexity, and aid rich couplings both within the machine and with the external environment, leading to emergent, responsive behaviors. By materializing the concepts of embodied memory, soft dynamical systems, physical synchronization of limbs, and active oscillations, this work as a whole lays the foundation for future artificial creatures that will autonomously roam around our world, exhibiting rich and robust behaviors while not possessing, or fully depending on, intricate brains.

CONTENTS

1 Introduction 1
- 1.1 Nature embodies autonomy, even in seemingly simple organisms . . . 2
- 1.2 Soft machines . . . 6
- 1.3 Embodying complex responses in soft machines . . . 8
- 1.4 Research objectives . . . 13
- 1.5 Thesis contributions . . . 14

2 Embodying mechano-fluidic memory in soft machines to program behaviors upon interactions 17
- 2.1 Introduction . . . 18
- 2.2 A self-oscillating soft fluidic machine . . . 20
- 2.3 Memory via a bistable mechano-fluidic capacitor . . . 22
- 2.4 Fluidic circuits for long-term and short-term memory . . . 25
- 2.5 Fluidic touch sensing via kinking tubes . . . 29
- 2.6 Integrated memory and sensing for programmable behaviors 31
- 2.7 Autonomous obstacle avoidance via short-term memory . 34
- 2.8 Discussion . . . 35
- 2.9 Supplementary information . . . 38

3 On the coexistence of pressure regulation and oscillation modes in soft hysteretic valves 53
- 3.1 Introduction . . . 54
- 3.2 Observation: two distinct modes at the same conditions . 56
- 3.3 Lumped-parameter model of the valve system . . . 61
- 3.4 Potential behaviors of the initial model . . . 66
- 3.5 Modified valve model . . . 78
- 3.6 Suppressing the regulation mode . . . 90
- 3.7 Discussion . . . 94
- 3.8 Supplementary information . . . 96

4 Physical synchronization of soft self-oscillating limbs for fast and autonomous locomotion 103
- 4.1 Introduction . . . 104
- 4.2 A self-oscillating limb . . . 105
- 4.3 Explicit internal coupling of multiple limbs . . . 111
- 4.4 Implicit environmental coupling for autonomy . . . 112
- 4.5 Discussion . . . 115
- 4.6 Supplementary information . . . 117

5 Active oscillations of elastic membranes arising from the coupling with a catalytic reaction 189
5.1 Introduction . . . 190
5.2 An active fluidic oscillator with embodied energy . . . 191
5.3 The active oscillation self-sustains for hours . . . 192
5.4 The active oscillation is affected by physical parameters . 197
5.5 A lumped-parameter model of the active oscillation . . . 198
5.6 The model explains the active oscillation . . . 206
5.7 Influence of parameters on the active oscillation . . . 210
5.8 Discussion . . . 216
5.9 Supplementary information . . . 217

6 Discussion 225
6.1 Conclusion . . . 226
6.2 Perspective . . . 227

Bibliography 233

Author's publications 253

Acknowledgments 255

About the author 261

1

INTRODUCTION

'The world of the made will soon be like the world of the born: autonomous, adaptable, and creative but, consequently, out of our control. I think that's a great bargain.'

Out of Control, Kevin Kelly (1994)

Will man-made machines ever behave like natural creatures? Will 'artificial creatures' ever roam around us, interacting and making decisions autonomously, performing actions as if they had a life of their own [1–4]?

To even try to answer such science-fiction-like questions, we will first show how the natural counterparts of machines, animals, display autonomous behaviors in the first place (Section 1.1). Surprisingly, more often than not, animals do not require a brain and are just fine with behaviors embedded in their bodies to explore their surroundings and find food for survival.

Inspired by soft animal bodies, researchers built soft machines that embody some basic functionalities in the deformable structure they are made of (Section 1.2). However, soft machines still require a computer (in biological terms, a brain) to exhibit more complex behaviors such as making decisions or adapting to different environments when locomoting.

As we learn from nature, for machines to accomplish such feats, we should increase the behavioral complexity of their body. Initial efforts in this direction include embedding nonlinearities in the machines' internal structure and leveraging emergent behaviors arising from external interactions (Section 1.3). Inspired by these approaches, can we provide autonomy to brainless soft machines that locomote? Derived from this general question, we will delineate specific research objectives and how we approach them in Sections 1.4 and 1.5.

Hopefully, by the end of this Thesis you will entertain the idea that seemingly simple devices such as popper toys, elastic tubes, and ketchup bottle valves hide a great amount of complexity, which can be harnessed to provide artificial creatures' bodies with the capability of roaming around our world autonomously.

1.1 NATURE EMBODIES AUTONOMY, EVEN IN SEEMINGLY SIMPLE ORGANISMS

All around us, autonomy[1] is ubiquitous, as natural systems relentlessly accomplish tasks on their own. From flowers blooming at the right time in spring [5] to maple seeds spinning and landing far away from the parent tree [6] to cats perfectly landing on their feet [7, 8] (Fig. 1.1A), nature seems to have it all figured out.

1 We define an autonomous system as a system that successfully accomplishes a task without requiring the intervention of agents from outside the system itself. Accomplishing the task is useful in terms of achieving a goal. A task can be defined by an external observer, such as a designer or evolution. For example, in the case of an autonomous car, the designer defines the tasks of following the road and avoiding pedestrians with the goal of reaching a certain location.

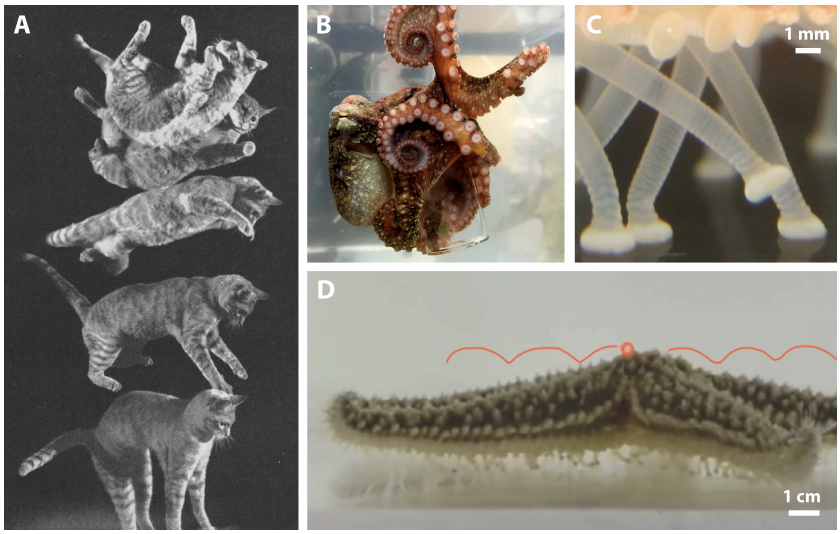

Figure 1.1
IN NATURE, ORGANISMS EMBODY AUTONOMOUS BEHAVIORS. (**A**) When dropped from a height, cats usually fall on their feet through a righting reflex. Reproduced with permission from ref. [8]. (**B**) Because of their softness, animals often intrinsically adapt their shape to their surroundings. In the photograph, the octopus conforms to the shape of the glass vial it is holding. Original photograph (from PNAS cover vol. 121, no. 41) reproduced with permission from Ekaterina D. Gribkova. (**C**) Sea stars have hundreds of hydraulic tube feet on their bottom side. (**D**) The mechanical coupling induced by the body of the sea star and the substrate leads to synchronization of the tube feet, which oscillate in unison, resulting in a relatively fast galloping gait used to escape predators. C and D are reproduced with permission from ref. [9].

It is particularly astonishing how animals autonomously perform highly intricate tasks, ranging from foraging to constructing shelters to building social structures, with the goal of survival and reproduction. Sometimes, one forgets how complex all of these phenomena actually are. Even the seemingly simpler act of locomoting from one place to another involves a tremendous number of variables, including the coordination between multiple limbs [10], synchronization of hundreds of thousands of muscle cells [11], and feedback from the dynamically changing external world [12].

Considering this high level of complexity, it is even more surprising to find that animals often accomplish locomotion tasks by relying on their bodies and bypassing the brain [13–15], through a variety of physical phenomena. For instance, animals often have soft bodies that passively adapt to the external world, intrinsically conforming without the need for computing adjustments (Fig. 1.1B). Physical couplings within the

body, such as central pattern generators [16, 17] and intra-limb neural connections [18], produce well-synchronized walking gaits. When you walk along a bumpy path, your body deals with rocks and holes on the ground by continuously correcting the gait through closed-loop signal pathways to the spinal cord, reflexes [19], without often involving your brain.

A particularly illustrative behavior is peculiar to sea stars. Usually, sea stars slowly explore the environment in search of food, but when threatened by predators, they quickly gallop away as an escape response, synchronizing in unison hundreds of their tube feet (Fig. 1.1C,D). It turns out that this synchronized behavior arises spontaneously from the mechanical coupling between the body and the external substrate [9] without involving a central brain, which would likely be energy-costly for these creatures with relatively low metabolism [20].

More broadly, these biological examples suggest that the need for autonomous behaviors in animals drove much of the required complexity into the body. In this sense, the body of organisms is more than a simple, passive appendage controlled by an advanced brain; instead, the body carries a large amount of richness in behavior, which is useful for the autonomous accomplishment of various tasks.

Complex behaviors are not exclusive to highly developed multicellular organisms. Even simpler organisms made of a single cell and without neurons can accomplish a wide range of functions by relying on their physical structure. One of the most notable examples is the rapid shapeshift of the body of the unicellular predatory ciliate *Lacrymaria olor*, which hunts prey by extending a neckline proboscis up to 1.2 mm in less than 30 s (Fig. 1.2A). Remarkably, the control of this extension is not attributed to a central processor, as this organism does not have neurons. Instead, the behavior emerges from the morphology, through the geometrical unfolding of a curved crease origami-like structure of the cytoskeleton and membrane via topological singularities [21] (Fig. 1.2B). Besides this layer of emergence at the level of extension and contraction, *Lacrymaria olor* embodies even the higher-level goal of searching for food. In fact, the activity of the cilia on the outer surface of the organism generates a follower force that induces a buckling instability when contracting, resulting in the emergence of a chaotic reorientation of the 'head' in new directions. After multiple consecutive cycles of extension and contractions, this reorientation allows the neck to autonomously map a wide area in search of food [22] (Fig. 1.2C).

Another illustrative example of complexity embodied in seemingly simple organisms is the slime mold *Physarum polycephalum*, a single-celled amoeboid that explores the environment in search of food through growth, creating a tubular network between food sources [23]. What is impressive about these networks is the combination of high global

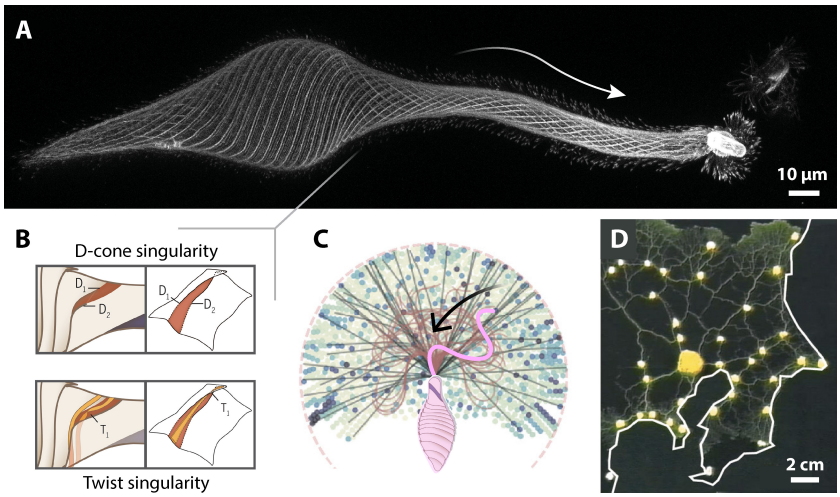

Figure 1.2
EMBODIED AUTONOMOUS BEHAVIORS CAN EMERGE EVEN FROM SEEMINGLY SIMPLE ORGANISMS. (**A**) The unicellular organism *Lacrymaria olor* displays a rapid extension of the neck up to 1.2 mm in less than 30 s. (**B**) This is the result of a specialized body morphology, which enables the physical unfolding of a curved crease origami-like structure of the cytoskeleton and membrane via topological singularities. A and B are reproduced with permission from AAAS from ref. [21]. (**C**) During cycles of extension and compression, the active neck of *Lacrymaria olor* undergoes buckling instabilities that induce head reorientation, resulting in the exploration of space in search of prey. Adapted with permission under CC BY NC ND from ref. [22]. (**D**) The slime mold *Physarum polycephalum*, a single-celled amoeba-like organism, explores the world to find food and forms tubular networks with efficiency comparable to real-world man-made infrastructure networks, such as the Tokyo railway system (at the organism scale), despite being brainless. Reproduced with permission from AAAS from ref. [24].

efficiency, fault tolerance, and low cost that emerges from the local interactions. When food is placed at locations that represent the geographical locations of cities in the Tokyo area, at the scale of the organism, the slime mold quickly grows and, within 26 hours, creates a tubular network that is comparable in effectiveness to the artificial railway network designed by engineers [24] (Fig. 1.2D).

These examples highlight how single-celled organisms can still display intricate behaviors autonomously despite their simplicity—they do not even possess neurons. A key observation to be made is that the complexity of such global behaviors emerges from local interactions of the organisms with their environment, augmented by morphological instabilities. This behavioral richness arises from the physics of the nonlinear system, and it is not controlled by a center of command. Behaviors are

uncontrolled and free to emerge, yet effective and robust, as demonstrated by these organisms still being alive and well out there on Earth. We will come back to this important point later in this chapter, where we discuss how we can implement similar strategies when building artificial soft machines that exhibit autonomous behaviors despite being brainless.

1.2 SOFT MACHINES

In the past few decades, researchers started developing soft machines [25–27] inspired by the softness of biological systems [28]. Made of compliant structures and soft materials [29], soft machines carry several practical advantages over traditional rigid robots, such as safety when interacting with humans [30] and resilience to damage [31]. Therefore, soft machines are promising candidates when we think of building artificial creatures that can coexist with us in the real world.

As a direct consequence of the deformability of their body, soft machines intrinsically adapt their shape to what they are interacting with [32]. This idea was pioneered in the seventies, with probably the first[2] soft gripper made of multiple interconnected rigid links and just two pulleys as input [33]. The softness at the structural level, arising from the many links connected with a flexible cable, enabled the machine to grasp objects of various shapes given the same control input, the cable tensioning. Recent work evolved from this fundamental idea. Inspired by the shape of animal appendages, such as the elephant trunk and the octopus arm, the linkage can be shaped in the form of the logarithmic spiral, obtaining versatile grasping across a wide range of scales (Fig. 1.3A) when the length of the cables is externally controlled [34].

Perhaps the characteristic that most distinguishes soft machines from rigid ones is how their deformable body mediates relatively simple control inputs into complex output motions. An example is one of the first locomoting soft machines, the 'multigait soft robot' [35], essentially a silicone rubber balloon with a design that is more involved than that of party balloons. Upon pressurization, the carefully arranged internal chambers inflate. This inflation, combined with a strain-limiting layer made of a stiffer rubber, induces the bending of various appendages of the machine (Fig. 1.3B). Hence, from one single input (pressurization), one can obtain a complex continuum deformation as output. Importantly, by varying the phase and amplitude of these relatively simple control inputs, the machine displays distinct gaits so that it crawls until it

2 To the best of our knowledge, the 1978 paper [33] is one of the earliest examples of a soft robotic gripper. In the article, the authors present a soft gripper to grasp various objects and introduce concepts of adaptability and complexity of deformations from simple inputs. Historically speaking, they were three decades earlier than the 2011 article of Ilievski et al. [26], which kick-started a broader interest in the scientific community.

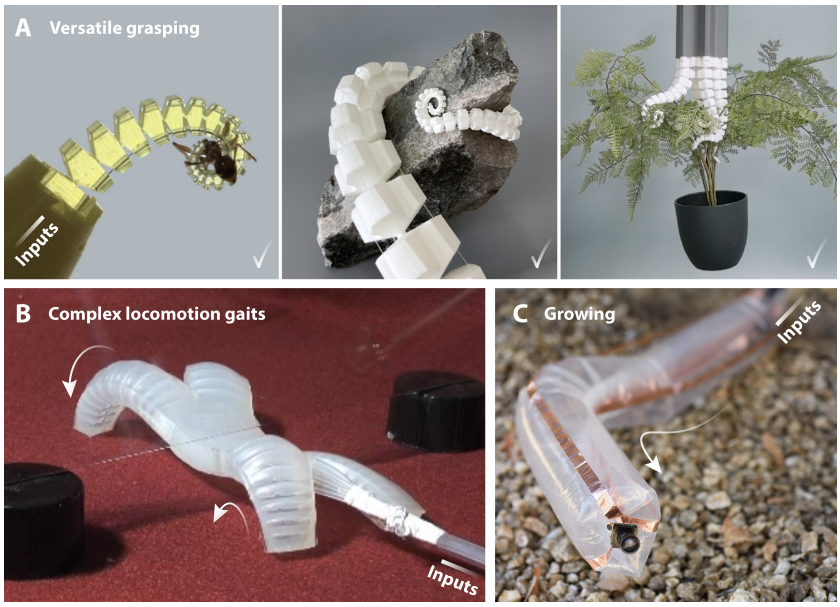

Figure 1.3
SOFT MACHINES EMBODY BASIC FUNCTIONALITIES AS INSPIRED BY BIOLOGICAL SYSTEMS. (**A**) Inspired by the logarithmic spiral shape of animal appendages such as octopus arms and elephant trunks, soft robots achieve versatile grasping across scales. Reproduced with permission under CC BY NC ND from ref. [34]. (**B**) Soft robots exhibit intricate deformations of their bodies upon activating control inputs such as pressurization. This softness at the material level enables complex functionalities, such as walking with multiple gaits. Reproduced with permission from ref. [35]. (**C**) Inspired by tip growth peculiar to natural systems such as developing neurons and trailing plants, soft robots can locomote through growth [36]. Photograph credit: Stanford, L.A. Cicero. The examples in A, B, and C do not embody autonomous capabilities, as they require multiple control inputs to be provided by an external processor.

encounters a narrow passage, after which it undulates under it (Fig. 1.3B). However, note that the machine has to rely on an external computer, or a human operator in this case, that delivers these input profiles through tethers, limiting its autonomy.

Soft machines can perform other formidable behaviors that are simply not accessible by the rigid body of hard machines. A prime example is locomotion through growth shown by 'vine robots' [36]. These machines are made of an inverted, soft, thin-walled tube that everts when pressurized, thereby lengthening from the tip (Fig. 1.3C). Because they do not slide along the surroundings when growing, vine robots can move through harsh environments such as viscous liquids and even squeeze through narrow gaps. When the relative lengths of the sides of the tube

are externally controlled while everting, these machines can steer and explore three-dimensional spaces. For the purpose of the discussion on autonomous behaviors, note that vine robots are not autonomous and still require multiple external control inputs (a pressurization profile and steering cues) to perform all these tasks.

These are just a few examples of the large number of soft machines being developed as the field of soft robotics is rapidly growing [37]. In general, soft machines display this passive adaptability at the level of material and structure, often called mechanical or embodied intelligence [38]. However, as exemplified by the representative cases in Figure 1.3, soft machines typically rely on a processor external to the body to perform more complex, autonomous tasks. For instance, an external user decides which cables are being pulled with what intensity to grip various different objects (Fig. 1.3A). An external user decides which chambers to inflate, at which pressure values, and in what sequence, to switch between gaits of the multigait robot (Fig. 1.3B).

An initial approach to solving the autonomy problem would involve placing the computer and all the required valves and pumps on board the robot [39]. However, introducing a relatively heavy, fragile, and rigid computer on board defeats the purpose of a lightweight, resilient, and soft body. Instead, here we take a more holistic approach: Do we really need to move the external brain on board? Can a soft machine[3] perform tasks autonomously without a brain?

1.3 EMBODYING COMPLEX RESPONSES IN SOFT MACHINES

In the absence of a brain, biological systems manage to exhibit autonomous behaviors by increasing the complexity of their body, as we discussed in Section 1.1. This complexity stems from the rich physics of their deformation and their interactions with the surrounding environment. We will now introduce recent discoveries that demonstrate that harnessing nonlinear responses and emergent phenomena increases the complexity of soft machines' bodies.

1.3.1 *Nonlinearities in fluidic machines*

In nature, even seemingly simple organisms present rich morphologies, where nonlinear interactions carry considerable complexity (Fig. 1.2A-C).

3 We refer to these systems as soft machines to clearly distance them from classical robots. Typically, robots are described as a computer with a body. Instead, we define machines as not carrying a computer on board. The early works in Figure 1.3 still require external computers to operate, so they have characteristics of both machines and robots. As we will see in Section 1.4, one of the main goals of this Thesis is to remove this requirement for a brain, moving further away from the concept of a robot.

Similarly, researchers recently started introducing nonlinear responses directly in the structure of soft machines to increase their behavioral complexity [40]. In this direction, a pioneering work [41] introduced a peculiar soft balloon enclosed in inextensible braids (Fig. 1.4A) with a special characteristic: when inflated with an increasing volume of fluid in input, the pressure response follows a nonlinear, non-monotonic trend (Fig. 1.4B).

The nonlinear response of each balloon leads to rich global behaviors when coupled with others. Specifically, the non-monotonic individual curves lead to a global curve that has multiple unstable regions. Interestingly, when being close to the unstable regime, a small increase in the input volume causes the system to skip the entire unstable path. The system will find the next stable solution, which can be characterized by a very different internal state than the previous one. For instance, supplying just 1 mL to three connected balloons that are on the verge of instability will lead to a fast transition to another stable state, causing a large internal volume exchange of ~ 20 mL (Fig. 1.4C). In biology, this kind of amplification of responses through instabilities is found, for instance, in the mantis shrimp [42], where geometric latching through linkages accumulates elastic energy and suddenly releases it to achieve rapid movement [43], and in nematodes, where a kink instability in their soft cylindrical body rapidly releases energy, allowing jumps up to 20 body lengths in height [40].

Hence, nonlinearities at the structural level increase the available richness in responses. For instance, these consecutive transitions between balloon states have been later harnessed to obtain a soft machine that sequences the activation of nonlinear actuators and generates locomotion gaits without using a computer but solely relying on a timed, oscillatory pressure input [44].

To move past the need for an external oscillatory signal, recent efforts involved harnessing similar nonlinearities to generate oscillations internally with so-called fluidic circuits [45] embedded inside the soft machines. Fluidic circuits consist of networks of soft pneumatic tubings [46–48] and valves [49–55] with nonlinear responses, which when combined can lead to self-sustained internal oscillations [53, 54, 56–58].

A representative example of these systems, stemming from our group, is a fluidic analog of an electronic relaxation oscillator [53]. The oscillator is based on the nonlinear response of a hysteretic valve, i.e., an elastic shell with a cut at its pole, often found in ketchup bottle caps [59]. When pressurized, the valve can be in a closed state (with the shell in rest condition and the cut closed) or in an open state (shell snapped, cut open) (Fig. 1.4D). For constant input airflow, when the valve is closed, pressure will rise until a critical pressure is reached, and the valve will snap to the open state (Fig. 1.4E, white arrows). In this open state, flow

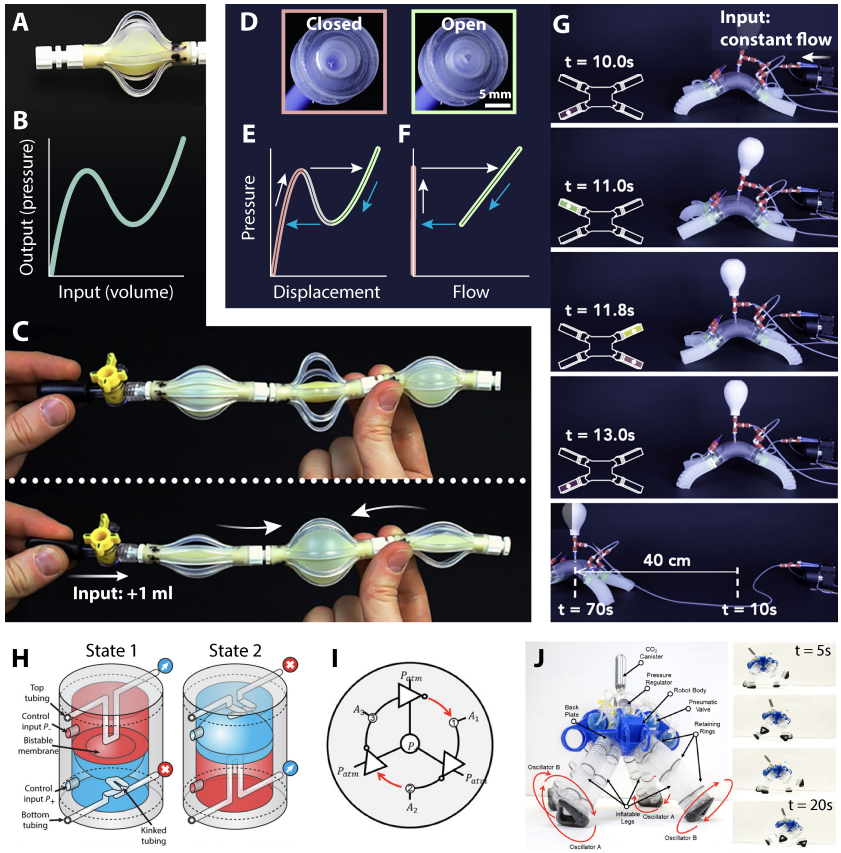

Figure 1.4

SOFT MACHINES' BODIES WITH COMPLEX BEHAVIORS THROUGH NONLINEAR FLUIDIC CIRCUITS. (**A**) Inflatable balloons enclosed in braids (**B**) display a nonlinear, non-monotonic input-output response. (**C**) When multiple of these balloons are interconnected in series, they display rich responses: in the photograph, when a small amount of volume is provided in input, the system undergoes large internal volume changes and global deformations. A and C are reproduced with permission from ref. [41]. (**D**) A hysteretic valve—a shell with a cut at its pole—switches between a closed state and an open state [53]. (**E**) Pressure applied to the valve as a function of pole displacement shows a nonlinear trend, with two positive slope regimes corresponding to the closed and open states. The valve snaps between these two states, (**F**) leading to a hysteretic self-oscillating cycle. (**G**) This self-oscillation provides pulsatile flow to the soft legs of a machine, given only constant flow from a pump. The locomotion sequencing results from the fluidic coupling of the valves. D, E, F, and G are adapted with permission under CC BY NC ND from ref. [53]. (**H**) The two stable states of a bistable shell inside a soft valve result in the opening and closing of channels through the kinking of soft tubes. Reproduced with permission from AAAS from ref. [50]. (**I**) The channels can be connected so that three valves are arranged as a ring oscillator [56], (**J**) sequencing the limbs' motion in a quadruped machine [57]. I and J are reproduced with permission from AAAS from ref. [57].

is provided in output (Fig. 1.4F, green line), thereby inducing a decrease in pressure. When pressure decreases past a low critical value, the valve snaps back to the closed state (Fig. 1.4E,F, blue arrows), and the cycle will repeat.

When multiple relaxation oscillators are connected to the same flow source, they spontaneously sequence their activation. This sequencing enables a soft-limbed machine (equipped with a ketchup valve for each limb) to locomote forward, performing one step at a time when powered by a single pump (Fig. 1.4G).

Another representative example of nonlinear fluidic devices that generate internal oscillations is a valve made of a bistable elastic shell connected to soft tubes [50] (Fig. 1.4H). The valve has two chambers, one on each side of the shell, which is encapsulated in a soft container. When the pressure difference between the two chambers reaches a critical snap-through pressure, the shell snaps to the other stable state. Since the shell is mechanically connected to soft tubes, the tube on the snapped side kinks when the shell snaps, blocking airflow and thereby pressurizing the associated air channel. When the pressure in output from one valve is connected to the input of another one, three valves can be arranged in a ring oscillator architecture [57] (Fig. 1.4I). Given a constant pressure source, the ring oscillator sustains an oscillation at the system level, where the three valves pressurize in a sequence. By connecting the pressurized chambers of the valves to the inflatable legs of a quadruped machine, the legs activate alternatively. With only a pressure canister on board, this soft-legged machine locomotes forward [57] (Fig. 1.4J).

These examples highlight how nonlinearities at the structural level can enable a soft machine's body to exhibit relatively complex responses, such as coordination of locomotion gaits, which traditionally would require extensive control signals provided by an external processor (for instance, see the multigait robot in Figure 1.3B).

1.3.2 *Toward autonomous behavior in soft machines*

As we have seen, nonlinearities in fluidic circuits that are embedded in the structure of soft machines enable complex internal responses. In addition, besides this internal form of behavioral richness, complex behaviors can emerge from the interactions of the machines with the external environment.

A prime example is 'bucklebot' [60], a locomoting device made of two vibrating toy microbots (Hexbug Nano®) held together by a thin elastic beam (Fig. 1.5A). When the two microbots vibrate vertically, they exert a horizontal active force that is enough to buckle the connecting beam, hence aligning the microbots and allowing the overall buckle-

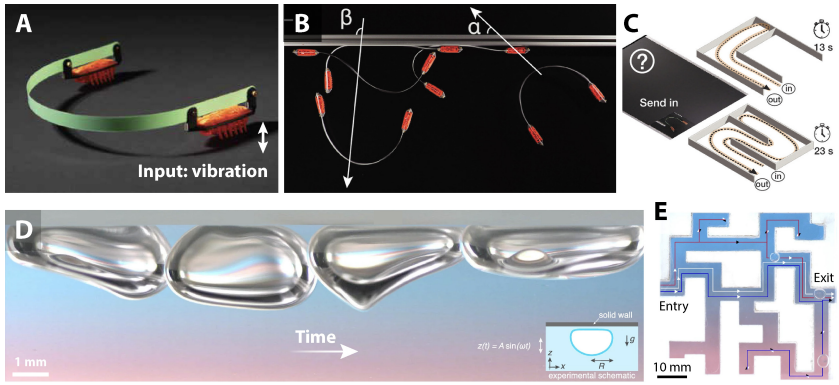

Figure 1.5
TOWARD EMERGENT AUTONOMOUS BEHAVIORS THROUGH INTERACTIONS WITH THE SURROUNDINGS. (**A**) 'Bucklebot' is a locomoting device made of two vibrating toy microbots (Hexbug Nano®) connected by a thin polyester beam. When the toys are turned on, the vibrational input induces asymmetric frictional interactions with the substrate, resulting in locomotion. (**B**) Bucklebot displays rich responses that emerge from the interactions with the surroundings, such as temporary wall-following succeeded by bouncing away with an angle that differs from the approach angle. (**C**) The emergent wall following response enables bucklebot to map unknown environments. A, B, and C are reproduced with permission under CC BY NC ND from ref. [60]. (**D**) Even extremely under-engineered agents can achieve the complex task of locomotion: air bubbles immersed under a vibrating substrate gallop forward through asymmetries emerging from the deformation of the soft body that interacts with the substrate. (**E**) When interacting with boundaries, the bubbles solve a maze. D and E are adapted with permission under CC BY from ref. [61].

bot to move forward. The elastic beam, despite its simplicity, allows bucklebot to exhibit complex but tunable responses when interacting with the surroundings. For instance, Figure 1.5B shows a bucklebot that temporarily follows a wall and then bumps away from it. Figure 1.5C shows a bucklebot that maps an environment and differentiates between long and short paths depending on the run time.

Even vastly under-engineered agents can exhibit complex behaviors when their interactions with the surroundings are understood and harnessed. For instance, air bubbles immersed in a fluid and trapped under a substrate gallop forward when the substrate vibrates [61]. Their movement is a result of symmetry breaking that spontaneously arises in the deformable body of the bubbles (Fig. 1.5D). Similar to bucklebots, the interaction with boundaries allows bubbles to solve a maze (Fig. 1.5E).

These initial results highlight that even in the absence of a centralized processor or a designed internal circuitry, seemingly simple agents can

passively exhibit complex behaviors that appear to be autonomous, which emerge from the interactions with the surroundings alone.

1.4 RESEARCH OBJECTIVES

As we have shown in the previous section, soft machines without a processor can encode basic behaviors in their physical structure. For instance, internal mechano-fluidic nonlinearities can program specific fixed behaviors such as walking straight [53], and passive deformations can induce real-time adaptation to external cues [60]. Inspired by these promising approaches, in this Thesis we ask: Can we take a step further, and embody autonomous capabilities, such as reflexes, environmental feedback, and switching of behaviors, in soft machines with nonlinear fluidic circuits? We will delineate four research objectives to address this general question.

Most soft machines run fixed programs and passively adapt to the environment while locomoting. Beyond real-time adaptation, could soft fluidic machines use their body to remember interactions that occurred in the past, and perhaps forget them when not needed anymore? Would this embodied form of memory enable the machines to program distinct behaviors in response to interactions? Would this approach result in robust autonomous responses when exploring an environment? These questions are summarized within our first research objective:

> OBJECTIVE 1: *Develop fluidic circuits to embody memory effects in the physical structure of soft machines, to enable remembering past interactions beyond passive real-time adaptation.*

With our effort to move complexity in the body of soft machines using fluidic circuits, new challenges arise when trying to understand these phenomena. These challenges are associated with the interactions of internal fluids with the nonlinear mechanical devices, geometric nonlinearities of elastic elements coupled with fluids, and nonlinear dynamics of the various deforming parts. How do we understand such phenomena? What kinds of descriptions are required to gain valuable insights that enable the design of desired behaviors? As a first step in trying to answer these questions, we focus on the hysteretic valve [53] as a case study. We experimentally observed that this valve displays bistability of behaviors. For a given value of input airflow, the valve can be both in a dynamic oscillatory state and in a static, pressure-regulating state. Developing an understanding of this specific coexistence phenomenon can open doors to general analytical tools that could be leveraged to explain also other nonlinear phenomena typical of agents with embodied fluidic circuits. This leads to our second research objective:

> OBJECTIVE 2: *Elucidate the coexistence, in a hysteretic valve, of two qualitatively distinct modes of operation, pressure regulation and oscillation, given the same operating conditions.*

With these approaches, we are able to design in detail the nonlinear internal structure of the legged machines, as if it were a processor that gives instructions to the various limbs. Beyond these designer approaches, can we remove the internal fluidic processor and still obtain rich responses that lead to basic forms of autonomy? Without a clearly defined internal processor, what kind of locomotion strategy could enable robust, responsive coordination of multiple legs? For instance, could legged soft machines switch gaits to avoid obstacles or move in different media solely by relying on phenomena that emerge from interactions between their limbs and the outside world? These questions can be summarized as my third research objective:

> OBJECTIVE 3: *Develop a locomotion strategy for legged soft machines for which autonomy emerges from the physical coupling of their limbs with the surroundings, without a central controller of any kind.*

To operate, these kinds of oscillating fluidic machines need a pneumatic power source that allows inflation of the various body parts. Often, this means relying on bulky and rigid air compressors or pumps and batteries, either external to the machine or placed on board. Instead, can energy be embodied [62] directly in the structure the machines are made of? Could this embodied form of energy spontaneously lead to activity? In summary, our fourth research objective is:

> OBJECTIVE 4: *Investigate an embodied form of energy to instill activity directly in the structure of soft machines, thereby increasing their autonomy by removing the need for external energy sources to oscillate.*

1.5 THESIS CONTRIBUTIONS

In each chapter of this Thesis, we will individually address the four research objectives introduced above.

In Chapter 2, we address Objective 1. We harness the nonlinear response of elastic shells to provide bistability to the fluidic properties of an enclosed cavity. We demonstrate that this bistability enables a locomoting self-oscillating machine to switch between stable frequency states. To program such memory states upon external interactions, we develop fluidic circuits that surround the shell with soft tubes that kink and unkink when touched. We demonstrate both long- and short-term

memory in a soft machine that selects new behaviors in response to a user and that autonomously changes direction after detecting a wall.

In Chapter 3, we address Objective 2 by explaining the phenomenon of the coexistence of pressure regulation and oscillation modes in the soft hysteretic valves used in Chapter 2. We introduce a lumped-parameter model that couples the fluidic domain with the mechanical domain with a set of ordinary differential equations. Drawing from tools from dynamical systems theory, we elucidate the stability characteristics of limit cycles (oscillation) and nodes (regulation). We will then demonstrate that, informed by the model, we can learn specific design strategies with practical implications. As an example, we gain knowledge on a design approach to inhibit the regulation regime, for applications such as the fluidic control of total artificial hearts that should not stop beating.

In Chapter 4, we address Objective 3. We introduce a soft self-oscillating limb made of a single kinked tube that only requires a constant flow of air to perform cyclic stepping motions at frequencies reaching 300 Hz. When multiple limbs are fluidically coupled together, they synchronize and induce locomotion gaits for high-speed locomotion, orders of magnitude higher than comparable state-of-the-art. When similar limbs are implicitly coupled through the mechanical interactions with the environment, synchronized gaits spontaneously emerge from the physics, without the need for control signals. The synchronization patterns dynamically respond to variations in the environmental conditions, enabling these seemingly simple devices to exhibit autonomy, including obstacle avoidance, amphibious gait transitions, and phototaxis.

In Chapter 5, we address Objective 4 by exploring active oscillations that arise from the coupling between a catalytic reaction of an energy-dense fuel and the mechanical response of elastic membranes. We introduce an experimental apparatus where a catalyst connected to an elastomeric membrane is held over a container filled with liquid hydrogen peroxide as fuel. We observe a self-sustained limit cycle where the reaction subsequently activates and deactivates, and the membrane inflates and deflates cyclically. With a lumped-parameter model, we learn that the active oscillation arises from a separation of timescales between the capillary action and the catalytic reaction, and a negative feedback induced by the membrane deformation. Hence, this soft device embodies activity in its physical composition, in that the internal energy release is a state variable responsible for sustaining the self-oscillation.

Overall, this Thesis on embodying autonomy in soft machines sets the foundation for the design and physical understanding of artificial creatures that will roam around our world autonomously, displaying life-like, rich, and responsive behaviors despite not relying on complex brains.

2

EMBODYING MECHANO-FLUIDIC MEMORY IN SOFT MACHINES TO PROGRAM BEHAVIORS UPON INTERACTIONS

PUBLISHED AS: Comoretto, A., Koppen, S., Mandke, T., and Overvelde, J.T.B., Embodying mechano-fluidic memory in soft machines to program behaviors upon interactions, *Device* 3, 100863 (2025)

ABSTRACT

Soft machines display shape adaptation to external circumstances due to their intrinsic compliance. To achieve increasingly responsive behaviors upon interactions without relying on centralized computation, embodying memory directly in the machines' structure is crucial. Here, we harness the bistability of elastic shells to alter the fluidic properties of an enclosed cavity, thereby switching between stable frequency states of a locomoting self-oscillating machine. To program these memory states upon interactions, we develop fluidic circuits surrounding the bistable shell, with soft tubes that kink and unkink when externally touched. We implement circuits for both long-term and short-term memory in a soft machine that switches behaviors in response to a human user and that autonomously changes direction after detecting a wall. By harnessing only geometry and elasticity, embodying memory allows physical structures without a central brain to exhibit autonomous feats that are typically reserved for computer-based robotic systems.

2.1 INTRODUCTION

Soft robots are being developed for autonomous operation in the complex real world [63]. Often inspired by biological systems [28], soft robots passively adapt to external stimuli due to their intrinsic compliance [64]. This passive adaptability at the level of material and structure, often called mechanical or embodied intelligence [38], enables soft robots to accomplish tasks such as grasping a wide variety of objects using the same gripper [65], walking over uneven terrain [66], resisting from external damage [31, 39], and even self-healing [67].

Their natural counterpart, animals, achieve feats that are more complex than mechanical adaptation: they often dynamically change their behaviors in response to external stimuli. For instance, sea stars typically slowly explore the environment in search of food, but when threatened by predators, they suddenly enter a fast galloping gait as an escape response [9, 68]. Salamanders switch between two stable locomoting gaits: undulatory swimming in the water and slower stepping motions on the ground [69, 70]. Even the relatively simple organism *Caenorhabditis elegans* switches between basic behavioral states of locomotion, such as forward moving and turning, depending on the surroundings, previous experiences, and internal factors [71]. In general, this switching of behaviors can be seen as a form of memory, where each adopted behavior is a stable memory state that depends on past events.

In an effort to provide soft machines with this kind of responsiveness, researchers developed artificial systems that harness structural phenomena to passively exhibit distinct behaviors depending on external cues. Mechanical robots, in which geometric nonlinearities combined with elasticity lead to reprogrammable mechanisms with multi-welled energy landscapes, continuously change the internal activation sequences as a direct response to interactions [72]. Soft twisting liquid crystal elastomers [73] and elasto-active structures [60] exploit environmental interactions and passive shape reconfiguration to solve mazes. Soft modular machines sense and respond to different external stimuli by harnessing responsive materials [74]. In Chapter 4, we will introduce soft machines with self-oscillating limbs [75] that passively tune their synchronization pattern depending on external cues through implicit coupling with the surrounding medium. These exciting initial advances point toward embodying switchable behaviors within the physical structure of the machine itself. In this direction, there is ample room for further investigation in understanding and then utilizing structural phenomena not only for mechanical shape adaptation but also for behavioral adaptation [76].

In particular, the implementation of memory, where current behaviors depend on past stimuli [77–84], has been explored in multistable struc-

tures such as elastic beams [79], origami [80], corrugated sheets [81], and crumpled paper [82]. Multistability allows these systems to transition from one stable state to another upon applying a stimulus (for instance, at time t^*). Crucially, at a later time t when the system is in this new state and the stimulus is not applied anymore, the state is stable, and thereby it carries information of the past stimulus that occurred at time $t^* < t$. This kind of memory remains largely unexplored in locomoting soft machines. Embodying memory in the physical structure of the machines would enable them to selectively program desired, stable behaviors in response to external interactions.

Focusing in this work on soft fluidic machines, fluidic circuits [45], consisting of interconnections of pneumatic tubings [46–48] and nonlinear inflatable elements [41, 85] and valves [49, 50, 52–55, 86], represent a promising platform for implementing behaviors at the centimeter scale. In fact, multiple tools and tools are available to designers, including viscous flow [46, 47], snap-through instabilities [41, 44, 87], transistors [51] and oscillators [50, 53, 54, 58, 75, 88]. Fluidic circuits have proven effective for a variety of behaviors, including sequential activation of soft fingers [53], automatic gripping [50, 52], and open-loop gait control for walking robots [44, 53, 55, 57, 58]. Despite the progress at the component and circuitry level, integration in autonomous systems capable of responding and adapting to changing environmental circumstances remains elusive. One exception consists of changing behavior in response to external cues only once, as seen in a walker that changes locomotion direction when obstructed [57], and in an extensible gripper developed in our group that transitions from searching to retrieving a sensed object [89].

Here, by instilling memory effects in the physical body of soft fluidic machines, we enable the programmability of stable behaviors upon repeated interactions with the surroundings. We start from a soft robotic crawler (Section 2.2), to which we provide memory by harnessing the bistability of elastic shells [90] (Section 2.3). Through fluidic circuits that surround the shells, we show both long-term and short-term memory of touch interactions (Sections 2.4 and 2.5). After each interaction, the memory state is rewritten, and the response of the machine changes accordingly (Section 2.6). Equipped with fluidic antennae, the machine detects the presence of obstacles, memorizes the information of the detection, and responds by autonomously steering away (Section 2.7). By introducing such a physical form of memory, we expand the repertoire of design tools for autonomous soft machines [60, 72–75], which can now remember interactions after they occur, in addition to passively responding to them.

2.2 A SELF-OSCILLATING SOFT FLUIDIC MACHINE

We start by designing a self-oscillating locomoting machine consisting of a single pneumatic bending actuator (Fig. 2.1A). Given a constant pressure source, the machine crawls in a pulsatile fashion, because it is cyclically activated through a hysteretic valve [53] mounted inside the machine. Given constant inflow, the valve oscillates between a closed state (Fig. 2.1B) and an open state (Fig. 2.1C). While oscillating, the valve goes through several stages (Fig. 2.12), as we will analyze in depth in Chapter 3. *i)* When the valve is closed, no air flow is delivered to the actuator, and pressure upstream increases. *ii)* When a critical pressure is reached, the valve snaps to the open state, allowing flow to the actuator, decreasing pressure upstream. *iii)* When a low critical pressure difference is reached, the valve snaps back to the closed state. This hysteresis in opening and closing results in cyclic inflation and deflation of the actuator, leading to forward locomotion.

The fluidic circuit carried by, and activating, the machine (Fig. 2.1D) is characterized by six key physical parameters. *i)* The pressure source value together with the *ii)* pre-resistor with resistance R_{pre} determine the amount of inflow to the valve. That is, both a larger pressure source and a smaller pre-resistance lead to higher inflow. *iii)* The pre-capacitance with volume V_{pre} is responsible for the timescale of charging, where larger volume leads to longer charging. After the valve, we place *iv)* the actuator that acts as a capacitance with geometric volume $V_{actuator}$, *v)* the after-capacitance with volume V_{after}, and *vi)* the after-resistance R_{after}, responsible for the amount of inflation of the actuator and the discharge time [53].

Practically, we build the pre-resistor as a custom-made silicone tube with a small inner diameter of 0.35 mm, outer diameter 5 mm and length 40 mm through injection molding; the after-resistor is an off-the-shelf needle (20 Gauge, 0.5 in length); the capacitors are thin inextensible pouches custom-made through heat-sealing of nylon-coated thermoplastic polyurethane (TPU) sheets [91]; the pneumatic bending actuator is a two-material PneuNet custom-made through injection-molding [92] (Section 2.9.2).

The pulsatile inflation of the actuator induced by the fluidic circuit causes the machine to move forward at a speed of 0.76 cm/s (2.85 body lengths per minute) (Fig. 2.2A,B) through consecutive crawling motion of ~ 5.3 mm each (0.03 body lengths for each cycle) (Fig. 2.2C). This single-input crawling machine is purposefully simple in its behavior, that is, moving forward at a specific average speed. Throughout the article, we will use this unit and its associated fluidic circuit as a building block to construct more complex behaviors by adding memory and sensing features to the circuit and assembling multiple units together.

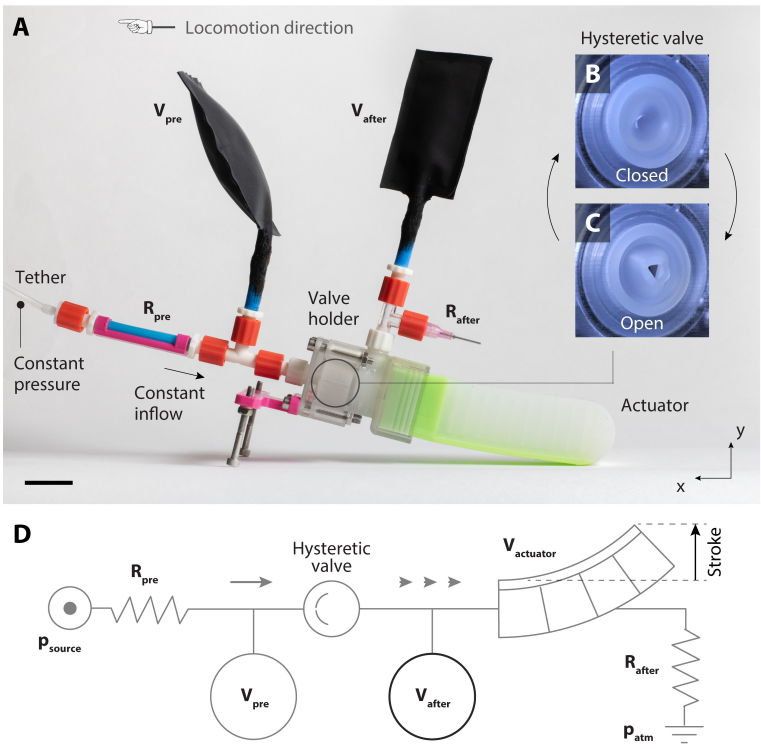

Figure 2.1
A SELF-OSCILLATING SOFT FLUIDIC MACHINE. (**A**) A soft crawling machine is equipped with a bending actuator, pre- and after-capacitances (V_{pre} and V_{after}), pre- and after-resistances (R_{pre} and R_{after}), and a hysteretic valve mounted in a rigid holder. Scale bar is 2 cm. A single tether provides constant pressure to the pre-resistance. Given the approximately constant inflow from the pre-resistance, the soft hysteretic valve oscillates between (**B**) closed and (**C**) open states, enabling pulsatile actuation of the bending actuator. (**D**) Schematic of the fluidic circuit embedded in the soft machine.

As a start, we observe that varying the physical parameters of the circuit directly results in a change of behavior of the machine. For example, in a benchtop experiment with the actuator not interacting with the ground (Section 2.9.3), increasing the volume of the after-capacitance from 0 mL to 40 mL results in the activation frequency decreasing from 1.65 Hz to 1.39 Hz (Fig. 2.2D) and the vertical stroke of the actuator lowering from 2.7 cm to 1.6 cm (Fig. 2.2E). This change in after-capacitance volume has a direct consequence on the speed of the locomoting machine. Adding an after-capacitance with volume 40 mL causes the machine to crawl slower at 0.4 cm/s, at approximately one third of the original speed (1.1 cm/s) (Fig. 2.2F). Varying other physical parameters also affect the

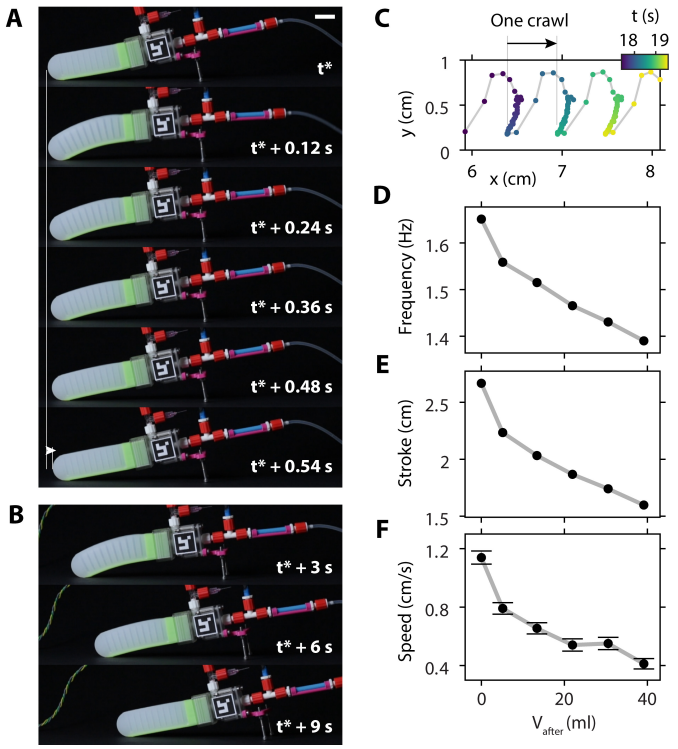

Figure 2.2
THE SOFT FLUIDIC MACHINE LOCOMOTES FORWARD. (**A**) Locomotion of the crawler during one oscillation cycle lasting 0.54 s. Scale bar is 2 cm. (**B**) Location of the crawler after 3 s, 6 s, and 9 s. (**C**) Horizontal and vertical coordinates of the rigid holder of the locomoting machine. Influence of the after-capacitance geometrical volume V_{after} on (**D**) the oscillation frequency of the actuator, (**E**) the vertical stroke of the actuator as defined in Fig. 2.1D, and (**F**) the average speed of the machine.

behavior. For instance, increasing the pre-capacitance from 0 mL to 70 mL leads to a higher vertical stroke of the actuator (Fig. 2.13).

2.3 MEMORY VIA A BISTABLE MECHANO-FLUIDIC CAPACITOR

To introduce memory in the system, we provide bistability to a physical parameter of the self-oscillating circuit, so that the crawling behavior also becomes bistable. In our specific case, we focus on the after-capacitance, as the speed of the machine is particularly sensitive to this parameter. This is because increasing the after-capacitance leads to a decrease in both the actuator's stroke and frequency, while increasing the pre-

capacitance leads to an increase in stroke but a decrease in frequency, with a negligible net change in speed (Fig. 2.13).

To provide bistability to the after-capacitance, we use elastic shells, as they are well-studied structures and exhibit rich nonlinear behavior [50, 90, 93–98]. The design parameters such as thickness, base width, and shallowness angle (Fig. 2.14) can be tuned [50] so that the shell displays bistability [90], with a 'rest' stable state (Fig. 2.3A) and a 'snapped' stable state (Fig. 2.3B). We mount the soft shell in a rigid shell-shaped holder, obtaining a fluidic capacitor with a relatively small (compared to the soft actuator) geometric volume of ~ 0.8 mL enclosed between the two shells when the elastic shell is in its rest state (Fig. 2.3C). The second stable state of the bistable capacitor is accessed by popping the shell to the snapped state, obtaining a relatively large geometric volume (~ 34 mL) (Fig. 2.3D).

The behavior of the bistable capacitor upon inflation is highly nonlinear. The pressure-volume curve of the capacitor (Fig. 2.3E) highlights two stable regimes that cross the zero-pressure line, which is essential to enable bistability. Increasing (or decreasing) pressure past the critical snap-through (or snap-back) pressure allows for switching from one stable regime to the other (Fig. 2.3E, pink arrows). Once the system is placed in one regime, removing pressure results in the capacitor being stable at one of the two states (0.8 mL or 34 mL). Note how this highly nonlinear, non-monotonic behavior fundamentally differs from capacitors (i.e., actuators) typically used in fluidic circuits [53]. Such capacitors are often characterized by a monotonic pressure-volume curve, even when displaying nonlinear behaviors, such as stiffening or softening (Fig 2.15).

We physically mount the bistable capacitor on the crawler (Fig. 2.3F), fluidically connected in the circuit as after-capacitance V_{after} (Fig. 2.3G). We start by setting the bistable capacitor to the snapped state with large volume (Fig. 2.3F). When we provide a constant pressure of 1.3 bar to the tether, the machine locomotes at a speed of ~ 0.4 cm/s (Fig. 2.3H,I). After ~ 30 s, we manually pop the shell to the rest state, so that the capacitance snaps to the small-volume state (Movie 2.1). After this external interaction, the machine is moving at a higher speed of ~ 0.8 cm/s (Fig. 2.3H,J), as expected from Figure 2.1, because of the lower after-capacitance. Crucially, the bistability of the fluidic after-capacitance directly results in two stable outcome behaviors of the machine. We refer to this mechano-fluidic bistability as memory, as the state of the system at a given current time t reflects interactions that occurred in the past at time $t^* < t$ [77–84]. In the example experiment in Figure 2.3H-J, the speed of the machine at time $t = 60$ s reflects the past interaction of popping the shell that occurred at time $t^* \approx 35$ s.

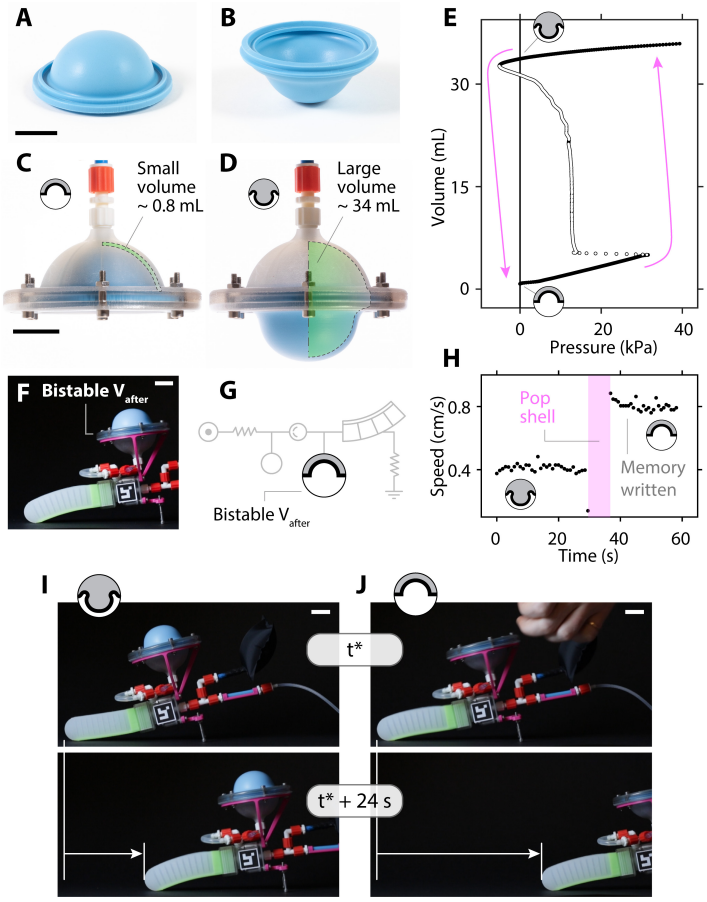

Figure 2.3

EMBODYING MEMORY VIA A BISTABLE MECHANO-FLUIDIC CAPACITOR. An elastomeric shell with thickness 3 mm, base width 55 mm, and shallowness angle 80° displays two stable states, (**A**) a rest state and (**B**) a popped state. When the soft shell is mounted on a rigid shell-shaped holder, the geometric volume between the two shells also displays two states, (**C**) a small volume state and (**D**) a large volume state. (**E**) Increasing (or decreasing) pressure above (or below) the critical snap-through (or snap-back) pressure allows for switching between the two states (pink arrows). Markers filled in white are consecutive datapoints for which pressure decreases for increasing volume, hence representing the negative slope of the pressure-volume curve. (**F**) We physically mount the bistable capacitor on top of the crawler, (**G**) fluidically connected as an after-capacitance. (**H**) We write the memory state by popping the shell while the machine crawls so that the machine switches from the first stable state with speed ~ 0.4 cm/s to the second stable state with speed ~ 0.8 cm/s. Snapshots of the crawling machine in (**I**) the low-speed state and in (**J**) the high-speed state. All scale bars are 2 cm.

2.4 FLUIDIC CIRCUITS FOR LONG-TERM AND SHORT-TERM MEMORY

We demonstrated a bistable behavior through a mechano-fluidic memory element. So far, the memory state could be written only once by manually popping the shell from the snapped state to the rest state. In addition, we needed a relatively high external force to write the memory state ($\sim 13\,\mathrm{N}$, given the surface area of the human thumb $\sim 3.2\,\mathrm{cm}^2$ [99] and the internal pressure $\sim 40\,\mathrm{kPa}$). We now aim to repeatably change behavior upon consecutive limited-power interactions with the environment. We develop fluidic circuits around the bistable capacitor to obtain long-term memory (Fig. 2.4A) and short-term memory (Fig. 2.5A) that require lower power to switch states (compared to $\sim 1\,\mathrm{W}$ when manually popping the dome with a force in the order of $10\,\mathrm{N}$ at a speed in the order of $10\,\mathrm{cm/s}$). Note that we refer to the concepts of short- and long-term memory from a behavioral neuroscience point of view: short-term memories of the stimuli are temporary and last for a short amount of time before they fade out, while long-term memory refers to permanently lasting memories of events [100, 101].

We develop a long-term memory circuit (Fig. 2.4B) by building upon the circuit with the bistable capacitor in Figure 2.3G. *i)* We add a branch in parallel to the source, connected to the bottom chamber of the memory element, opposite to the actuator. *ii)* In this new branch, we introduce a normally closed (NC) valve upstream and a venting resistance R_{vent} downstream (22 Gauge, 0.5 in). *iii)* We add a normally open (NO) valve in the actuator branch, between the actuator and the downstream resistance. We can interact with this circuit by closing (and opening) the NO (and NC) valves. To design and test these circuits, we make use of solenoid valves controlled with an input/output electronic board (Section 2.9.3), which we will replace in later Sections with soft tubes that kink and unkink [48].

By closing the NO valve, the actuator line pressurizes (Fig. 2.4C). When the pressure reaches the snap-through pressure of the shell, the shell snaps to the other state, and the capacitor is in the large volume state. This, in turn, causes the system behavior to operate at low frequency and stroke. Then, we can open the NC valve (Fig. 2.4D), so that the bottom line pressurizes. When the pressure difference between the bottom and top lines reaches the snap-back pressure of the shell, the shell snaps back to the rest state, causing the system behavior to operate at high frequency and stroke.[1] Each time the memory is set to either state, the reached state is stable until the next interaction, as a consequence of

1 Note that the NC (or NO) valve could be opened (or closed) even when the shell is already in the desired rest (or snapped) state: this stimulus would not change the output, as the shell would stay in the state it already is.

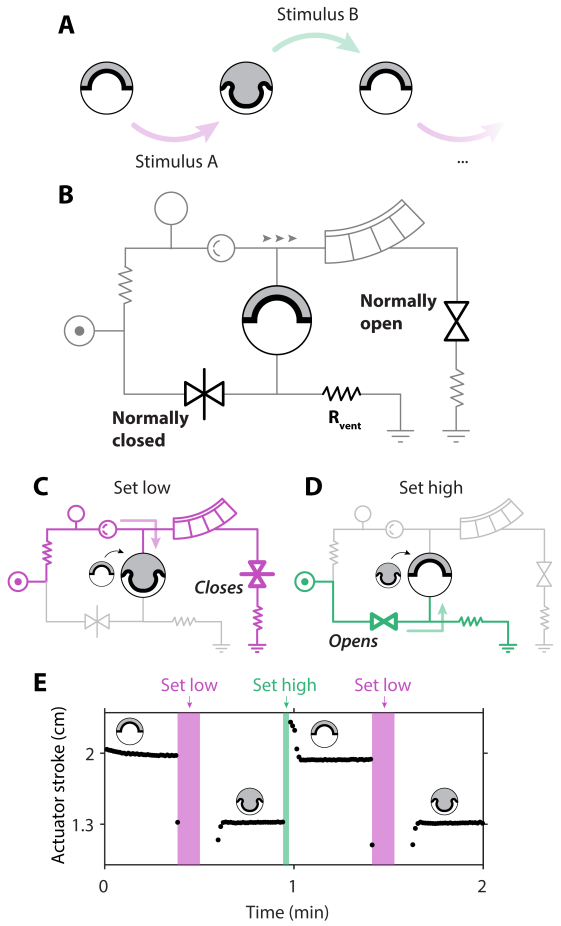

Figure 2.4
FLUIDIC CIRCUIT FOR LONG-TERM MEMORY. (**A**) Long-term memory involves programming stable states given occurring stimuli. (**B**) The long-term memory circuit is equipped with a normally open (NO) valve, a normally closed (NC) valve, and a venting resistance R_{vent} placed at the bottom chamber line. (**C**) We set the system to the state with low stroke and frequency (high after-capacitance) by closing the NO valve, thereby pressurizing the top chamber and snapping the shell. (**D**) We set the system to the other state by opening the NC valve, resulting in snap-back of the shell. (**E**) Actuator stroke in time, with consecutive events of writing memory.

the bistability of the shell (Fig. 2.4E and Movie 2.2). Therefore, each time a stimulus occurs (opening/closing of NC/NO valves), the system expresses the memory of the past stimulus through its current behavior (frequency and stroke).

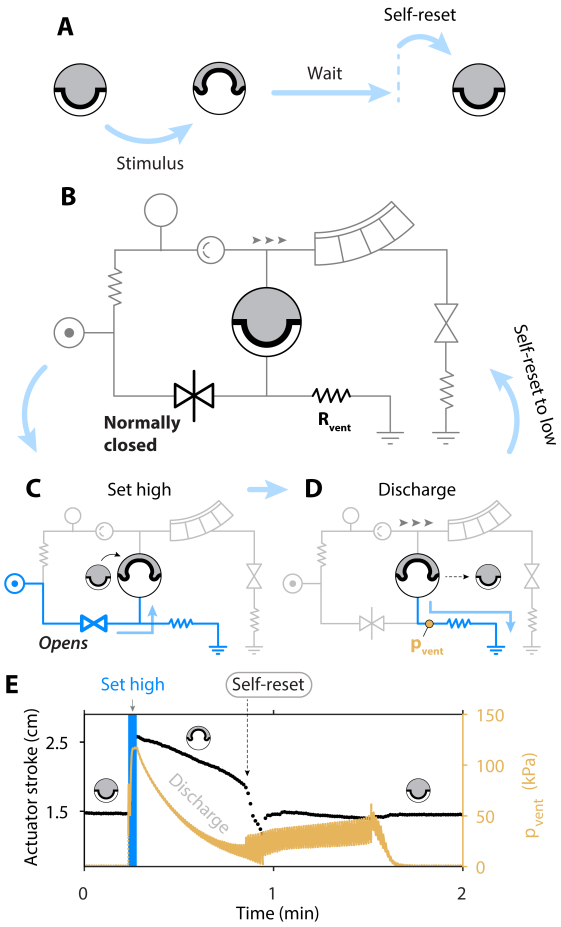

Figure 2.5
FLUIDIC CIRCUIT FOR SHORT-TERM MEMORY. (**A**) Short-term memory stores information of the past stimulus for a determined amount of time, and then self-resets to the initial state. (**B**) The short-term memory circuit is equivalent to the long-term memory circuit, with the only differences being the orientation of the shell in its rest state and the NO valve not being used. (**C**) We write the memory by opening the NC valve, resulting in the shell snapping. (**D**) After this writing action, the bottom chamber is pressurized (p_{vent}), and air leaks through the venting resistance, causing a pressure discharge in time, until the shell snaps back, causing a self-reset of the system to the low-stroke state in B. (**E**) Actuator stroke (black) and p_{vent} (yellow) in time.

Starting from the design of the long-term memory circuit, we develop a short-term memory circuit (Fig. 2.5B). This circuit is equivalent to the long-term memory circuit, with the only differences being a higher venting resistance (32 Gauge, 0.25 in needle), and the shell flipped so

that, in the rest state, the chamber connected to the actuator line is in the high-capacitance state (Fig. 2.5B, grey area above the shell). By opening the NC valve, the pressure in the bottom line increases until the shell snaps, and the system behavior is set to the state with high frequency and stroke (Fig. 2.5C).

After this initial interaction that sets the memory element to the other state, a seemingly counterintuitive behavior occurs, resulting in short-term memory. Given the bistability of the shell, at first, one would expect this system to be bistable as well and, as a consequence, to stabilize at the high state until the next interaction occurs. However, at a system level, two phenomena with two distinct timescales occur simultaneously after the NC valve has been opened: i) pressure p_{vent} in the bottom chamber decreases relatively slowly in time as air vents to the atmosphere through the resistance R_{vent} (Fig. 2.5D and Fig. 2.5E, yellow); ii) pressure in the top chamber oscillates between ~ 1 kPa and ~ 35 kPa, because of the hysteretic valve oscillating with a timescale which is faster than the discharge mentioned above. Given these two phenomena with different timescales, as long as the difference between the bottom and top chamber is greater than the snap-back pressure of the shell (~ −10 kPa), the shell is in the stable snapped branch, because the stability of the shell is determined by the pressure difference between its top and bottom surface (Fig. 2.3E). When the pressure difference between the bottom chamber and the top chamber decreases below ~ −10 kPa, the shell snaps back spontaneously, without external interactions (Fig. 2.16 and Movie 2.2). As a consequence, the system self-resets to the low state (Fig. 2.5E, black).

Note that the snap-back of the shell is not instantaneous, but instead, it lasts approximately 45 s. This is a consequence of the high venting resistance R_{vent} (32 Gauge, 0.25 in needle) limiting airflow. Once the shell initiates the snap-back, it fights against this high venting resistance, effectively compressing the air in the bottom chamber. The signature of this effect, which counters the snap-back of the shell, can be seen in the sudden increase of the pressure p_{vent} in the bottom chamber when the shell initiates the snap-back (Fig. 2.16 and Fig. 2.5E, yellow). During this intermediate phase, the shell is operating in the negative-stiffness regime highlighted with white markers in Figure 2.3E. When the shell is completely snapped back, at around 90 s in the experiment, p_{vent} finally drops to zero (Fig. 2.5E, rest symbol). Nevertheless, we identify the initiation of the snap-back as the instant when the behavior of the system self-resets to the initial state, because this event is associated with the stroke of the actuator returning to approximately the initial value (Fig. 2.5E, black).

Therefore, the short-term memory circuit temporarily stores information by setting the memory element to the snapped state. After a specific

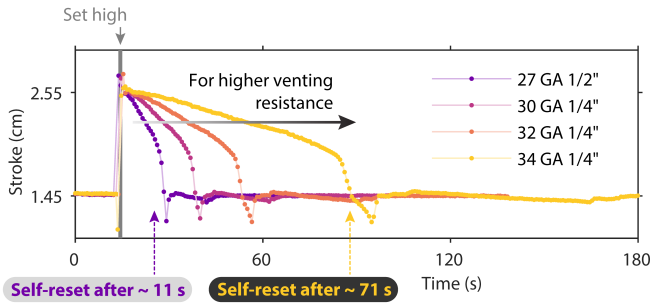

Figure 2.6
INCREASING THE VENTING RESISTANCE LEADS TO A HIGHER MEMORY-RETENTION TIME. We test the short-term memory circuit (Fig. 2.5) for different values of venting resistance (different commercial needles, Metcal). After opening the normally closed valve, the memory element snaps, and the system is set to the high-stroke state. In the case of the lowest resistance tested (27 Gauge, 0.5 in needle), the system self-resets to the low state (the shell snaps back) after ~ 11 s (purple line). For higher venting resistance, the time required to self-reset (memory-retention time) increases. In the case of the highest resistance tested (34 Gauge, 0.25 in needle), the memory-retention time is ~ 71 s (yellow line).

memory-retention time, the system spontaneously self-resets to the rest state (as it was before the interaction occurred) and hence the memory of the occurred stimuli fades away. The memory-retention time can be tuned by selecting different values of venting resistance: higher venting resistance results in slower discharge and, therefore, longer memory-retention time. Within the set of venting resistances that we tested, the memory-retention time ranged from 11 s to 71 s (Fig. 2.6).

2.5 FLUIDIC TOUCH SENSING VIA KINKING TUBES

So far, we could interact with the long- and short-term memory circuits through NO and NC solenoid valves, requiring a 24 V signal to close and open the valves (Section 2.9.3). With the goal of developing fully-fluidic machines that can interact with the surroundings, we aim to develop NO and NC touch sensors harnessing the kinking behavior of soft tubes [48]. We build a NO sensor by bending a commercial elastomeric tube with inner diameter 3 mm, thickness 1 mm, and length 70 mm (Fig. 2.7A). We mechanically compress the tube to a maximum displacement u_{max} corresponding to the top part of the tube touching the bottom rigid holder. At the same time, we measure the fluidic resistance R_t of the tube as the ratio between the inlet-outlet pressure difference and the flow through the tube. While loading, we observe an initial deformation, followed by a sudden formation of two kinks (Fig. 2.7A).

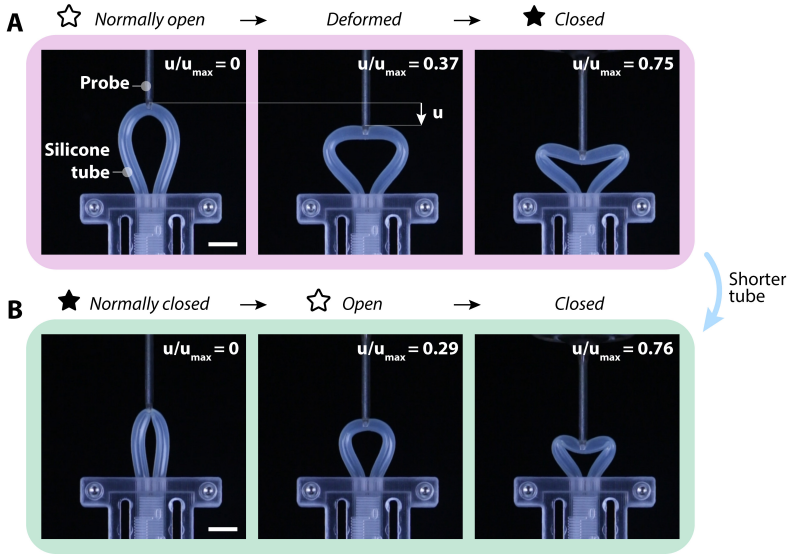

Figure 2.7
FLUIDIC TOUCH SENSING VIA NORMALLY OPEN AND NORMALLY CLOSED KINKING TUBES. A silicone tube (inner diameter 3 mm, thickness 1 mm, and length 70 mm) is bent 180°. (**A**) A probe compresses the tube by moving vertically with a displacement u, first inducing the tube's deformation and then forming two kinks that close the channel. (**B**) A shorter tube of length 50 mm displays a kink in its rest state (normally closed), it unkinks (opens) when compressed, and it forms two kinks when further compressed. All scale bars are 1 cm.

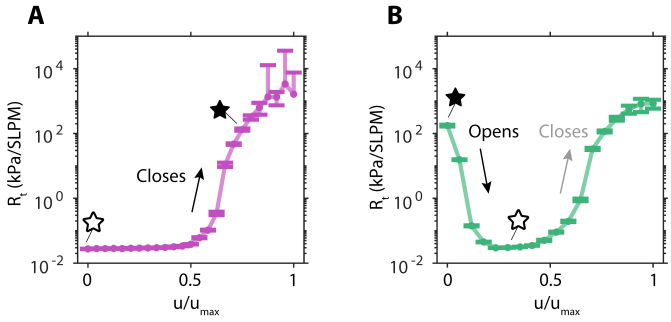

Figure 2.8
FLUIDIC RESISTANCE OF THE TUBES AS A FUNCTION OF PROBE DISPLACEMENT. (**A**) The fluidic resistance of the tube R_t sharply increases when the two kinks form (tube closes). (**B**) The fluidic resistance of the normally closed tube shows an initial drop (when the tube unkinks, opening) with a subsequent increase (when the two kinks form, closing). Labels ☆ and ★ relate to the photos in Figure 2.7.

The flow resistance is relatively low ($\sim 1.5 \times 10^{-2}$ kPa/SLPM) when the tube is not deformed ($u/u_{max} = 0$) (Fig. 2.8A, white star). The resistance stays at approximately the same value until half the maximum probing displacement ($u = 0.5 \cdot u_{max}$). Then, the resistance suddenly increases to $\sim 1 \times 10^{1}$ kPa/SLPM when $u = 0.6 \cdot u_{max}$. This increase corresponds with the formation of two kinks that block air flow (Fig. 2.7A, black star). The resistance then increases exponentially with increasing probing displacement, as the kinks sharpen further. We call this high-resistance state the closed state (Fig. 2.8A, black star), as leakage is limited. So, effectively, the tube is a sensor that transduces information from the mechanical domain (that is, the compressing interaction) into the fluidic domain (that is, the resistance of a fluidic channel).

To build the NC sensor, we found that we can act on a single design parameter of the tube. In fact, by reducing the length of the tube from 70 mm to 50 mm, a kink spontaneously forms when the tube is not probed (Fig. 2.7B, black star). This is accompanied by the resistance being relatively high ($\sim 1 \times 10^{2}$ kPa/SLPM) (Fig. 2.8B, black star): the sensor is in a normally closed state. By compressing, the tube unkinks (Fig. 2.7B, white star), opening the channel and suddenly decreasing the resistance to $\sim 1.5 \times 10^{-2}$ kPa/SLPM (Fig. 2.8B, white star). So, the shorter tube is an NC sensor that opens upon interaction. In addition, by further probing the tube after the opening event, it closes again, as two kinks form (Fig. 2.7B).

Therefore, we obtained a touch sensor that, depending on the design parameters, can be in a NO or a NC setting. Interestingly, the NO and NC mechano-fluidic sensors transduce qualitatively equivalent mechanical inputs (compression in one direction) in distinct fluidic information, consisting of closing and opening of channels.

2.6 INTEGRATED MEMORY AND SENSING FOR PROGRAMMABLE BEHAVIORS

So far, we introduced a number of separate ingredients that, when integrated together, we will show can result in programmable behaviors. We have *i)* the forward crawling platform (Fig. 2.1 and Fig. 2.2); *ii)* the mechano-fluidic memory element (Fig. 2.3), responsible for providing memory of a stimulus in the form of change in behavior; *iii)* the short- and long-term memory circuit designs (Fig. 2.4 and Fig. 2.5), that read fluidic stimuli in the form of opening and closing of channels; *iv)* the touch sensors (Fig. 2.7 and Fig. 2.8), to transduce mechanical stimuli into fluidic ones when a user vertically compresses the tube.

Now, we integrate these ingredients in a locomoting soft machine that senses external mechanical cues and reacts accordingly (Fig. 2.9A). The

machine has two mirrored sides. Each side is built starting from the single-actuator crawling platform, with the memory element and the NO and NC touch sensors placed on top. Internally, the fluidic circuit of each mirrored side is identical to the circuit in Figure 2.4. The two sides of the machine are physically connected with a bearing, to allow rotation of the two sides relative to each other, as the crawling behavior relies on the rotation induced by the bending actuator (Fig. 2.17). In total, the machine integrates two bending actuators, two hysteretic valves, two memory elements, four touch sensors, and a single tether connected to a pressure source of 1.3 bar.

With two bistable memory elements, the machine has four stable locomoting behaviors (Fig. 2.9B): *i)* forward slow, when both individual capacitors are set to the large volume state; *ii)* forward fast, when both are set to the small volume state; *iii)* steer left, when the right capacitor is set to small volume state and the left to large volume state, as the right side of the machine moves at a faster speed compared to the left side, causing global steering; *iv)* steer right, when the right capacitor is set to large volume and the left to small.

In Figure 2.10A, we report the trajectory of the machine locomoting in an arena when receiving touch cues from a human user, with both circuits set to the long-term memory configuration from Figure 2.4A. The machine starts with both capacitors set to small volume (both shells set to the rest state). Hence, the machine starts locomoting with the fast-forward behavior. Then, the human interacts with the left NO sensor, closing it. After the interaction, the machine steers to the left because the left memory element is set to the large-volume state, and the resulting speed of the left side is lower than the right side. The memory is retained until a new mechanical cue occurs. After the operator closes the right NO sensor by touching it, the machine displays the slow-forward behavior. With the next two interactions, the machine steers to the right and then goes back to the initial fast-forward behavior (Movie 2.3). Additionally, we can interact with two sensors at the same time, closing one and opening the other, to directly switch between sterring left and steering right (Movie 2.3).

When we set the internal circuit to the short-term memory configuration of Figure 2.5B by flipping the orientation of the memory element and increasing the venting resistance (replacing it with a 34 Gauge, 0.25 in needle), the machine also displays short-term memory (Fig. 2.10B). The machine starts with the slow-forward locomoting behavior. After the user interacts with the left sensor, the left side is set to the high-speed state, and the machine displays the right-steering behavior. After approximately one minute, the left memory element self-resets to the initial state, and the machine returns to the forward-locomoting behavior (Movie 2.3). Therefore, the memory of the interaction is retained for approximately

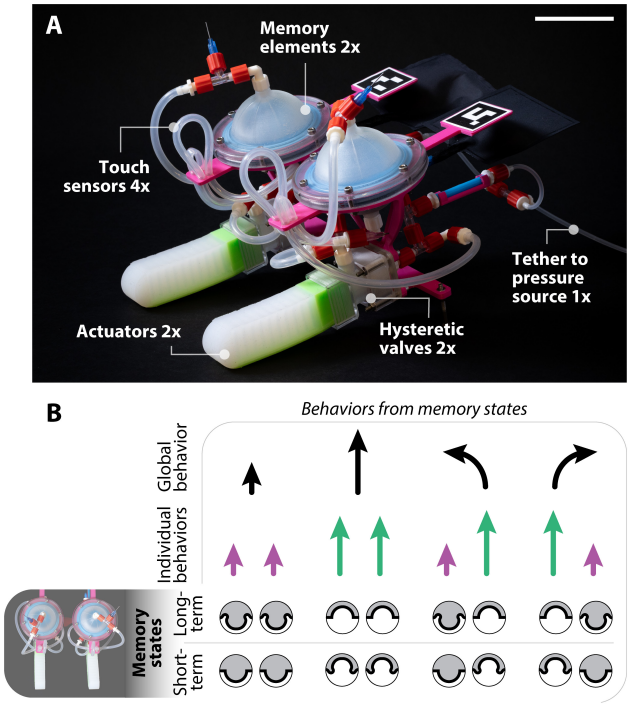

Figure 2.9
INTEGRATION OF MEMORY AND SENSING FOR PROGRAMMABLE BEHAVIORS UPON USER INTERACTIONS. (**A**) We build a two-limb machine by mirroring our single-limb platform in Figure 2.3. The machine is powered by one pressure tether and is equipped with two hysteretic valves, two actuators, two memory elements (bistable shells), and four touch sensors (of which two NO and two NC). Scale bar is 5 cm. (**B**) The individual states of the two memory elements impact the individual behavior of the two halves of the machine (low speed: purple, high speed: green), resulting in four different global behaviors of the machine.

one minute so that the machine steers ~ 90°. After this amount of time, the memory of the stimulus is forgotten, and the machine goes back to the default behavior, which is moving forward without steering. Short-term memory implies that we can design a preferred behavior, in this case, moving forward, and a temporary behavior, such as steering, that, upon interaction, overrides the default one for a determined amount of time.

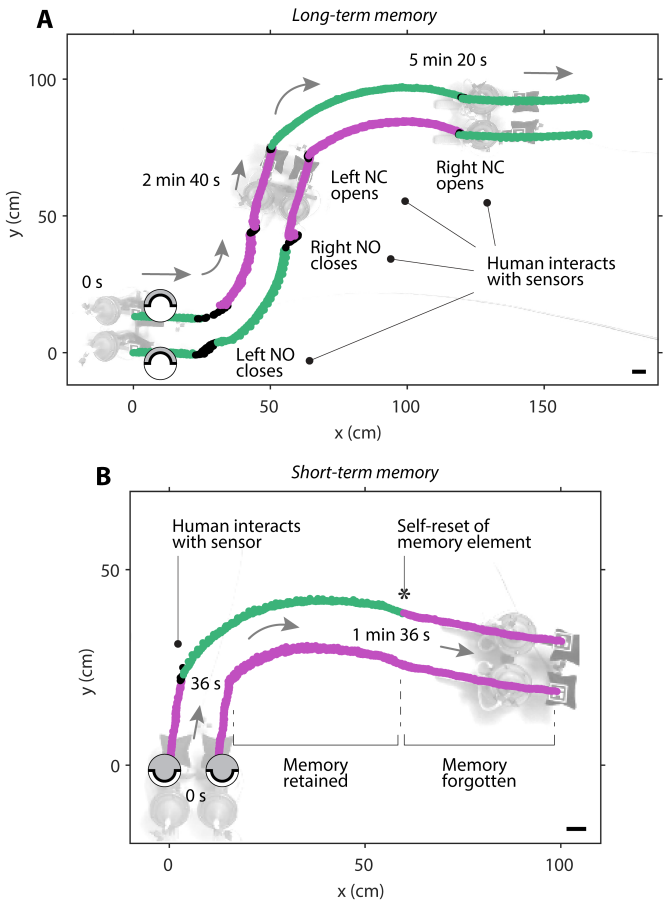

Figure 2.10
THE MACHINE PROGRAMS BEHAVIORS UPON USER INTERACTIONS. (**A**) With long-term memory settings, the machine locomotes in an arena and switches between steering and forward behaviors when an operator interacts with the touch sensors, by closing the NO and opening the NC sensors. (**B**) With short-term memory settings, the machine switches to steering behavior when a human interacts with the sensor, and after ~ 1 min, it spontaneously returns to the initial forward-locomoting state. All scale bars are 5 cm. Purple: slow; green: fast.

2.7 AUTONOMOUS OBSTACLE AVOIDANCE VIA SHORT-TERM MEMORY

So far, the machine was designed for only a specific kind of interaction, where a human user touches the sensor. To demonstrate the potential of integrating memory and sensing for autonomous behaviors, where the machine itself senses the environment without external inputs from

a human, we design an antenna taking inspiration from insects. Often, insects sense the external world with antennae made of relatively rigid flagella and softer pedicel-flagellum junctions (hinges). The hinges are the crucial site for mechanoreception, as they are equipped with dense mechanosensory structures [102]. When the flagellum bends, the receptors in the hinge sense an increase in bending torque, so that the insect detects obstacles [103] or changes in the wind direction [103, 104].

We develop an artificial antenna (Fig. 2.11A-C and Fig. 2.18) composed of a rigid 3D-printed flagellum that rotates around a hinge when it interacts with an external obstacle, such as a wall (Fig. 2.11A). Crucially, when the flagellum rotates, a kinked tube placed at the hinge unkinks (Fig. 2.11B,C), acting like the NC touch sensor from Figure 2.7B. Hence, we localize at the soft hinge the transduction from external mechanical stimuli into internal fluidic information.

We let a machine equipped with two antennae and two short-term memory circuits walk toward a wall with a 45° angle of attack (Fig. 2.11D and Movie 2.4). When the right antenna touches the wall, it rotates around the hinge, unkinking the tube (Fig. 2.11D, label 'Interaction'). This sensing event results in the memory element snapping to the snapped state, following the same mechanism as previously introduced in Figure 2.5C. Then, the machine steers away from the wall for approximately one minute, because the memory of the interaction is retained (Fig. 2.11D, label 'Retain memory'). After this memory-retention time, the memory element self-resets to the initial state, in the same fashion as explained in Figure 2.5D,E. At this moment in time, the machine forgets the previous interaction with the wall, returning to the forward-locomoting behavior (Fig. 2.11D, label 'Forget').

2.8 DISCUSSION

By embodying mechano-fluidic memory in soft machines we obtained programmable behaviors upon interaction with the environment without requiring electronics or software for control. We introduced memory in a soft, self-oscillating crawler through the bistability of a physical parameter of the machine, the capacitance, by leveraging a bistable elastic shell. With long- and short-term memory circuits and kinking tubes as touch sensors, the machine could detect interactions with a user and obstacles, and consequently switch behavior between walking straight and steering.

We instilled memory and feedback effects by coupling together selectively a low number of components (shells and tubes) that display highly nonlinear behavior. This approach parts ways from general-purpose robotics, which instead typically relies on a large number of relatively

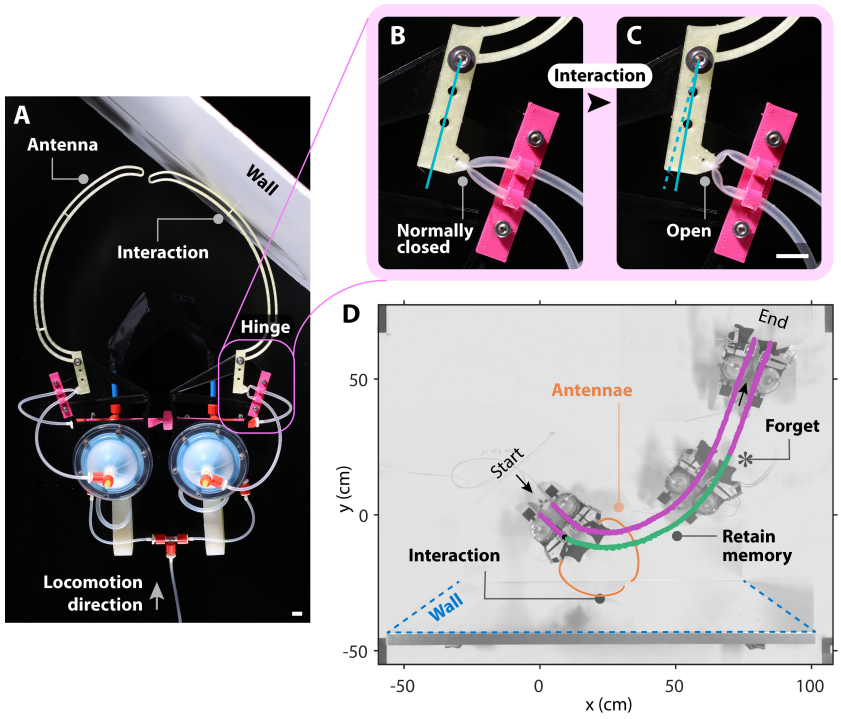

Figure 2.11
AUTONOMOUS OBSTACLE AVOIDANCE THROUGH SHORT-TERM MEMORY AND INSECT-INSPIRED SENSING. (**A**) We place two 3D-printed antennae on board the machine, allowing rotation around a hinge upon external interaction with an obstacle, such as a wall. (**B**) At the hinge, the antenna is equipped with a kinked tube as an NC sensor. (**C**) The tube unkinks upon interaction, effectively sensing the bending moment applied to the antenna and transducing it into fluidic information (drop in fluidic resistance). Scale bars in A and C are 1 cm. (**D**) The autonomous machine senses the presence of a wall, temporarily retains the memory of the interaction by steering away, and finally, forgets the memory of the interaction, going back to the default forward-locomoting behavior.

simple components in a central computer, in the range of billions of nanoscale transistors [105]. We envision that this approach of integrating a limited number of nonlinear components will prove effective for task-specific applications [106] where specialized tasks are pre-specified and robustness is of the essence, as it reduces the overall design complexity in terms of number of components. For instance, in biomedical applications, microrobots could autonomously navigate inside the human body [107] and detect cancer tissues by sensing a difference in stiffness [108, 109] without carrying microelectronics [110]. We also foresee using these mechanical effects as 'reflexes' embedded in the structure of machines,

to which some tasks can be offloaded from a central controller. For example, in space applications, robots could delegate the autonomous exploration task to their mechanical body, preventing the breakdown of the locomoting apparatus in case of solar storm events [111]. For environmental monitoring applications [112], self-oscillating machines could autonomously crawl or swim by harnessing their responsive body. By removing the need for electronics carried on board, the machines could potentially be constructed monolithically [52, 113] with biodegradable materials. By deploying a large number of biodegradable, simple yet robust machines [114] with basic capabilities of sensing and memory, instead of a few general-purpose and relatively complex robots, we envision monitoring remote areas with minimal impact on the surrounding environment. To close the gap between our current exploratory work (focused on the principles of embodied memory) and these real-world applications, further research is required, especially around the topics of energy efficiency and scalability.

Even though our work mainly focused on conceptually demonstrating a way to introduce fluidic circuits with memory and sensing, it is important to note that from a practical perspective, our current implementation of the machines as assemblies of various custom-made parts carries the main downside of limited reliability for real-world applications. For instance, the hysteretic valves have a limited lifetime, as the elastomer degrades around the slits after ~ 100.000 cycles, leading to a change in frequency [53]. The pouch capacitors tend to rupture around the corners after prolonged use (on the order of tens of hours), likely due to stress concentrations. Moreover, the two-actuator locomoting machine intrinsically relies on symmetry between the two halves to avoid drifting while crawling straight. To achieve symmetric behavior, we had to manufacture a relatively large number of samples for each component and select pairs that behaved similarly. For these reasons, in future work, we will focus on more robust manufacturing approaches. For instance, using fluidic oscillators that do not require cutting silicone, such as those that use magnets [115], could improve the machines' lifetime. Moreover, we envision that developing components where multiple functionalities coexist, such as the actuators that also self-oscillate [75] in Chapter 4, will increase the machines' simplicity and, consequently, their reliability.

Our proposed approach will particularly benefit from carefully tuning the interactions [116], both internal to the machines and with the external environment. However, this potential will come with the associated downside of an increased complexity of the design process that takes into account the interactions, especially when they occur in the context of an unknown environment. While here we specifically focused on memory effects, other complex behaviors are within reach through mechanical interactions, as demonstrated by initial results on self-learning

mechanical circuits [117] and many-agent cooperation through implicit mechanical couplings [118]. This 'integrative mechanics' approach is the artificial parallel to integrative biology [119], where complex dynamic behaviors emerge from the interplay between interactions within the agent and with the environment in which the agent is situated. These specialized, distributed, and redundant interactions found in biological systems enable high levels of robustness, while not sacrificing functionality: autonomous machines have the potential to tap into this vast complexity as well, with embodied memory being one step further in this direction.

2.9 SUPPLEMENTARY INFORMATION

Links and descriptions of the movies are reported in Section 2.9.1. The design and manufacturing of the components are reported in Section 2.9.2. We describe the experimental setups in Section 2.9.3. Supplementary figures are reported in Section 2.9.4.

2.9.1 *Movies*

All the movies related to this chapter are available at this link. If you are holding a paper version, you can scan this QR code:

MOVIE 2.1

MEMORY THROUGH A BISTABLE SHELL. (i) Snapping the bistable shell reprograms the behavior of the soft fluidic machine, which changes locomotion speed. (ii) Side-by-side speed comparison between the two stable states.

MOVIE 2.2

LONG- AND SHORT-TERM MEMORY. (i) The long-term memory circuit allows to write and rewrite memory states. (ii) The short-term memory circuit spontaneously self-resets to the initial state after a memory-retention time.

MOVIE 2.3

SWITCHING BEHAVIORS VIA INTERACTIONS. (i) The soft machine integrates two actuators, two hysteretic valves, two memory elements, and four kinking tubes as touch sensors, with only one tether to a pressure source. (ii) In long-term memory configuration, we repeatedly switch the behavior of the soft machine by touching the tubes placed on board. (iii) Close-up view of the machine steering to the right as a consequence of the right shell being snapped and the left shell being in rest state. (iv) In short-term memory configuration, we switch the behavior of the soft machine, which then spontaneously self-resets to the initial behavior.

MOVIE 2.4

AUTONOMOUS BEHAVIOR THROUGH ANTENNAE. (i) We equip the machine with antennae, which detect interactions (mechanical moment) by unkinking a soft tube placed at the hinge. (ii) Equipped with antennae and in short-term memory configuration, the soft machine autonomously changes direction after the interaction with a wall, and then spontaneously returns to the forward-locomoting behavior.

2.9.2 *Design and manufacturing*

The STL files of all the 3D-printed parts required to build the components as described below are available at our Zenodo repository [120] (DOI: 10.5281/zenodo.14621970).

Hysteretic valves, bending actuators, soft resistors, and inextensible capacitors

The design and the manufacturing procedure of the hysteretic valves are based on the original design we previously introduced [53]. We scaled up the original design by a factor of 2 in all dimensions, and we introduced a notch in the rigid holders in the same way as described in detail in Chapter 3 [88].

The bending PneuNet actuator was previously reproduced by our lab, and both its design and the manufacturing steps are described in detail in our previous work [89, 92]. The actuator presents two sides, manufactured via two consecutive injection molding steps. The inflating side with hollow chambers is made of DragonSkin 10 (DS10) silicone (Smooth-On). The stiffer side is made of Elite Double 32 (ED32) silicone (Zhermack), with an embedded inextensible grid fabric (Penelope 70/10, Garenenzo). Before injecting ED32, it is essential to wait for DS10 to be partially cured (3.5 h of the total 5 h curing time), to allow for stronger bonding between the two silicones.

The soft resistors, implemented as pre-resistances in all the circuits, are elastomeric hollow cylinders made of Smooth-Sil 950 (Smooth-On), with outer diameter 5 mm, inner diameter 0.35 mm, and length 40 mm. The soft resistors are manufactured via injection molding, with a two-part outer mold and a metal rod with diameter 0.35 mm as the inner mold.

The inextensible capacitors are made of two TPU-coated nylon sheets ('nylon 70den TPU-coated one side 170g/sqm heat-sealable', extremtextil) that we heat-seal along a specified path. The path is a rectangle, with an opening on one of the short sides (Fig. 2.19). Given the width w and the height h, we calculate the geometric volume V of the pouch when inflated as the solution to the paper bag problem [121]:

$$V = w^3 \cdot \left(\frac{h}{\pi w} - 0.142 \cdot (1 - 10^{-h/w}) \right). \tag{2.1}$$

The two sheets are heat-sealed using the 3D printer Felix Tec 4. The printer presents a custom-made hot head, previously used by our group [91], that consists of a spherical hot nozzle and a spring that ensures even sealing lines. A silicone mat is placed between the printer bed and the sheets, and oven paper is placed on top of the sheets. To the printer, we send a G-code based on an Adobe Illustrator file containing the desired tool path. After sealing, we cut the residual material surrounding the sealing lines and, in the open side of the pouch, we heat-seal the sheets to a TPU Festo^{TM} tube with a soldering iron at 300°. Finally, we place Luer^{TM} connectors (MLRL007-1 Male Luer to 500 Series Barb 3/32" 2.4 mm with Lock Ring FSLLR-3) in the Festo^{TM} tubes.

Throughout the article, we place a fixed pre-capacitor with volume V_{pre} = 60 mL (with w = h = 68 mm) on the machines (except in Figure 2.13A-C, where we purposefully vary the pre-capacitance).

Bistable shells

The bistable shells are defined by four parameters, as illustrated in Figure 2.14A: the thickness t, the angle α from the vertical axis, the base width w, and the boundary radius R_b. Throughout our study, the shells have t = 3 mm, α = 80°, w = 55 mm, and R_b = 2.28 mm. In addition, the shells have an outer notch and rim that allows for centering when being mounted in the rigid holders. The rigid holder clamps the shell along the outer rim, held together with screws (Fig. 2.14B). The rigid holders compress the silicone rim of 0.95 mm (~ 30% of its thickness).

The shells are manufactured via injection molding of Smooth-Sil 950 silicone (Smooth-On) using a two-part outer mold. The outer molds were printed in VeroClear (Stratasys) with a PolyJet 3D printer (Eden260VS, Stratasys). Before molding, we sprayed a thin layer of release agent

(Ease release 200, Smooth-On) on the inner surface of the molds to ease demolding after curing.

Crawling soft machines

The single-actuator crawling soft machine reported in Figure 2.1 consists of various individual components (Fig. 2.17). The first component consists of two rigid 3D-printed parts that hold the hysteretic valve in place. The part on the outlet side of the valve has a cavity where the bending actuator is press-fit. Both inlet and outlet parts have a hole with diameter 5.5 mm that, after tapping with a 1/4-28 UNF tap, allows for the insertion of a threaded Luer™ connector (Luer™ quick-turn tube coupling 1/4"-28 UNF). These Luer™ connectors allow for the other modules (heat-sealed pouches, resistors, and shells) to be quickly connected. In addition, on the inlet side, we attach a 3D-printed adapter, on which we place screws that act as rigid legs of height 25 mm.

The two-actuator crawling soft machine (Fig. 2.9) consists of two identical copies of the single-actuator crawler. The only difference lies in the adapter for the rigid legs, which is designed to accommodate a bearing (Fig. 2.17). The bearing allows for the rotation of the two single-actuator sides with respect to each other, decoupling the two rotational degrees of freedom. In this way, when the two actuators activate at different frequencies and amplitudes, the two sides locomote at different speeds. Without the bearing, when one side actuates, the other side would drag along.

2.9.3 *Experimental setups*

Measuring fluidic quantities

To regulate and measure the fluidic quantities of interest (pressure and flow), we use a custom-made acquisition setup previously used by our group [53, 89]. The setup is based on the National Instruments IN USB-6212 input/output board, with software developed in-house. A proportional pressure regulator (Festo™ VEAB-L-26-D18-Q4-V1-1R1) is controlled using an analog port of the board. The regulator is connected to an upstream precision pressure regulator (Festo™ LRP-1/4-10), connected to the building pressure source. The setup has various analog input ports, which read the voltage from the pressure sensors (NXP MPX4250DP) and flow sensors (Honeywell AWM5101VN, Honeywell AWM5104VN). The fluidic connection between the parts (regulators, valves, sensors, and samples) is implemented with silicone tubes (Rubbermagazijn 2x4mm and 3x6mm), Festo™ tubes (PUN-6X1-BL), and Luer™ connectors (male-female, Luer-to-barb, and T connectors).

In the benchtop fluidic experiments in Figure 2.2D,E,F, Figure 2.4, Figure 2.5, Figure 2.6, and Figure 2.13A,B,D,E, the soft machine is held in place with the actuator not interacting with the ground, free to bend mid-air. Detecting an ArUco marker placed at the tip of the actuator allows for determining the vertical stroke of the actuator when it does not interact with the ground. The normally closed and normally open 24 V solenoid valves (SMC Solenoid Valve VDW250-5G-2-01F-Q) used in the benchtop experiments are controlled through digital output ports of the input/output board.

Compressing the fluidic touch sensors

To measure the fluidic resistance of the kinking tubes as a function of their deformation (Fig. 2.7 and Fig. 2.8), we make use of a fluidic analog of a resistive voltage divider circuit. Using the fluidic-electrical analogy [53, 122], we treat pressure as voltage. The kinking tube is placed in series with a resistor (a needle) that vents to atmosphere. This resistor has a fixed known resistance $R_0 \approx 0.5\,\mathrm{kPa/SLPM}$ that we measured separately as the slope of the characteristic pressure-flow curve of the needle. We then connect the kinking tube to a pressure regulator upstream (1.5 bar), and we measure the pressure before the kinking tube p_{in} and the pressure after the kinking tube p_{out} from which we can derive the resistance of the kinking tube R_t:

$$R_t = R_0 \cdot \left(\frac{p_{in}}{p_{out}} - 1 \right). \tag{2.2}$$

The pressure data is acquired for various static deformation states of the tube. The tube is deformed in increments of 1 mm using a rigid probe, controlled with a tensile-testing machine Instron 5965. The starting moment of each Instron compression is triggered by a digital output signal from the fluidic setup, ensuring that the acquisitions in both setups are synchronized. In Figure 2.8, each datapoint is the average fluidic resistance (with standard deviation) over 5 s of this static compression condition.

Obtaining the pressure-volume curves

To obtain the pressure-volume curves of the capacitors in Figure 2.3 and Figure 2.15, we quasi-statically inject a controlled amount of water into the capacitors. We mechanically connect a syringe to the tensile-testing machine Instron 5965, and we fluidically connect it to the capacitors making sure all air bubbles are removed. We ramp the displacement of the tensile-testing machine at a rate of 100 mm/min. Since water is incompressible, controlling the displacement of the syringe means controlling the geometric volume provided to the capacitors. Knowing the

diameter of the syringe 26.4 mm, volume is therefore ramped at a rate of 54.74 mL/min. While controlling volume, we measure pressure inside the capacitors with a water-compatible pressure sensor (Honeywell 6DF5G). Since the injected water has substantial mass, to remove the effect of gravity on the pressure-volume curves, we submerge the capacitors in a water tank while performing the tests.

Tracking machines' location

To extrapolate the location of the locomoting machines, we place ArUco markers on board the machines, and we use the Python library OpenCV to detect the ArUcos for each frame of the GoPro videos. We first convert each frame to greyscale using the command `cv2.cvtColor`. We then correct for warp and distortion of the GoPro camera, using four static ArUco markers placed as a reference at the corners of the canvas, with the command `cv2.warpPerspective`. Then, we detect the ArUcos with the command `cv2.aruco.detectMarkers`.

2.9.4 *Supplementary figures*

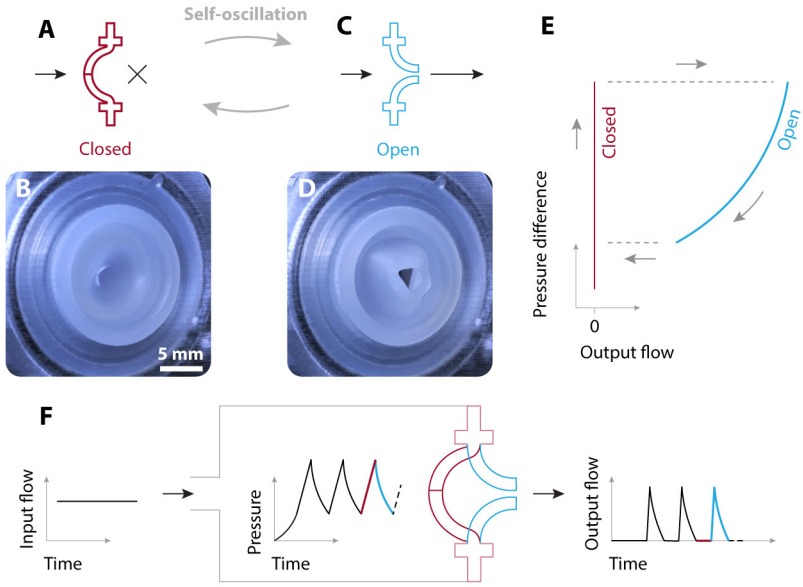

Figure 2.12
THE HYSTERETIC VALVE SELF-OSCILLATES GIVEN CONSTANT INPUT FLOW. The hysteretic valve is an elastomeric shell with a slit at the apex. (**A**) Valve in closed state: when pressure builds up, the slit is closed, and output flow is not provided. (**B**) Photograph of the closed valve as seen from the outlet side. (**C**) Valve in open state: when the shell snaps to the collapsed state, the slit opens, allowing flow in output. (**D**) Photograph of the open valve. (**E**) Schematic relationship between the output flow and the pressure difference across the valve. When the shell is in the rest state (valve closed), pressure builds up with zero flow in output. When the pressure reaches the snap-through value, the shell snaps (valve opens). When the valve is in the open state, it acts as a nonlinear fluidic resistance that vents flow in output, hence, pressure decreases. When pressure decreases past the snap-back value, the shell snaps back to the rest state (valve closes). (**F**) When placed in a fluidic circuit with constant flow in input, the valve behaves as a relaxation oscillator [53], continuously transitioning between the closed state and the open state. The upstream pressure oscillates between a low and a high value, and the output flow alternates between zero and positive bursts. Adapted from Van Laake and Comoretto et al. [88] (Chapter 3 of this Thesis).

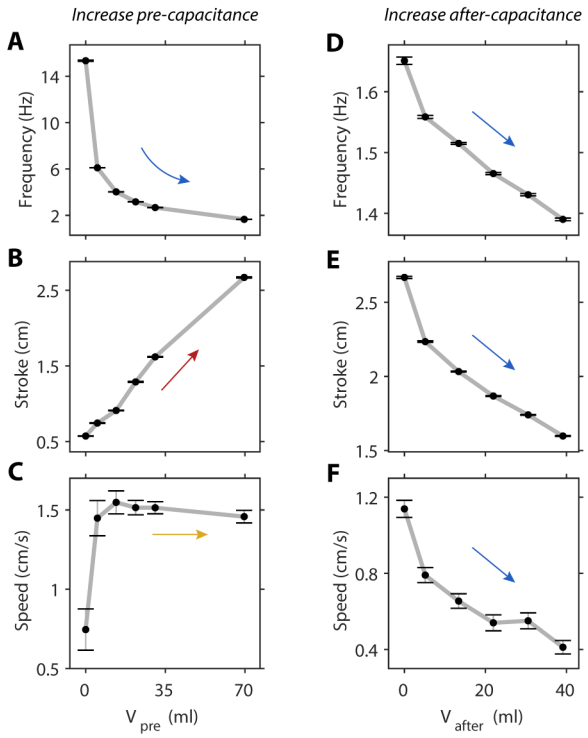

Figure 2.13

RESPONSE OF THE CRAWLER IN FIGURE 2.1 AS A FUNCTION OF PRE- AND AFTER-CAPACITANCES. We vary the pre- and after-capacitances of the circuit in the single-actuator machine (Fig. 2.1) by manufacturing various inextensible pouches (Section 2.9.2) with different height and width (Fig. 2.19). In particular, all the pouches have a fixed width of 30 mm, and we vary their height from 30 mm to 150 mm in increments of 30 mm. In the case of the pre-capacitance, we also test a larger value of volume (70 mL), as the sum of a pouch with height 120 mm and one with height 150 mm. The values of geometric volume reported in this figure result from applying Eq. (2.2). The frequency and vertical stroke of the actuator are measured in a benchtop experiment, with the actuator not interacting with the surroundings. The speed of the machine is measured by recording the crawler from above, and detecting the ArUco marker (Section 2.9.3). (**A**) Frequency of activation of the actuator, (**B**) vertical stroke of the actuator, and (**C**) speed of the machine as a function of pre-capacitance. (**D**) Frequency of activation of the actuator, (**E**) vertical stroke of the actuator, and (**F**) speed of the machine as a function of after-capacitance. Increasing the pre-capacitance volume causes a decrease in frequency (blue arrow in A) and an increase in stroke (red arrow in B), resulting in a negligible change in speed (yellow arrow in C) for positive pre-capacitance volumes. In contrast, increasing the after-capacitance causes a decrease in both the frequency and stroke of the actuator, leading to a net decrease in the resulting speed of the machine (blue arrows in D, E, F).

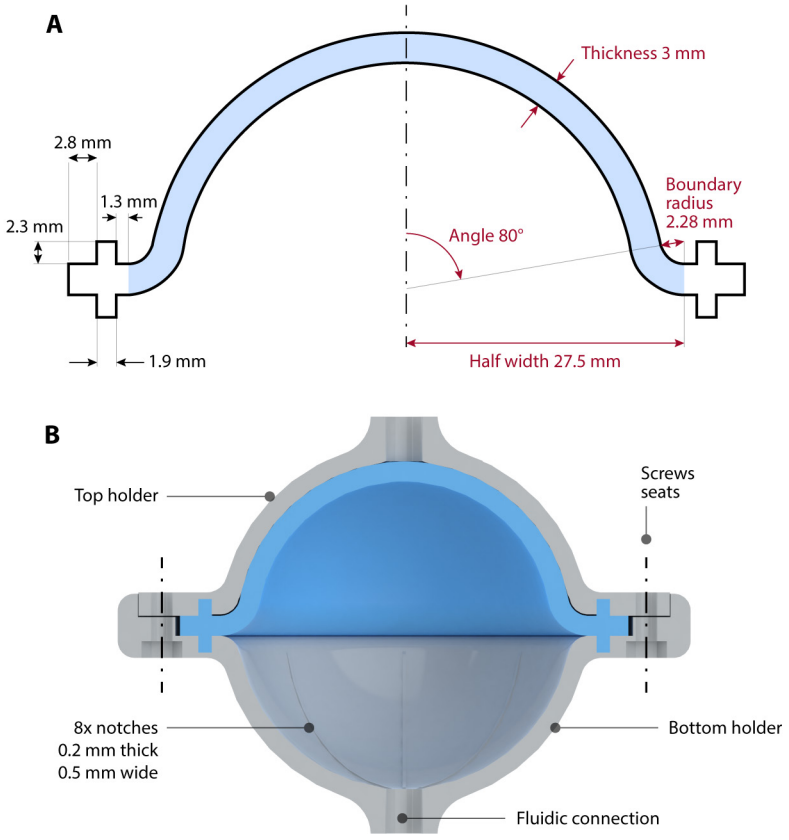

Figure 2.14
DESIGN OF THE BISTABLE ELASTIC SHELLS. (**A**) Schematic of the cross-section of the shell, with the unclamped section highlighted in blue, and the clamped section highlighted in white. The design parameters that affect the behavior of the shell when pressurized are the thickness, the shallowness angle, the width, and the boundary radius (red annotations). The shells used throughout the article have thickness 3 mm, angle 80°, width 55 mm, and boundary radius 2.28 mm. Practically, to clamp the shell in a rigid holder, we designed an extension on the outer edge consisting of a rim and a notch (black annotations). (**B**) Render of a cross-section view of the shell in its holder. The holder presents 8 notches on the inside of each rigid shell, to ensure that the air provided through the fluidic connections distributes pressure evenly on the surface of the silicone shell. The holder has 6 holes, placed radially outside the shell, used to clamp the shell in place using M3 screws and nuts.

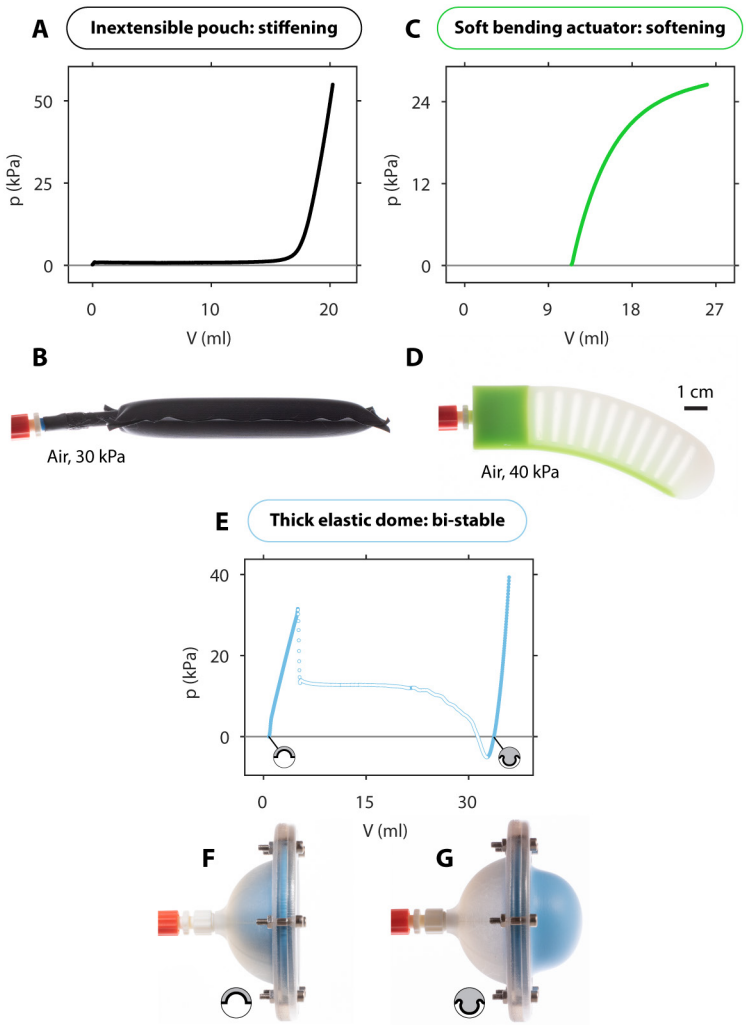

Figure 2.15

Pressure-volume curves of a pouch, an actuator, and a bistable dome. We inflate three fluidic capacitors under quasi-static volume-control conditions, by slowly injecting a controlled volume of water; while increasing volume, we measure pressure (Section 2.9.3). (**A**) The pressure-volume curve of an inextensible pouch with width 30 mm and height 120 mm. (**B**) Photograph of the pouch pressurized with air at 30 kPa. (**C**) The pressure-volume curve of a soft bending actuator. There is an initial volume at atmospheric pressure corresponding to the geometric volume of the inner chambers. (**D**) Photograph of the soft bending actuator pressurized with air at 40 kPa. (**E**) The pressure-volume curve of our bistable elastic shell. White markers indicate the negative stiffness branch (where an increase in volume causes a decrease in pressure). For increasing volume, pressure is non-monotonous. The positive-stiffness branches intersect the zero-pressure vertical line at two points: the system is stable in both these two states without applying pressure. (**F**) Photograph of the bistable shell in the rest state (volume 0.8 mL, zero pressure), and (**G**) in the snapped state (volume 34 mL, zero pressure).

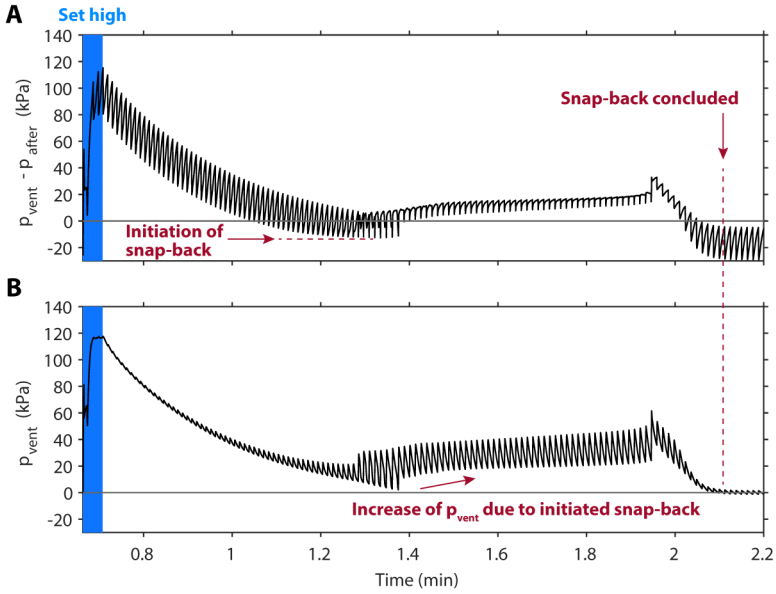

Figure 2.16

IN THE SHORT-TERM MEMORY CIRCUIT IN FIGURE 2.4, THE SPONTANEOUS SNAP-BACK IS NOT INSTANTANEOUS. (**A**) The pressure difference between the venting chamber and the chamber after the hysteretic valve ($p_{vent} - p_{after}$) decreases in time after the system is set to the snapped state, because air in the venting chamber vents to atmosphere through the venting resistance R_{vent}. Since the hysteretic valve oscillates, this pressure difference oscillates as well, while decreasing. When the pressure difference reaches the snap-back pressure of the shell, the shell initiates the snap-back. (**B**) After the shell initiates the snap-back, pressure in the venting chamber p_{vent} increases, because of the relatively high venting resistance R_{vent} connected to the venting chamber. This happens because the shell deforms toward the venting chamber, effectively compressing the air that does not immediately vent through the high resistance. Approximately 50 s after the initiation of the snap-back, the shell completes the snap-back (p_{vent} drops to zero).

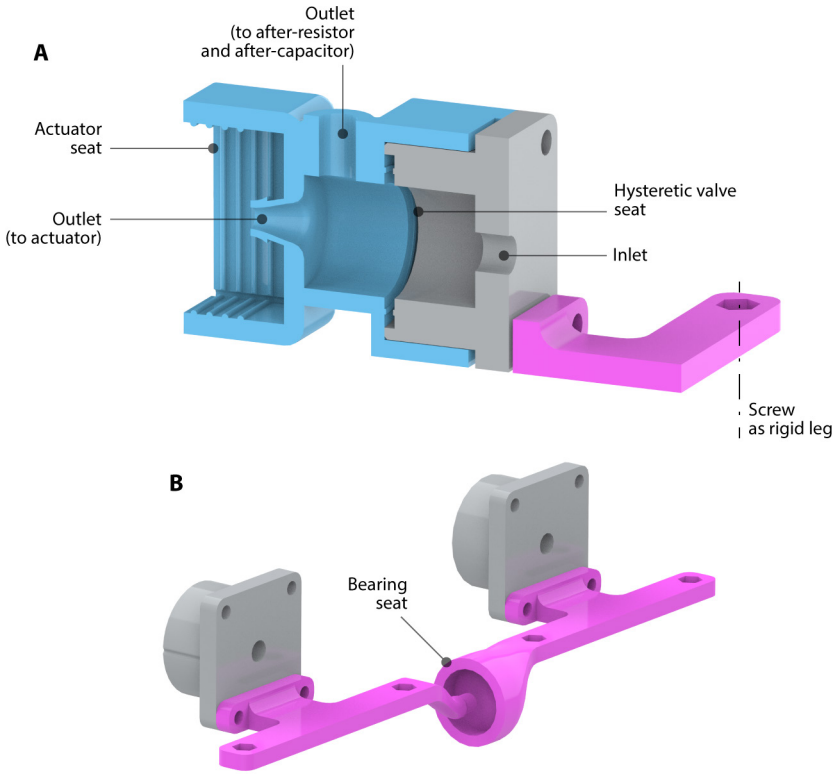

Figure 2.17
DESIGN OF THE MACHINES. (**A**) Cross-section view of the main module to which the rest of the components are connected to assemble the single-actuator machine. The hysteretic valve is seated between the inlet part (grey) and the outlet part (blue). The bending actuator connects to the outlet part via press-fit. An additional part (pink) connects to the inlet part, to allow for screws to be placed as rigid legs. (**B**) The two-actuator machine presents two mirrored copies of the single-actuator assembly, with the only difference being the rigid-legs parts (pink). These parts accommodate a bearing, to allow relative rotation of the two parts with respect to each other.

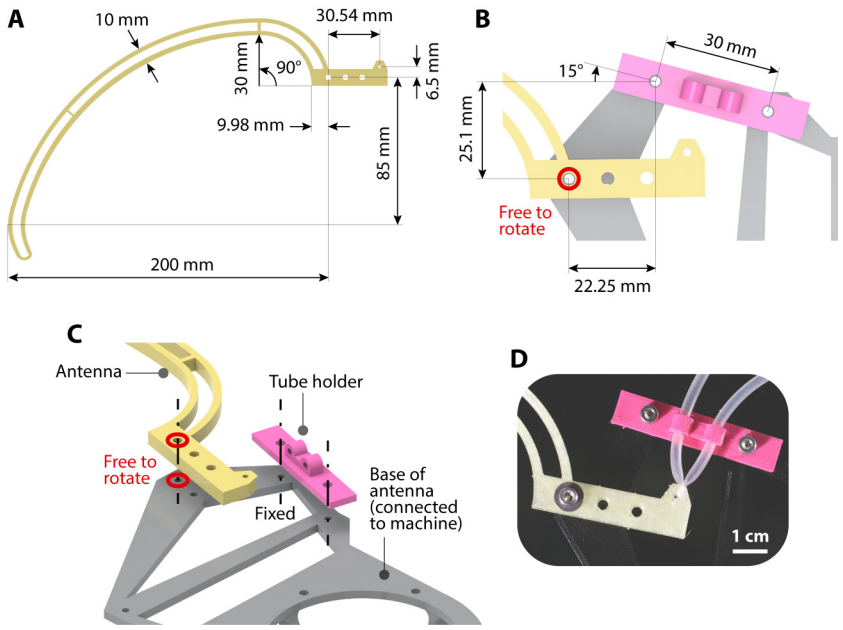

Figure 2.18
DESIGN OF THE ANTENNA. (**A**) Relevant design parameters of the rigid antenna in Figure 2.11. (**B**) Design parameters of the hinge, with the antenna (yellow) connected to the base (grey) with a loose screw that allows rotation (red mark). (**C**) Indication of the mounting holes of the antenna (yellow) and the tube holder (pink) to the base (grey). (**D**) Photograph of the assembled hinge, with the antenna (yellow) firmly attached to the silicone tube (inner diameter 2.5 mm, thickness 0.4 mm, length 30 mm, and inlet-outlet distance 10 mm) with a thin thread.

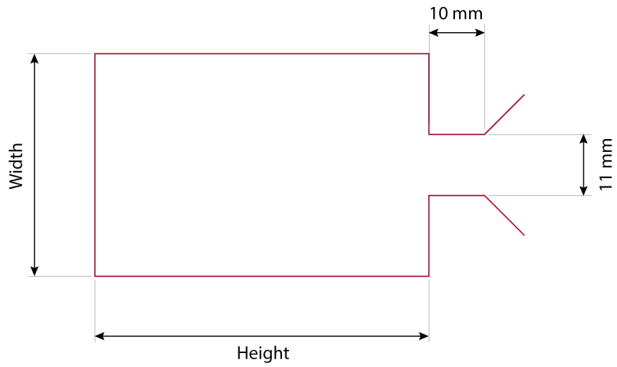

Figure 2.19
DESIGN OF THE INEXTENSIBLE POUCHES. The pouches are rectangular, with an opening at one of the shorter sides. An Adobe Illustrator file, containing the red lines reported here, is used to generate the G-code. The 3D printer follows this path to seal two TPU sheets together (Section 2.9.2).

3

ON THE COEXISTENCE OF PRESSURE REGULATION AND OSCILLATION MODES IN SOFT HYSTERETIC VALVES

PUBLISHED AS: van Laake, L.C.*, Comoretto, A.*, and Overvelde, J.T.B., On the coexistence of pressure regulation and oscillation modes in soft hysteretic valves, *Journal of Fluids and Structures* **126**, 104090 (2024)
(* equal contribution)

ABSTRACT

Fluidic circuits are a promising recent development in embodied control of soft robots. These circuits typically make use of highly nonlinear soft components to enable complex behaviors given simple inputs, such as constant flow or pressure. This approach greatly simplifies control, as it removes the need for external hardware or software. However, detailed fundamental understanding of the nonlinear, coupled fluidic and mechanical behavior of these components is lacking. Such understanding is needed to guide new designs and increase the reliability of increasingly autonomous soft robots. Here, we develop an analytical model that captures the coexistence of a pressure regulation mode and an oscillatory mode in a specific soft hysteretic valve design, that we previously used to achieve reprogrammable activation patterns in soft robots. We develop a model that describes the mechanics, fluidics and dynamics of the system by two coupled nonlinear ordinary differential equations. The model shows good agreement with the experiments, as well as correctly predicts the effect of design changes. Specifically, we experimentally show that we can remove the regulation mode at low input flow by changing the fluidic response of the valve. Taken together, the present study contributes to better understanding of system-level behavior of fluidic circuits for controlling soft robots. This may contribute to the reliability of soft robots with embodied control in applications such as autonomous exploration and medical prosthetic devices.

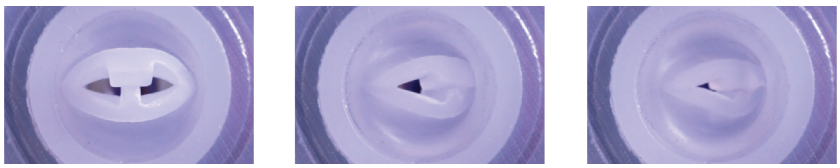

3.1 INTRODUCTION

Soft robots are robots that consist mainly of compliant structures and materials [26, 29]. This feature leads to a host of potential advantages over traditional (rigid) robotics, including intrinsic adaptability, safety, low weight, and resilience [30]. A specific challenge with soft robots in general is the design and integration of control systems. For fluid-driven soft robots in particular [123], which is our focus in this study, it is not straightforward to embed typical control elements such as active valves, sensors, and micro-controllers, due to the stiffness mismatch [45]. However, embedded control is a prerequisite for the development of more autonomous, untethered robotic applications [124]. Therefore, there is an incentive to develop alternative control strategies that can potentially be fully soft. For fluid-driven soft robots, a possible solution is to embed what we call fluidic circuits into their soft bodies. These fluidic circuits can be designed to behave equivalently to electronic control circuits, and can thus be used for basic control, such as actuator sequencing [46, 53, 57, 125–130].

A growing group of soft robots with fluidic circuits uses snapping shells to program behavior [53, 57, 85, 86], as seen in the memory elements in Chapter 2 [131]. The key characteristic of such shells in this context is the hysteresis, and in some cases bistability, under pressure loading that is due to a snapping instability. This hysteresis is an essential ingredient for the generation of periodic, timed actuation of soft actuators. In Chapter 2, we used a hysteretic valve based on an elastomeric spherical cap with a slit at its pole [53], similar to the cap of a ketchup bottle or shower gel container [59]. The slit functions as the valve element, as it is closed in the initial (pre-buckling) state, and open after snapping. These features enable the transformation of a constant inflow of air into timed pulses, which we used to periodically activate one or more soft bending actuators. In this relaxation oscillator circuit, the valve periodically closes and opens as a result of the dynamics of pressure build-up and release.

Outside of the scope of those works [53, 131], we observe an interesting effect that we study in more detail here. We observe that the valve can be in a different mode under the same conditions for which it can also oscillate. In this mode, the valve remains between the open and closed states, and maintains a nearly constant pressure drop for a wide range of flow rates. It is not well understood why this mode, which we call the regulation mode, exists and how we can control in which mode the valve will operate. On the one hand, the stability of this pressure-regulation mode is intriguing and in itself potentially useful in applications. On the other hand, its existence is troublesome when we use the hysteretic valve in applications where we rely on periodic oscillations for robot control,

such as for the actuation of a soft robotic walker [53, 131], or even a soft total artificial heart [132, 133]. Therefore, we want to understand *i)* under which conditions the pressure regulation and oscillation modes exist, and more specifically *ii)* what enables the key behavior, namely the coexistence of the two different modes at the same inflow rate.

A possible approach to this problem would be to look at the three-dimensional shell buckling problem in detail. In fact, although spherical shell snapping has been widely studied for decades, and remains an active topic to date [93, 134, 135], the case of a spherical cap with a slit or cut at its pole under uniform pressure loading has not been treated to our knowledge. We expect that the cut acts as only a minor imperfection in the initial configuration as long as the shell is in compression. On the other hand, during or after the dynamic transition, the cut opens and this will certainly affect the mechanics, but it is not exactly known how. In the existing literature, the work that is most relevant to the mechanics of the current problem is on the effect of small imperfections or probing on shell snapping [96, 97, 136, 137]. Existing work that is relevant for the dynamics of the current problem includes a study on the dynamics of snapping structures, including toy 'poppers' [90, 94] that are geometrically similar to our valves. Interestingly, snapping has been shown to slow down near critical points due to loss of stiffness [138]. When visco-elasticity is additionally considered, the effects compound to result in extremely long snapping times [139, 140]. Yet, it remains unclear how to take into account the discrete change when the unbuckled dome suddenly loses stiffness due to loss of contact in the cut.

In this work we aim to capture the essentials of the mechanics in the simplest possible spring model, and we focus on the system-level behavior of the valve in interaction with its fluidic environment. The reason for this approach is the observation that the regulation mode is not stable without fluid flow. This suggests that we must study the mechanics and dynamics of the whole system to find why the system-level bistability occurs. To do so, we develop a system-level model of the valve system with only two degrees of freedom. The model provides a mechanistic explanation for the existence of the regulation mode and thus suggests how this mode can be harnessed or suppressed. In a final step, we experimentally demonstrate our findings by creating a modified valve that cannot be in the oscillating and regulating states at the same inflow rate. This clearly demonstrates the utility of our simple model. Moreover, it is an important step toward the reliable application of hysteretic valves and fluidic circuits in real-world applications.

The remainder of this Chapter is organized as follows. In Section 3.2, the observed behavior is exemplified by three different experiments under varying load cases. In Section 3.3, we introduce a system-level model that describes the coupled fluidic and mechanical behavior. In Section 3.4,

we analyze potential behaviors of this model to determine if the model describes the behavior observed in experiments. The dynamical analysis (3.4) of the initial model attempt (3.3) reveals that a more complex model of the valve is required. Hence, in Section 3.5, we extend the mechanical model by introducing a sudden weakening of the dome upon buckling, as well as a second local pressure maximum, to account for additional hysteresis. Only after introducing these features, the model reproduces the coexistence of oscillation and regulation at the same conditions. In Section 3.6, we experimentally demonstrate our findings by creating and testing a modified valve. We share our concluding remarks in Section 3.7.

3.2 OBSERVATION: TWO DISTINCT MODES AT THE SAME CONDITIONS

In order to demonstrate the potential behaviors that the dome-shaped slit-valve can exhibit, we start with a basic experiment where we place an air chamber and a soft bellows actuator before a valve, and a silicone tube behind the valve (Fig. 3.1A). This setup is similar to the fluidic relaxation oscillator in Chapter 2 [131], where here the air-chamber and the bellows act as pre-capacitance, and the silicone tube acts as an after-resistance. The valve is made by casting a dome-shaped membrane from silicone elastomer (Dragon Skin 20, Smooth-On) in a 3D-printed mold (VeroClear, Stratasys). Three slits of 1.5 mm each are laser-cut at the apex, after which the valve is placed in a 3D-printed holder[1] (Fig. 3.20). We control the inflow rate Q_{in} to the air chamber using a pair of mass flow controllers (VEMD, Festo (up to 20 SLPM), in parallel with SLA5850, Brooks Instrument (up to 5 SLPM)), and measure pressures p_0 and p_1 immediately before and behind the valve, respectively, as well as flow rate Q_{out} through the valve. Throughout the first experiment, we apply a fixed inflow rate $Q_{in} = 4$ SLPM to the air chamber.

After applying the inflow, we observe that the valve is in its oscillation mode, where the pressure difference over the valve $\Delta p = p_0 - p_1$ oscillates between $\Delta p = 5$ kPa and $\Delta p = 77$ kPa (yellow shading in Fig. 3.1B, and Fig. 3.1C). We then press on the silicone tube behind the valve (red shading in Fig. 3.1B, and Fig. 3.1D), almost but not completely closing it. We observe that the valve oscillates briefly at high frequency during pinching, then stops oscillating and enters the regulation mode. After completely releasing the tube, the valve remains in this mode, and Δp stays constant at a value $\Delta p \approx 29$ kPa (green shading in Fig. 3.1B, and Fig. 3.1E), i.e., between the lowest and highest pressure observed during

1 In order to reduce production variability, the valves in the current study are uniformly scaled up by a factor of two with respect to the earlier work [53], in the same fashion as in Chapter 2 [131]. The detailed design is shown in Figure 3.20.

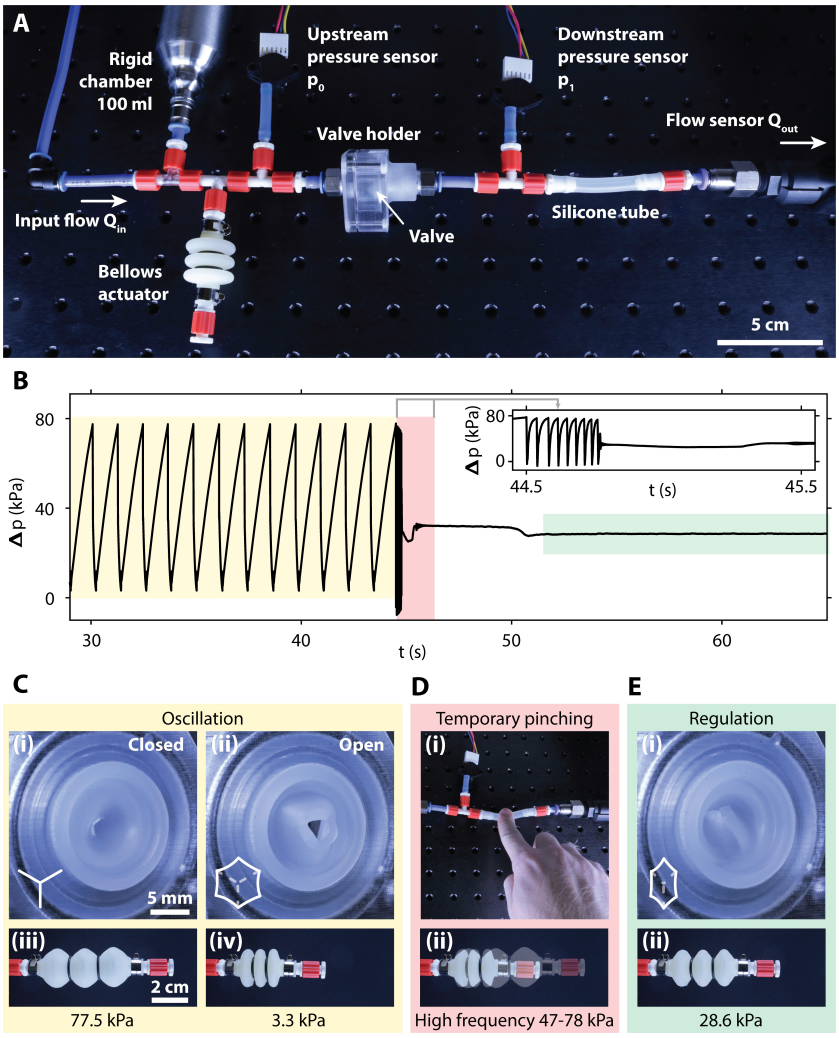

Figure 3.1

A DOME WITH A SLIT CAN BE IN TWO DISTINCT MODES AT THE SAME CONDITIONS. (**A**) Experimental setup with a bellows actuator and a rigid air chamber connected before a hysteretic valve, and a silicone tube directly behind the valve. (**B**) Pressure difference over the valve $\Delta p = p_0 - p_1$ before, during, and after temporarily pinching the silicone tube. (**C**) Before pinching, the valve oscillates between its (i) closed, and (ii) open states, while the actuator cycles between (iii) extended and (iv) contracted. (**D**) During (i) pinching, the actuator temporarily (ii) oscillates at high frequency. (**E**) After pinching, the valve is in its (i) pressure regulation mode, and the actuator is (ii) semi-extended.

oscillation. Therefore, under the same experimental conditions (before and after pinching), the valve is in two different modes. In a separate experiment, we place the same valve in a different holder (with the same clamping geometry) where we can observe the deformed state directly. Figures 3.1C(i), C(ii), and E(i) show the valve in its three different states, and Figures 3.1C(iii), C(iv), and E(ii) show the actuator in the corresponding situations.

To further describe the behavior of the valve in either mode, we perform three additional experiments. In the first additional experiment, we start from the pressure regulation mode and vary the inflow rate. Starting from an initial value of Q_{in} = 4 SLPM, we first increase the inflow rate to Q_{in} = 25 SLPM, then decrease to Q_{in} = 0 SLPM (Fig. 3.2A). We ensure the valve is in the regulation mode at the start of the experiment by briefly pinching the silicone tube. We observe that upon sweeping the inflow rate, the pressure drop over the valve remains almost constant for a wide range of inflow rates, varying between Δp = 28.1 kPa at Q_{in} = 4 SLPM and Δp = 37.6 kPa at Q_{in} = 25 SLPM (Fig. 3.2B), i.e., the pressure changes by 34% of the initial value. For comparison, we measured the pressure drop over a constant restriction (a needle, length 12.7 mm, internal diameter 1.54 mm). The pressure drop varies between Δp = 1.85 kPa at Q_{in} = 4 SLPM and Δp = 50 kPa at Q_{in} = 25 SLPM, i.e., 2600%, or 77 times more than the valve in regulation mode (Fig. 3.21B). Apparently, in the regulation mode, pressure is modulated by passive adaptation of the shape of the valve, especially around the opening. At higher flow rates the opening widens, significantly lowering the effective resistance to airflow, and vice versa. Meanwhile, the overall deformation state of the membrane is in between the initial and buckled states (Fig. 3.2D(i)-D(iii)). When we decrease the inflow rate to $Q_{in} < 2$ SLPM, at $t \approx 80$ s, the valve exits the pressure regulation mode. As an example of an application of the pressure regulation mode, it can be leveraged to control the extension of the soft bellows actuator (Fig. 3.2D(v)–D(vii)).

In the second additional experiment, we start from the oscillation mode and vary the inflow rate. In response to the same flow profile shown in Figure 3.2A, the oscillation frequency (Fig. 3.2C and E) initially increases, as the higher inflow rate causes the pressure in the air chamber to build up faster. This can be seen in Figure 3.2F from the decrease in the time the valve is closed during each cycle T_{closed}. Although T_{closed} continues to decrease with inflow rate, at the same time T_{open} increases, such that from $Q_{in} > 14$ SLPM the oscillation frequency starts to decrease. Ultimately, when $Q_{in} > 20$ SLPM, oscillations stop completely, and the valve remains in the fully open state. This coincides with the inflow rate where the pressure drop over the valve in the open state is high enough to prevent the valve from buckling back. When we decrease the inflow rate, the system restarts oscillating around the same inflow rate where it

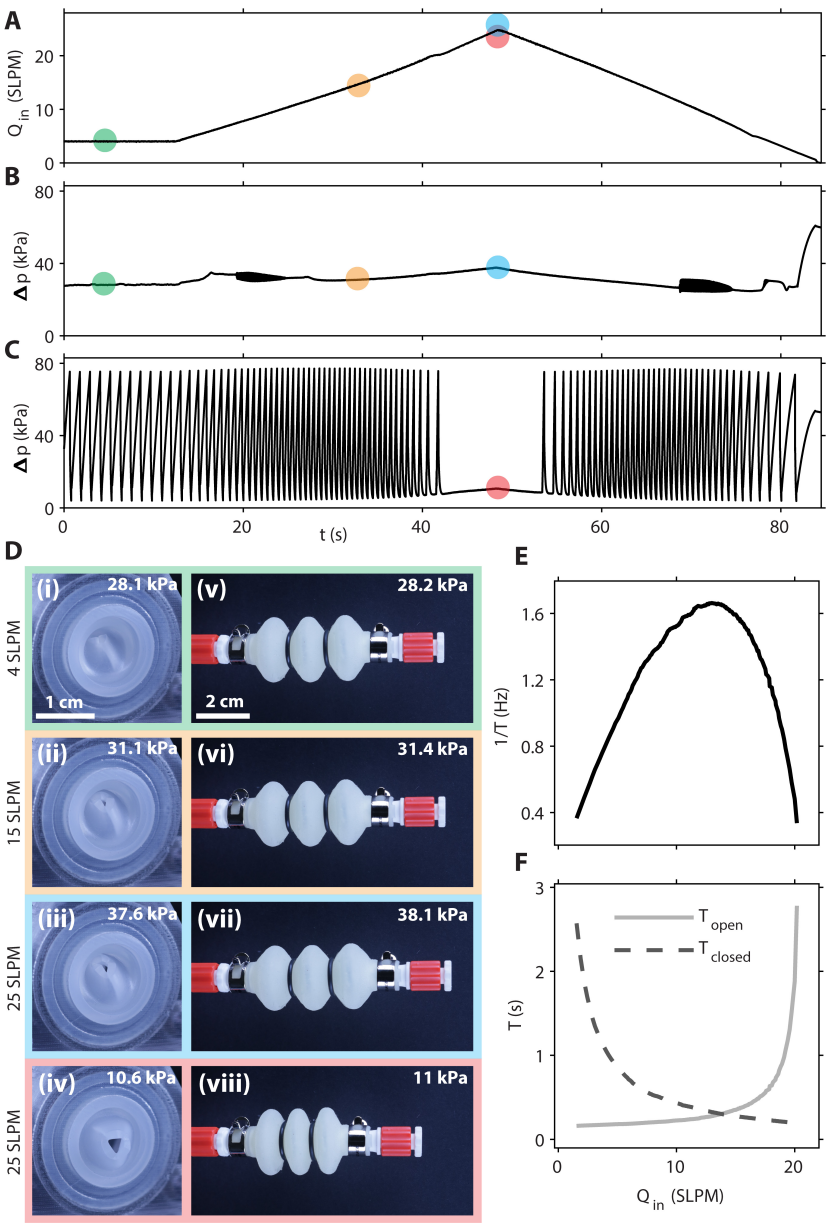

Figure 3.2
VARYING INFLOW RATE Q_{IN}. (**A**) Applied inflow rate profile. (**B**) Pressure difference over the valve for experiments started from the pressure regulation mode, and (**C**) from the oscillation mode. (**D**) The valve and actuator in the regulating and fully open states. Colored borders correspond to markers of the same color in panels A, B, and C. (**E**) Effect of Q_{in} on cycle frequency (inverse cycle time), and (**F**) on the time during each cycle in which the valve is closed (dashed line) or open (solid line).

stopped under increasing inflow rate. It remains in this mode until the end of the experiment.

Importantly, a clear difference in the deformed state between the fully open state and the regulation mode can be seen from comparing photographs and pressure drop over the valve at the same inflow rate $Q_{in} = 25\,\mathrm{SLPM}$ in Figure 3.2D. These are shown for the regulation mode in Figure 3.2D(iii) (corresponding to the blue markers in Figure 3.2A and B), and for the fully open state in Figure 3.2D(iv) (corresponding to red markers in Figure 3.2A and C).

The aim of the third additional experiment is to measure the quasi-static flow-pressure drop relation of multiple samples of the same valve design, as a basis for the development of our model, including its parameters. To measure the fully closed state and the fully open state, we connect the system to a manually controlled pressure regulator (LRP-1/4-10, Festo). This enables us to gradually vary pressure p_0, in order to accurately determine Δp_{open} and Δp_{close}. Moreover, the pressure regulator can provide higher flow rates that are beyond the range of our mass flow controller. We gradually increase the pressure p_0 before the valve until the valve opens at the pressure difference $p_0 - p_1 = \Delta p_{open}$. After the valve opens, we determine the flow-pressure drop relation in the fully open state. Finally, we decrease the pressure until the valve closes again at $p_0 - p_1 = \Delta p_{close}$. To measure the valve in its regulation mode, we connect it to a mass flow controller, and increase and decrease the flow rate, similarly to the experiment shown in Figure 3.2B. We repeat these experiments for six specimens of the same valve design (Fig. 3.21A). Finally, we record oscillations at $Q_{in} = 4\,\mathrm{SLPM}$ as a reference dynamic behavior. In Figure 3.3, we show the results for a representative specimen, as well as a least-squares fit to $\Delta p(Q_{out})$ in the fully open state (dashed curve). Using the fitting function $\Delta p = a\,(Q_{out})^b$ we obtain $a = 0.032(3)\,\mathrm{kPa/SLPM^b}$, $b = 1.68 \pm 0.04$. A constant orifice is expected to have $\Delta p \sim Q_{out}^2$ if compressibility effects are negligible [141] (compare Figure 3.21B).

Taken together, the experiments show that for a remarkably wide range of inflow rates $2\,\mathrm{SLPM} < Q_{in} < 20\,\mathrm{SLPM}$ the valve can be in either the regulation mode or the oscillation mode, while for a fixed inflow rate (e.g., $Q_{in} = 4\,\mathrm{SLPM}$) the valve can be made to go from the oscillation mode to the regulation mode by briefly pressing on a flexible tube behind the valve. For a range of inflow rates $20\,\mathrm{SLPM} < Q_{in} < 25\,\mathrm{SLPM}$ the valve can be in either the regulation mode or the fully open state.

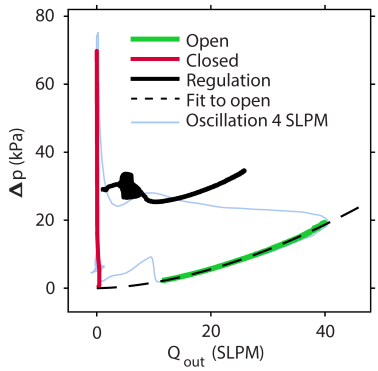

Figure 3.3
MEASURED QUASI-STATIC PRESSURE DROP AS FUNCTION OF OUTFLOW RATE $\Delta p(Q_{OUT})$. Fully closed (red curve) and fully open (green curve) states are obtained in a quasi-static experiment under pressure control. Dashed line shows a fit to the open state data ($\Delta p = 0.03\,(Q_{out})^{1.68}$). The regulation mode (black curve) is obtained in a quasi-static experiment under flow control. Dynamic oscillations for $Q_{in} = 4$ SLPM (blue curve) are shown as a reference to relate the quasi-static measurements to the dynamic behavior.

3.3 LUMPED-PARAMETER MODEL OF THE VALVE SYSTEM

With the goal of exploring essential ingredients for coexistence of the pressure regulation and oscillation modes, we develop a minimal lumped-parameter model. We start with the description of the first order dynamics in the fluidic domain, where the valve is treated as a variable restriction. Secondly, we define a spring-model with one degree-of-freedom (DOF), to approximate the equilibrium pressure-displacement behavior of the elastomeric dome. Thirdly, we define simplified dynamics of the mechanical DOF, that describes the transitions between the open and closed states. Lastly, we explicitly define the variation of the valve orifice as a function of position of the single DOF of the mechanical spring-model. Combining these four ingredients, we obtain two coupled nonlinear ordinary differential equations (ODEs) that describe the behavior of the system.

3.3.1 *Fluidic model*

The fluidic model is schematically shown in Figure 3.4A(ii). A source of constant flow rate Q_{in} is connected to a pneumatic capacitor C_o (i.e., a flexible or rigid air chamber). The valve is placed inline behind the air chamber. When the valve is open, there is an output flow Q_{out} through the valve. The pressure drop over the valve is $\Delta p = p_o - p_1$.

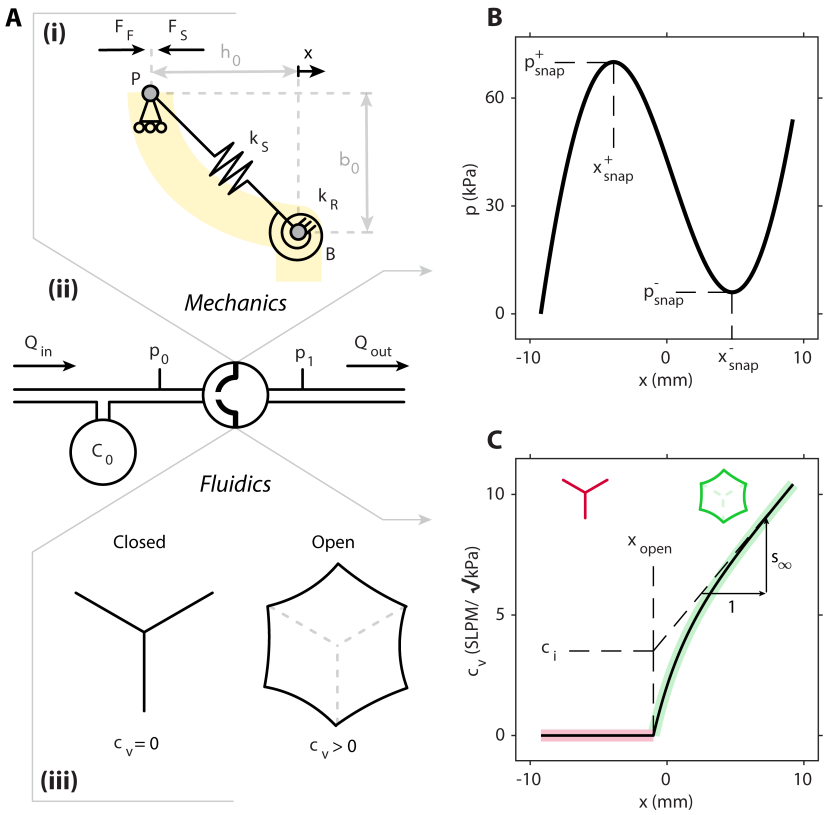

Figure 3.4
LUMPED-PARAMETER MODEL OF THE VALVE SYSTEM. (**A**) Schematic overview of the model. (i) Mechanical spring model of the dome. (ii) Fluidic model. (iii) Valve conduction model. (**B**) Sketch of pressure p as function of displacement of node P. The curve is non-monotonic, reflecting the behavior of pressurized domes [90]. (**C**) Sketch of the conductance behavior of the valve as a function of the displacement of node P. When the valve is open, conductance increases for increasing displacement, reflecting the orifice opening when the soft valve is increasingly stretched.

Using the fluidic-electrical analogy [53, 122], we treat pressure p as voltage and flow Q as current. With this analogy, and considering that the integral of air flow is air volume V, a capacitor C satisfies

$$Q = C\frac{dp}{dt}, \quad \text{or} \quad p = \frac{1}{C}\int Q\,dt, \quad \text{or} \quad p = \frac{1}{C}V. \tag{3.1}$$

Hence, we model the behavior of the capacitor linearly, where the standard volume of air V_S is related to pressure p_0 as

$$V_S = C_0 p_0, \tag{3.2}$$

where C_o is the capacitance in 1/60SL/kPa (the unusual unit is a result of using the convenient units SLPM (standard litre per minute) for flow, kPa for pressure, and seconds for time).

The instantaneous variation of standard volume in the chamber is the difference between input and output flows

$$\frac{dV_S}{dt} = Q_{in} - Q_{out}, \tag{3.3}$$

where Q_{in} and Q_{out} are standard flows in SLPM. We assume that the pressure drop over the valve Δp is proportional to Q_{out}^2, where the square is expected for flow through a constant orifice [141] (see also Figure 3.21B)

$$\Delta p = R_v Q_{out}^2, \tag{3.4}$$

where R_v is the restriction of the valve in kPa/SLPM^2, which in experiments and also in our model depends on the state of the valve (as discussed in Section 3.3.1). Conversely, output flow through the valve is approximately proportional to the square-root of the pressure drop

$$Q_{out} = c_v\sqrt{\Delta p}, \quad c_v = \sqrt{1/R_v}, \tag{3.5}$$

where c_v is the conductance of the valve in SLPM/$\sqrt{\text{kPa}}$.

From Eqs. (3.2), (3.3) and (3.5) we can write the dynamic equation for the fluidic system

$$C_o\frac{dp_o}{dt} = Q_{in} - c_v\sqrt{\Delta p}. \tag{3.6}$$

This can be simplified further if we assume p_1 is constant

$$C_o\frac{d\Delta p}{dt} = Q_{in} - c_v\sqrt{\Delta p}, \tag{3.7}$$

which is the case when the valve is venting freely to its surroundings at constant atmospheric pressure. In the general case, Eq. (3.6) should be used, for example when a restriction or a second air chamber, such as a soft actuator, is placed behind the valve.

The capacitance C_0 can be obtained from the slope dp_0/dV_S in a dedicated experiment, or analytically from the geometrical volume, using the ideal gas law. For known Q_{in}, C_0 can also be conveniently determined in experiments with a hysteretic valve, from the slope dp_0/dt when the valve is closed, i.e., $c_v = 0$, to also account for some parasitic capacitance that exists in the tubing, the valve holder, and the valve itself.

3.3.2 *Mechanics of the dome*

Figure 3.4A(i) shows a schematic of the model for the mechanics of the valve. A key characteristic of the mechanical response of our elastomeric dome is the existence of a local pressure maximum followed by a local pressure minimum. This behavior can be reproduced in a minimal model with only two springs. A linear spring with stiffness k_S and a rotational spring k_R account for stretching and bending, respectively.

We assume that node P is allowed to move only in the horizontal direction. Its position is equal to $x = -h_0$ at rest. Node B is constrained in both directions, therefore width b_0 is constant. An external load F_F is applied at node P in the horizontal direction. F_S is the opposing reaction force exerted by the structure. With the aim of obtaining an expression for F_S, we write the internal elastic energy E in the system, considering the geometry in Figure 3.4A(i)

$$E = \frac{k_S}{2}\left(\sqrt{h_0^2 + b_0^2} - \sqrt{x^2 + b_0^2}\right)^2 + \frac{k_R}{2}\left(\arctan\left(\frac{h_0}{b_0}\right) - \arctan\left(-\frac{x}{b_0}\right)\right)^2. \tag{3.8}$$

The equation of the force exerted by the structure is given by the derivative of the elastic energy along the degree of freedom x

$$F_S = \frac{dE}{dx} = -k_S \frac{\sqrt{h_0^2 + b_0^2} - \sqrt{x^2 + b_0^2}}{\sqrt{x^2 + b_0^2}} x + k_R \frac{\arctan\left(h_0/b_0\right) + \arctan\left(x/b_0\right)}{b_0\left(x^2/b_0^2 + 1\right)}. \tag{3.9}$$

We couple the spring model to the fluidic model by assuming the external load F_F is the net force exerted by the pressure difference over the valve, acting on the projected area of the valve A_v

$$F_F = A_v \Delta p, \quad A_v = \pi {b_o}^2, \tag{3.10}$$

Analogously, to transform the spring force F_S to a pressure, we divide by the valve area, such that

$$p_S = F_s / A_v. \tag{3.11}$$

We take b_0 to be equal to the physical radius of the valve, and h_0 the height of the dome. We then select k_s and k_r such that p_S has a local maximum $p^+_{snap}(x^+_{snap})$ and a local minimum $p^-_{snap}(x^-_{snap})$ that coincide with the experimentally observed values Δp_{open} and Δp_{close} in a slow, pressure-controlled experiment (Fig. 3.3). Note that the positions x^+_{snap}

and x^{-}_{snap} also result from these assumptions and are somewhat arbitrary. This is a consequence of using a highly simplified spring model for the actual three-dimensional mechanics of the dome. In Figure 3.4B we show the resulting $p_S(x)$ for $b_0 = 12\,mm$, $h_0 = b_0\,(1-\cos\theta)/\sin\theta = 9.2\,mm$, $k_S = 2.9\times10^7\,N/m$, and $k_R = 3.6\times10^8\,N\,m/rad$. Notice how the negative slope in the force-displacement behavior leads to an instability if the loading is pressure-controlled. This instability gives rise to the desired hysteresis of the valve. The left and right sections with positive slope represent the valve in the initial and buckled states, respectively.

3.3.3 *Simplified dynamics of the spring model*

We define the transitions between open and closed states of the valve by simplified dynamics of x. We first write the force balance for a concentrated mass m located at P

$$F_F = m\frac{d^2x}{dt^2} + b\frac{dx}{dt} + F_S, \tag{3.12}$$

where b is a damping coefficient. Based on the observation that the transitions occur relatively fast in experiments, we ignore inertial effects to minimize the number of DOFs, obtaining

$$\frac{dx}{dt} = \frac{1}{b}(F_F - F_S) = \frac{A_V}{b}(\Delta p - p_S). \tag{3.13}$$

We study the effect of parameter b in Section 3.4.3, where we analyze the asymptotic stability of the system.

3.3.4 *Valve conductance as function of node position*

The second coupling between the spring model and the fluidic model is *via* the valve conductance. The exact evolution of valve conductance (see Eq. 3.5 for its definition) during the opening and closing of the valve is not easily observable. However, we know that the conductance must vary significantly with x to enable the regulation mode, since the pressure drop over the valve varies little for a wide range of flow rates, while the overall deformation state (associated with x) also does not change considerably. Moreover, we observe that the valve remains hermetically closed ($c_v = 0$) at least until the valve buckles. We define a position x_{open} where the valve starts to open ($c_v > 0$ for $x > x_{open}$). Finally, the experimental data show that the pressure drop in the fully open state is approximately proportional to the outflow rate to the power 1.68, as shown in Figure 3.3. This exponent, less than 2, implies that the orifice size continues to grow moderately with increasing position in the

fully open state, according to our assumed quadratic relation between pressure and flow rate in a constant orifice in Eq. (3.4). This reasoning is consistent with visual observation of the orifice. We can reproduce these features by defining the conductance c_v as a function of position x as

$$c_v = \begin{cases} 0 & x \leq x_{open} \\ c_i \left(1 - e^{\psi(x_{open}-x)}\right) + s_\infty (x - x_{open}) & x > x_{open}, \end{cases} \tag{3.14}$$

where ψ is a constant that sets the rate at which c_v approaches the value c_i and s_∞ is a constant representing the remaining slope for $x \gg x_{open}$, as shown in Figure 3.4C. For different values of x_{open} and ψ, we can determine c_i, and s_∞ by fitting the model to measured values $\Delta p(Q_{in})$. We study the effect of these parameters in Section 3.4.2.

3.3.5 *System model*

Combining the fluidic model, the spring model, and the conductance behavior, we obtain the following set of two ordinary differential equations in Δp and x

$$\frac{d\Delta p}{dt} = \frac{1}{C_0}\left(Q_{in} - c_v(x)\sqrt{\Delta p}\right), \tag{3.15}$$

$$\frac{dx}{dt} = \frac{A_v}{b}\left(\Delta p - p_S(x)\right), \tag{3.16}$$

where $c_v(x)$ is defined in Eq. (3.14) (Fig. 3.4C), and $p_S(x)$ in Eqs. (3.9) and (3.11) (Fig. 3.4B). Note that Δp and all parameters are positive.

3.4 POTENTIAL BEHAVIORS OF THE INITIAL MODEL

Having established an initial and highly simplified model, we want to determine if the model can describe the observed behavior in the specific configurations for which we presented the experimental data in Figs. 3.1, 3.2, and 3.3. Therefore, rather than studying the model behavior for a wide range of parameter values, we fix as many parameters as possible based on the available experimental data. This is possible for the parameters of the spring model b_0, h_0, k_S, and k_R, as well as the parameters that we control in experiments Q_{in} and C_0. On the other hand, we cannot directly obtain all fluidics parameters x_{open}, ψ, c_i, s_∞, nor the damping parameter b from measurements. Therefore, we perform parameter scans for these parameters in order to find values that are qualitatively compatible with the observed behavior.

The observed behavior we are trying to describe consists of the coexistence of regulation and oscillation for $2\,\text{SLPM} < Q_{in} < 20\,\text{SLPM}$, and

coexistence of regulation and the fully open state for 20 SLPM < Q_{in} < 25 SLPM. The pressure drop over the valve in the regulation mode varies from $\Delta p \approx 25$ kPa at relatively low flow, to $\Delta p \approx 40$ kPa at relatively high flow. Importantly, the regulation mode is stable for a wide range of flow rates, based on two observations. *i)* The valve is attracted to the regulation mode when we temporarily perturb the system (Fig. 3.1). This leads to the conclusion that the regulation mode is a stable equilibrium. *ii)* The valve remains in the regulation mode when we vary the inflow rate (Fig. 3.2). This shows that the equilibrium remains stable at different inflow rates.

Therefore, to explain the regulation mode, we need to find equilibria at a range of pressure values around $\Delta p \approx 30$ kPa that are stable for a range of inflow rates around 2 SLPM < Q_{in} < 25 SLPM, similar to the black curve in Figure 3.3. At the same time, there must exist stable limit cycles, at the same flow rates, that describe the oscillation mode, similar to the blue curve in Figure 3.3. To determine if parameters exist for which the current model can describe both behaviors, we firstly analyze the general existence of equilibria, using arbitrary parameter values for the fluidics, in Section 3.4.1. In Section 3.4.2, we investigate the influence of fluidics parameters (x_{open} and ψ) on the shape of these equilibria. In Section 3.4.3 we analyze the effect of damping parameter b on the asymptotic stability of the existing equilibria. Finally, we look at the relation between the existence of stable equilibria (regulation mode) and limit cycles (oscillation mode).

3.4.1 *System equilibria*

To determine all possible equilibria, we begin by looking at the nullclines for Δp and x, respectively,

$$\frac{d\Delta p}{dt} = 0 \iff Q_{in} = c_v(x_{eq})\sqrt{\Delta p_{eq}}, \tag{3.17}$$

$$\frac{dx}{dt} = 0 \iff \Delta p_{eq} = p_S(x_{eq}). \tag{3.18}$$

When the valve is closed ($x \leq x_{open}$, $c_v = 0$) we find from Eq. (3.17) that the system is in equilibrium only for $Q_{in} = 0$, which is not of practical interest in our specific scenario where we have positive inflow $Q_{in} > 0$. Nevertheless, in that situation, the coupling between Δp and x would reduce to the mechanical model Eq. (3.16), and the equilibria follow from Eq. (3.18)

$$\Delta p(x_{eq}) = p_S(x_{eq}). \tag{3.19}$$

When the valve is open ($x > x_{open}$), we can substitute Eq. (3.18) in Eq. (3.17) to find the equilibria $(x_{eq}, \Delta p_{eq})$. At equilibrium, the outflow

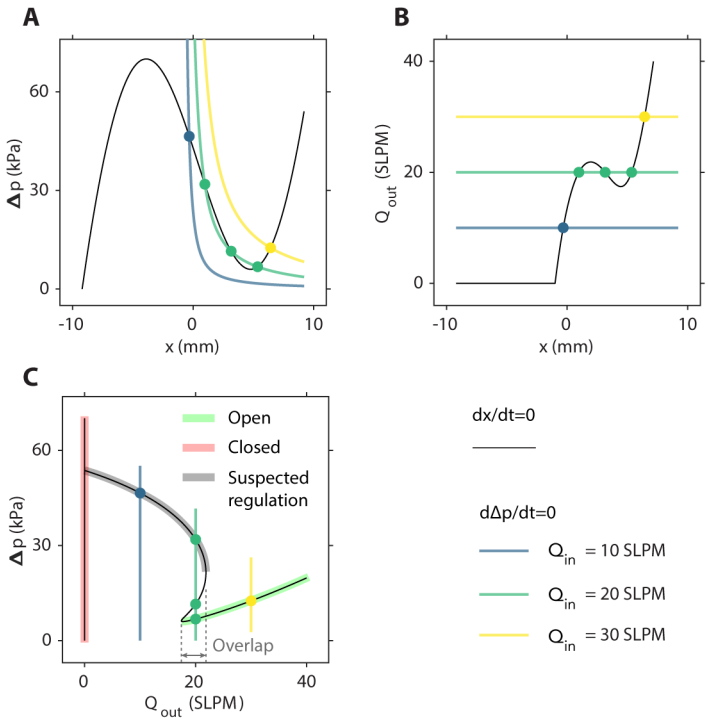

Figure 3.5
THREE PROJECTIONS OF THE NULLCLINES OF THE INITIAL MODEL. Nullclines $dx/dt = 0$ (black) and $d\Delta p/dt = 0$ (colored) in the (**A**) x-Δp plane, (**B**) x-Q_{out} plane, and (**C**) Q_{out}-Δp plane. Highlights in panel C correspond to features of the model that are similar to the experimentally observed behavior as shown in Figure 3.3.

rate must equal the inflow rate. All equilibria are therefore described by the single equation

$$Q_{in} = Q_{out} = c_v(x_{eq})\sqrt{p_S(x_{eq})}. \tag{3.20}$$

This observation allows us to project Eqs. (3.17) and (3.18) on any of the three two-dimensional projections of the system x-Δp-Q_{out}. We illustrate these projections in Figure 3.5, using representative values for the mechanics, but arbitrary parameter values for the fluidics. In Figure 3.5A we show the solutions to Eqs. (3.17) and (3.18) in the x-Δp plane for Q_{in} = 10, 20, and 30 SLPM. In this projection, the nullcline $dx/dt = 0$ (black line) is equivalent to the behavior of $p_S(x)$ (Fig. 3.4B). The nullclines $d\Delta p/dt = 0$ (colored lines) are determined by rewriting Eq. (3.17) as follows

$$\Delta p_{eq} = \left(Q_{in}/c_v(x_{eq})\right)^2. \tag{3.21}$$

The points where two nullclines cross indicate the points where the fluidic and mechanical pressure/force equilibrate. As such, higher flow rates lead to higher values of x. Moreover, for some flow rates (e.g., for $Q_{in} = 20\,\text{SLPM}$)) we observe multiple equilibrium points. In Figure 3.5B, we show the same nullclines in the x-Q_{out} plane. The nullclines $d\Delta p/dt = 0$ (colored lines) are conveniently transformed to straight lines, since $Q_{in} = Q_{out}$. This makes it straightforward to find the equilibria for any inflow rate Q_{in} from inspecting only the single nullcline $dx/dt = 0$. The nullcline $dx/dt = 0$ (black line) is described by Eq. (3.20). In Figure 3.5C, we show the mapping of the unique values $Q_{out}(x_{eq})$ and $\Delta p(x_{eq})$ onto the Q_{out}-Δp plane. This final mapping is most convenient for our purposes, since Δp and Q_{out} are the variables that we measure in experiments, such that this projection enables a direct comparison with experimental data.

Comparing the nullclines shown in Figure 3.5C to the experimentally observed behavior Figure 3.3, we see four similarities.

1. The closed state of the valve is described by a vertical section at $Q_{in} = 0$.
2. The fully open state of the valve is represented by a section starting at the local pressure minimum around $Q_{in} \approx 18\,\text{SLPM}$, $\Delta p \approx 5\,\text{kPa}$, and extending (infinitely) to higher flows and pressures.
3. There is a section connecting the previous two, that spans approximately the same pressure and flow ranges as the experimentally observed regulation mode. (In the following points we refer to this section as the suspected regulation mode.)
4. The range of inflow rates for which the suspected regulation mode exists, partially overlaps with the range of inflow rates for which the fully open state exists.

A qualitative difference is that in the model the suspected regulation mode has a negative $\Delta p(Q_{out})$ slope (Fig. 3.5C, grey highlight), while in the experiments the regulation mode has a dominant region with positive $\Delta p(Q_{out})$ slope (Fig. 3.3).

3.4.2 *Equilibria as function of conduction parameters*

We have determined the general existence of equilibria and identified a part of the nullcline $dx/dt = 0$ that potentially describes the regulation mode. In the current Section we study how the equilibria change when we vary model parameters. The nullclines of our initial model depend only on the spring model and conductance behavior. The assumptions presented in Section 3.3.2 fully constrain the parameters of the spring

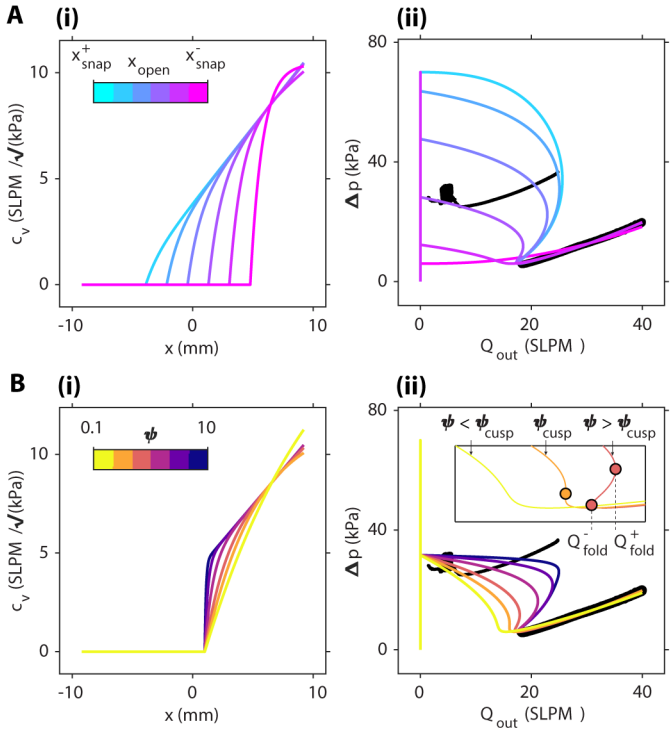

Figure 3.6

Effect of valve conduction parameters on system equilibria. (**A**) Effect of x_{open} for a constant value of $\psi = 1/\text{mm}$. (**B**) Effect of ψ for a constant value of $x_{open} = 1\,\text{mm}$. The left column (i) shows the relation $c_v(x_{eq})$. The right column (ii) shows the resulting nullcline $dx/dt = 0$ (colored lines). Solid black lines show the experimentally obtained reference curves for the regulation mode and fully open state. Note that fold bifurcations Q^-_{fold} and Q^+_{fold} arise from sweeping one parameter [142], which is flow Q_{out}. When varying two parameters simultaneously, Q_{out} and ψ, we observe a cusp bifurcation [142] at ψ_{cusp}.

model based on experimental data. We therefore turn our attention to the conductance behavior, i.e., the fluidics parameters x_{open}, ψ, c_i and s_∞.

We seek to optimize the fit between model and experimental values for $\Delta p(Q_{out})$ in the regulation mode, under the constraint that $\Delta p(Q_{out})$ in the fully open state is also matched. We select x_{open} and ψ as the free parameters. For different combinations of x_{open} and ψ we perform a two-parameter fit to open state data to obtain c_i and s_∞. In Figure 3.6 we show the resulting conductance behaviors and nullclines alongside the measured data.

Increasing x_{open} (Fig. 3.6A(i)) leads to a decrease of the pressure at low flow (Fig. 3.6A(ii)). The pressure at $Q_{out} = 0$ is equal to $p_S(x_{open})$. Experimentally, the regulation mode occurs at pressure differences around $\Delta p \approx 30\,\mathrm{kPa}$. This is best approximated for $x_{open} \approx 1\,\mathrm{mm}$.

Increasing ψ (Fig. 3.6B(i)) flattens $\Delta p(Q_{out})$, but the slope remains negative (Fig. 3.6B(ii)), in contrast with the experimental behavior, which has a slightly positive slope. Therefore, the fit to the measured data continues to improve as $\psi \to \infty$. As a result, we do not find an upper bound on ψ from this analysis. Conversely, decreasing ψ decreases the range of flow rates for which regulation and oscillation could coexist. This is understood when looking at the fold bifurcation Q^{+}_{fold} (arising from a sweep on one parameter [142], flow Q_{out}), which decreases in value for decreasing ψ (Fig. 3.6B(ii)). When sweeping two parameters simultaneously, Q_{out} and ψ, a cusp bifurcation [142] appears at ψ_{cusp}. Below this critical value $\psi = \psi_{cusp} \approx 0.22/\mathrm{mm}$, the regulation mode and the fully open state cannot coexist altogether. Since this contradicts the experimental observations, we will use $\psi > \psi_{cusp}$ as a lower bound in our further analysis.

The result of this Section is that we have narrowed the feasible range for four model parameters. We get the best fit with experimental data for $x_{open} \approx 1\,\mathrm{mm}$ and $\psi > \psi_{cusp} \approx 0.22/\mathrm{mm}$. For different values of ψ, we find c_i and s_∞ by fitting to experimental data. We show the resulting values for c_i and s_∞ in Figure 3.25.

The nullclines for $x_{open} = 1\,\mathrm{mm}$ and $\psi > 0.22/\mathrm{mm}$ show that there exist equilibria at pressure and inflow values similar to those we observed experimentally in the regulation mode, albeit with negative slope instead of the positive slope that we observe in experiments. This suggests that the model could potentially reproduce the observed behavior, but only if these equilibria are stable in the regulation mode, and only if there also exists an oscillation mode at the same inflow rates. To determine if this can be the case, we need to study the dynamics of the system, i.e., the asymptotic stability of the equilibria as well as the possible (co-)existence of stable points and limit cycles.

3.4.3 *Asymptotic stability of the equilibria*

Thus far, we have determined approximate values for all parameters except for ψ and b. In this Section, we study if there is any combination of values for ψ and b that leads to asymptotic stability of the regulation mode as well as the existence of the oscillation mode. This will finalize our analysis of the initial model, and allows us to determine if the model is capable of capturing the qualitative behavior observed in experiments.

We begin by assessing the asymptotic stability of the equilibria. For the valve in the closed state ($x \leq x_{open}$), the system reduces to Eq. (3.16), and asymptotic stability can be determined from

$$\partial\left(\frac{dx}{dt}\right)/\partial x < 0 \iff = -\frac{A_v}{b}\frac{\partial p_S}{\partial x} < 0 \iff \frac{\partial p_S}{\partial x} > 0, \quad x < x_{open}. \tag{3.22}$$

For $x > x_{open}$, we write the Jacobian matrix of the system

$$J = \begin{bmatrix} \partial\left(\frac{d\Delta p}{dt}\right)/\partial\Delta p & \partial\left(\frac{d\Delta p}{dt}\right)/\partial x \\ \partial\left(\frac{dx}{dt}\right)/\partial\Delta p & \partial\left(\frac{dx}{dt}\right)/\partial x \end{bmatrix}\Bigg|_{x_{eq}} = \begin{bmatrix} -\frac{c_v(x)}{2\,C_o}\frac{1}{\sqrt{p_S(x)}} & -\frac{\sqrt{p_S(x)}}{C_o}\frac{\partial c_v}{\partial x} \\ \frac{A_v}{b} & -\frac{A_v}{b}\frac{\partial p_S}{\partial x} \end{bmatrix}\Bigg|_{x_{eq}}, \tag{3.23}$$

where

$$\frac{\partial c_v}{\partial x} = \psi\, c_i\, e^{\psi\,(x_{open}-x)} + s_\infty, \tag{3.24}$$

and

$$\frac{\partial p_S}{\partial x} = \frac{1}{A_v}\left(\frac{k_r}{{b_o}^2\left(\frac{x^2}{{b_o}^2}+1\right)^2} - \frac{k_s\left(\sqrt{{b_o}^2+{h_o}^2}-\sqrt{{b_o}^2+x^2}\right)}{\sqrt{{b_o}^2+x^2}} + \frac{k_s\,x^2}{{b_o}^2+x^2} + \right.$$
$$\left. + \frac{k_s\,x^2\left(\sqrt{{b_o}^2+{h_o}^2}-\sqrt{{b_o}^2+x^2}\right)}{\left({b_o}^2+x^2\right)^{3/2}} - \frac{2\,k_r\,x\left(\operatorname{atan}\left(\frac{h_o}{b_o}\right)+\operatorname{atan}\left(\frac{x}{b_o}\right)\right)}{{b_o}^3\left(\frac{x^2}{{b_o}^2}+1\right)^2}\right). \tag{3.25}$$

Note that the inflow rate does not appear in the Jacobian. That is because for any equilibrium position the associated inflow rate $Q_{in}(x_{eq})$ can be inferred, according to Eq. (3.20).

If both eigenvalues λ_1 and λ_2 of the Jacobian, evaluated at an equilibrium position x_{eq}, have negative real part, the equilibrium is stable. For a two-DOF system, this can be determined following

$$\Re(\lambda_i) < 0 \quad (i = 1,2) \quad \iff \quad \det(J) = \lambda_1\,\lambda_2 > 0 \quad \wedge \quad \operatorname{tr}(J) = \lambda_1 + \lambda_2 < 0. \tag{3.26}$$

Considering the first condition needed for asymptotic stability, we write the determinant of the Jacobian

$$\det(J) = \frac{A_v\left(c_v(x)\frac{\partial p_s}{\partial x} + 2\,p_S(x)\frac{\partial c_v}{\partial x}\right)}{2\,b\,C_o\sqrt{p_S(x)}}\Bigg|_{x_{eq}} > 0. \tag{3.27}$$

Since the isolated spring model, without fluidic effects, is monostable,

$$p_S(x) > 0 \quad \forall \quad x > -h_0, \tag{3.28}$$

Eq. (3.27) holds if

$$c_v(x)\frac{\partial p_S}{\partial x} + 2\,p_S(x)\frac{\partial c_v}{\partial x} > 0. \tag{3.29}$$

As p_S, $c_v(x)$, and its derivative $\partial c_v/\partial x$ are greater than zero for $x > x_{open}$, the determinant is positive for positions where the pressure-displacement curve has positive slope, i.e., where the spring model has positive differential stiffness

$$\frac{\partial p_S}{\partial x} > 0 \Rightarrow \det(J) > 0. \tag{3.30}$$

In the negative differential stiffness region, the Jacobian only has a positive determinant if

$$\frac{\psi\, e^{\psi(x_{open}-x)} + s_\infty/c_i}{1 - e^{\psi(x_{open}-x)} + s_\infty/c_i\,(x - x_{open})} > -\frac{1}{2\,p_S(x)}\frac{\partial p_S}{\partial x}, \quad x > x_{open}, \tag{3.31}$$

where we use Eq. (3.24) to highlight the dependence on ψ.

Note that Eq. (3.29) is equivalent to positive slope $\partial Q_{out}/\partial x$, since for $p_S > 0$ we have

$$\begin{aligned}
&Q_{out,eq} = c_v(x)\sqrt{p_S},\\
&\frac{\partial Q_{out}}{\partial x} = \frac{\partial c_v}{\partial x}\sqrt{p_S} + c_v(x)\frac{1}{2\sqrt{p_S}}\frac{\partial p_S}{\partial x},\\
&\frac{\partial Q_{out}}{\partial x} > 0 \iff c_v(x)\frac{\partial p_S}{\partial x} + 2\,p_S(x)\frac{\partial c_v}{\partial x} > 0 \Rightarrow \det(J) > 0,
\end{aligned} \tag{3.32}$$

which further implies negative slope $\partial p_S/\partial Q_{out}$ in the negative differential stiffness region of the mechanics ($\frac{\partial p_S}{\partial x} < 0$), since

$$\begin{aligned}
&\frac{\partial Q_{out}}{\partial x} = \frac{\partial p_S}{\partial x}\Big/\frac{\partial p_S}{\partial Q_{out}},\\
&\frac{\partial Q_{out}}{\partial x} > 0 \iff \operatorname{sign}\left(\frac{\partial p_S}{\partial x}\right) = \operatorname{sign}\left(\frac{\partial p_S}{\partial Q_{out}}\right).
\end{aligned} \tag{3.33}$$

This means that those equilibria for which $\partial p_S/\partial Q_{out} > 0$ and $\partial p_S/\partial x < 0$ are unstable (saddle points, $\det(J) < 0$) for any value of damping parameter b.

For the second condition for stability, we require that the trace of the Jacobian is negative

$$\operatorname{tr}(J) = -\frac{c_v(x)}{2\,C_o}\frac{1}{\sqrt{p_S(x)}} - \frac{A_v}{b}\left.\frac{\partial p_S}{\partial x}\right|_{x_{eq}} < 0. \tag{3.34}$$

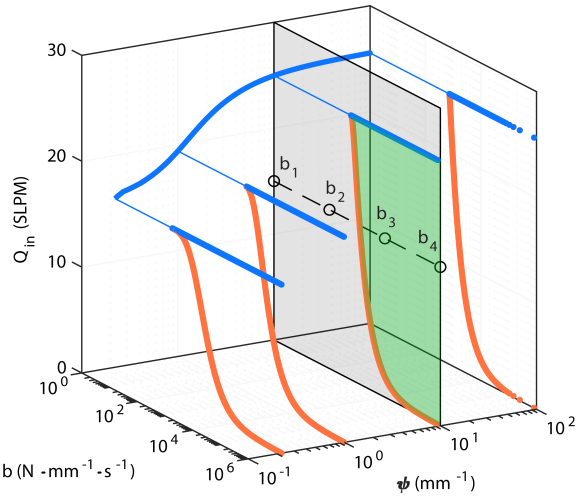

Figure 3.7
ASYMPTOTIC STABILITY OF THE SUSPECTED REGULATION MODE. Areas between blue lines and orange curves correspond to a (locally) asymptotically stable equilibrium. As an example, the locally asymptotically stable region for ψ = 10/mm is colored green. The dynamic response of markers b_1, b_2, b_3, and b_4 is exemplified in Figure 3.8. The used parameter values are listed in Table 3.1.

The first term of Eq. (3.34) is always less than or equal to zero. Therefore, the trace is always negative when the spring model has positive differential stiffness

$$\frac{\partial p_S}{\partial x} > 0 \Rightarrow \mathrm{tr}(J) < 0 \tag{3.35}$$

For the region of the spring model behavior that has negative differential stiffness, the trace of the Jacobian is only negative for a minimum value of damping, as we see from rearranging Eq. (3.34)

$$b > -\left(\frac{2 A_V C_o}{c_v(x)}\right) \frac{\partial p_S}{\partial x} \sqrt{p_S(x)}, \quad x > x_{open}. \tag{3.36}$$

From Eqs. (3.22), (3.26), (3.30) and (3.35) we find that equilibrium positions where the spring model has positive differential stiffness are always stable. For the region with negative slope, Eqs. (3.31) and (3.36) allow us to determine parameter values ψ and b for which the regulation mode is stabilized. We can see that these values will be different for varying equilibrium positions x_{eq}. Since we also know the unique equilibrium inflow rate associated with any equilibrium position $Q_{in}(x_{eq})$ according to Eq. (3.20), we can determine a range of inflow rates for which the regulation mode is stable, as function of ψ and b.

In Figure 3.7 we show the flow rates for which the regulation mode is stable, for $\psi = \psi_{cusp}$, 1, 10, and 100/mm, and damping value $1 \leq b \leq 1 \times 10^6$ N s/mm. The minimum flow rate (orange curve) follows from Eq. (3.36) ($\mathrm{tr}(J) < 0$). The maximum flow rate (blue lines and blue projected curve) follows from Eq. (3.31) ($\det(J) > 0$). As an example, we highlight the stable region in the plane defined by $\psi = 10$/mm (green area in Figure 3.7). To illustrate the effect of b, we study the system response in more detail for four points marked b_1, b_2, b_3, b_4 on the line defined by $\psi = 10$/mm and $Q_{in} = 15$ SLPM. For these values of ψ and Q_{in}, the minimum damping to achieve asymptotic stability is $b = 1230$ N s/mm. The first two points ($b_1 = 1$ and $b_2 = 100$ N s/mm) are in the unstable regime. The other two points ($b_3 = 1 \times 10^4$ and $b_4 = 1 \times 10^6$ N s/mm), are in the stable regime.

In Figure 3.8 we show the system response for different values of damping parameter b (corresponding to markers b_1 to b_4 in Figure 3.7). The other parameter values are summarized in Table 3.1. Although we use $\psi = 10$/mm, similar transitions are observed for higher or lower values of ψ and other values of inflow rate $0 < Q_{in} < Q^-_{fold}$ (see Figure 3.6 for an indication of the fold bifurcation point Q^-_{fold}). In Figure 3.8A and B we show the nullclines in the Q_{out}-Δp plane and x-p plane, respectively. We evaluate the asymptotic stability and color the stable parts of the nullcline green. Note that green coloring means these points are stable if and only if the associated inflow rate $Q_{in,eq} = Q_{out,eq}$ is applied. We also show two trajectories, one starting close to the expected limit cycle for oscillation (blue star and curve), and another starting close to the regulation mode (magenta star and curve), both for $Q_{in} = 15$ SLPM. Additionally, we show these trajectories as a function of time in Figure 3.8C. We obtain these trajectories by forward integration of the ODEs in Eqs. (3.15) and (3.16) with the MATLAB `ode23s` solver, which uses a modified Rosenbrock method to solve stiff ODEs.

As expected from Figure 3.7, at low damping (Fig. 3.8A-C (i) and (ii)) there are no flow rates for which the regulation mode is stable. Only the fully open and closed states are colored green. For higher values of b, the suspected regulation mode is stable for a wide range of inflow rates (iii) and (iv). Note that the applied flow rate $Q_{in} = 15$ SLPM lies within this range and the equilibrium is therefore stable.

These results show that the suspected regulation mode can be stabilized by sufficiently high damping. However, increased damping also strongly affects the oscillation mode. At low damping (Fig. 3.8A-C (i)) we see relaxation oscillations with maximum pressure close to Δp_{open}, i.e., close to the value at which the valve opens in a quasi-static experiment (Fig. 3.3). This agrees with the observed behavior in experiments (Figs. 3.2 and 3.3). Higher damping still results in relaxation oscillations,

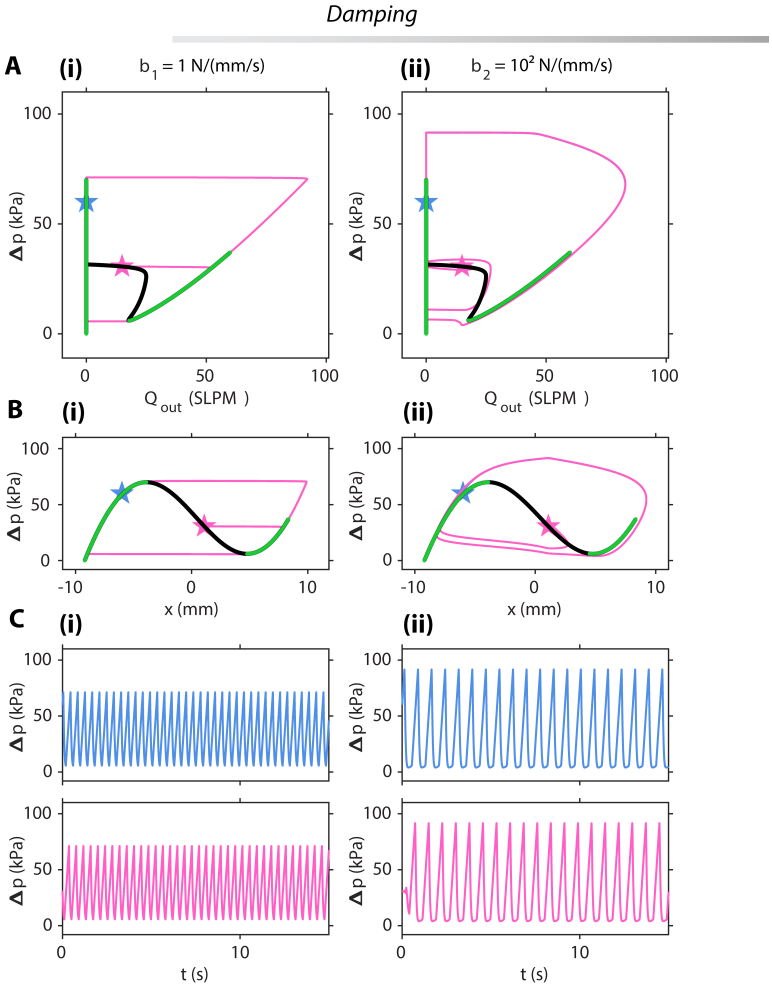

Figure 3.8

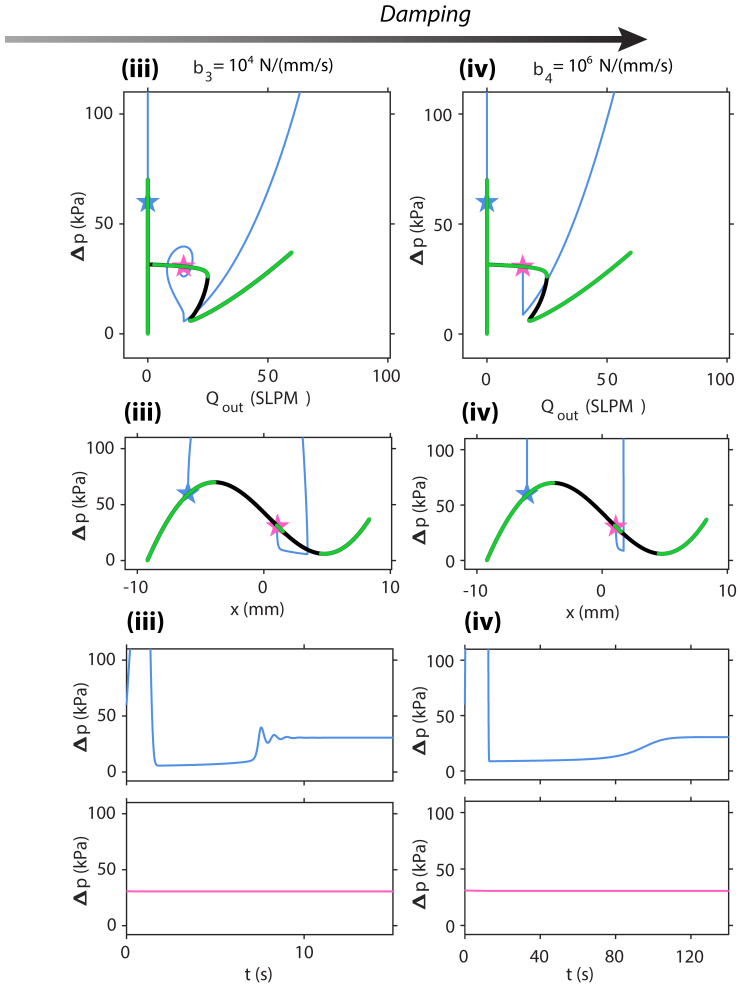

Figure 3.8

SIMULATED EFFECT OF DAMPING PARAMETER b ON THE DYNAMIC RESPONSE OF THE INITIAL MODEL. (**A**, **B**) Simulated trajectories (blue and magenta curves) for two different initial conditions (blue and magenta stars), both for Q_{in} = 15 SLPM, are shown in the Q_{out}-Δp plane in A, and in the x-Δp plane in B. Black curves represent the nullcline dx/dt = 0, where green overlay corresponds to stable equilibria. (**C**) Simulated pressure difference Δp over the valve for the same trajectories shown in A and B. Columns (i) to (iv) show results for increasing values of b, as indicated at the top. Parameter values are listed in Table 3.1.

but with slowed-down transitions between open and closed states, which increase Δp_{max} and decrease the cycle frequency (Fig. 3.8A-C (ii)). More importantly, at the same step in damping value for which the suspected regulation mode appears, the oscillation mode disappears altogether (Fig. 3.8A-C (iii) and (iv)). Therefore, in this analysis, we do not find any combination of parameters in line with experimental observations, for which the current model explains the coexistence of the regulation and oscillation modes.

Note that the step in damping value from b_2 to b_3 is still two orders of magnitude. To better understand this transition and to confirm that coexistence does not exist at intermediate values, we perform a numerical bifurcation analysis. We determine the eigenvalues of the Jacobian for the equilibrium at Q_{in} = 15 SLPM as a function of b, and we find the limit cycle of the system by forward integration of the ODEs in Eqs. (3.15) and (3.16) (Fig. 3.9). The results shown in Figure 3.9 suggest that the equilibrium transitions in a continuous manner from an unstable node to an unstable spiral, then in what appears to be a supercritical Hopf bifurcation, to a stable spiral, and finally to a stable node (Fig. 3.9B) [143]. The limit cycle disappears at the Hopf bifurcation, where the stable node appears (Fig. 3.9A). This strongly suggests that the initial system description can only explain the oscillation mode and not the regulation mode, as the stability of the suspected regulation mode depends heavily on damping, which is unphysical in comparison to our experiments.

3.5 MODIFIED VALVE MODEL

The initial model of the valve is based on a basic spring model that shows a snap-through instability (due to the compressing springs), without being bistable at zero load, and an intuitive model for the conduction of air through the valve opening. In Section 3.4.3, we show that this model cannot explain the regulation mode. In the current Section, we aim to improve the model so that it will capture the observed behavior. Thereto, we revisit the experimental results and perform an additional experiment to understand what we are still missing in our model. We then update the model to reflect these insights and perform a similar analysis as we did for the initial model.

3.5.1 *Definition of the modified model*

When comparing the initial model with experiments, one important difference is the slope of the regulation mode in the Q_{out}-Δp plane (Fig. 3.6). Experimentally, we observe that the regulation mode has a

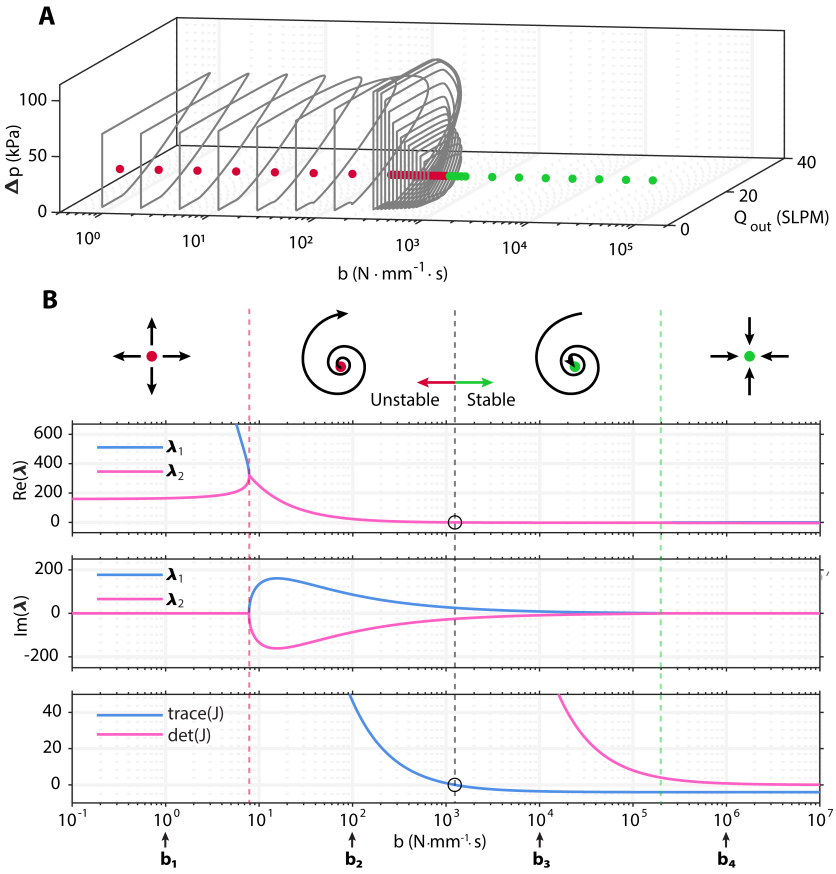

Figure 3.9

SIMULATED EFFECT OF DAMPING ON STABILITY OF OSCILLATION AND SUSPECTED REGULATION MODES IN THE INITIAL MODEL, FOR Q_{IN} = 15 SLPM. (**A**) Stable limit cycles (grey curves) in the Q_{out}-Δp plane for different values of damping b. The single equilibrium changes from unstable (red) to stable (green). (**B**) Real and imaginary parts of the eigenvalues of the Jacobian and trace and determinant of the Jacobian. Flow symbols indicate (from left to right) unstable node, unstable spiral, stable spiral, stable node. Open circular marker indicates transition to asymptotic stability. Parameter values are listed in Table 3.1.

positive slope, i.e., $d\Delta p/dQ_{out} > 0$, and this cannot be reproduced by the model we derived in Section 3.3. That is because the regulation mode is located at a displacement value that is characterized by negative differential stiffness $d\Delta p/dx < 0$, which requires $d\Delta p/dQ_{out} < 0$ for asymptotic stability according to Eq. (3.33). We hypothesize that the experimentally observed positive slope of the regulation mode in the Q_{out}-Δp plane is essential and should be featured in a modified model.

That implies that the regulation mode must be associated with positive differential stiffness, i.e., $d\Delta p/dx > 0$.

To qualitatively test if there exists another state (besides the fully open state) that has positive differential stiffness and where the valve is open, we conduct an experiment where we deform a valve with a probe (Fig. 3.10A). We control the position of the probe while monitoring the reaction force and the deformation of the valve. Despite the difference in loading conditions compared to loading with pressurized air, this experiment still provides important clues about the general mechanical behavior of the valve. Specifically, there are two distinct paths, during loading and unloading (Fig. 3.10B), and the difference seems too large to be explained from material dissipation alone. Indeed, as evidenced by its deformation, the valve follows different paths during loading and unloading (Figs. 3.10C and D). The shape of the valve during loading is symmetric (Fig. 3.10C), while the shape during unloading is asymmetric (Fig. 3.10D) and similar to the shape observed in the regulation mode (Fig. 3.1E(i) and Fig. 3.2D(i)–(iii)).

We recognize that these results may be influenced by the indenter. Especially along the loading path beyond the pressure maximum, the indenter seems to stabilize a symmetrically deformed shape that may not be seen when the valve is loaded with air pressure. We are led to this belief by experiments where we vary the maximum indentation distance, as shown in Figure 3.24. That experiment shows that when the valve is probed to sufficient displacement, representative of the case where the valve transitions from the fully open state to its initial shape, it follows the (green) unloading path shown in Figure 3.10B.

Even if the loading path measured with a probe may not be fully representative of the hydrostatic load case, these observations indicate there is hysteresis under displacement control that we do not take into account in our initial model. To represent this finding, we define an idealized description of the observed behavior with a stiffer loading curve and a softer unloading curve, as shown schematically in Figure 3.11A(i), and we define $x^{+}_{\text{snap, stiff}}$ of the stiffer curve as the point where the valve switches between the two curves during loading. During unloading, the softer path is followed. Since the valve follows different paths during loading and unloading, the valve orifice does not need to close upon unloading at the same displacement value where it opens upon loading. Crucially, such hysteresis in the valve conduction may result in the existence of the required displacement range where the valve is open, and differential stiffness is positive (grey highlight in Figure 3.11A(i)). As an idealized description of this conduction behavior, we assume two identical conduction curves, modulo a certain (as of yet unknown) translation x_{shift}, as shown schematically in Figure 3.11A(ii).

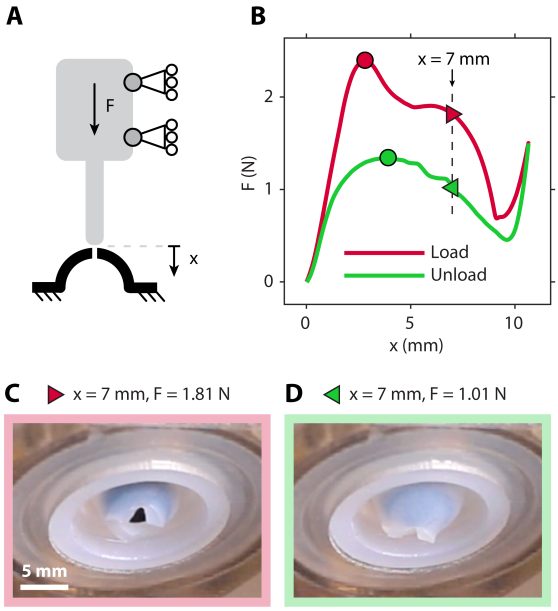

Figure 3.10
DISPLACEMENT-CONTROLLED LOADING EXPERIMENT OF THE VALVE. (**A**) Schematic of the experimental setup. A custom probe is attached to a universal testing system, Instron (see Figure 3.23 for a detailed overview of the setup). (**B**) Measured force during loading (red curve) and unloading (green curve). Circular markers indicate local maxima, and triangles mark an identical displacement value during loading (red, pointing right) and unloading (green, pointing left). (**C**) Deformed valve during loading, at $x = 7\,\text{mm}$. (**D**) Deformed valve during unloading, at $x = 7\,\text{mm}$.

However, explicitly implementing even this highly simplified additional hysteresis behavior complicates the model, because both c_v and p_S are no longer functions of x. We prefer to maintain a uniquely defined model in x, and to keep the number of DOFs in our model to a minimum, while still introducing this potentially crucial additional behavior. To obtain this result, we firstly ensure that the conduction behavior is uniquely defined. Thereto, we translate the conduction curve associated with unloading by $-x_{\text{shift}}$, such that it overlaps with the conduction curve associated with loading (Fig. 3.11B(ii)). Secondly, to maintain the assumed relation between pressure and valve conduction, we translate the softer mechanical curve by the same amount (Fig. 3.11B(i)). Note that the value of x_{shift} will later be determined from a fit to experimental data. This procedure artificially makes the relevant part of the unloading curve accessible, without introducing additional hysteresis.

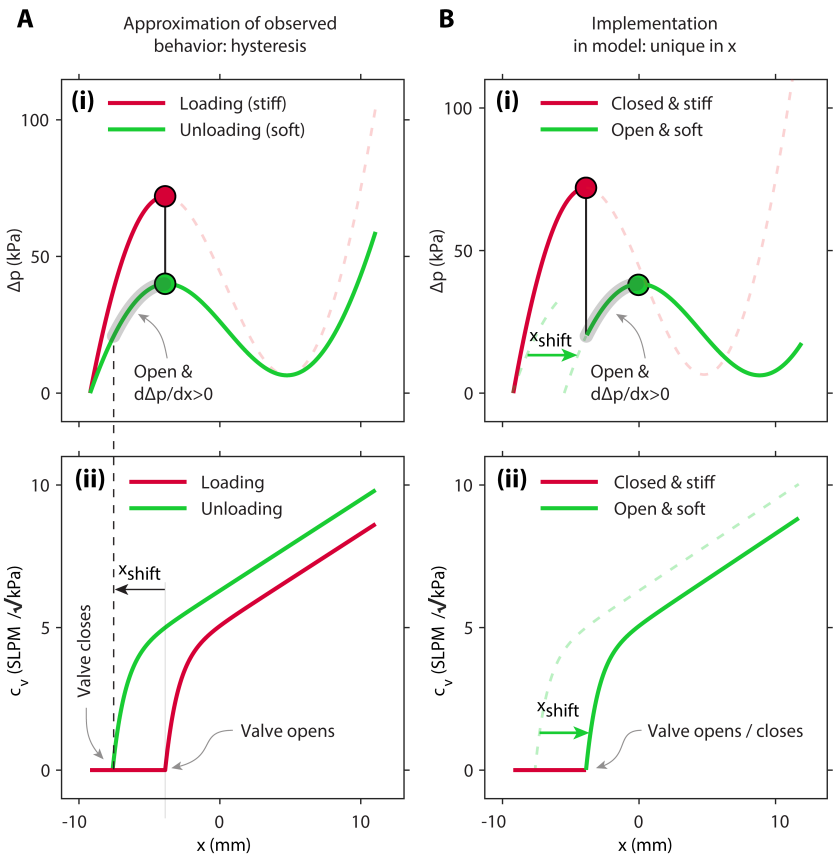

Figure 3.11

A MODIFIED MODEL TO ACCOUNT FOR ADDITIONAL HYSTERESIS IN THE MECHANICS AND CONDUCTION BEHAVIOR. (**A**) Idealization of the actual, observed behavior (see Figure 3.10), with hysteresis in mechanics and valve conduction. (i) Equilibrium pressure difference over the valve as function of displacement of the dome. The loading curve (red) is stiffer than the unloading curve (green). At $x_{open} = x^{+}_{snap,\,stiff}$ the pressure-displacement curve switches between the stiff and soft curves. (ii) Valve conduction as function of displacement of the dome. During loading (red curve), the valve opens around the pressure maximum of the corresponding pressure-displacement curve (red circular marker), but during unloading (green curve) the valve closes at a smaller displacement than the local maximum of the corresponding pressure-displacement curve (green circular marker). (**B**) Modified model implementation. (i) The soft curve is shifted to the right. (ii) The unloading conduction curve is shifted on top of the loading curve.

The modified model is described by the same differential equations (Eqs. (3.15) and (3.16)) and conduction model (Eq. (3.14)) as the initial

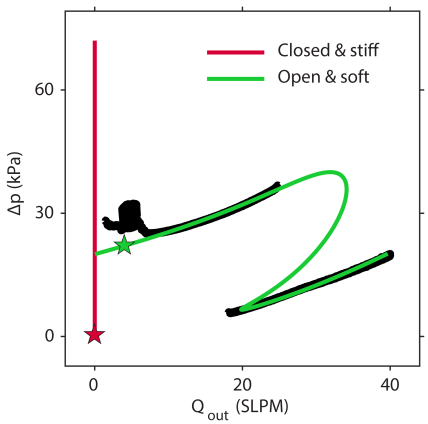

Figure 3.12
NULLCLINE $dx/dt = 0$ OF THE MODIFIED MODEL. The red line corresponds to the stiffer behavior for $x \leq x_{open}$, where the valve is closed. The green curve corresponds to the softer behavior at $x > x_{open}$, where the valve is open. The nullcline fits measured values $\Delta p(Q_{out})$ (black curves) both in the regulation mode and in the fully open state. Parameter values are listed in Table 3.2.

model. The spring model is piece-wise identical to the initial definition of Eq. (3.9), i.e.,

$$F_{S,\,mod} = \begin{cases} F_S(x), & k_S = k_{S,stiff}, k_R = k_{R,stiff} & x \leq x_{open} \\ F_S(x - x_{shift}), & k_S = k_{S,soft}, k_R = k_{R,soft} & x > x_{open}, \end{cases} \tag{3.37}$$

where we leave the stiffer curve unchanged with respect to the initial model.

We introduce three new variables $k_{S,soft}$, $k_{R,soft}$ and x_{shift} that describe the softer curve. We link their values to experimental observations as follows. First, we take the values of $k_{S,soft}$ and $k_{R,soft}$ such that the local pressure minimum is equal to the value Δp_{close} found in a static experiment ($\Delta p_{close} \approx 5\,kPa$, see Figure 3.3), so $p^-_{snap,soft} = p^-_{snap,\,stiff} = \Delta p_{close}$. Then, for different values of $p^+_{snap,soft}$ we determine the values of x_{shift} and valve conduction parameters ψ, s_∞ and c_i that minimize the least-squares error between model and experimental data. Hence, for each $p^+_{snap,soft}$, we obtain those parameters that allow the best fit with the experiments in terms of least-squares error. Then, we compare various of these curves (each obtained from one value of $p^+_{snap,soft}$), and we visually observe that a good fit is obtained for $p^+_{snap,soft} = 40\,kPa$.

The resulting nullcline $dx/dt = 0$ is shown in Figure 3.12, alongside measured data. The modified model allows a good fit to data both in the fully open state and in the regulation mode. Importantly, the modified

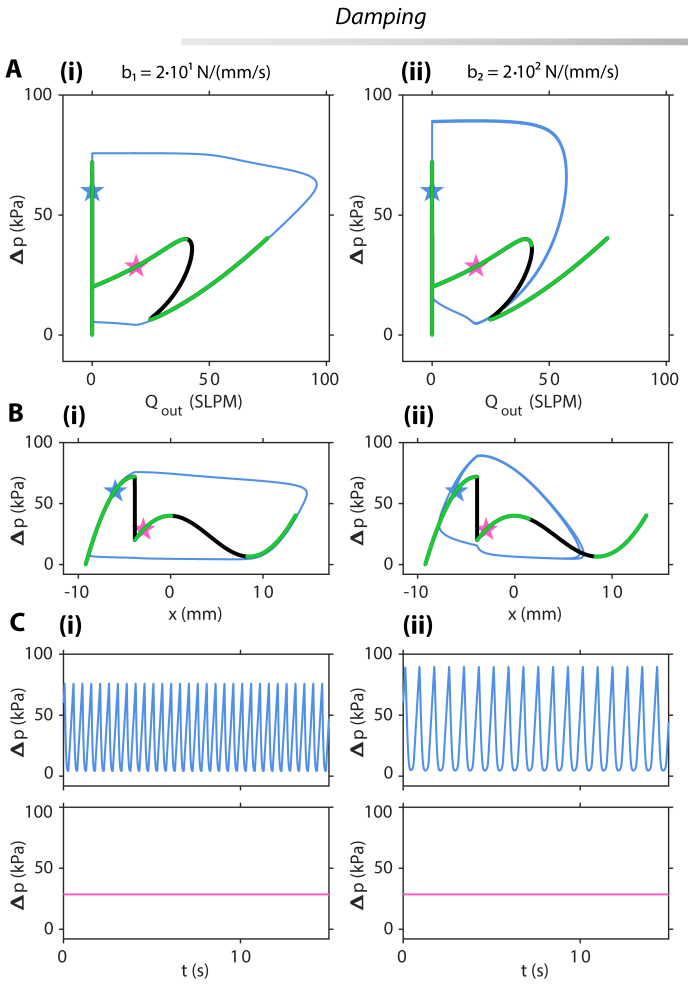
Damping
A
(i)
b1 = 2·10^1 N/(mm/s)
(ii)
b2 = 2·10^2 N/(mm/s)
Δp (kPa)
Q out (SLPM)
B
x (mm)
C
t (s)

Figure 3.13

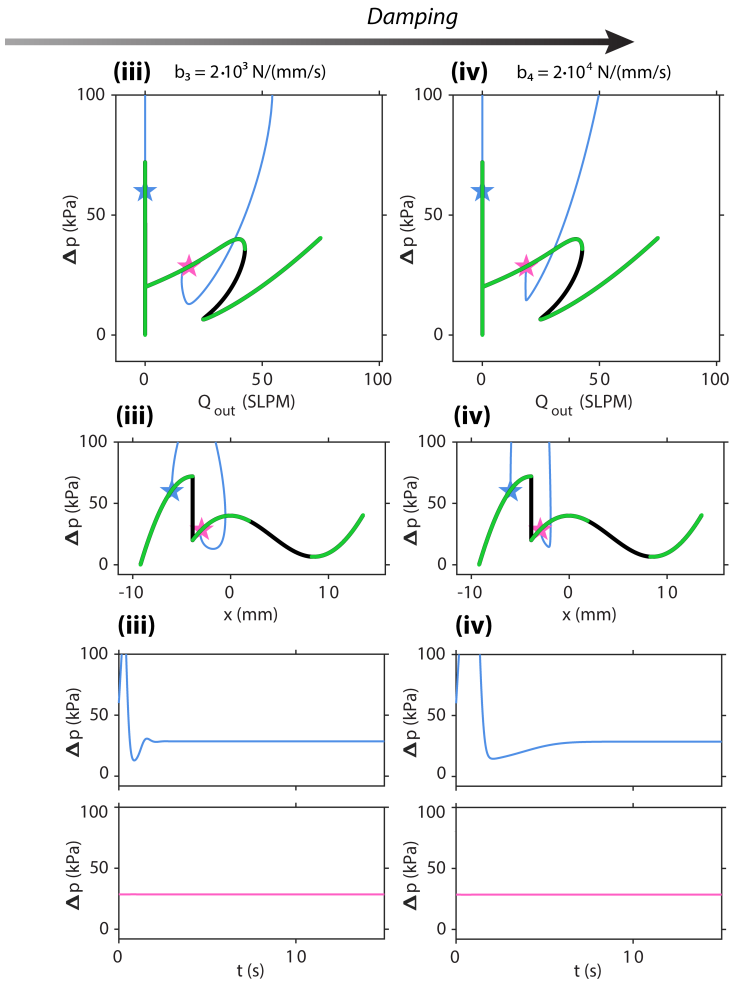

Figure 3.13

SIMULATED EFFECT OF DAMPING PARAMETER b ON THE DYNAMIC RESPONSE OF THE MODIFIED MODEL. Simulated trajectories (blue and magenta curves) for two different initial conditions (blue and magenta stars) and Q_{in} = 15 SLPM, shown in (**A**) the Q_{out}-Δp plane, and in (**B**) the x-Δp plane. Black curves represent the nullcline $dx/dt = 0$, where green overlay corresponds to stable equilibria. (**C**) Simulated pressure difference Δp over the valve for the same trajectories shown in A and B. Columns (i) to (iv) show results for increasing values of b, as indicated at the top. Parameter values are listed in Table 3.2.

model results in the existence of a displacement range with positive slope $\partial\Delta p/\partial Q_{out} > 0$.

Note that we develop our model based on measurements of the regulation mode for inflow rates $Q_{in} \leq 25\,\text{SLPM}$, which is a limitation of our mass flow control equipment. At $Q_{in} = 25\,\text{SLPM}$, the valve is still in the regulation mode, but the model predicts that the valve must transition from the regulation mode to the fully open state if we increase the flow rate even further (Fig. 3.12). For completeness, we qualitatively verify this prediction, by connecting the valve directly to a pressure regulator, while we measure pressure before and behind the valve and flow through the valve (Fig. 3.22). That is the same setup we use to measure the fully open state at higher flow rates (green curve in Figure 3.3). Interestingly, we observe not only the transition to the open state, but even the pressure decrease before the transition, although we continue to manually increase the pressure setpoint. The pressure drop is able to decrease while we increase the setpoint, because there is restriction (tubes, connectors) between the pressure regulator and the valve, such that this setup approximates flow control rather than pure pressure control. The extended experiment qualitatively verifies the final part of the nullcline that was not observed at lower flow rates in the experiments using a dedicated flow controller (black curve in Figure 3.3).

3.5.2 *Coexistence of regulation and oscillation in the modified model*

To determine if the modified model can explain coexistence of the regulation mode and the oscillation mode, we numerically analyze the effect of damping parameter b, as we did for the initial model. In Figure 3.13 we show the system response for four values of damping, and for a constant inflow rate $Q_{in} = 15\,\text{SLPM}$.

Crucially, and differently from the initial model, at any of the studied values of damping there exists an asymptotically stable equilibrium for a wide range of inflow rates, specifically for any inflow rate where $\partial p_S/\partial x > 0$. For increasing damping values, the stable range of inflow rates grows to include also the part where $\partial Q_{out}/\partial p_S < 0 \wedge \partial p_S/\partial x < 0$. Similarly to the initial model, we observe a limit cycle that corresponds to the oscillation mode. Increasing damping affects the oscillation mode. Higher damping slows down the transitions between open and closed states, which increases Δp_{open}, and decreases the cycle frequency (Fig. 3.13(i) and (ii)). As in the initial model, the oscillation mode disappears altogether at high damping (Fig. 3.13(iii) and (iv)). Excitingly, the modified model thus reproduces the coexistence of the oscillation and regulation mode (for moderate values of the damping parameter).

In the modified model, the oscillation mode is surrounding a stable equilibrium. Therefore, for the stable limit cycle to exist, there must also exist an unstable limit cycle between the stable regulation mode and the stable oscillator. To probe the existence of such unstable limit cycle, we integrate differential equations Eqs. (3.15) and (3.16) both forward and backward in time, where we use the modified model Eq. (3.37) for the mechanics, using `if` statements to distinguish soft and stiff domain. We integrate with the MATLAB `ode23s` solver, which uses a modified Rosenbrock method to solve stiff ODEs. We start from initial conditions near the expected limit cycle, near the stable equilibrium, and in between.

In Figure 3.14A we show stable (grey) and unstable (red) limit cycles for different values of b. At lower damping values, we find a single unstable limit cycle between the stable oscillating and regulation modes, as required for the coexistence of both modes. Interestingly, both limit cycles deform for increasing damping, until at $b \approx 220\,\mathrm{N\,s/mm}$ they disappear in a fold of limit cycles. This is in contrast to the situation in the initial model, where the oscillation mode disappeared in a Hopf bifurcation, giving rise to the regulation mode. In the modified model, the regulation mode transforms from a stable node to a focus and back for increasing damping values, but never becomes unstable (Fig. 3.14B).

Having determined the coexistence of regulation and oscillation, as well as the effect of damping, we can now try to replicate key results observed in experiments. Firstly, recall that the system can enter the regulation mode as a result of a disturbance (Fig. 3.1). In the experiment we temporarily pinch a tube behind the valve. In our numerical replication of the experiment, we approximate this disturbance by temporarily increasing damping parameter b (Fig. 3.15A). This is a rough approximation of the experimental conditions, motivated by the assumption that the increase in downstream resistance induces a temporary vacuum effect when the valve snaps back, effectively slowing down the snap-back transition. In the simulation, this increase in damping causes the system to transition from the oscillation mode to the regulation mode. That is because increased damping temporarily removes the oscillation mode, conform Figs. 3.13 and 3.14. The system is therefore attracted to the regulation mode. Once in the regulation mode, the system stays in that mode even when the damping value is restored to its original value, because it is now inside the unstable limit cycle that separates the two modes.

Secondly, recall that upon varying the inflow rate over a wide range in an experiment, the system remains in the mode in which it started (Fig. 3.2). Numerically, we similarly apply a varying inflow rate (Fig. 3.15 B(i)) and first start the system from an initial condition corresponding to the regulation mode (green star in Figure 3.15B(ii)). As in the experiment, the system remains in the regulation mode as the flow rate is increased

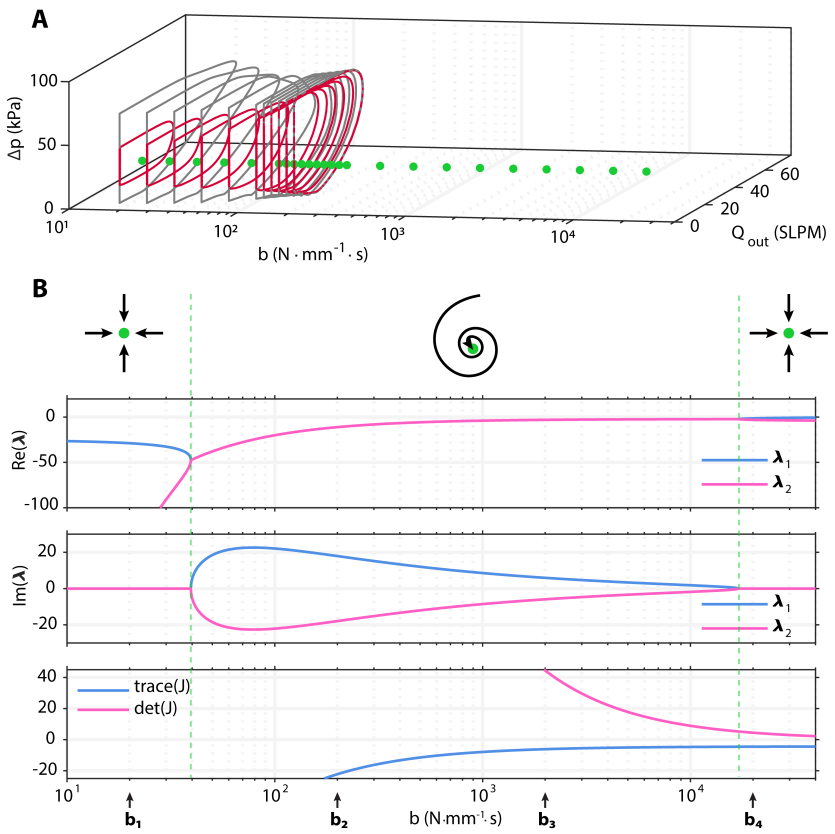

Figure 3.14
SIMULATED EFFECT OF DAMPING ON ASYMPTOTIC STABILITY OF OSCILLATION AND REGULATION MODES IN THE MODIFIED MODEL, FOR Q_{IN} = 15 SLPM. (**A**) Stable (grey curves) and unstable (red curves) limit cycles in the Q_{out}-Δp plane for different values of damping b. For all values of b, the single equilibrium is stable (green marker). (**B**) Real and imaginary parts of the eigenvalues of the Jacobian and trace and determinant of the Jacobian. Flow symbols indicate (from left to right) stable node, stable spiral, and stable node. Parameter values are listed in Table 3.2.

and decreased. Differently from the experiment, the simulated system does not exit the regulation mode until the flow completely stops. Then, we start from an initial condition corresponding to the oscillation mode (red star in Fig. 3.15B(iii)). The simulated system continues to oscillate when the inflow rate is changed. The oscillation frequency first increases, then decreases until the system stops oscillating as it enters the fully open state. Upon decreasing the inflow rate the system restarts oscillating at the same inflow rate where it stopped.

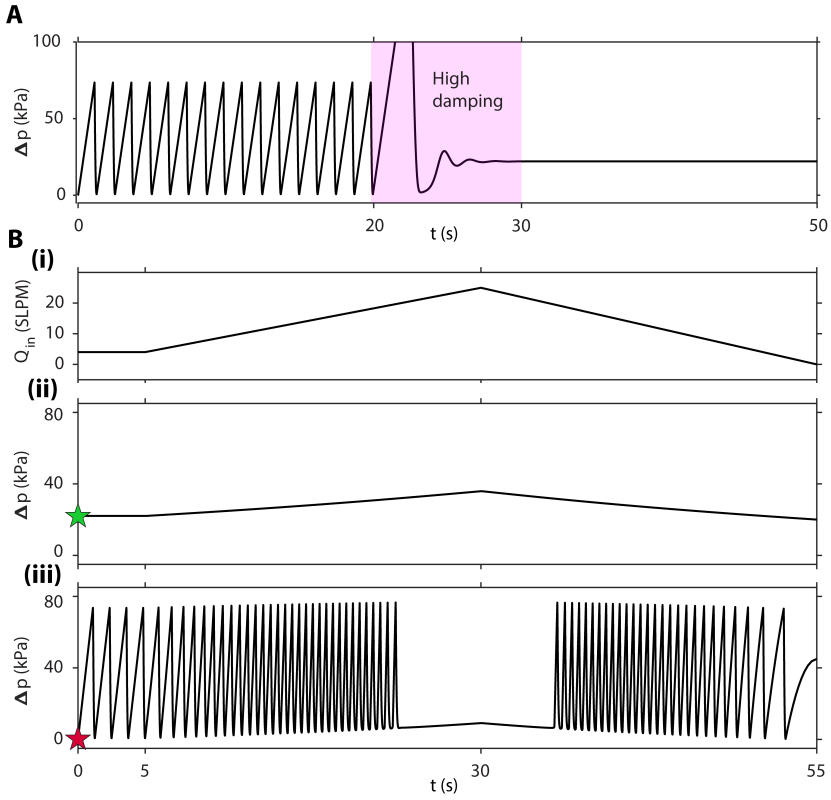

Figure 3.15

NUMERICAL REPLICATION OF EXPERIMENTAL RESULTS. (**A**) A temporary disturbance permanently moves the system from the oscillation to the regulation mode (compare to the experiment in Figure 3.1). Simulated pressure difference Δp for a constant inflow rate $Q_{in} = 4\,\mathrm{SLPM}$. $b = 20\,\mathrm{N\,s/mm}$ for the first twenty seconds, $b = 1 \times 10^4\,\mathrm{N\,s/mm}$ between $t = 20\,\mathrm{s}$ and $t = 30\,\mathrm{s}$, then $b = 20\,\mathrm{N\,s/mm}$ again. (**B**) The system remains either in regulation or oscillation mode for a wide range of inflow rates (compare to the experiment shown in Figure 3.2). (i) Inflow rate $Q_{in} = 4\,\mathrm{SLPM}$ in the first five seconds, then increases to $Q_{in} = 25\,\mathrm{SLPM}$ at $t = 30\,\mathrm{s}$, and decreases to $Q_{in} = 0$ at $t = 55\,\mathrm{s}$. (ii, iii) Simulated pressure difference Δp for $b = 20\,\mathrm{N\,s/mm}$, when starting from initial conditions close to the regulation mode (ii) or oscillation mode (iii). Parameter values are listed in Table 3.2.

3.6 SUPPRESSING THE REGULATION MODE

The modified model provides a mechanistic explanation for the existence of the regulation mode. In the remainder of this work, we will test the predictive power of the model by using it as a design tool to avoid the existence of the regulation mode. This goal is motivated by the application of hysteretic valves in soft robot control, where the existence of the regulation mode could be a risk, such as when controlling the pulsatile activation of soft total artificial hearts [133]. As we have seen, the system can enter this mode by temporary disturbances, which may not always be avoidable once the heart is implanted in the human body.

Of several available routes to avoid regulation, here we focus on changing only the valve conduction behavior, without significantly changing the mechanics. The regulation mode exists at low flow rates because it maintains a large enough pressure drop to prevent the valve from snapping back to its initial state (Figs. 3.1B and 3.2B). This is possible because the valve orifice is almost completely closed (Fig. 3.1E(i) and 3.2D(i)–(iii)). This prompts us to study what happens when the valve never completely closes, except in its initial state.

In Figure 3.16 we show an implementation of this concept in our model. We study the effect on the nullclines when we assume that a finite orifice opening remains for all $x > x_{open}$. We implement this inhibition of premature closing by adding a factor ρ to the definition of conduction

$$c_v = \begin{cases} 0 & x \le x_{open} \\ \rho\, c_i + (1-\rho)\, c_i \left(1 - e^{\psi(x_{open}-x)}\right) + s_\infty\,(x - x_{open}) & x > x_{open}. \end{cases} \tag{3.38}$$

In Figure 3.16A we show the resulting conduction behavior, and in Figure 3.16B we show the effect on the nullcline $dx/dt = 0$. Varying parameter ρ between 0 and 1, i.e., increasing the minimum conduction value from 0 to 1 times c_i, results in the disappearance of equilibria in the range $0 < Q_{in} < Q^-_{reg}$, where

$$Q^-_{reg} = c_v(x_{open})\sqrt{p_S(x_{open})} = \rho\, c_i \sqrt{p_S(x_{open})}, \tag{3.39}$$

such that Q^-_{reg} increases linearly with ρ (Fig. 3.16C). Intuitively, this effect of disappearing equilibria arises because we are imposing the orifice to stay open (which means it enforces positive Q_{out}) when the mechanics is in the soft regime. Setting $\rho = 1$ all but completely suppresses the coexistence of the oscillating and regulation modes. From an application perspective, Q^-_{reg} is a safe maximum operating inflow rate, below which the regulation mode cannot exist.

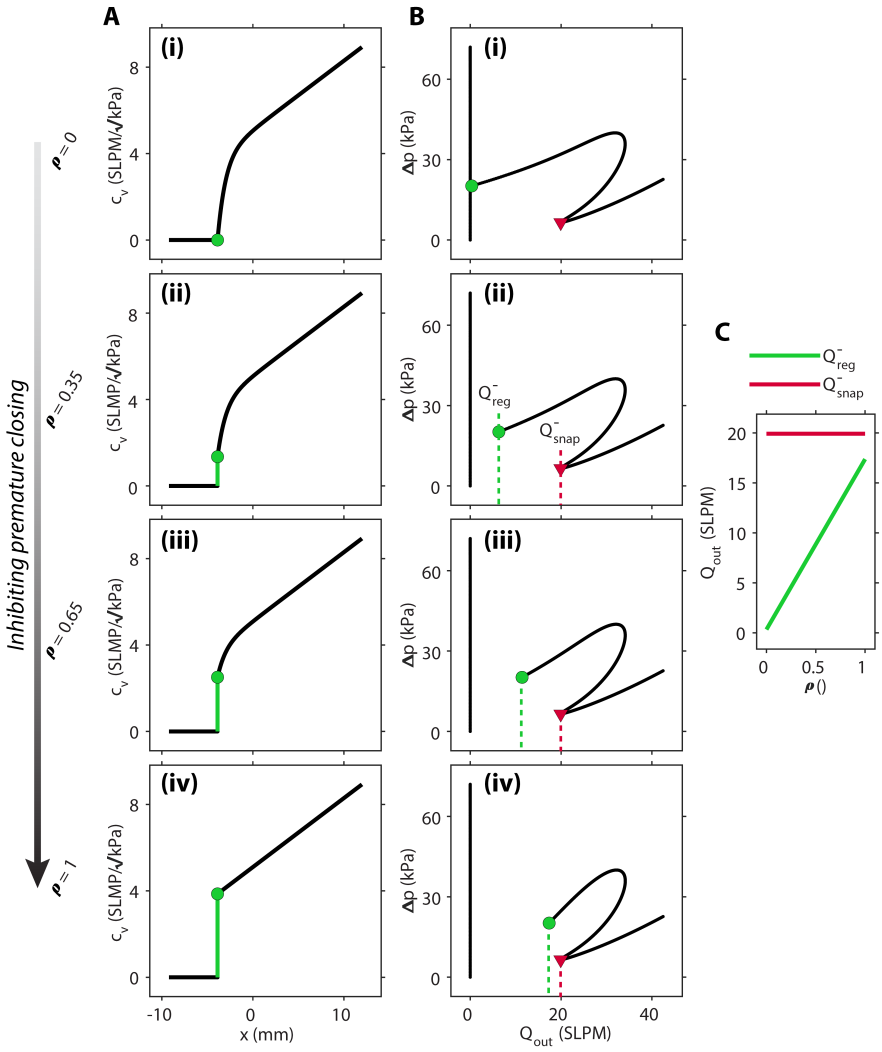

Figure 3.16

AVOIDING REGULATION BY AVOIDING COMPLETE CLOSURE OF THE VALVE. (**A**) The effect of design parameter ρ on valve conduction. For increasing values of ρ, valve closure in the open state is increasingly inhibited. $\rho = 0$ represents the original valve design where the valve closes completely before snapping back to the fully closed state, $\rho = 1$ nullifies the effect of ψ and maximizes the discontinuous jump at x_{open}. Green circular markers indicate conduction value $c_v(x_{open}) = \rho\, c_i$ at valve opening and closing. Green lines indicate a jump. (**B**) Effect of ρ on nullcline $dx/Dt = 0$. Green circular markers correspond to outflow rate $\bar{Q}_{reg}$ at valve opening and closing. Red triangles correspond to the local flow rate minimum $\bar{Q}_{snap}$ (associated with the local pressure minimum $\Delta\bar{p}_{snap}$). (**C**) Evolution of $\bar{Q}_{reg}$ and $\bar{Q}_{snap}$ as function of ρ.

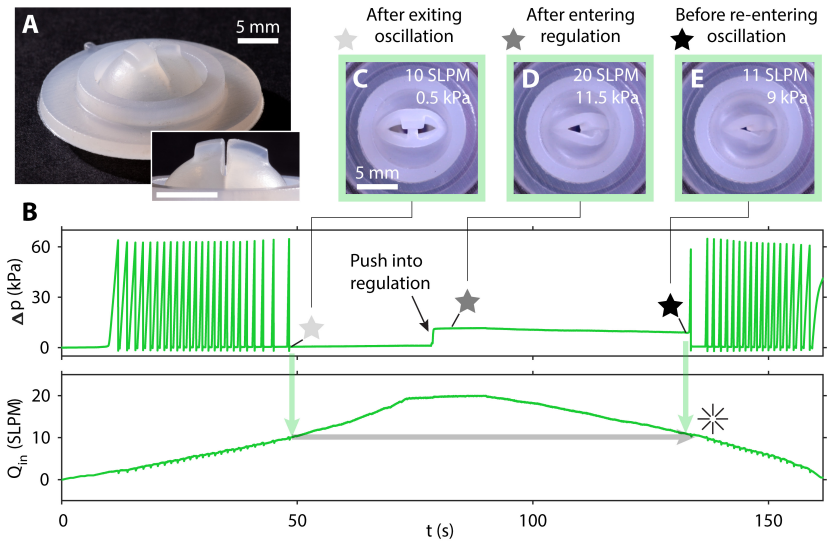

Figure 3.17
EXPERIMENTAL REALIZATION OF SUPPRESSION OF THE REGULATION MODE. (**A**) Oblique view photograph of the modified valve. The inset shows a side view of the protrusions and the slit (scale bar 5 mm). (**B**) Measured pressure drop Δp over, and measured inflow rate Q_{in} through the valve. There are no flow rates for which the regulation and oscillation mode coexist. Star symbols refer to panels C-E. (**C**) The valve has entered the fully open state (light grey star), (**D**) the valve has been forced into the regulation mode (grey star), (**E**) the valve is about to restart oscillating (black star).

To experimentally validate this predicted behavior, we fabricate a valve that has additional features aimed at preventing the valve from closing completely when it is in the regulation mode. Thereto, the valve has protrusions on the convex side of the dome, around the cut. Moreover, instead of three shorter slits, we cut a single longer slit, as shown in Figure 3.17A. The detailed design is shown in Figure 3.20. We conduct an experiment where we first increase the flow rate from $Q_{in} = 0$ to $Q_{in} = 20\,\text{SLPM}$ in 70 s. We observe that the valve enters the fully open state at $Q_{in} = 10\,\text{SLPM}$ (light grey star in Figure 3.17B). While we hold the flow rate at $Q_{in} = 20\,\text{SLPM}$, we physically push the valve, causing it to enter the regulation mode (grey star). Excitingly, when we then decrease the flow rate, the modified valve exits the regulation mode and restarts oscillations around the same inflow rate (black star) where it entered the open state. This means that there is no longer coexistence between the regulation mode and the oscillation mode at any flow rate, demonstrating the validity of the model-based prediction.

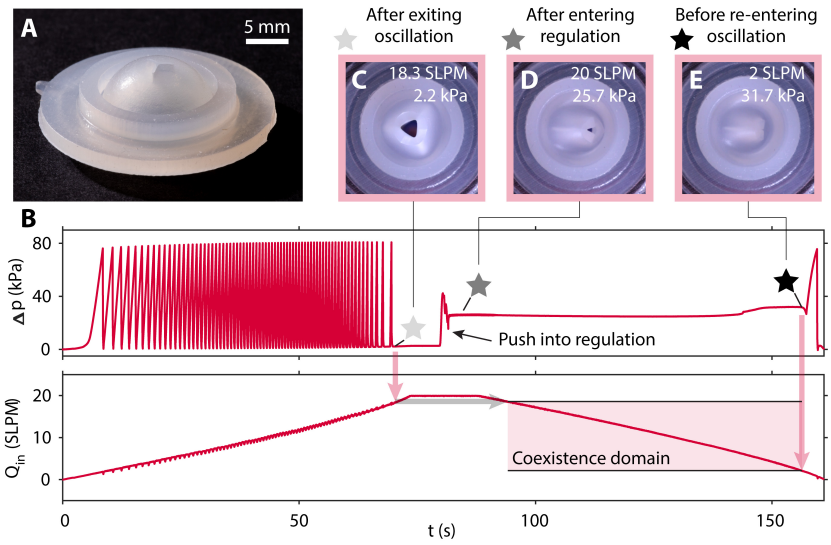

Figure 3.18

REFERENCE EXPERIMENT WITH ORIGINAL VALVE DESIGN. (**A**) Oblique view photograph of the original valve. (**B**) Measured pressure drop Δp over, and measured inflow rate Q_{in} through the valve. Star symbols indicate three important moments in the experiment, and the valve deformation at these moments is shown in panels C-E. (**C**) The valve has entered the fully open state (light grey star), (**D**) the valve has been forced into the regulation mode (grey star), (**E**) the valve is about to restart oscillating (black star). Red shaded area indicates the flow rates for which the regulation and oscillation modes coexist.

As a reference, in Figure 3.18 we show results of the same experiment using the original valve design. The valve enters the fully open state at Q_{in} = 18 SLPM, which is higher than the modified valve. Again, we physically push the valve, causing it to enter the regulation mode (grey star). When we decrease the flow rate, the valve remains in the regulation mode until Q_{in} = 2 SLPM (black star), as expected from the other experimental evidence (e.g., in Figure 3.2).

These results demonstrate that we can prevent the valve from closing completely in the regulation mode, which in turn removes the existence of the regulation mode at lower flow rates, as predicted by the model. This high-level result is summarized in Figure 3.19, where we depict the inflow rates for which the oscillation mode, the regulation mode, and the fully open state exist for the two valve designs. Note that, besides the desired effect, modifying the design also causes the valve to enter the fully open state at a significantly lower flow rate compared to the original design. The model did not predict this decrease of the maximum flow rate for the oscillation mode as a result of changing ρ. In reality,

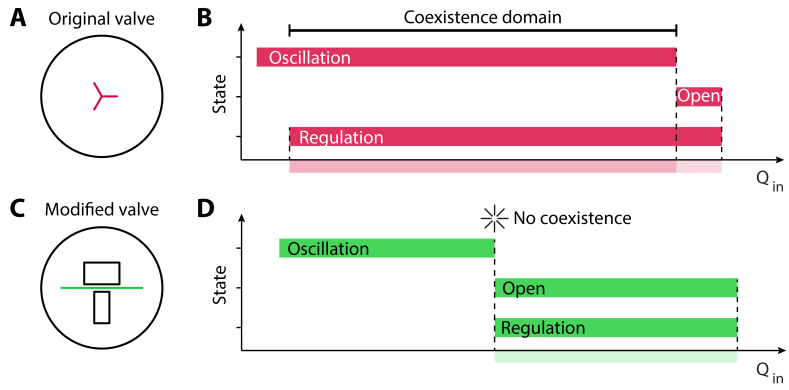

Figure 3.19
FLOW RATES FOR WHICH THE ORIGINAL AND MODIFIED VALVES CAN BE IN EACH OF THREE STATES: THE OSCILLATION MODE, REGULATION MODE, OR FULLY OPEN STATE. (**A**) Top view schematic of the dome (black) and cut pattern (red) for the original valve. (**B**) Red bars indicate for each mode at which range of flow rates the valve can be in that mode, showing significant overlap between oscillation and regulation. (**C**) Top view schematic of the modified valve with added features (black), and cut pattern (green) for the modified valve. (**D**) Green bars indicate for each mode at which range of flow rates the valve can be in that mode, showing no overlap between oscillation and regulation.

the modifications to the design do not only change the fluidics, but also affect the mechanics to some extent, resulting in a decrease of p^{-}_{snap}. We measure a pressure drop at closing of the valve $\Delta p_{close} \approx 0$, indicating that the modified valve is nearly bistable. In future work, this could potentially be mitigated by also changing mechanical parameters such as thickness and dome angle.

3.7 DISCUSSION

The goal of the present study is to understand the coexistence of a pressure regulation mode and an oscillation mode in soft hysteretic valves, and more generally to better describe the mechanics and dynamics of the valve in a fluidic circuit. In previous work, we model the same valves as pressure-controlled switches that can be either in a fully open, or a fully closed state [53]. Using that approach we can, by definition, only describe the behavior of the valve in the oscillation mode and the fully closed and open states. Therefore, in the present work, we aim to develop a more complete, but minimal model that captures also the regulation mode.

We conclude from our analysis that an essential feature to explain the coexistence of the regulation and oscillation modes at the same inflow

rate and realistic damping values is the existence of a displacement range with positive differential stiffness. Moreover, the regulation mode relies on near-complete closure of the orifice, which we can prevent by changing the valve design. Taken together, our analysis provides a mechanistic explanation of the observed behavior, and can be used for informed design change decisions.

This work is limited to a specific valve design, of which we change the fluidic characteristics in order to remove the regulation mode at low flow. However, we conclude that specifics of the mechanics are also essential for the existence of the regulation mode. Therefore, in future work, it will be interesting to study the effect of the undeformed shape of the valve, such as the thickness and shallowness of the dome, as well as its boundary conditions.

Furthermore, in this work, we neglect visco-elastic effects, although visco-elasticity may cause some detailed effects that we currently do not capture in our model. For example, our model predicts a continuous increase of Δp_{open} for increasing Q_{in} (Fig. 3.15). In experiments, we see that Δp_{open} initially increases, then decreases (Fig. 3.2). We hypothesize that this is caused by a memory effect. At higher flow rates, the valve remains longer in the open state before snapping back (T_{open} increases), such that it increasingly relaxes in that deformation state. At the same time, the valve spends less time in its initial state (T_{close} decreases). The net outcome could be an increased effect of residual stress on the forward snap-through event, which results in a lower effective Δp_{open}. A better understanding of this relation could be valuable in applications where small imperfections between multiple valves affect activation patterns of multiple actuators [53].

We focus on the development of a minimal model, ultimately geared toward promoting one or the other mode in our hysteretic valves. However, we notice that our system shows behavior that may be interesting for more fundamental future studies as well. The valve in its oscillating mode slows down considerably as we increase the inflow rate, until it stops oscillating. Potentially, our valve could provide an interesting platform for studying dynamics around critical points [138].

Finally, we note that circuits with hysteretic valves, and fluidic circuits in general, are increasingly used to control fluid-driven soft robots [46, 53, 57, 85, 86, 125–131]. Multidisciplinary studies (mechanics, fluidics, and dynamics) like the present one, may contribute to better understanding of system-level behavior. This is especially important in the field of soft robotics, where embodied intelligence and safe interaction with humans are important claimed benefits, while formal robustness and other performance criteria are still underdeveloped. As a result of the present study, we better understand stability criteria of the regulation mode in a specific type of hysteretic valves. This may contribute to the

reliability of future soft robotic applications such as autonomous walking robots, and medical prosthetic devices.

3.8 SUPPLEMENTARY INFORMATION

Table 3.1
PARAMETERS USED FOR THE ASYMPTOTIC STABILITY ANALYSIS OF THE INITIAL MODEL.

Parameter	Value	Unit
b_0	12	mm
h_0	9.2	mm
θ	75	deg
A_v	452.4	mm^2
k_S	2.9×10^7	N/m
k_R	3.6×10^8	N m/rad
C_o	0.06	1/60SL/kPa
x_{open}	1	mm
ψ	10	1/mm
c_i	4.5	SLPM/$\sqrt{\text{kPa}}$
s_∞	0.7	SLPM/$\sqrt{\text{kPa}}$/mm

Table 3.2
PARAMETERS USED FOR THE ASYMPTOTIC STABILITY ANALYSIS OF THE MODIFIED MODEL.

Parameter	Value	Unit
b_0	12	mm
h_0	9.2	mm
θ	75	deg
A_v	452.4	mm^2
k_S	3.0×10^7	N/m
k_R	3.7×10^8	N m/rad
$k_{S,soft}$	1.6×10^7	N/m
$k_{R,soft}$	2.2×10^8	N m/rad
C_o	0.06	1/60SL/kPa
x_{open}	−3.9	mm
x_{shift}	3.7	mm
ψ	1.1	1/mm
c_i	3.9	$SLPM/\sqrt{kPa}$
s_∞	0.3	$SLPM/\sqrt{kPa}/mm$

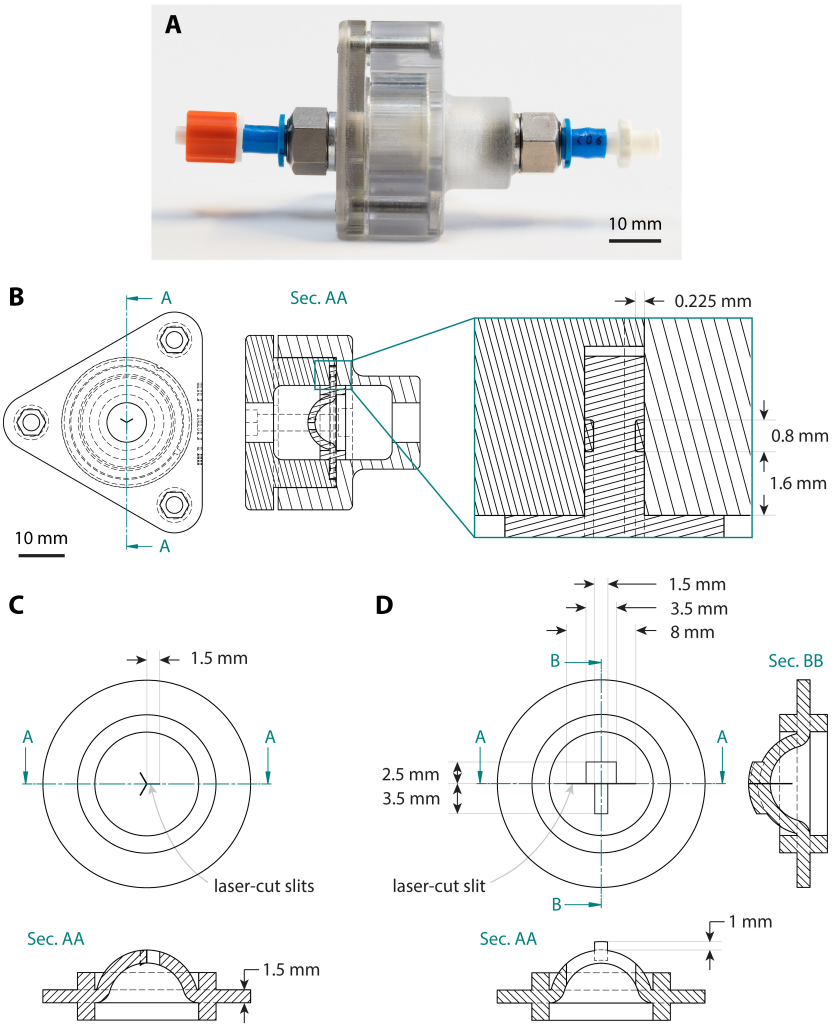

Figure 3.20
VALVE AND HOLDER DESIGNS. (**A**) Assembled valve holder. (**B**) Valve holder design. (**C**) Original valve design (uniformly scaled up by a factor two with respect to the design used in our previous work [53]). (**D**) Modified valve design.

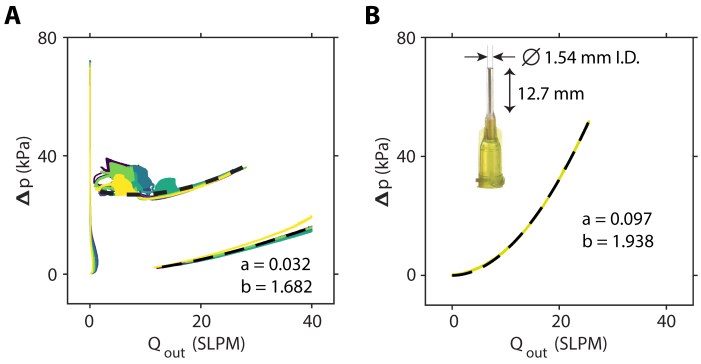

Figure 3.21

PRESSURE DROP OVER THE VALVE, COMPARED TO PRESSURE DROP OVER CONSTANT ORIFICES. (**A**) Measured pressure drop Δp over the valve, as function of flow rate Q_{out} obtained in quasi-static experiments, under pressure control for the fully open state, and under flow control in the regulation mode. Different colors refer to six specimens of the same valve design. a and b are mean fitting parameters for six valves, for the open state behavior. (**B**) Measured pressure drop Δp over a needle (length L = 1.27 mm, internal diameter D = 1.54 mm), as function of flow rate Q_{out}, obtained in a quasi-static experiment under flow control. In A and B, a and b are fitting parameters for the fitting function $\Delta p = a\,(Q_{out})^b$.

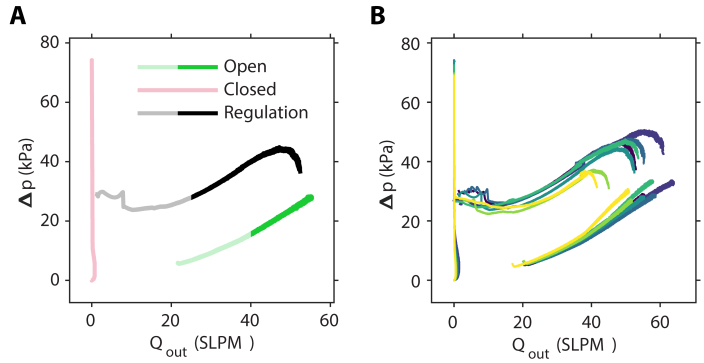

Figure 3.22

EXPERIMENT OF QUASI-STATIC PRESSURE DROP AS FUNCTION OF OUTFLOW RATE $\Delta p(Q_{OUT})$ FOR EXTENDED RANGE OF FLOW RATES COMPARED TO FIGURE 3.3. (**A**) One representative sample. All curves, i.e., the closed (light red curve) and fully open (light and solid green curves) states, as well as pressure regulation mode (light and solid black curves) are obtained in the same quasi-static experimental setup using a pressure regulator connected to the valve holder. Solid black and green data represent the extended flow rate range. (**B**) Seven samples.

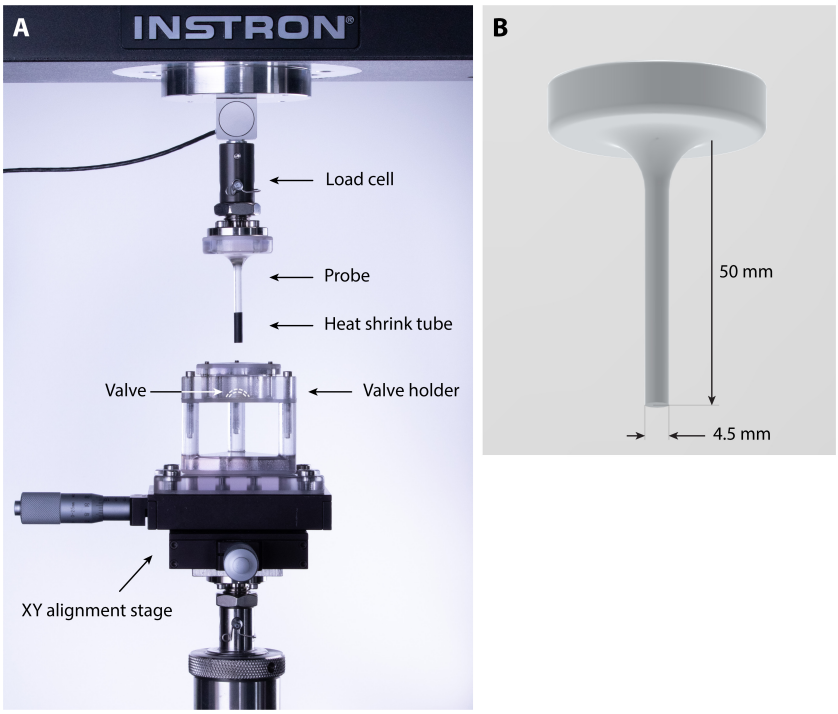

Figure 3.23
EXPERIMENTAL SETUP FOR PROBING VALVE HYSTERESIS. (**A**) Overview of the setup. The valve (not visible) is mounted inside the holder with its convex side up. The holder and probe are 3D-printed (VeroClear, Stratasys). The probe is fitted with a length of shrink tube to increase friction. (**B**) Probe design.

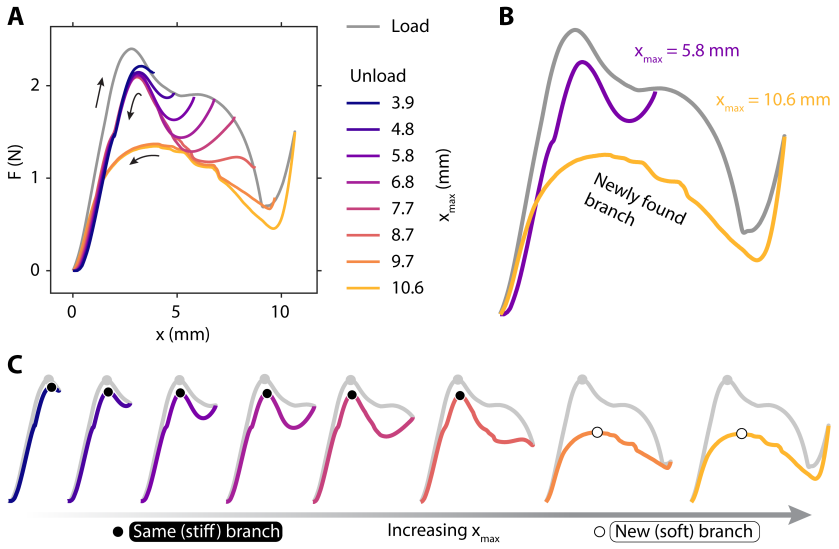

Figure 3.24
DISPLACEMENT-CONTROLLED LOADING EXPERIMENT OF THE VALVE. We vary the maximum displacement x_{max} of the probe. (**A**) Measured reaction force F as a function of probe displacement x for different values of x_{max}. A single representative loading curve (grey) is reported, as for all values of x_{max} the loading curves overlap. Unloading curves are colored by x_{max} according to the legend. (**B**) Loading curve (grey) and two representative unloading curves, one for probing with low displacement (purple), and one for high displacement (yellow). (**C**) Full loading/unloading trajectories for increasing values of x_{max} (from left to right). Circular markers indicate local maxima.

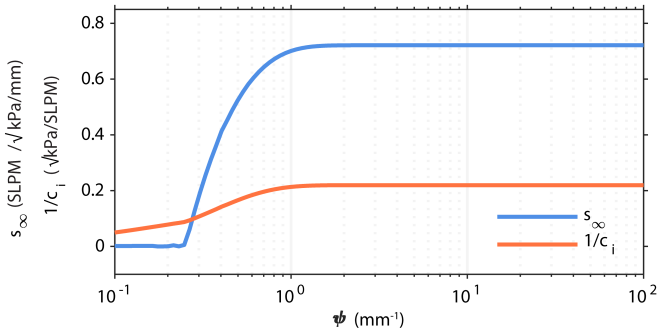

Figure 3.25
FOR DIFFERENT VALUES OF x_{OPEN} AND ψ, WE DETERMINE c_I, AND s_∞ BY FITTING TO MEASURED VALUES $\Delta p(Q_{IN})$. Here, we show the resulting values for the (inverse) valve conduction $1/c_i$ ($\sqrt{\text{kPa}}$/SLPM), and slope s_∞ (SLPM/$\sqrt{\text{kPa}}$/mm) for $x_{open} = 1$ mm.

4

PHYSICAL SYNCHRONIZATION OF SOFT SELF-OSCILLATING LIMBS FOR FAST AND AUTONOMOUS LOCOMOTION

PUBLISHED AS: Comoretto, A., Schomaker, H.A.H., and Overvelde, J.T.B., Physical synchronization of soft self-oscillating limbs for fast and autonomous locomotion, *Science* **388**, 610-615 (2025)

ABSTRACT

Animals achieve robust locomotion by offloading regulation from the brain to physical couplings within the body. In contrast, locomotion in artificial systems often depends on centralized processors. Here, we introduce a rapid and autonomous locomotion strategy with synchronized gaits emerging through physical interactions between self-oscillating limbs and the environment, without control signals. Each limb is a single soft tube that only requires a constant flow of air to perform cyclic stepping motions at frequencies reaching 300 hertz. Physical synchronization of several of these self-oscillating limbs enables locomotion speeds that are orders of magnitude faster than those of comparable state-of-the-art robots. Through body-environment dynamics, these seemingly simple devices exhibit autonomy, including obstacle avoidance, amphibious gait transitions, and phototaxis.

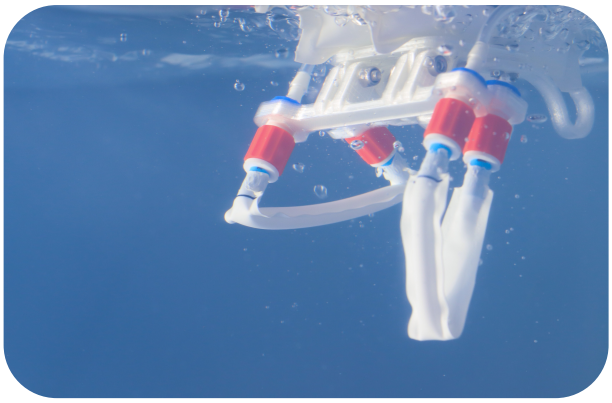

4.1 INTRODUCTION

Nature masters the complex problem of locomotion through embodied solutions, harnessing the synergy between the nervous system, body, and environment [13]. The foundation of animal locomotion lies in the periodic and asymmetric motion of individual limbs [14, 144] (Fig. 4.1A). Multiple oscillating limbs are typically coordinated through a variety of embodied couplings, which are computationally and metabolically inexpensive by diminishing or even eliminating the need for sequential individual inputs from a central brain [14]. These embodied couplings are often implemented through both internal neural connections (i.e., explicitly) and external interactions with the environment (i.e., implicitly). For instance, stick insects achieve synchronized walking gaits through both explicit neural connections and implicit body-environment interactions, avoiding centralized patterning [18]. Sea stars explicitly coordinate their five arms in a decentralized fashion through a nerve ring [145] and occasionally exhibit a fast bouncing gait as an escape response, with their hundreds of tube feet achieving synchronization[1] through implicit mechanical coupling with the external substrate [9] (Fig. 4.1A).

Inspired by nature, robots can delegate the locomotion task to their bodies [72, 146], thus minimizing energy and time costs associated with a central computer. For instance, by harnessing the dynamics of the body, rigid robots based on passive-dynamic walkers [147] and synergy-based quadrupeds [148] reduce, but do not eliminate, the amount of control required for locomotion. Without processors, soft robots based on twisting liquid crystal elastomers [73] and elasto-active structures [60] harness shape reconfiguration to avoid obstacles autonomously. However, due to the lack of limbs, their applicability is limited to specific tasks and environments [149], in contrast to the wide spectrum of robust behaviors typical of animals, which is often enabled by interactions between multiple self-oscillators [70].

Among soft-limbed robots, fluidic circuits [45] sequence the activation of limbs [125] for walking gaits [44, 53, 55, 57] without the need for electronic processors. However, fluidic circuits still emulate their electronic counterpart [51], involving multiple, macroscopic, digital or analog components that deliver sequential control signals. This architecture leads to energy losses and delay across the fluidic network, causing slow sequencing of the limbs in the order of one hertz, with consequent ineffective locomotion of only a few body lengths (BLs) per minute [44, 46, 49, 50,

1 We refer to synchronization as the emergence of a stable oscillatory pattern, which does not necessarily require exact matching of the frequency and phase of the oscillators. In nature, for instance, sea stars do not engage all their tube feet identically when synchronizing. However, globally, a synchronized behavior emerges [145].

53, 55, 57, 58, 150], which is impractical for most real-world applications [112, 151, 152]. Moreover, autonomous behavior of walkers with fluidic processors remains elusive, with the exception of one-time-use touch sensing [57] and reprogrammable sequencing of non-integrated soft fingers [53].

Inspired by the movement principles of animals that do not require centralized processing, we aim to harness physical synchronization of limbs for rapid and autonomous locomotion in soft-limbed robots with embedded fluidic circuits. To do so, in this work we introduce three levels of behavioral hierarchy (Fig. 4.1B) based on *i)* asymmetric self-oscillating motion at the limb level, *ii)* explicit internal fluidic coupling leading to synchronized gaits, and *iii)* implicit coupling between body dynamics and environmental interactions resulting in autonomous behavior. Based on these principles, we develop robotic demonstrations that display rapid locomotion and adaptive behaviors, providing fundamental and general insights into how to instill autonomy in systems without electronic, electronic-like mechanical [78], or fluidic [51] processors.

4.2 A SELF-OSCILLATING LIMB

To enable rapid locomotion without a central processor, here we develop a limb that undergoes periodic and asymmetric motions by harnessing a self-oscillating behavior of thin soft tubes, analogous to oscillations occurring in flat tubes with flowing water [153], and reminiscent of promotional air dancers [154] often seen by the roadside. We build the limb by simply bending a thin-walled commercial silicone tube 180° and constraining it at the inlet and outlet in a 3D-printed holder (Fig. 4.1C and Fig. 4.34). If no airflow is provided, the tube displays two stable states with either one [48] or two kinks (Fig. 4.1C,D). However, when we apply a constant airflow of 15 standard liter per minute (SLPM) to the inlet on the left side of the tube, the tube starts to spontaneously oscillate between states with one and two kinks, at a frequency of approximately 100 Hz (Fig. 4.1E and Movie 4.1) (standard units of airflow in Table 4.4).

The motion of the tube during the oscillation cycle is intrinsically asymmetric due to the applied directed airflow. As a result, the tip of the limb, which we define as the point on the tube closest to a defined surface (Fig. 4.1F and Fig. 4.12), traces a hysteretic trajectory in the x-y plane orthogonal to the surface (Fig. 4.1G and Fig. 4.12). The tube, therefore, acts as a limb that undergoes a full-step motion, with a periodic closed-loop sequence of stance and swing phases (Fig. 4.1G and Movie 4.1), reminiscent of animals' limbs [14] (Fig. 4.1A). For constant input airflow, we delegate both the oscillation generation and the sequencing of the tip motion within each cycle directly to the limb itself,

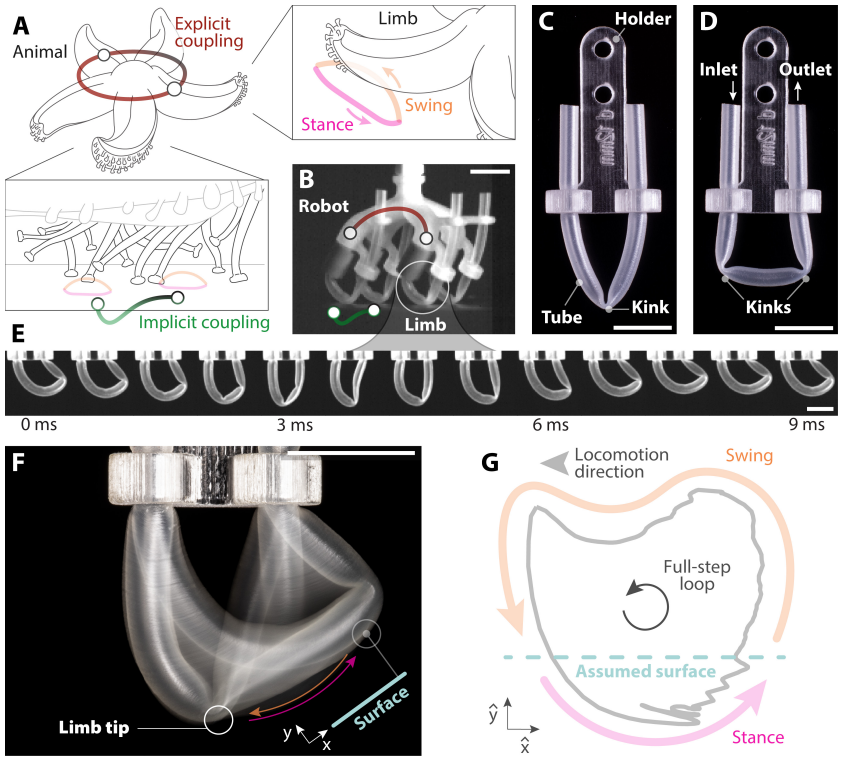

Figure 4.1
SELF-OSCILLATING LIMBS THAT CYCLICALLY PERFORM FULL-STEP MOTIONS. (**A**) Animals locomote by coordinating multiple limbs via explicit coupling through neural connections or implicit coupling through interaction with the environment [9, 18, 145]. Each limb of the animal performs oscillating and asymmetric (full-step) motions with stance and swing phases [14, 144]. (**B**) We exploit these principles of explicit and implicit couplings between self-oscillating limbs for autonomous locomotion in robots. Our artificial limb is a soft tube bent 180° that, in static conditions, displays (**C**) one or (**D**) two kinks. (**E**) When constant airflow of 15 standard liter per minute (SLPM) is provided at the inlet on the left end, the tube self-oscillates at a frequency of 115 Hz (snapshots of one oscillation cycle). (**F**) The tip of the limb is the point on the tube closest to a defined surface (photograph with 0.5 s exposure time, capturing ~ 50 consecutive oscillations). (**G**) The tip cyclically undergoes a full-step loop trajectory, with a stance phase followed by a swing phase (the reported tip trajectory coordinates $\hat{x}$ and $\hat{y}$ are normalized). Scale bars are 1 cm.

bypassing the requirement of additional circuitry [45], either fluidic [55, 57] or electronic [39].

We next aim to empirically understand the switching behavior between one and two kinks in the self-oscillating limb. To do so, we detect the

outer and inner edges of the tube (Fig. 4.2A and Section 4.6.8) and we map them on a new coordinate system along the center line of the tube (Fig. 4.2B, Fig. 4.15, and Fig. 4.38). Focusing on the local minima of the tube width, we indeed identify one or two kinks (Fig. 4.2B and Movie 4.2). We refer to the kink with the smallest width as the dominant kink, and the second kink (if present at that instant) as the non-dominant kink.

From the location of the kinks in time (Fig. 4.2C and Fig. 4.15), and the inlet pressure (Fig. 4.2D), we can identify four key steps during a single oscillation cycle. At ~ 5 ms (Fig. 4.2E), we observe two kinks staying approximately at the same location on the tube until ~ 35 ms (Fig. 4.2F). During this time, the pressure at the inlet decreases, causing the non-dominant kink to increasingly sharpen (Fig. 4.25). Between ~ 35 ms and ~ 40 ms the non-dominant kink becomes dominant, while the other kink disappears at ~ 40 ms (Fig. 4.2G). Until ~ 60 ms, the only kink in the tube starts to travel along the tube (Fig. 4.2H), as a result of an increase in pressure before the kink (Fig. 4.17). Finally, after ~ 60 ms, a new kink forms upstream again due to an increase in bending moment (Fig. 4.25). This state (equivalent to Figure 4.2E) is characterized by a lower fluidic resistance than the single kink state in Figure 4.2G, as both kinks have a larger angle (Fig. 4.25), and thus causes pressure to drop again.

From a basic mass-spring model (Section 4.6.2), we gain insight into three ingredients that lead to the self-oscillating behavior (Fig. 4.8): *i)* a local nonlinear torque-angle curve under bending leads to localized kinking of the tube (Fig. 4.9); *ii)* the local flow resistance increases at the kink location, leading to increased pressure before the kink (Fig. 4.24); *iii)* pressurization of the tube increases the torque required for kinking and unkinking (Fig. 4.9 and Fig. 4.11). Overall, for a constant inflow of air, the internal pressure varies depending on the kinks' resistance. In turn, pressure decrease favors kink growth, and pressure increase causes kinks to travel. This interaction between tube stiffening, kink growth and travel, and change in resistance sets up a hysteric actuation loop (Fig. 4.17) that results in the self-oscillating behavior for constant inflow.

We find that the frequency of the self-oscillation can be tuned by varying the flowrate through the tube. When we sweep the inflow between 0 and 20 SLPM, we observe three domains, with sharp transitions between them (Fig. 4.3A). For inflow values below ~ 3.8 SLPM, the tube leaks and does not oscillate (Fig. 4.16). For flowrates between ~ 3.8 SLPM and ~ 11.4 SLPM, the system oscillates at frequencies between ~ 13 and ~ 45 Hz. For even higher flowrates the frequency suddenly jumps to higher frequencies above ~ 90 Hz.

This last sudden jump in frequency seems to be the result of structural resonance (Movie 4.2). This can be seen from the increase in the distance traveled by the kink (Fig. 4.3B,C and Fig. 4.15) and by the dramatic in-

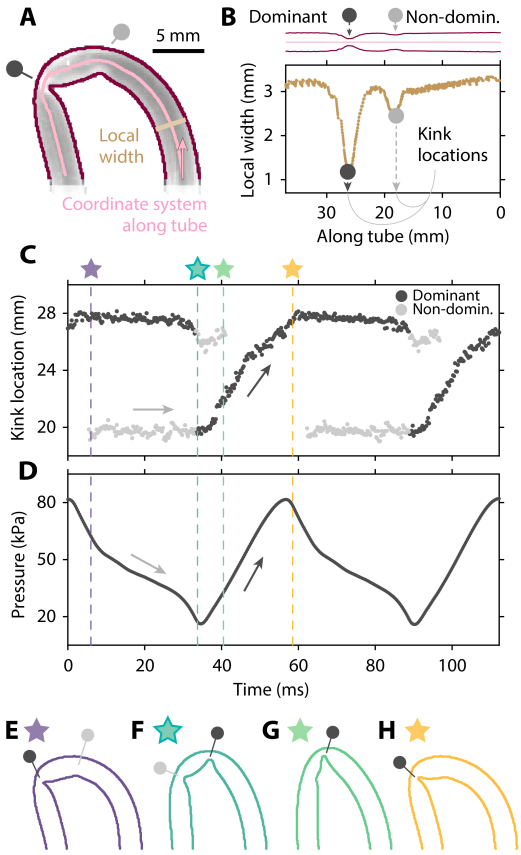

Figure 4.2
INTERPLAY BETWEEN PRESSURE AND KINKS' STATE ENABLES SELF-OSCILLATION. (**A**) Detected edges of the tube (dark red) and coordinate system along the tube (pink). (**B**) The dominant and non-dominant kinks correspond to the local minima (black and grey dots) of the local width along the tube. The (**C**) location of the kinks along the tube and (**D**) pressure inside the tube are coupled. (**E**, **F**, **G**, **H**) State of the tube at four instants of the oscillating cycle.

crease in the kink velocity, that approaches a sinusoidal trend (Fig. 4.3D) (Section 4.6.8 for the definitions of kink distance and velocity). In comparison, the kink location along the tube does not change considerably when the flow is increased (Fig. 4.3E), therefore not constituting the origin of the sudden increase in frequency. Another clue that resonance is the reason for the high oscillation frequency lies in the observation that the instant when the non-dominant kink forms is aligned with the entire structure displacing backward (Movie 4.2). This results in the non-dominant kink relatively quickly becoming dominant. This is apparent

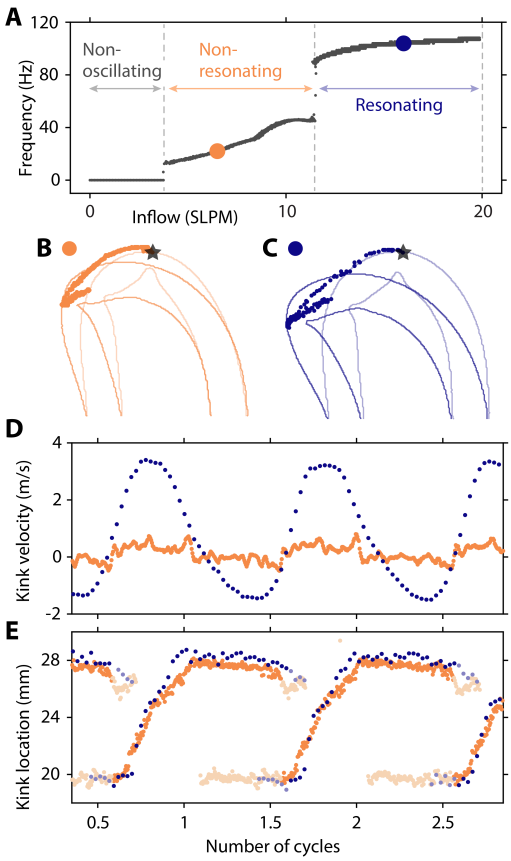

Figure 4.3
STRUCTURAL RESONANCE ENABLES HIGH OSCILLATION FREQUENCIES. (**A**) The oscillation frequency displays three regimes for different inflow rates. Orange and blue dots correspond to the non-resonating and resonating study cases at 6.5 SLPM and 16 SLPM, respectively. The tube has lower structural displacement in the (**B**) non-resonating domain than in the (**C**) resonating domain, as shown by the kink covering a shorter distance. (**D**) In the resonating case, the structure undergoes high quasi-sinusoidal velocities, in comparison to the near-zero velocities of the non-resonating case. (**E**) The kink locations along the tube itself, for the two cases, overlap.

when comparing the duration of the non-dominant kink within an oscillating cycle for the two cases: the non-resonating tube shows a longer delay required for the kink to become dominant (Fig. 4.3E, shaded dots at kink location ~ 20 mm). We conclude that we can significantly increase the oscillation frequency by exploiting the resonance of the structure, as well as by varying design parameters (Fig. 4.14 and Fig. 4.22).

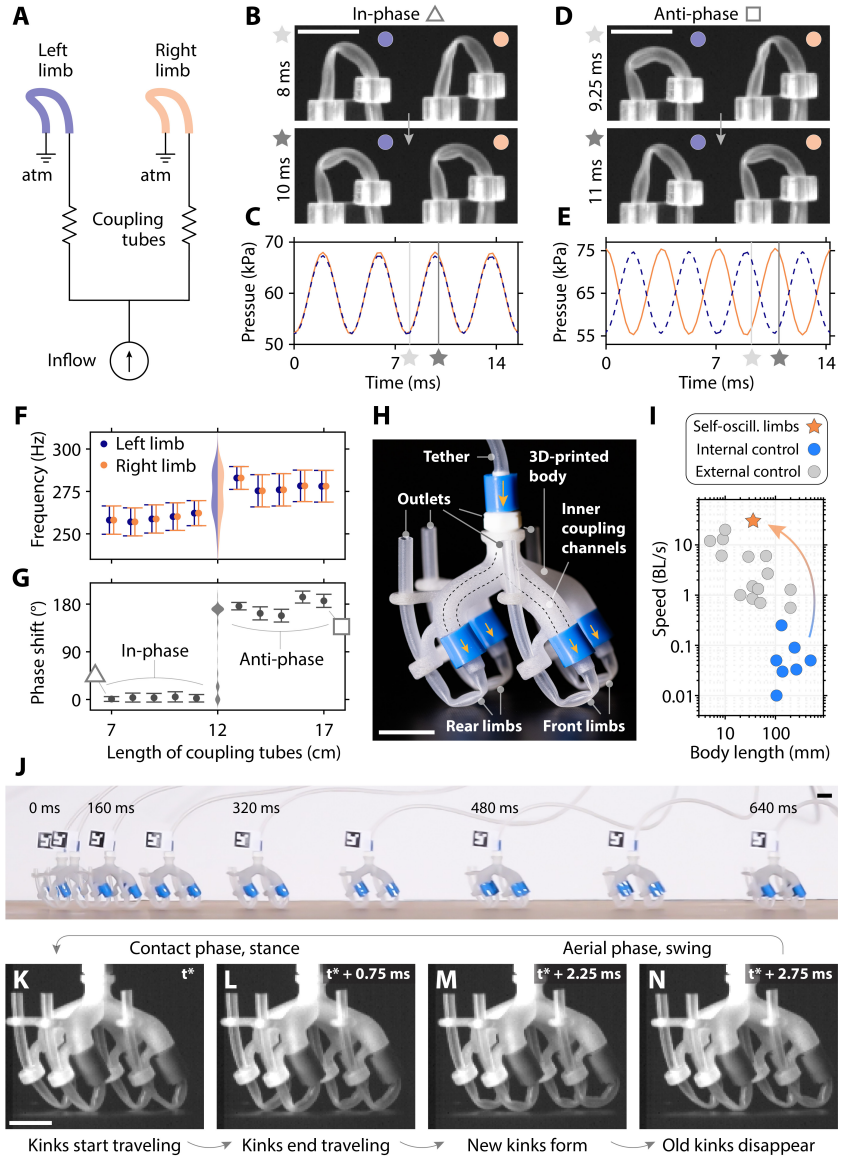
A
Left limb
Right limb
atm
atm
Coupling tubes
Inflow
B
In-phase
8 ms
10 ms
C
Pressure (kPa)
70
60
50
0
7
14
Time (ms)
D
Anti-phase
9.25 ms
11 ms
E
Pressure (kPa)
75
65
55
0
7
14
Time (ms)
F
Frequency (Hz)
300
275
250
Left limb
Right limb
G
Phase shift (°)
180
90
0
In-phase
Anti-phase
7
12
17
Length of coupling tubes (cm)
H
Tether
3D-printed body
Outlets
Inner coupling channels
Rear limbs
Front limbs
I
Self-oscill. limbs
Internal control
External control
Speed (BL/s)
10
1
0.1
0.01
10
100
Body length (mm)
J
0 ms
160 ms
320 ms
480 ms
640 ms
Contact phase, stance
Aerial phase, swing
K
t*
L
t* + 0.75 ms
M
t* + 2.25 ms
N
t* + 2.75 ms
Kinks start traveling
Kinks end traveling
New kinks form
Old kinks disappear

Figure 4.4

Figure 4.4
On the left side.
SYNCHRONIZATION OF MULTIPLE LIMBS THROUGH EXPLICIT, INTERNAL COUPLING FOR ULTRAFAST LOCOMOTION. (**A**) We couple two limbs in parallel to the same input flow source of 15 SLPM with two identical silicone tubes. We observe in-phase synchronization, with (**B**) simultaneous kink traveling and (**C**) aligned pressure signals, or anti-phase synchronization, with (**D**, **E**) alternate activation of the limbs. We scan the length of the coupling tubes, observing two separated in-phase and anti-phase domains, as (**F**) the oscillation frequency of left and right limbs match, and (**G**) the phase-shift is either ~ 0° or ~ 180°. (**H**) The tethered robot has four limbs connected to a 3D-printed monolithic body, with four inner coupling channels. (**I**) Comparison between tethered soft robots with internal and external control and our robot equipped with synchronizing self-oscillating limbs, in terms of relative speed and body length. (**J**) The robot achieves ultrafast locomotion on a flat surface (speed ~ 30 BL/s, 1.1 m/s). The four limbs, within ~ 3 ms, simultaneously go through a (**K**, **L**) stance phase, followed by a (**M**, **N**) swing phase. All scale bars are 1 cm.

4.3 EXPLICIT INTERNAL COUPLING OF MULTIPLE LIMBS

The individual self-oscillating limb requires integration with other limbs in a multi-limbed system to enable locomotion and autonomy in robotic applications. With the goal of synchronizing the activation of several limbs to generate specific gaits, we couple two limbs by connecting them in parallel to a single input, using two identical coupling tubes with an inner diameter of 2 mm (Fig. 4.4A). When providing a constant airflow to the inlet we observe that coupling tubes shorter than 12 cm lead to in-phase synchronization. The result is that the two kinks travel simultaneously (Fig. 4.4B) and the pressure signals align (Fig. 4.4C and Movie 4.3), even though the natural frequencies of the two limbs are not identical and differ by ~ 5 Hz (~ 2%) (Fig. 4.19). In contrast, coupling tubes longer than 12 cm result in anti-phase synchronization where the limbs alternatively activate with a phase shift of ~ 180° (Fig. 4.4D,E and Movie 4.3).

When scanning a wide range of the coupling tubes' length, we note a sharp transition between the in-phase and anti-phase eigenmodes (Fig. 4.4F,G). When placed at this transition, the system continuously switches between the in-phase and anti-phase eigenmodes (violin plot at 12 cm in Figure 4.4G, Figure 4.19, and Movie 4.3).

This synchronization effect is reminiscent of strong coupling between the two oscillators [155]. In soft systems, strong coupling has previously been observed in mechanically-coupled liquid crystalline oscillators [156], while here the coupling is induced by the fluidic interconnections.

Based on these findings, we build a robot with four strongly-coupled self-oscillating limbs, assembled onto a 3D-printed body with short inner channels with length ~ 1.5 cm, connected in parallel to a single tether (Fig. 4.4H, Fig. 4.36, and Fig. 4.37). We orient the limbs with a 30° angle to the surface to optimize the effective stance (Fig. 4.12 and Fig. 4.13). When we provide a constant inflow of ~ 28 SLPM to the tether (Fig. 4.26), the robot accelerates (Movie 4.4), reaching a steady-state speed of 30 ± 2.5 BL/s (1.1 m/s) (Fig. 4.4I,J), with a response time of 0.66 s (Fig. 4.26) and Froude number ~ 20.6 (Section 4.6.5). This speed is two orders of magnitude higher than comparable state-of-the-art tethered robots with internal actuation sequencing [55], and similar to current ultrafast tethered soft robots that need external control [157] (Fig. 4.4I, Fig. 4.32, and Table 4.1).

Looking closely at the gait in Figure 4.4K-N and Movie 4.4, we observe that all the limbs autonomously activate in synchrony, since we used short inner coupling channels. The robot runs with a stotting gait, typical of gazelles [158], reached after some initial transient asynchronous behavior which lasts ~ 0.2 s (Movie 4.4). Note that the four limbs oscillate at a frequency of ~ 300 Hz (Fig. 4.4K-N), about three times higher than the case of the single limb that we analyzed in Figure 4.2, because the tubes are smaller in diameter by a factor ~ 0.8 and shorter in length by a factor ~ 0.5 (Section 4.6.5).

4.4 IMPLICIT ENVIRONMENTAL COUPLING FOR AUTONOMY

Even though our robot achieved ultrafast locomotion without external control, it still required a tether that provides a power of ~ 85 W, leading to a relatively high cost of transport of ~ 1926 (Section 4.6.5). At the moment, it is not possible to generate this power from a lightweight on-board pressure source, making this robot not directly suited for untethered applications. We find that the main limitation comes from the required flow of ~ 3.8 SLPM for the individual limb to not leak through the kink and start oscillating (Fig. 4.3A and Fig. 4.16). We hypothesize that an increase in kink resistance can reduce the leakage and thus the minimum flow needed to achieve self-oscillation, thus reducing the required power.

We modified the design of our tubes by heat-sealing two thermoplastic polyurethane (TPU) sheets along two parallel lines. We mount this TPU component to a hinge joint to obtain a self-oscillating pouch limb (Fig. 4.35). This updated limb has a much higher flow resistance upon kinking (Fig. 4.25) and performs the full-step oscillation (Fig. 4.5A) with a minimum input airflow of only 0.1 SLPM (Fig. 4.20). Compared to the silicone tube limb, we observe a lower oscillation frequency of maximum

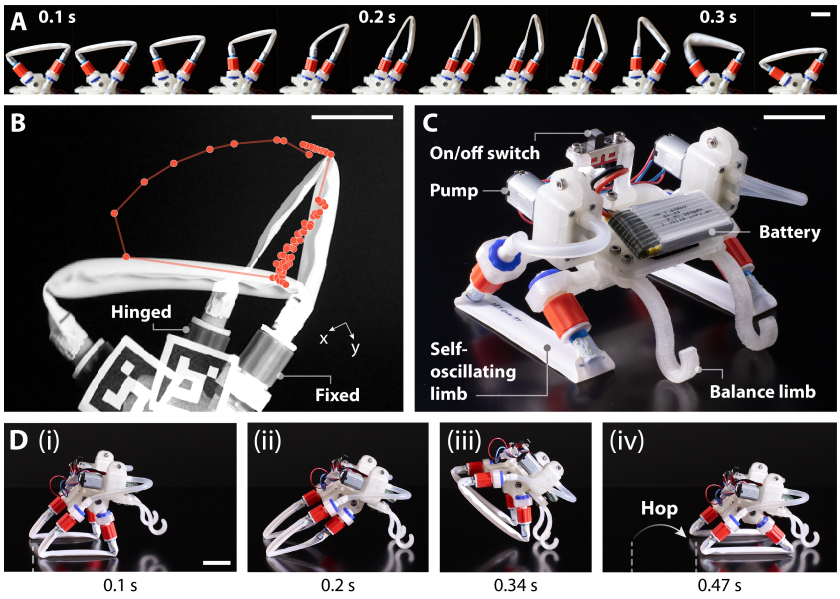

Figure 4.5
A POUCH LIMB FOR UNTETHERED LOCOMOTION. The updated pouch limb (**A**) cyclically performs full-step motions with a low inflow of 0.3 SLPM, (**B**) displaying large hysteresis and stroke enabled by a hinge joint. (**C**) We mount two self-oscillating limbs on an untethered robot that carries a LiPo battery and two pumps. (**D**) The robot cyclically hops with (i, ii) a stance phase followed by (iii, iv) a swing phase. All scale bars are 2 cm.

~ 3.5 Hz (Fig. 4.20 and Fig. 4.22). This is likely due to the higher geometric volume of air required for the kink to travel (~ 2.5 mL compared to ~ 0.04 mL, Section 4.6.3) which leads to a longer kink traveling time, and the absence of a resonant mode. However, this frequency reduction is compensated by a larger stroke per cycle of the pouch limb (Fig. 4.5B, Fig. 4.20 and Movie 4.1).

We build an untethered robot with two pouch tubes as soft limbs, each requiring only ~ 0.06 W of fluidic power (Section 4.6.3 and Fig. 4.21), and each connected to its own 3 V air pump, powered by a 3.7 V LiPo battery with 380 mA h (Fig. 4.5C, Fig. 4.36, and Fig. 4.37). The total weight of the assembled robot equals 76.7 g, which is ~ 6 times lower than the maximum force two pouch-based limbs can provide (Fig. 4.23). When we turn the pumps on, the robot starts to cyclically hop at a rate of ~ 2 Hz (Movie 4.5), with each hopping cycle characterized by a stance phase followed by a swing phase (Fig. 4.5D). The untethered robot moves with a speed of 1.93 ± 0.07 BL/s (18.1 cm/s) (Fig. 4.26), which is one order of magnitude faster than untethered soft fluidic robots [49], and comparable

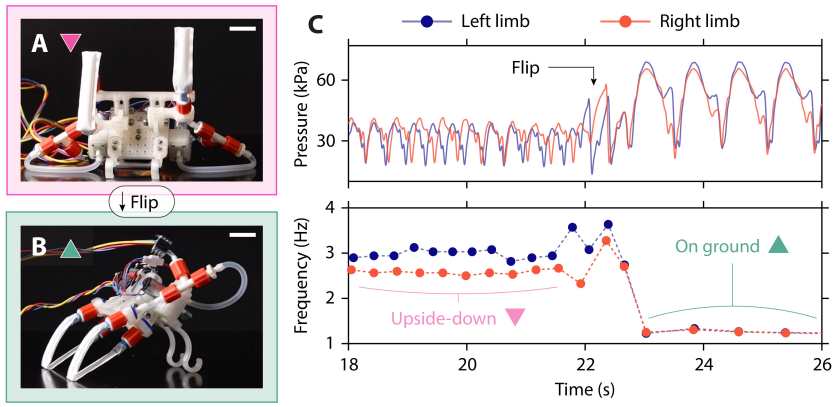

Figure 4.6
SYNCHRONIZATION OF LIMBS THROUGH IMPLICIT INTERACTION FOR FAST, UNTETHERED LOCOMOTION. (**A**) The two limbs are not synchronized when the system is upside down, because they are independently powered by the two pumps. (**B**) When the robot interacts with the ground, the two limbs synchronize. (**C**) While interacting, the pressure signals of the two limbs increase, and the frequencies equalize. Scale bars in A and B are 2 cm.

to state-of-the-art untethered soft robots [159] (Fig. 4.33 and Table 4.2). Under the tested conditions, the robot locomotes with a cost of transport ~ 11, in the same order of land animals of comparable size such as mice [160], and with Froude number ~ 0.16 (Section 4.6.5).

In this untethered scenario, the robot's high speed is attributed to the synchronization of the soft limbs. However, in this case, synchronization emerges due to implicit interactions with the environment, and not through embedded fluidic connections as was the case for the tethered robot, as each limb has its own power source. In principle, we observe that the two limbs actuate at different natural frequencies and thus out of phase when placed upside down (Fig. 4.6A and Movie 4.5). When we flip the robot into the working position where the two limbs interact with the ground, either on a flat surface (Fig. 4.6B) or on gravel (Fig. 4.27 and Fig. 4.29), the limbs start to actuate simultaneously and in-phase, while requiring higher pressures (Fig. 4.6C and Movie 4.5). This in-phase synchronization results from the positive coupling between the limbs, where the activation of one limb stimulates the activation of the other limb. Additional mass stabilizes the in-phase synchronized mode and improves the tolerance to imbalance in left and right input flows (Section 4.6.5 and Fig. 4.31).

Harnessing such implicit interactions to achieve synchronization also enables autonomous behaviors, as external cues can affect the coupling

between the body dynamics and the environment. For instance, through implicit coupling with its surroundings, the robot autonomously transitions to a new locomotion gait when interacting with an aquatic environment (Fig. 4.7A and Movie 4.6), without requiring any control input [70] or morphological change [160]. After diving into the water, the in-phase hopping gait within seconds transitions to an anti-phase gait (Fig. 4.7B), which is stable in steady-state conditions, with a phase shift of $181 \pm 8°$ (Section 4.6.5). The anti-phase gait seems to be stabilized by a sideways swaying of the robot, leading to negative coupling in which the activation of a limb suppresses the activation of the other limb (Movie 4.6). To confirm this, we check that manually constraining the swaying motion causes the limbs to not synchronize anymore (Movie 4.6). Therefore, the coupling between the body dynamics and the surrounding medium determines the stability of a specific gait for the robot and, thus, its behavior.

When encountering an obstacle, too, the mechanical interactions between the body and an obstacle cause temporary asynchronous activation of the legs, resulting in the robot steering in place and avoiding the obstacle (Fig. 4.7C and Movie 4.6). By harnessing these environmental cues, the robot changes behavior and autonomously escapes a U-shaped obstruction after noisy and consecutive random changes of direction (Fig. 4.30 and Movie 4.6).

As the amphibious locomotion is unidirectional and the body-obstacle interactions result in random outcomes (Movie 4.6), we propose that additional sensing is still needed to provide the robot with a high-level sense of direction. We take inspiration from Braitenberg's 'aggressive vehicle 2b' [1], and design internal connections by equipping the robot with two 'eyes' (LDR light sensors) that activate the opposite soft limbs when sensing light (Fig. 4.7D and Fig. 4.37). This relatively simple robot achieves autonomous phototaxis, as it steers in place when only one eye detects light and implicitly coordinates the limbs to hop forward when both eyes do (Fig. 4.26 and Movie 4.7). Outside of the lab, this allows the robot to move from a dark room to a brighter one (Movie 4.7) and to continuously follow an operator who carries a light (Fig. 4.7E).

4.5 DISCUSSION

In conclusion, we leverage kinks traveling along a soft tube to create a self-oscillating limb that cyclically performs a full-step motion at high frequencies. Inspired by nature, we blur the boundaries between actuation, control, and body-environment feedback by physically synchronizing multiple limbs via explicit and implicit couplings, realizing rapidly moving, autonomous robots.

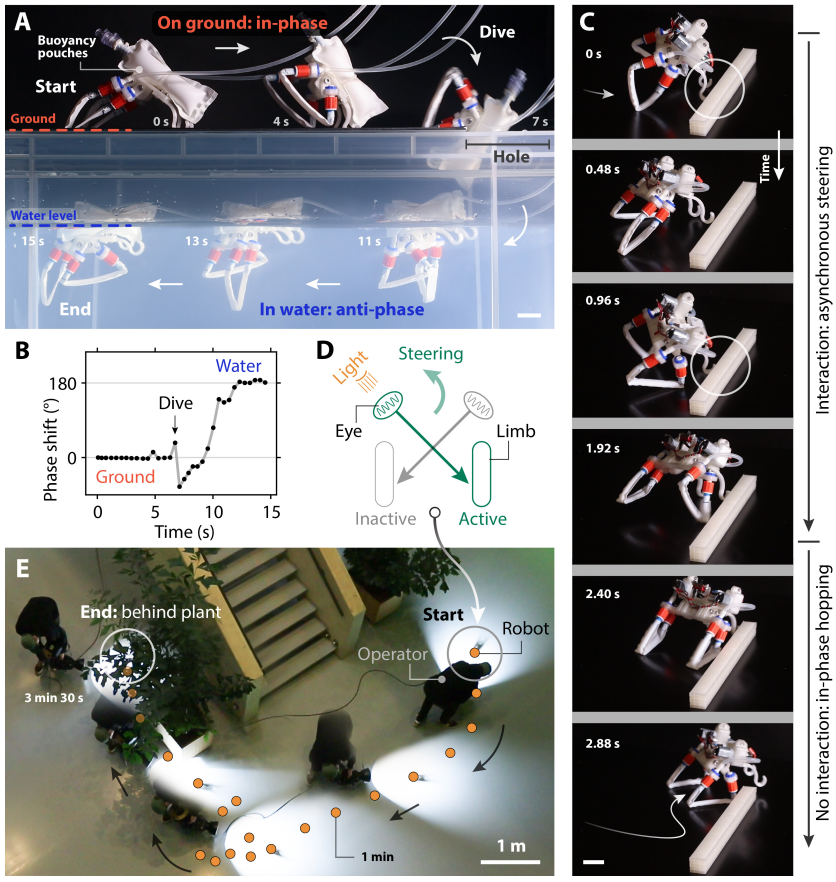

Figure 4.7

AUTONOMY THROUGH PHYSICAL INTERACTIONS WITH THE ENVIRONMENT. (**A**) After diving into the water, the robot equipped with buoyancy pouches (50 mL of air) autonomously transitions to an anti-phase swimming gait, through the implicit coupling with the new aquatic environment. (**B**) The phase shift between the two self-oscillating limbs is ~ 0° (in-phase) when hopping on the ground and spontaneously transitions to ~ 180° (anti-phase) when interacting with water. (**C**) When encountering an obstacle, the mechanical interactions (white circles) cause the limbs to activate asynchronously and, as a consequence, the robot steers in place, avoiding the obstacle. (**D**) To provide the robot with a high-level sense of direction, and inspired by Braitenberg's 'aggressive vehicle' [1], we cross-link light sensors (eyes) and the pumps so that a limb is active when the opposite eye detects light. (**E**) This robot achieves autonomous phototaxis by steering in place when only one eye is active and hopping forward when both eyes are, following an operator that carries a light in a real-world environment. Scale bars in A and C are 2 cm.

The observations from the various robotic demonstrations we performed point toward the potential of a holistic and overarching approach when designing robots, to achieve robust and adaptive behavior across diverse environments. This approach does place emphasis on the physical design of the highly interacting robot, and therefore, it will likely require the development and improvement of available design tools for these types of integrated systems [161] to discover or design useful and robust emergent dynamic behaviors.

In addition, we envision opportunities in utilizing the coupled systems as physical models [162, 163] for exploring how morphology and body-environment interactions result in autonomous behaviors across scales, from non-neuromuscular multi-cellular organisms [164] through microrobots with no microelectronics [110] to meter-scale devices [165] and animals [68].

Such a holistic approach opens up a playground of opportunities for versatile, autonomous behaviors without the need for a central controller, of which here we have only scratched the surface.

4.6 SUPPLEMENTARY INFORMATION

Links and descriptions of the movies are reported in Section 4.6.1. The mass-spring model is reported in Section 4.6.2. Additional experiments on the self-oscillating limbs are reported in Section 4.6.3. In Section 4.6.4, we study the kink formation in thin tubes undergoing bending. Additional experiments on the locomoting robots are reported in Section 4.6.5. We describe the manufacturing procedure of limbs and robots in Section 4.6.6. The details of the experimental setups are reported in Section 4.6.7. In Section 4.6.8, we describe our pipeline for the numerical analysis of the high-speed recordings data. For brevity, we refer to the self-oscillating limb as the 'actuator'. All data, code, and manufacturing tools are available at our Zenodo repository [166].

4.6.1 *Movies*

All the movies related to this chapter are available at this link. If you are holding a paper version, you can scan this QR code:

MOVIE 4.1

THE SELF-OSCILLATING LIMB. The self-oscillating limb is a soft tube bent 180° and constrained in a rigid holder. *i)* The limb performs a full-step motion while self-oscillating at a high frequency of ~ 100 Hz, when constant input airflow of 15 SLPM is provided. High-speed recordings highlight the asymmetric cyclic motion of the limb, in slow motion (200x slower, repeated movies of two consecutive oscillations). The trajectory of the limb's tip on the actuating plane shows that the x- and y-coordinates are intrinsically sequenced, tracing the full-step loop in the plane. *ii)* The TPU pouch version behaves similarly to the silicone tube limb, while exhibiting higher stroke and hysteresis in the actuation, at lower frequencies. *iii)* The self-oscillating limb is versatile, operating with both compressible (air) and incompressible (water) driving fluids. We supply water flows of 333 mL/min to the silicone tube limb and 56 mL/min to the TPU pouch limb, respectively.

MOVIE 4.2

THE RESONATING BEHAVIOR. High-speed recordings highlight that the resonating behavior of the limb enables high frequencies of oscillation. *i)* We detect the edges of the tube for each frame of the recording. The kinks are the points along the tube corresponding to the minima of the tube width (distance between edges). The behavior of the tube width in time (40x slower, repeated movies of two consecutive oscillations) shows that the kinks arise, travel, and disappear along the tube. *ii)* The distance covered by the kinks on the plane and their velocity show that high frequencies of oscillation are triggered by resonance. The distance covered by the kink in the resonating case overshoots by ~ 50% the one of the non-resonating case. The kink velocity in the resonating case is quasi-sinusoidal and reaches ~ 3.5 m/s, while in the non-resonating case is not quasi-sinusoidal and stays close to zero.

MOVIE 4.3

SYNCHRONIZING VIA FLUIDIC COUPLING. We realize strong coupling between two self-oscillating limbs through parallel connection to the same flow source of 15 SLPM using Y-connected tubes. We vary the length of these coupling tubes, and we display the measured pressure and the high-speed recordings (200x slower). For short coupling tubes of 7 cm, we observe in-phase synchronization (same frequency, phase ~ 0°). For longer coupling tubes (17 cm), we observe anti-phase synchronization (same frequency, phase ~ 180°). There is a critical length for which the behavior transitions from in-phase to anti-phase. When the system is placed

at this transition (12 cm), the self-oscillating limbs continuously alternate between the two eigenmodes.

MOVIE 4.4

THE TETHERED ROBOT. The tethered robot runs at more than one meter per second with a stotting gait. As a reference for scale, the body length of the robot is 36 mm. *i)* The robot design consists of a monolithic rigid body and four tubes as self-oscillating limbs. The robot moves at 30 ± 2.5 body lengths per second (1.1 ± 0.09 m/s) among six runs. *ii)* High-speed recordings of the robot (400x and 800x slower) show that the four limbs perform full steps with in-phase synchronization, being fluidically coupled through the inner channels. The robot is locomoting with a stotting gait. When the robot is not in contact with the ground, the four limbs are still synchronized, confirming that the coupling arises from the fluidic internal connections and not from the interaction with the ground. *iii)* When the four limbs are not synchronized, the robot stumbles, and ultrafast speeds are not reached anymore (10x slower).

MOVIE 4.5

THE UNTETHERED ROBOT. The untethered robot exploits environmental interactions to achieve in-phase synchronization of two limbs, moving at 1.9 body lengths per second. All the recordings are in real time. *i)* The untethered robot is equipped with two self-oscillating limbs, two mini air pumps, a LiPo battery, and two rigid balance limbs. When the pumps are turned on, the robot displays a hopping gait. *ii)* Occasionally, we observe a transient phase with no synchronization of the limbs during the startup of the pumps. *iii)* When upside-down, the limbs do not synchronize, as they are independently powered by two distinct fluidic lines (one pump for each limb). *iv)* When we flip the robot into locomotion position, the limbs synchronize thanks to the interaction with the environment, as shown by the pressure signals of the two limbs aligning.

MOVIE 4.6

AUTONOMY THROUGH PHYSICAL INTERACTIONS WITH THE ENVIRONMENT. The untethered robot exploits body-environment interactions to transition between locomotion gaits depending on the medium, and to navigate obstacles autonomously. *i)* Before diving into the water, the robot hops on the ground with an in-phase gait. After diving, the robot autonomously transitions to an anti-phase swimming gait. This change in behavior occurs spontaneously via the implicit coupling with the new medium, without any control input or change in morphology. The phase shift of the swimming gait, obtained from the measured pressure

signals, is stable around ~ 180°. *ii)* We prevent lateral swaying by manually blocking the body of the robot. In these conditions, the implicit coupling between the buoyant body and water is inhibited, and the limbs do not synchronize anymore, as seen by the phase shift assuming all values between 0° and 360°. *iii)* When hopping on the ground, the limbs temporarily get out of synchronization when the robot is externally perturbed, and then return to the stable synchronized mode. *iv)* When encountering an obstacle, too, the robot exits the synchronized mode and steers in place, randomly either to the left or right. This behavior is stochastic, as it relies on noisy, friction-dominated interactions. *v)* The robot harnesses the noisy body-obstacle interactions to escape a U-shaped obstruction autonomously, through consecutive random changes of direction (8x and 16x faster). *vi)* When the robot navigates among multiple (seven) obstacles, the outcome is unpredictable due to the stochasticity of the interactions. We overlay eight different runs recorded from above (6x faster).

MOVIE 4.7

AUTONOMOUS PHOTOTAXIS THROUGH INTERNAL CONNECTIONS. The untethered robot exhibits autonomous phototaxis through internal connections directly between sensors and limbs. *i)* We design a high-level sense of direction through internal connections between the limbs and two photoresistors. The photoresistors are placed facing the front-left and front-right directions. The front-left photoresistor is connected to the right limb, and vice-versa for the front-right sensor, inspired by Braitenberg's 'aggressive vehicle' [1]. In this way, when the light is coming, for example, from the front-left direction, the right limb will be active, and the robot will steer to the left. The robot autonomously moves toward the light (real time and 8x faster). *ii)* We place the robot in a dark room. When we open the door of another room, the robot prefers the brighter one (real time). *iii)* The robot autonomously follows an operator that carries a light in a real-world environment, the coffee corner at AMOLF (16x faster).

4.6.2 *Mass-spring model of the self-oscillating behavior*

To gain fundamental insight into the self-oscillating behavior, we developed a basic mass-spring model. In summary, from the model, we learn three fundamental reasons behind the self-oscillating behavior: *i)* the localized kinking of the tube is associated with a local nonlinear

torque-angle curve under bending; *ii)* the local flow resistance increases when kinks are formed, leading to increased pressure before the kink; *iii)* the internal pressurization increases the torque required for kinking and unkinking. We will now proceed to elaborate in detail on the development of the model and on the results of the simulations.

Model description

We represent the tube (mechanically) as a series of point masses connected by linear and torsional springs, simulating both stretching and bending resistance (Fig. 4.8A). The tube is discretized into N point masses, each of mass m, connected by linear springs of rest length L_0 and spring constant k_s, and torsional springs with stiffness k_b. The positions of the nodes are denoted by:

$$\mathbf{r}_i = (x_i, y_i), \tag{4.1}$$

for $i = 1, 2, \ldots, N$. We implement the model using a non-dimensionalized framework to view the relative differences of the parameters in the equations and describe the qualitative behavior.

The dynamics of each node i are governed by Newton's second law:

$$m\frac{d^2\mathbf{r}_i}{dt^2} = \mathbf{F}_{\text{linear},i} + \mathbf{F}_{\text{torsional},i} - c\frac{d\mathbf{r}_i}{dt}, \tag{4.2}$$

where c is the damping coefficient[2], $\mathbf{F}_{\text{linear},i}$ is the net force due to linear springs, and $\mathbf{F}_{\text{torsional},i}$ is the net force due to torsional springs acting on node i.

The linear spring forces[3] are calculated based on Hooke's law for adjacent nodes:

$$\mathbf{F}_{\text{linear},i} = -k_s\left[(\ell_{i,i-1} - L_0)\frac{\mathbf{r}_i - \mathbf{r}_{i-1}}{\ell_{i,i-1}} + (\ell_{i,i+1} - L_0)\frac{\mathbf{r}_i - \mathbf{r}_{i+1}}{\ell_{i,i+1}}\right], \tag{4.3}$$

where $\ell_{i,j} = \|\mathbf{r}_i - \mathbf{r}_j\|$ is the distance between nodes i and j.

The torsional spring forces arise from the resistance to bending between consecutive segments:

$$\mathbf{F}_{\text{torsional},i} = -k_b \cdot (\theta_i - \theta_0), \tag{4.4}$$

2 Note that we implement numerical damping (and not mechanical damping), as the damping coefficient c multiplies the derivative of the nodes' coordinates (and not the nodes' physical velocity).

3 Experimentally, we observe that the tubes in our operating conditions tend to bend more than contract or extend, so the contribution of the linear springs could be neglected. For completeness, we build the model considering both contributions, and we will assign a larger stiffness to the linear spring than to the torsional springs.

where θ_i is the angle at node i between segments $\mathbf{r}_i - \mathbf{r}_{i-1}$ and $\mathbf{r}_{i+1} - \mathbf{r}_i$, and θ_0 is the rest angle. In our case, the rest configuration is when the tube is straight, so $\theta_0 = \pi$. The angle θ_i is computed using:

$$\theta_i = \arctan 2\,(C_i, D_i)\,, \tag{4.5}$$

where C_i and D_i are, respectively, the cross product and the dot product of vectors $\mathbf{r}_i - \mathbf{r}_{i-1}$ and $\mathbf{r}_{i+1} - \mathbf{r}_i$:

$$\begin{aligned} C_i &= (x_i - x_{i-1}) \cdot (y_{i+1} - y_i) - (y_i - y_{i-1}) \cdot (x_{i+1} - x_i) \\ D_i &= (x_i - x_{i-1}) \cdot (x_{i+1} - x_i) + (y_i - y_{i-1}) \cdot (y_{i+1} - y_i)\,, \end{aligned} \tag{4.6}$$

where we used the notation for $\mathbf{r}_{i-1}$, $\mathbf{r}_i$, and $\mathbf{r}_{i+1}$ in Eq. (4.1).

Non-dimensionalization

To reduce the complexity of the equations, we non-dimensionalize the system using characteristic scales:

- length scale: the rest length of the linear springs, L_0;
- time scale: $t_0 = \sqrt{\frac{m}{k_s}}$;
- mass scale: the mass of each node, m.

We further define the non-dimensional variables as:

- non-dimensional position, with $\mathbf{r}$ being the dimensional position:

$$\mathbf{r}' = \frac{\mathbf{r}}{L_0}, \tag{4.7}$$

- non-dimensional time, with t being the dimensional time:

$$t' = \frac{t}{t_0}, \tag{4.8}$$

- non-dimensional velocity:

$$\mathbf{v}' = \frac{d\mathbf{r}'}{dt'} = \frac{t_0}{L_0}\frac{d\mathbf{r}}{dt}. \tag{4.9}$$

The non-dimensional parameters are:

$$\eta = \frac{k_b}{k_s L_0^2}, \quad \zeta = c\frac{t_0}{m}, \tag{4.10}$$

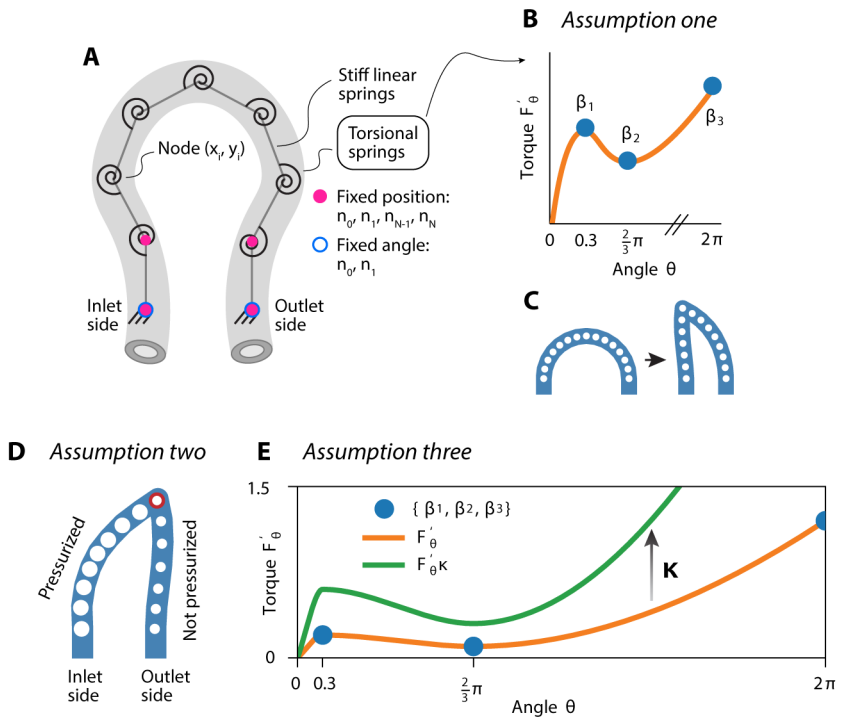

Figure 4.8

MASS-SPRING MODEL TO SIMULATE THE SELF-OSCILLATING BEHAVIOR OF A TUBE. (**A**) Mechanical mass-spring model representation of the tube, with point masses at nodes connected by linear and torsional springs that simulate stretching and bending. (**B**) Assumption one: nonlinear torque-angle curve $\beta(\theta)$ of the torsional springs. We also report the reference points used for interpolation (β_1, β_2, and β_3). (**C**) As a consequence of assumption one, when inlet and outlet are moved closer together, a kink forms in the tube, because that specific torsional spring snaps to the other stable branch between β_2 and β_3. (**D**) Assumption two: the section of the tube before the dominant, sharpest kink (red dot), on the inlet side, is pressurized because the kink locally increases fluidic resistance under flow-controlled conditions (Fig. 4.24 and Fig. 4.25) (larger white dots correspond to higher pressure). (**E**) Assumption three: the torsional springs on the pressurized section of the tube are stiffer by a factor κ. In this specific case, we assigned $\kappa = 2$.

resulting in the equations of motion in non-dimensional form:

$$\frac{d^2\mathbf{r}'_i}{dt'^2} = \mathbf{F}'_{\text{linear},i} + \mathbf{F}'_{\text{torsional},i} - \zeta\frac{d\mathbf{r}'_i}{dt'}, \tag{4.11}$$

where the non-dimensional forces are calculated similarly to their dimensional counterparts but using non-dimensional variables. The non-dimensional linear spring forces are:

$$\mathbf{F}'_{\text{linear},i} = -\left[(\ell'_{i,i-1} - 1)\frac{\mathbf{r}'_i - \mathbf{r}'_{i-1}}{\ell'_{i,i-1}} + (\ell'_{i,i+1} - 1)\frac{\mathbf{r}'_i - \mathbf{r}'_{i+1}}{\ell'_{i,i+1}}\right], \tag{4.12}$$

where $\ell'_{i,j} = \|\mathbf{r}'_i - \mathbf{r}'_j\|$. The non-dimensional torsional spring forces are:

$$\mathbf{F}'_{\text{torsional},i} = -\eta \cdot (\theta'_i - \pi), \tag{4.13}$$

with θ'_i computed using the non-dimensional positions.

Assumption one: nonlinear bending stiffness

Since we model the system with a set of torsional springs and near-rigid bars (linear springs with high stiffness compared to the torsional springs), we experimentally characterize the behavior of the tube under controlled bending. This will inform us about the torque-angle curve of the kinking tube. We will transfer this information to the torque-angle curve of the non-dimensional torsional springs in the model.

We use a microtorsion testing machine (Instron MT1-E1) to increase the bending angle quasi-statically, at a rate of 130 °/min. At the same time, we measure the torque exerted on the tube (load cell W-5510-T4 with torque capacity 0.225 N m), and we regulate pressure inside the tube with a Festo^{TM} pressure regulator (details on the setups in Section 4.6.7). In Figure 4.9A, we report the measured torque-angle curve of the silicone tube (with inner diameter 2.5 mm, thickness 0.4 mm) for a pressure of 20 kPa. In Figure 4.9B, we also report snapshots of the experiment at four angle values. We observe that the torque-angle curve is non-monotonic, displaying the negative-stiffness regime typical of snapping structures (parallel to the negative stiffness of the pressure-volume curves of nonlinear inflatable elements [167], but in the torque-angle regime). While kinking, the tube goes through an unstable regime when bending stiffness is negative, displaying a peak and a valley (Fig. 4.9A, red and blue dots).

To qualitatively capture the experimentally observed non-monotonic mechanical behavior of the tube during the kinking process, we redefine the torque-angle curve for each node $\mathbf{F}'_{\text{torsional}}$ as a nonlinear function of the torque with respect to the bending angle θ:

$$\mathbf{F}'_{\text{torsional}} = \beta(\theta). \tag{4.14}$$

We introduce a negative stiffness regime in $\beta(\theta)$ by using interpolation techniques that allow us to specify the peaks and minima of the torque

angle curve. This approach enables us to simulate the nonlinear behavior of the tube when the kink forms, which is assumption one (Fig. 4.8B). We define a set of control points representing the desired torsional force values at specific angles. These points are determined by a vector of stiffness parameters $k_b = [\beta_0, \beta_1, \beta_2]$, corresponding to the torque at key angular positions. The torsional force function $\beta(\theta)$ is constructed using a Piecewise Cubic Hermite Interpolating Polynomial (PCHIP). The control points are given by:

$$\begin{aligned} \theta_{data} &= [0, 0.3, \tfrac{2\pi}{3}, 2\pi], \\ k_{b,data} &= [0, \beta_0, \beta_1, \beta_2]. \end{aligned} \tag{4.15}$$

Using these points, the bending stiffness function becomes:

$$\beta(\theta) = \mathrm{PCHIP}(\theta_{data}, k_{b,data})(\theta), \tag{4.16}$$

where PCHIP denotes the interpolation operator.

The negative stiffness regime in the $\beta(\theta)$ curve introduces an unstable equilibrium at a bending angle of 0.3 (Fig. 4.8B). When the tube's ends are brought closer together, the bending angles at the nodes increase, and the system seeks to minimize its elastic potential energy. The negative stiffness regime results in a sudden increase in the bending angle of an element (a kink) as the system moves toward the local energy minima. This phenomenon effectively models the kinking behavior observed when bending flexible tubes [48]. To introduce the kink in our simulated system in the most natural way, we initialize the system in half a circle with a curvature where the stable equilibrium of the system does not have a kink; we then drive the outer ends of the system closer together to a point where the system kinks (Fig. 4.8C). After we bring the endpoints closer together, we fix their positions for the rest of the simulation. Mathematically, we defined a movement function for the first two nodes:

$$x_i'(t') = \begin{cases} v'_{move} \cdot t', & \text{if } t' \leq 400, \\ v'_{move} \cdot 400, & \text{if } t' > 400, \end{cases} \tag{4.17}$$

where $v'_{move} = \dfrac{4}{400}$ is the non-dimensional movement rate.

Assumption two: the local flow resistance increases at the kink location

In the case of the self-oscillating tube, we assume that the point of highest curvature acts as a dominant fluidic resistance in the tube (Fig. 4.2, Fig. 4.24, and Fig. 4.25). This higher fluidic resistance will cause a pressure difference before and after the kink (point of highest curvature). As

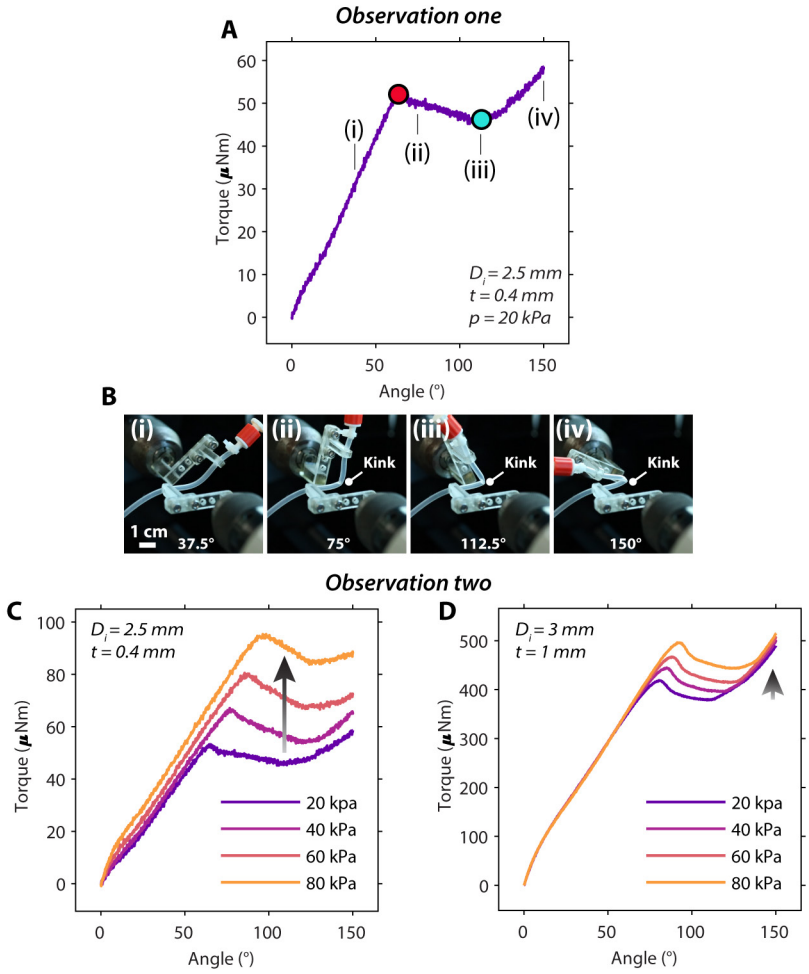

Figure 4.9

TWO EXPERIMENTAL OBSERVATIONS THAT INFORM THE MASS-SPRING MODEL TO SIMULATE THE SELF-OSCILLATING TUBE. Using a microtorsion testing machine, we increase the bending angle of a silicone tube of length 36 mm, and we measure the torque while regulating pressure inside the tube. (**A**) Observation one: we observe a non-monotonic torque-angle response, with a negative stiffness branch between a peak (red dot) and a valley (blue dot): the formation of the kink is a mechanical instability. (**B**) Snapshots of the tube at angle (i) 37.5°, (ii) 75°, (iii) 112.5°, (iv) 150°. (**C**) Observation two: when increasing the pressure inside the tube, higher torques are required to kink and unkink the tube. (**D**) A thicker silicone tube with inner diameter 3 mm and thickness 1 mm still displays the non-monotonic response, but the relative change in behavior upon pressurization is lower than in the case of the thinner tube in C.

a result, the nodes on the side of the air inflow (left) up to and including the kink (point of highest curvature) will be under more pressure than the nodes on the other (right) side of the kink (Fig. 4.8D). In our model, we do not directly model the flow. Instead, we assume that the kink leads to infinite fluidic resistance.

Assumption three: pressurization of the tube increases the torque required for kinking and unkinking

Experimentally, we observe that the torque required to form a kink increases as the pressure in the tube increases (Fig. 4.9C,D). Mathematically, we represent this effect by introducing a stiffness multiplier, denoted as κ, which multiplies the baseline torque-angle curve (Fig. 4.8E). The torque-angle curves for nodes that are in a "pressurized" state (i.e., that are on the left to the kink, including the kink) are modified as follows:

$$\beta'(\theta) = \kappa \cdot \beta(\theta), \tag{4.18}$$

where:

- $\beta'(\theta)$ is the torque-angle curve for nodes under higher pressure.
- κ is the stiffness multiplier ($\kappa \geq 1$) representing the effect of pressure-induced stiffening.
- $\beta(\theta)$ is the baseline torque-angle curve, as previously defined in Eq. (4.16).

Implementation of the three assumptions in the model

To incorporate these two assumptions into our numerical simulation, we perform the following steps.

1. Forming the kink: at the start of the experiment, we drive the fixed nodes closer together to form the kink (Fig. 4.8C). From $t' = 400$ onwards, we fix their positions for the rest of the simulation.
2. Kink detection: at each time step starting from $t' = 600$, we identify the node with the maximum deviation from the rest angle $\theta_0 = \pi$. This node corresponds to the location of the kink (red dot in Figure 4.8D).
3. Pressure-induced stiffening: once the kink is identified, we increase the bending stiffness of all nodes to the left of the kink (including the kink node) (Fig. 4.8D) by multiplying their torque-angle curve by κ (Fig. 4.8E).

4. Time-dependent stiffening: to approximately model the gradual effect of pressure buildup, we use a sigmoid function to smoothly transition the stiffness increase over time:

$$\kappa(t') = 1 + \delta\kappa \cdot S\left(t' - t'_{kink}\right), \tag{4.19}$$

where:

- $\delta\kappa = \kappa_{assigned} - 1$ is the maximum scalar with which the force is multiplied. So, effectively, κ transitions smoothly from 1 to the assigned value $\kappa_{assigned}$. Note that in the remainder of the text, for simplicity, when we refer to the assigned stiffness multiplier, we use κ.
- t'_{kink} is the non-dimensional time when the kink is formed.
- $S(t')$ is the generalized sigmoid function:

$$S(t') = \frac{1}{1 + e^{-k(t'-x_0)}}, \tag{4.20}$$

with parameters k controlling the slope and x_0 the midpoint of the transition.

5. Updating torsional forces: the torsional spring forces for nodes i on the left of the kink $i <= i_{kink}$ are recalculated using the increased torque:

$$\mathbf{F}'_{torsional,i} = -\kappa(t') \cdot \beta(\theta_i - \pi), \quad \text{for } i <= i_{kink}. \tag{4.21}$$

6. Time-dependent softening: for the torsional spring force acting on the nodes on the right side of the kink, we use the inverse of Eq. (4.20) to smoothly transition back to the initial $\beta(\theta)$ curve. t'_{kink} is updated to the t' where $i > i_{kink}$.

Results of the model

When we drive the inlet and the outlet closer together, a kink forms (Fig. 4.10A). At non-dimensional time $t' = 600$ (start), we enforce assumptions two and three, i.e., the stiffening of the springs on the left of the kink (Fig. 4.10B). We observe the kink propagating along the simulated tube (Fig. 4.10C). Since assumption one also holds for the stiffer springs (that is, the stiffer springs are also nonlinear in the torque-angle behavior), a new kink forms in the stiffer region of the tube (Fig. 4.10C, pink star). This kink will then travel again due to the stiffening, and the cycle repeats.

We visualize the evolution of the simulated system[4] in the spatiotemporal domain (Fig. 4.10D), noticing the single kink with one angle at a

4 We refer to our Zenodo repository [166] for the implementation of the Python simulations.

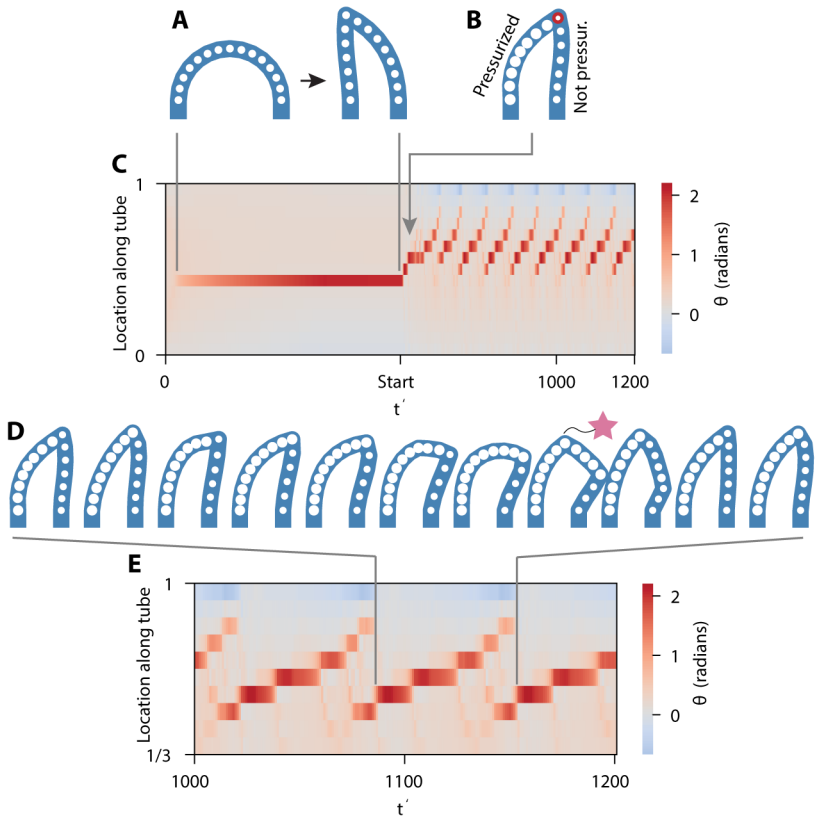

Figure 4.10

SIMULATION OF THE MASS-SPRING MODEL OF THE TUBE. (**A**) We start the simulation by displacing the inlet side toward the outlet side, and, as a consequence of assumption one (Fig. 4.8), a kink forms around the center. (**B**) We enforce assumptions two and three (Fig. 4.8). (**C**) As a consequence of the three assumptions, after the kink forms, the stiffening on the left side of the kink results in the kink traveling along the tube. When the kink reaches a critical location along the tube, a new kink forms in the stiffer section (pink star), because the springs in the stiffer part of the tube still exhibit the nonlinear behavior of assumption one. (**D**) Spatiotemporal signature of the system, i.e., the angles of the springs on all locations along the tube, over time. From non-dimensional time $t' = 600$ (start), the stiffening (assumption two and three) is enforced, and the kinks arise, travel, and disappear cyclically at a stable frequency. (**E**) Spatiotemporal signature for two full oscillation cycles, showing how the second instability causes two kinks to briefly appear simultaneously. A switch in the dominant kink is then observed, leading to the spontaneous reset of the system, such that the cycle repeats.

high value (red) and all other angles at a low value (grey) until $t' = 600$. After switching on assumptions two and three, the system self-oscillates at a stable frequency (Fig. 4.10D). We look at the spatiotemporal signature of two consecutive oscillations in Figure 4.10E. For a short amount of time, two kinks exist simultaneously on the tube, in accordance with the experimentally observed behavior (Fig. 4.2). The duration of this two-kink state is, however, shorter (in relation to the traveling duration) when compared with the experiments in Figure 4.2C. Indeed, in terms of this two-kink state duration, it seems that our model is capturing the dynamic, resonating case in Figure 4.3E. When the newly formed kink eventually becomes dominant, it will travel again in the next cycle.

These results confirm that the model captures the essential features of a self-oscillating tube, including kink formation, traveling, and spontaneous cyclic resetting. This self-sustained oscillatory behavior emerges from three experimentally proven assumptions. Note that this model still captures the oscillating behavior despite approximating the dynamics of the fluidics. In fact, for simplicity, we model a sudden increase in pressure as a consequence of the kink. However, in reality, the fluidic resistance would suddenly increase, and pressure would smoothly increase as a consequence. As we learned in Chapter 3 [88], the variable pressure, given constant inflow, would follow the orifice dynamics, which we did not include in this coarse-grained model.

From this model, we also learn that when the stiffening of the pressurized section is not high enough, the kink does not travel along the tube. In fact, when the stiffness multiplier κ is low, up to 1.5 (Fig. 4.11A), the formed kink does not propagate along the tube (Fig. 4.11B,C,F,G). For $\kappa = 1.7$ we observe the kink traveling once, likely due to inertia effects, but subsequent oscillations are not sustained (Fig. 4.11D,H). When the stiffening is high enough (for $\kappa = 1.9$), the kink is able to travel, and a new kink forms when the previous one reaches the critical position along the tube (Fig. 4.11E). This results in the system sustaining subsequent self-oscillations (Fig. 4.11I).

This key role of the pressure-induced stiffening in enabling the self-sustained oscillations is in line with experimental observations. In Figure 4.9D we report the experimental torque-angle curves of a thicker silicone tube with inner diameter 3 mm and thickness 1 mm for different pressurization levels. For this tube, assumption one still holds (the curves present a peak and a valley, and we observe the formation of a kink), and assumption two as well (the kink locally increases fluidic resistance). However, when controlling the input flow up to 20 SLPM, we do not observe the kink traveling and the tube oscillating: this is the well-known static behavior of a kinked thick soft tube previously studied [48]. With the observations from the model, we now have a better indication of why, in this specific case, the kink does not travel along the tube: the

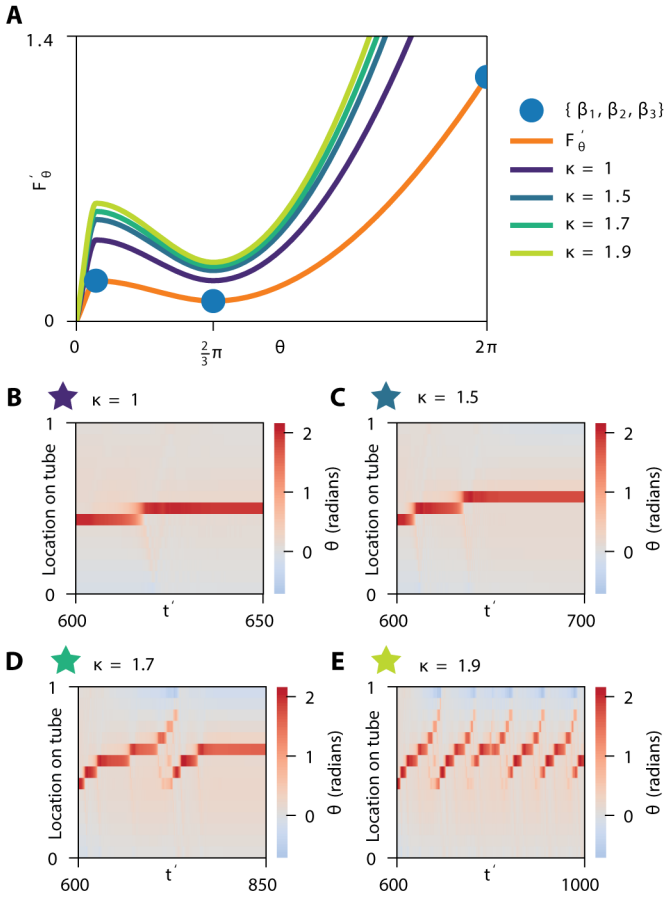

Figure 4.11

IN THE SIMULATION, INCREASING THE PRESSURE-INDUCED STIFFENING ENABLES THE SELF-OSCILLATION. (**A**) Torque-angle curves of the springs in the soft region after the kink (orange line) and in the stiff region before the kink (blue to green lines), for different values of stiffness multiplier κ (1, 1.5, 1.7, and 1.9). (**B**) Bending angles of the nodes along the tube (location 0 being the inlet, and location 1 the outlet) over time for κ = 1. Insufficient stiffening prevents the kink from traveling further than the middle of the tube, and the oscillation is not sustained. (**C**) Angles over time for κ = 1.5. The kink is able to propagate further along the tube because of the increased stiffness but does not reach the point where a new instability forms in the stiff region, so oscillation is not sustained. (**D**) For κ = 1.7, the kink propagates far enough to reach a second instability and initiate a restart of the process once due to initial momentum, but it is not able to sustain the oscillation over multiple cycles. (**E**) Angles over time for κ = 1.9. This is the lowest value of κ that enables the tube to sustain subsequent oscillations. (**F**, **G**, **H**, **I**) State of the tube over time corresponding to the situations in B-E.

increase in the critical torque to induce kinking due to pressurization (from assumption three) is considerably lower than in the case of the softer tube (compare Figure 4.9C with Figure 4.9D). The stiffening effect is not sufficient to induce the kink to travel, similar to the case of the model with κ up to 1.5 (Fig. 4.11B,C,D).

Practical information about the simulations

The parameters used in the simulations are:

- Number of nodes (including boundary nodes): $N = 17$.
- Dimensionless damping coefficient: $\zeta' = 0.4$.
- Dimensionless bending stiffness parameters: $\beta = [1.20, 0.1, 0.2]$.
- Sigmoid function parameters: $k = 5$, $x_0 = 1.5$.

The kink propagation was managed by updating an `extra_array` that keeps track of the state and timing of each node's stiffening and softening due to the kink. When a kink is detected at a node (based on a threshold angle deviation), the bending stiffness at that node is increased over time following the sigmoid function.

We followed the following steps for each simulation:

1. Initialization:
   - set initial positions along a half-circle and zero initial velocities;
   - initialize parameters and non-dimensional variables.
2. Time integration loop:
   - at each time step, compute linear and torsional forces;
   - update positions and velocities using the ODE solver;
   - apply boundary conditions;
   - update the bending stiffness at nodes affected by the kink.
3. Data recording: store positions, velocities, and other relevant variables for analysis.
4. Post-processing: analyze the results to observe the oscillatory behavior and the effect of the kink-induced stiffening.

4.6.3 *Actuator analysis*

We aim to obtain an overview of the behavior of the actuator by studying *i)* the full-step actuation cycle, *ii)* the frequency dependencies of the silicone tube actuator, iii) the kinks' behavior in time, *iv)* the response under flow and pressure control, *vi)* the fluidic coupling of two actuators, *vii)* the frequency and stroke of the TPU pouch actuator compared to the silicone tube actuator, viii) the power consumption of the TPU pouch actuator, ix) the characterization of the TPU pouch actuator in terms of design parameters, and x) the constrained actuation of the TPU pouch actuator against an external load.

Full-step actuation cycle

Given the non-trivial behavior of our actuator, which displays kinks traveling on the continuity of the tube, the definition of the actuator tip is not straightforward. For each frame of the high-speed video of the oscillating tube (details on the recording setup in Section 4.6.7) we detect the outer edge of the tube (details on the algorithm in Section 4.6.8). For each time instant, we define the actuator tip as the point of the outer edge furthest from the horizontal axis of the reference frame defining the actuating plane[5] (Fig. 4.12A). Importantly, if we rotate the actuating plane, the actuator tip is represented by another point in the plane (Fig. 4.12B).

The actuator tip trajectory in the actuating plane has different shapes depending on the amount of rotation of the actuating plane. We report three example cases for plane angle equal to 0°, 15°, and 30° in Figure 4.12C,D,E. Note that the actuator is in the non-resonating oscillation regime—the input airflow is 6.5 SLPM. Also, note that each trajectory is reported for two subsequent oscillation cycles.

We report the normalized x and y displacement of the actuator tip in time for the three example cases of plane angle equal to 0°, 15°, and 30° in Figure 4.12F,G,H. Note that non-optimized motions show either an anticipation (in the case of 0°) or a delay (in the case of 30°) of the y-motion. The optimized motion (at 15°) is approaching the shape of an ideal full-step cycle, where the stance (increase in x displacement) is performed when the y displacement is low, and the swing (decrease in x displacement) when the y displacement is high.

To find the value of the plane angle that optimizes the full-step cycle, we define a cost function as the ratio between the y-stroke and the x-

5 This defines the actuator tip as the point on the outer edge closest to the surface on which the actuator will perform the full-step. This definition holds for non-zero curvature, which is typically ensured under the experimental conditions of the bent tubes.

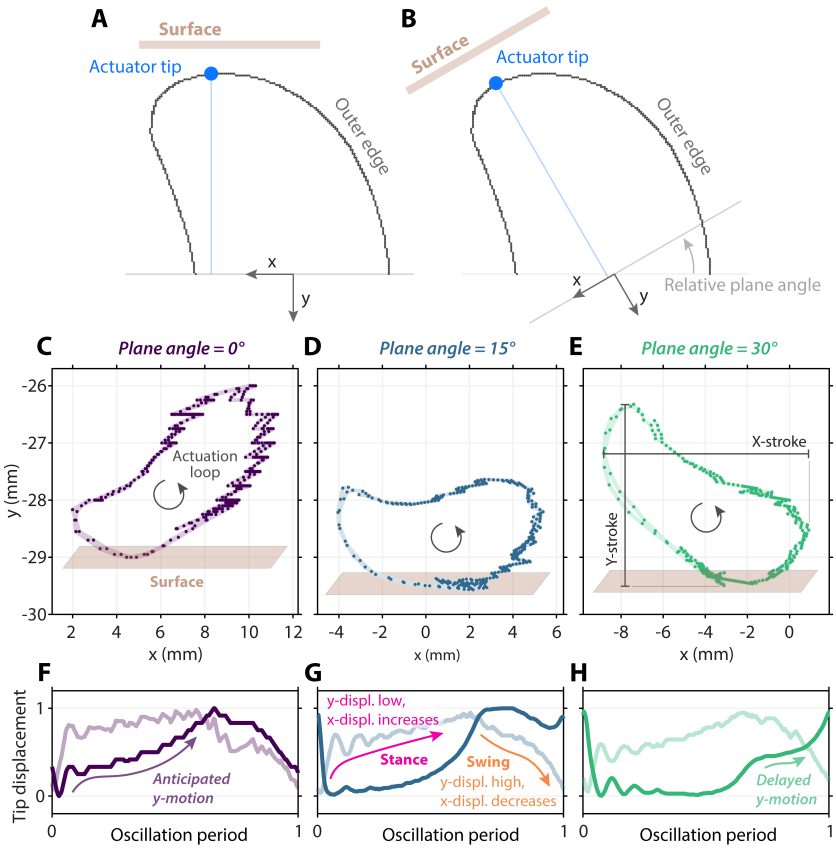

Figure 4.12

THE FULL-STEP ACTUATION CYCLE IS INFLUENCED BY THE RELATIVE ANGLE BETWEEN THE LIMB AND THE SURFACE. (**A**) The limb tip is defined as the point of the outer edge furthest from the x-axis of the actuating plane reference frame (the x-axis is parallel to the surface on which the limb will step). (**B**) When the reference frame of the surface is rotated, the limb tip is, by definition, a different point. (**C**, **D**, **E**) Limb tip trajectory for plane angle 0°, 15°, and 30°, for input airflow of 6.5 SLPM. (**F**, **G**, **H**) Normalized x and y displacement (in the actuating plane reference frame) of the limb tip in time, for plane angle equal to 0°, 15°, and 30°. In F, G, and H, we refer to x (light curves) and y (dark curves) as the displacements of the limb tip along the two axes of the reference frame of the actuating plane defined in A.

stroke. These strokes are defined as the difference between the maximum and the minimum value of, respectively, the x-coordinates and the y-coordinates of the trajectory points. Therefore, qualitatively, the cost function is maximizing the 'effective' stance, so reducing the portion of the stance that is 'lost' by not being in contact with the ground. The cost

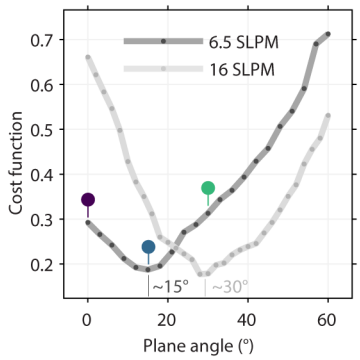

Figure 4.13
COST FUNCTION OF THE FULL-STEP ACTUATION CYCLE. The shape of the cost function, defined as the ratio between the y-stroke and the x-stroke, for plane angle between $0°$ and $60°$, shows a global minimum. Colored dots relate to the three cases in Figure 4.12C-H.

function shows a global minimum at ~ 15° for inflow 6.5 SLPM and at ~ 30° for inflow 16 SLPM (Fig. 4.13).

Frequency dependencies of the silicone tube actuator

The oscillation frequency of the silicone tube actuator depends on various design parameters (Fig. 4.14). For example, scaling a reference design (with $l = 36\,mm$, $D_i = 2.5\,mm$, $t = 0.4\,mm$, and $d = 10\,mm$) by a factor of ~ 0.8 results in an increase in the activation frequency by a factor ~ 1.4 for the 15 SLPM (resonant) case and ~ 2.1 for the 5 SLPM (non-resonant) case (Fig. 4.14A). In fact, scaling down the tube by a factor $k \approx 0.8$ decreases the volume of air required for the kink to travel forward in one cycle by a factor $k^3 \approx 0.512$. This is because we approximate the volume of air as a cylinder, with height being the distance covered by the kink and radius being the inner radius of the tube. Therefore, in principle, this factor approximately doubles (1/0.512) the frequency of oscillation, as it halves the time required for the kink to travel, given the same inflow. As shown in the experimental results reported in Figure 4.14A, when the tube is not resonating, frequency indeed doubles from ~ 40 Hz to ~ 80 Hz. Instead, in the dynamic resonating case, in practice, the frequency scales by a factor ~ 1.4, likely because of inertia playing additional roles that we did not take into account.

We also tune the frequency by acting on the parameters of the surrounding fluidic circuit. We increase the downstream fluidic resistance by decreasing the diameter of an orifice placed in line after the outlet of the actuator. As orifices, we use the Luer-to-barb connectors with different

nominal ID diameters (1.6 mm, 2.4 mm, 3.2 mm, and 4 mm). Note that we manually measure the internal diameter of the orifice with a caliper, obtaining 1.2 mm, 1.8 mm, 2.3 mm, and 3 mm. For higher downstream resistance, the frequency of oscillation decreases, both in the resonant (Fig. 4.14B) and non-resonant (Fig. 4.14C) cases.

We study the influence of structural asymmetry on the oscillation frequency by adding a design parameter h, the height of the inlet over the outlet. Note that, for each h value, we adjust the length l of the tube by subtracting h from a reference length l_0. With this design choice, h represents the portion of the tube that is being clamped at the inlet side. We observe a non-monotonic trend of the oscillation frequency over h, for samples with $l = 36$ mm, $D_i = 2.5$ mm, $t = 0.4$ mm, and $d = 10$ mm (Fig. 4.14D). This non-monotonic frequency trend is accompanied by a monotonic decrease in the x-stroke of actuation (Fig. 4.14E). We can calculate an estimated value of the locomotion speed for a hypothetical one-limb robot by multiplying the x-stroke by the activation frequency, observing an optimal value for h between 4 mm and 6 mm (Fig. 4.14F).

Given these various design parameters, we can achieve higher frequencies using a combination of them. For example, the tethered robot reaches 300 Hz (Figure 4.4K-N) because we chose low downstream fluidic resistance, the optimal asymmetry value, and small tubes with diameter scaled by a factor ~ 0.8 and length scaled by a factor ~ 0.5 relative to the reference design (Section 4.6.5).

Kinks behavior in time

To ease the understanding of the behavior of the kinks forming, traveling, and disappearing along the tube reported in Figure 4.2, we report additional data in Figure 4.15. For clarity, refer to the definitions reported in Section 4.6.8.

For each pixel belonging to the outer edge cluster (for example, the 180-th pixel in the cluster is the green dot), we find the closest pixel belonging to the inner edge (magenta dot) (Fig. 4.15A). The pixel with the coordinates average of these two points (black dot) is assigned to the center line cluster. We resolve the outer and inner edges along the center line (Fig. 4.15B), and we plot the local width along the tube every 5 ms (Fig. 4.15C). The local minima of the local width are the two kinks. If only one local minimum is detected, then only one kink is present. In Figure 4.15D, the history of the individual kink (pink highlight) shows that the kink location doesn't change when the kink is not dominant (grey arrow), while it increases once the kink becomes dominant (black arrow). Moreover, in Figure 4.15E we see that the kink sharpens (the width

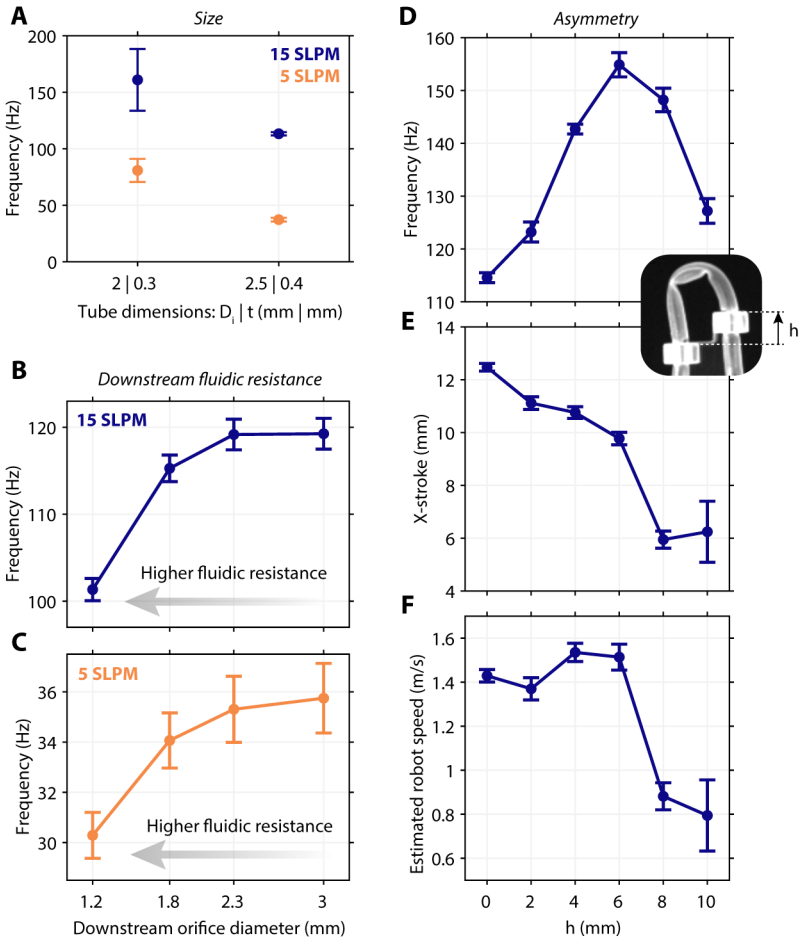

Figure 4.14
FREQUENCY DEPENDENCIES OF THE SILICONE TUBE ACTUATOR. (**A**) Oscillation frequency of a reference silicone tube design (with l = 36 mm, D_i = 2.5 mm, t = 0.4 mm, and d = 10 mm), and a factor ~ 0.8 scaled design, for the 15 SLPM (resonant) case and for the 5 SLPM (non-resonant) case. (**B**, **C**) We place a needle in series with the actuator, connected to the outlet, to introduce a downstream fluidic resistance. Influence of the downstream orifice diameter over the frequency for the resonant case in B and the non-resonant cases in C. Influence of the asymmetry parameter h over (**D**) the oscillation frequency, (**E**) the x-stroke of actuation, and (**F**) the locomotion speed of a hypothetical one-limb robot, for inflow 15 SLPM.

decreases) while being non-dominant and non-moving (grey arrow), until it becomes dominant (blue star).

In the resonating oscillation regime (16 SLPM), the kink covers a larger distance in the x-y plane. The kink distance overshoots the non-resonating case of approximately 50% (Fig. 4.15F). Note that the 'kink distance' fundamentally differs from the 'kink location'. The kink distance is defined on the x-y reference frame and, therefore, carries information regarding the structural displacement of the tube in the actuating plane. On the other hand, the kink location is defined on the reference frame along the tube itself (center line) (Section 4.6.8 for details on these definitions).

Flow-controlled and pressure-controlled response

We take a silicone tube actuator with l = 36 mm, D_i = 2.5 mm, t = 0.4 mm, and d = 10 mm. We decrease the input airflow from 20 SLPM to 0 SLPM in 2 min (Fig. 4.16A), observing two different oscillating pressure regimes (Fig. 4.16B) corresponding to the two frequency regimes (Fig. 4.16C) analyzed in Figure 4.3B-E. At ~103 s (~ 3.8 SLPM) the system stops oscillating because the flow is not high enough to build up pressure, and the tube stays in the two-kinks state. When pressure is low enough (at ~ 112.5 s), the non-dominant kink becomes dominant and the other kink disappears. The fluidic resistance increases, so the upstream pressure increases too, but without resulting in oscillation, since the kink is static.

We investigate the direct influence of pressure over the kinks' states by quasi-statically controlling the upstream pressure using a proportional pressure regulator (details on the setup in Section 4.6.7). We first increase the upstream pressure to 130 kPa in one minute, and then we decrease it to atmospheric pressure in one minute (Fig. 4.17A).

The output flow through the tube throughout the experiment (Fig. 4.17B) is directly related to the structural state of the system (Fig. 4.17C). Initially, the actuator is in a 'leaky state', with air flowing through. The actuator is then 'closed' because a sharp kink forms, blocking the airflow. For increasing pressure, the kink travels along the tube. When the kink reaches the left side of the tube, the kink angle increases, causing the kink to leak and, therefore, the actuator to 'open'. When pressure decreases, the actuator follows a different pathway, staying open and forming a new, non-dominant kink. When pressure is low enough (around 20 kPa), the new kink fully forms, and the actuator goes back to the leaky state. The pressure-flow profile emphasizes this fluidic hysteresis that arises under pressure-controlled conditions (Fig. 4.18).

In summary, by experimentally simulating the pressure build-up and release, we confirm that the kinks' state is a direct consequence of the pressure state, with a hysteretic dependence. Throughout our work, under flow-controlled conditions, the kinks' state is, in turn, affecting the

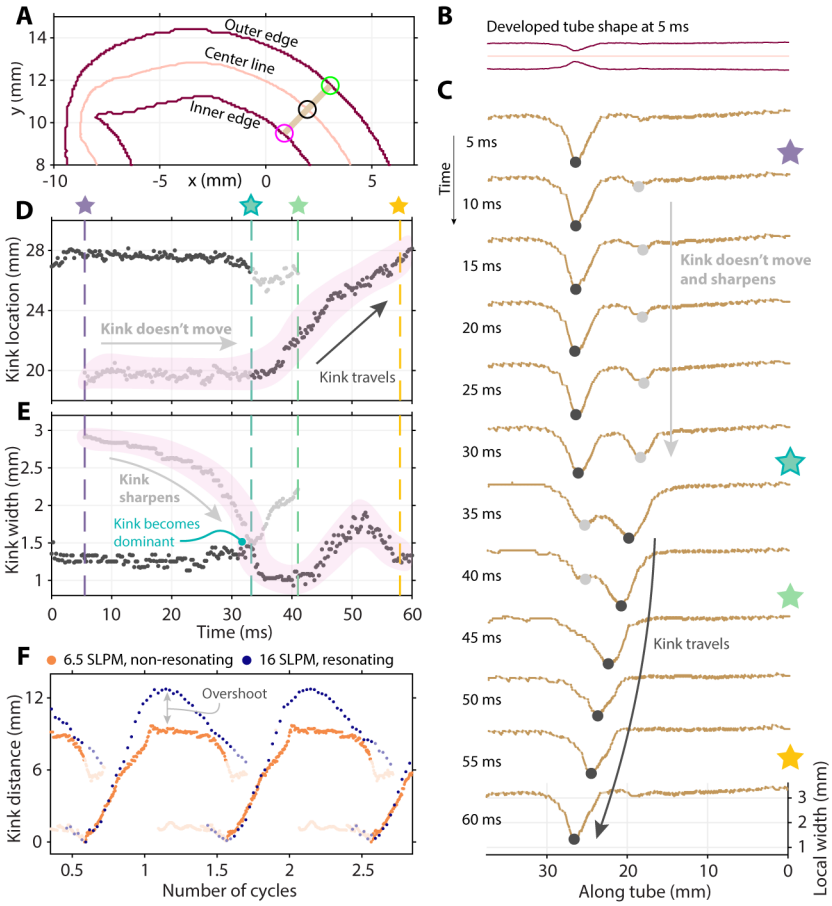

Figure 4.15
KINKS BEHAVIOR IN TIME. (**A**) Visualization of the outer and inner edges of the tube (red), the center line (pink), and the local width (brown). (**B**) Tube resolved on the center line. (**C**) Local width along the tube every 5 ms. (**D**) History of the individual kink location (pink highlight), with an initial non-moving state (grey arrow) and a subsequent traveling state (black arrow). (**E**) History of the individual kink width, with the kink sharpening while being non-dominant and non-moving (grey arrow), until it becomes dominant (blue star). (**F**) Kink distance for the non-resonating (6.5 SLPM) and resonating (16 SLPM) cases.

pressure state, causing pressure build-up when the actuator is 'closed', and pressure release when the actuator is 'open', inducing the self-oscillatory behavior.

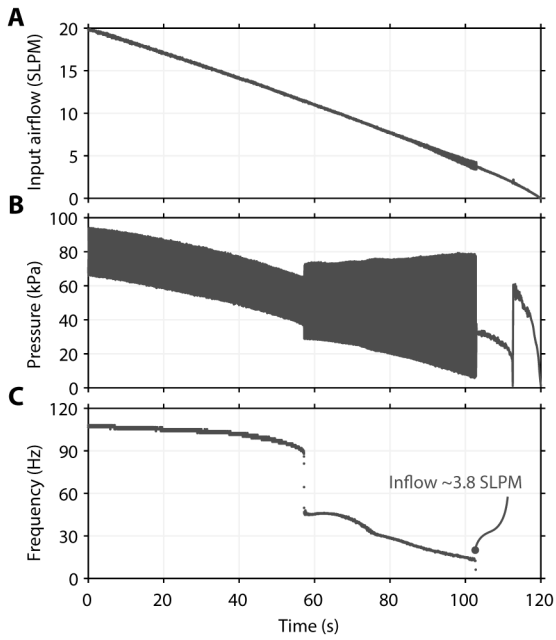

Figure 4.16
FLOW-CONTROLLED RESPONSE. We take a silicone tube actuator with $l = 36\,mm$, $D_i = 2.5\,mm$, $t = 0.4\,mm$, and $d = 10\,mm$. (**A**) Applied input airflow profile, linearly decreasing from 20 SLPM to 0 SLPM in 2 min. Measured (**B**) pressure and (**C**) frequency.

Fluidic coupling

We fluidically couple two self-oscillating actuators by connecting them in parallel to the same flow source using two identical tubes (Fig. 4.4A-G). The actuators have $l = 18\,mm$, $D_i = 2\,mm$, $t = 0.3\,mm$, $d = 7.8\,mm$, and $h = 3.9\,mm$. The coupling tubes used for the experiments all have the same inner diameter of 2 mm. The minimum length of each coupling tube is ~ 7 cm, which includes the Luer^{TM} T-connector and the additional length of the actuator at the inlet side. For each experiment, the input flow rate is set to 15 SLPM.

When we couple the two self-oscillating actuators using tubes of length 12 cm, we observe a distribution of the oscillation frequencies with two maxima at the two characteristic frequencies for in-phase and anti-phase activation (Fig. 4.19A). The system alternates between the in-phase and the anti-phase eigenmodes, as highlighted by the distribution of the phase shift (Fig. 4.19B). The pressure signals in time show how the two actuators are smoothly transitioning in and out of the two eigenmodes (Fig. 4.19C).

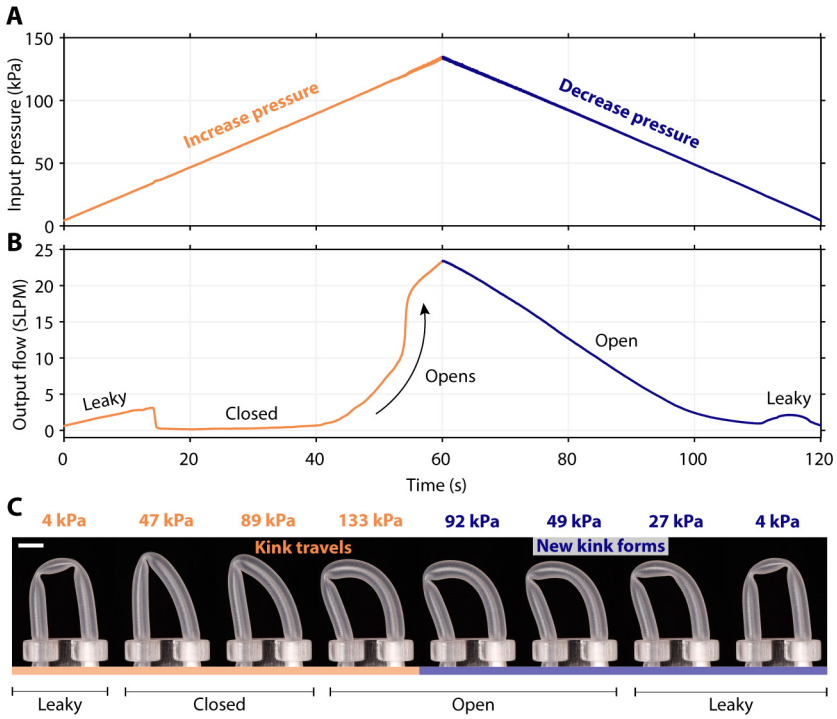

Figure 4.17
QUASI-STATIC PRESSURE-CONTROLLED RESPONSE. We take a silicone tube actuator with l = 36 mm, D_i = 2.5 mm, t = 0.4 mm, and d = 10 mm. (**A**) The applied pressure profile increases to 130 kPa in one minute, and then decreases to atmospheric pressure in one minute. (**B**) The output flow through the tube throughout the experiment. (**C**) Snapshots of the tube state in time.

For coupling tubes' length between 24 cm and 47 cm, we observe the frequencies of the two actuators becoming different, as a consequence of weaker coupling. With tubes longer than 52 cm, coupling effects disappear, as we see the frequencies approaching the natural frequencies of the individual actuators, measured separately by providing half the inflow (7.5 SLPM) to each actuator alone (Fig. 4.19D).

Comparison of frequency and stroke in silicone tube and TPU pouch actuators

The inflow required to activate the oscillation for the TPU pouch actuator is ~ 0.1 SLPM, which is lower than the inflow provided by the two 3 V mini air pumps used to power the untethered robot (~ 0.54 SLPM and ~ 0.64 SLPM when connected to the LiPo battery) (Fig. 4.20A). Note that,

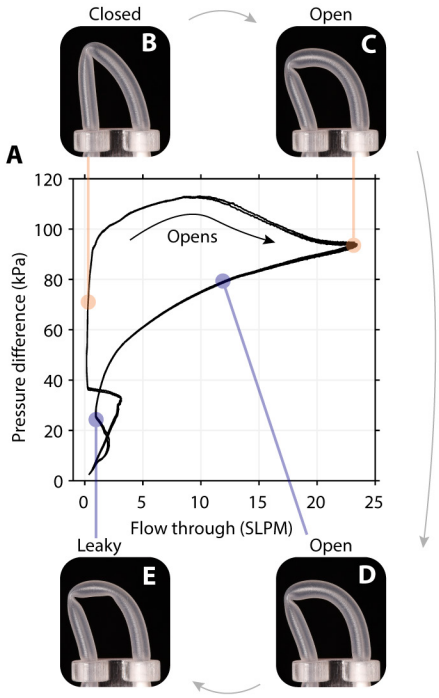

Figure 4.18
HYSTERETIC PRESSURE-FLOW CURVE UNDER PRESSURE-CONTROLLED CONDITIONS. (**A**) Pressure-flow profile, for two subsequent cycles of pressure loading and unloading. (**B**, **C**, **D**, **E**) Snapshots of four key states.

in comparison, the activating inflow of the silicone tube actuator is ~ 3.8 SLPM (Fig. 4.16), which the mini air pumps cannot provide.

The maximum measured frequency of the TPU pouch actuator (with length 80 mm, width 10 mm, and holder angle 55°) is ~ 3.5 Hz (Fig. 4.20A). The reason for this lower oscillation frequency compared to the silicone tube design is likely the absence of a resonant mode and the higher geometric volume of fluid required for the kink to travel. We approximate the geometric volume V_{kink} associated with the traveling kink as the volume of a cylinder with area equal to the circular cross-section of the tube (with inner diameter D_i) and the height equal to the length of the tube covered by the traveling kink L_{kink}:

$$V_{kink} = \left(\frac{D_i}{2}\right)^2 \cdot \pi \cdot L_{kink}. \tag{4.22}$$

In the case of the silicone tube, we have D_i = 2.5 mm by design and $L_{kink} \approx$ 8 mm, since the kink moves from ~ 20 mm to ~ 28 mm along the tube (Fig. 4.15D). In the case of the TPU pouch, we know that at

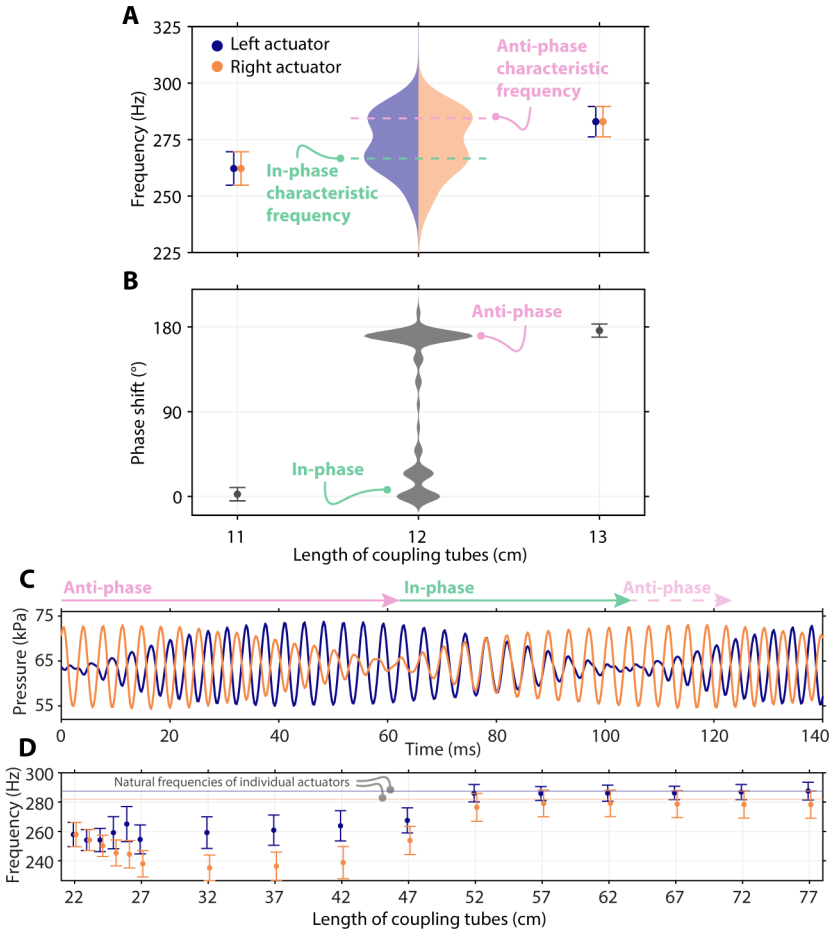

Figure 4.19
FLUIDIC COUPLING. (**A**) Distribution of the oscillation frequencies of two actuators coupled through two coupling tubes of length 12 cm (data reported in Figure 4.4F). The actuators have $l = 18\,mm$, $D_i = 2\,mm$, $t = 0.3\,mm$, $d = 7.8\,mm$, and $h = 3.9\,mm$. (**B**) Distribution of the phase shift (data reported in Figure 4.4G). (**C**) Pressure signals of the two actuators in time. (**D**) Frequency of the two actuators for coupling tubes' length between 22 cm and 77 cm.

rest, the perimeter of the cross-section is two times the pouch width, which is $W = 10\,mm$ by design. Therefore, approximating the shape of the pressurized pouch's cross-section as a circle, the diameter of the pressurized cross-section is $D_i = 2 \cdot W/\pi \approx 6.366\,mm$. From Fig. 4.5A and Fig. 4.20B, we notice that the kink travels approximately from the beginning to the end of the tube, therefore $L_{kink} \approx 80\,mm$. Therefore, we

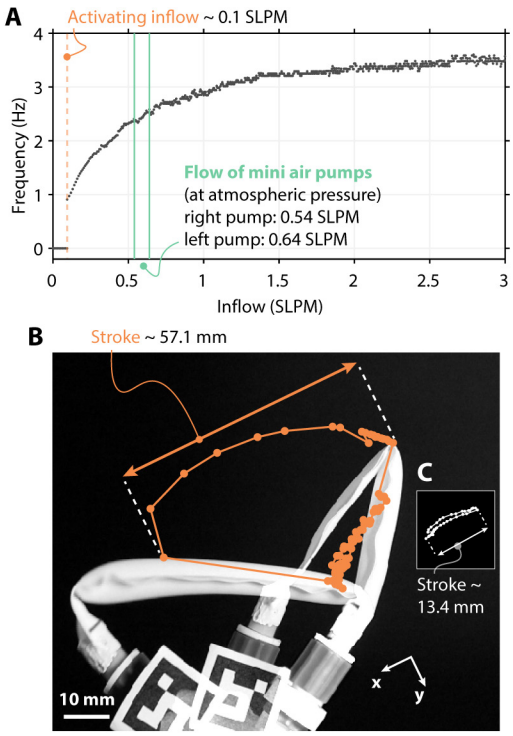

Figure 4.20
FREQUENCY AND STROKE OF THE TPU POUCH ACTUATOR. (**A**) Frequency of the TPU pouch actuator for increasing input airflow from 0 SLPM to 3 SLPM. (**B**) Trajectory of the actuator tip on the rotated x-y reference frame (data reported in Figure 4.5B). (**C**) Tip trajectory of the silicone tube actuator in the same scale as the TPU pouch actuator.

obtain the geometric volume associated with the kink traveling in the silicone tube as:

$$V_{\text{kink}}^{\text{tube}} \approx \left(\frac{2.5}{2}\right)^2 \cdot \pi \cdot 8 \approx 39\,\text{mm}^3 \approx 0.039\,\text{mL}, \tag{4.23}$$

and in the TPU pouch as:

$$V_{\text{kink}}^{\text{pouch}} \approx \left(\frac{6.366}{2}\right)^2 \cdot \pi \cdot 80 \approx 2546\,\text{mm}^3 \approx 2.546\,\text{mL}. \tag{4.24}$$

The stroke of the TPU pouch actuator is ~ 57.1 mm, higher than the stroke of the silicone tube actuator, which is ~ 13.4 mm (Fig. 4.20B). Note the stroke of the actuator is obtained as the difference between the maximum and minimum x-coordinates of the actuator tip trajectory on the 26° rotated x-y reference frame. The tip trajectory is obtained

from the tip coordinates of four subsequent cycles (Section 4.6.8 for details), re-ordered as nearest neighbors. We also report the silicone tube actuator's tip trajectory in the same scale as the TPU pouch actuator to highlight the higher actuation hysteresis of the TPU pouch actuator (Fig. 4.20C).

Power consumption of the TPU pouch actuator

We are interested in the fluidic power needed for the TPU pouch actuators to locomote (as the product between flow through the actuators and upstream pressure), in addition to the electric power consumed by the pumps, which is ~ 1.5 W (Section 4.6.5). This analysis removes the contribution of the efficiency of the pumps, indicating the effective power consumed by the limbs to operate.

To compute the flow through the limbs while the robot locomotes, we use the measured pressure signals reported in Figure 4.6C. We do so by using the pump curve, which relates the downstream pressure to the flow the pump delivers. In principle, higher downstream pressure implies a lower flow delivered by the pump. With no downstream pressure, the pump delivers the maximum flow. We measured the pump curve by placing the pump in line with a pressure sensor, a variable resistance, and a flow sensor. We manually increased the resistance, while measuring pressure and flow. In Figure 4.21A,B, we report the measured curves of the pumps connected to the left and right limbs, respectively. We used MATLAB to fit the data with a function $Q = Q(p)$ that is the sum of two exponential terms:

$$Q(p) = a \cdot e^{b \cdot p} + c \cdot e^{d \cdot p}, \tag{4.25}$$

obtaining a, b, c, d that minimize the error between the data and the curve (Fig. 4.21A,B).

Next, we compute the flow through the limbs by applying the function (4.25) to the pressure signals of the limbs (Fig. 4.21C), obtaining the flow signals reported in Figure 4.21D. We convert the flow from SLPM to liters per minute by using Equation (4.32) (with T_{gas} being the temperature in the lab 295.65 K, and p_{gas} being atmospheric pressure plus the pressure in Figure 4.21C). We obtain the flow in cubic meters per second by dividing by $6 \cdot 10^4$.

We compute the fluidic power provided to each limb by multiplying the pressure in pascals and the flow in cubic meters per second, obtaining the curves shown in Figure 4.21E. The average fluidic power provided to each limb is ~ 0.06 W. We obtain the total fluidic power provided to the locomoting robot (Fig. 4.21F) as the sum of the power provided to each

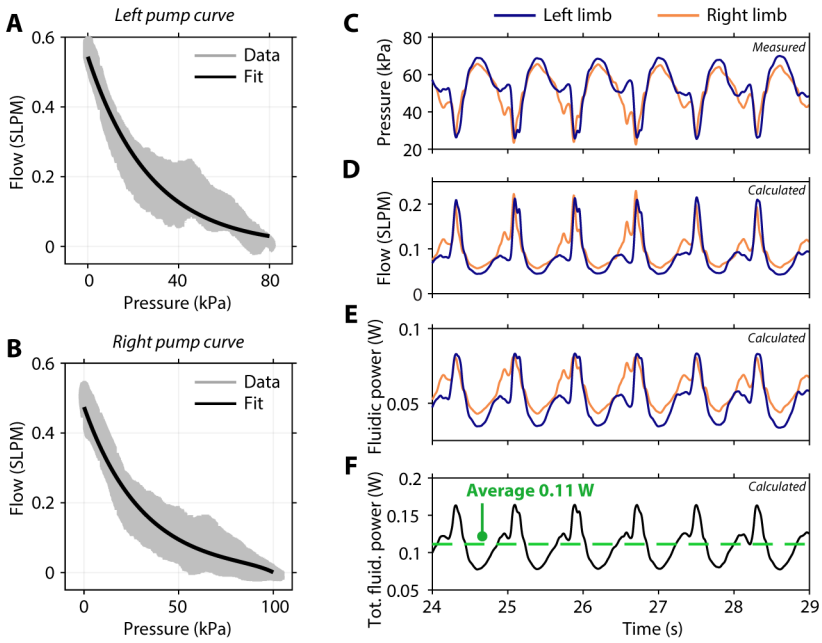

Figure 4.21
FLUIDIC POWER REQUIRED FOR THE TPU POUCH ACTUATORS TO OPERATE IN THE UNTETHERED SCENARIO. The pressure-flow curves of the pumps connected to (**A**) the left actuator and (**B**) the right actuator of the untethered robot. (**C**) The measured pressures of the left and right actuators of the robot locomoting on the ground (experiment shown in Figure 4.6A-C). (**D**) The flow provided to each actuator, determined from the pressure values in C and the pump curves in A and B. (**E**) The fluidic power provided to each actuator, determined by multiplying the pressure in C in pascal and the flow in D converted to cubic meters per second. (**F**) The total fluidic power provided to the robot, obtained by summing the fluidic power provided to the two actuators in E.

limb. From this signal, we obtain the average fluidic power provided to the robot ~ 0.11 W.

For an analysis of the locomotion efficiency compared to other animals or robots, we refer to the cost of transport analysis in Section 4.6.5.

Characterization of the design parameters of the TPU pouch actuator

In this section, we will provide quantitative design guidelines to select soft tubes that display the self-oscillating behavior, based on the learnings from the mass-spring model (Section 4.6.2). We then characterize the self-oscillating behavior in response to changes in the design parameters of the tubes.

Our mass-spring model (Section 4.6.2) highlights three key characteristics that the tube must satisfy in order to achieve self-oscillation, namely:

(A) a non-monotonic torque-angle curve, with a negative stiffness regime. This characteristic is a requirement for the formation of a single kink;

(B) an increase in torque needed for kink formation (which typically also relates to stiffening upon pressurization);

(C) a significant increase in flow resistance at the location of the kink (Fig. 4.24 and Fig. 4.25).

Material-wise, since the options of commercially available tubes are limited, throughout this Chapter, we tested off-the-shelf elastomeric tubes with shore hardness 60 A, and we manufactured TPU tubes with shore hardness 85 A. A complete experimental study on the effect of Young's modulus is therefore difficult to perform. Our coarse-grained model is also not suitable to validate the effect of stiffness. Yet, we can hypothesize the effect of the stiffness, and we believe that increasing the stiffness of the tubes will overall decrease the frequency of oscillation. Note that the kinking of tubes is formed when specific strains are reached, which correlates to the amount of volume in the tube (and thus to the flow). As the input flow is constant in our implementation, we expect the tube to go through the same deformation sequence, independently of stiffness. Yet, higher Young's modulus requires higher pressures, which, in the case of air, requires more air input and will also lead to more leakage through the kink. These two effects will delay the formation of kinks and thus decrease the frequency. Still, it should be noted that stiffer tubes are expected to increase the resonance frequency, such that there might be specific inflows where the stiffness could have a positive effect on frequency.

Various other parameters are more straightforward to change (and therefore more useful in practice). Since the options of commercially available thin tubes are fairly limited, we addressed the characterization of the self-oscillating tube by manufacturing custom-made TPU tubes of various lengths, inner diameters, and thicknesses (details of the manufacturing steps in Section 4.6.6). We measured the average oscillation frequency and stroke, given various input flows (Fig. 4.22). As a whole, the results serve as a guideline for a designer who would have specific requirements in terms of stroke and frequency, so that they could select the appropriate parameters to achieve it.

The TPU pouch tube is characterized by three design parameters: the thickness of the TPU sheet, the length of the sealing lines, and the width

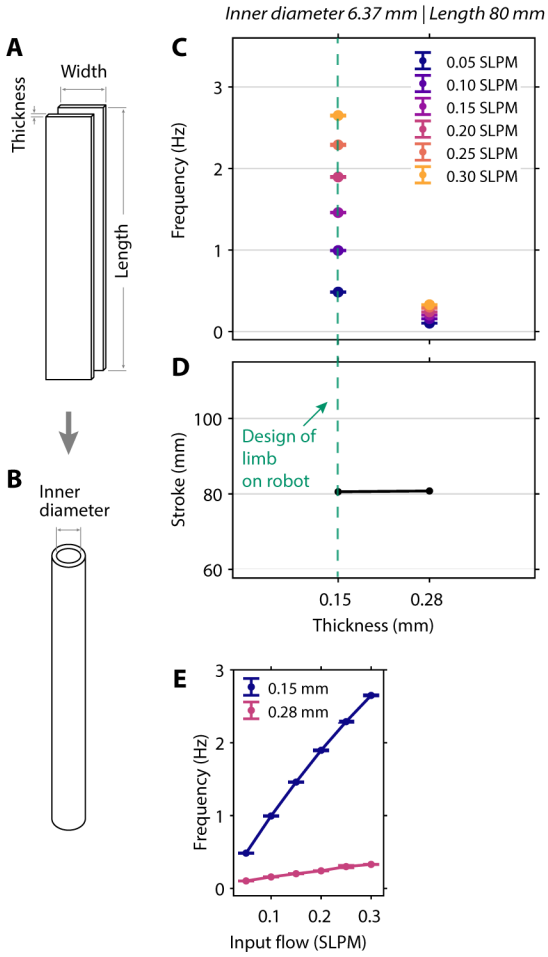

Figure 4.22
Continues to the right.
CHARACTERIZATION OF THE TPU POUCH ACTUATOR FOR SEVERAL DESIGN PARAMETERS. (**A**) The TPU pouch actuator is characterized by three design parameters: the thickness t of the TPU sheet, the length L of the sealing lines, and the width W between the sealing lines. (**B**) When inflated with air and at atmospheric pressure, these design parameters result in a tube with the same length, the same thickness, and inner diameter equal to $2 \cdot W/\pi$. (**C**) Frequency and (**D**) stroke of the actuator as a function of thickness. The tubes have fixed inner diameter 6.37 mm and length 80 mm. (**E**) Frequency as a function of the input flow for the tubes with thickness 0.15 mm and 0.28 mm.

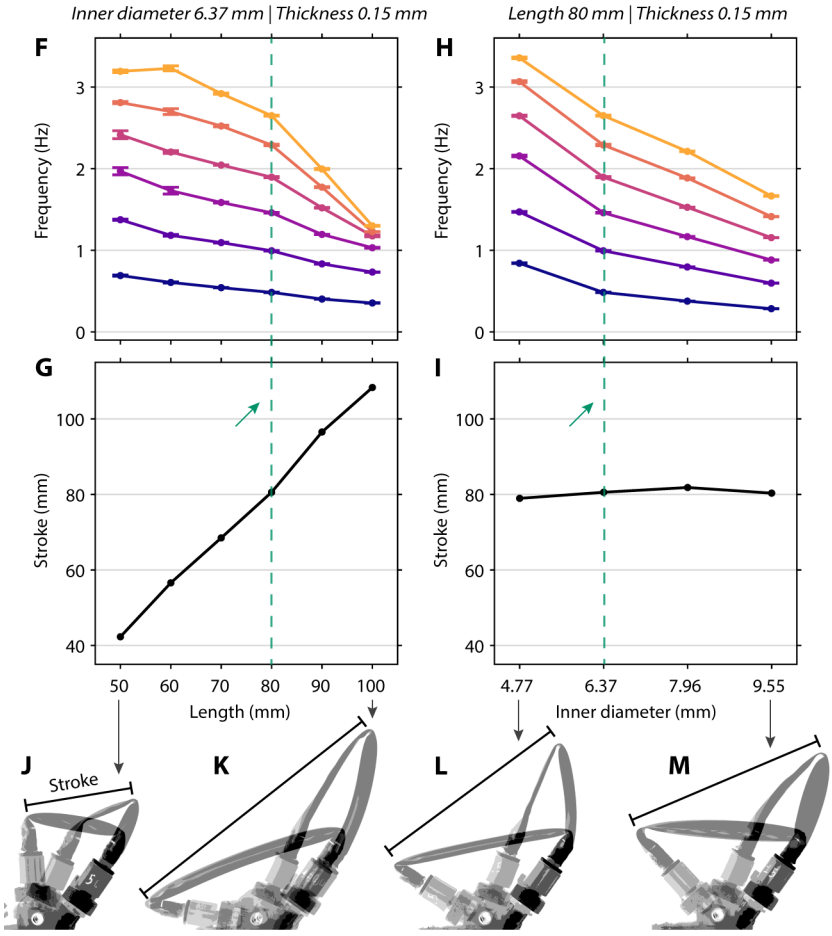

Figure 4.22
Continues from the left.
CHARACTERIZATION OF THE TPU POUCH ACTUATOR FOR SEVERAL DESIGN PARAMETERS. (**F**) Frequency and (**G**) stroke of the self-oscillating tube as a function of length for various input flows between 0.05 SLPM and 0.30 SLPM. The tubes have fixed inner diameter 6.37 mm and thickness 0.15 mm. (**H**) Frequency and (**I**) stroke of the actuator as a function of width. The tubes have fixed length 80 mm and thickness 0.15 mm. In panels C, D, F, G, H, and I, the green dashed line refers to the design parameters of the limb that we placed on the untethered robot. In panels C, F, and H, each dot represents the average frequency and standard deviation over 20 s of steady-state oscillation. (**J**,**K**,**L**,**M**) Overlapped photographs highlight the stroke of the actuator for four example cases.

W between the sealing lines (Fig. 4.22A). These design parameters result in a tube with the same length, same thickness, and an inner diameter equal to $2 \cdot W/\pi$, because the circumference is twice the width between the sealing lines (Fig. 4.22B).

We start by comparing tubes with thickness 0.15 mm and 0.28 mm, and same length 80 mm and inner diameter 6.37 mm. We observe a considerably lower frequency for the thicker tube (Fig. 4.22C). In this case, the stroke is unaffected by the increase in thickness (Fig. 4.22D). The flow-frequency trend is qualitatively similar in the two thickness cases and scaled by a factor ~ 6.9, approximately equal to the cube of the thickness ratio $(0.28\,\text{mm}/0.15\,\text{mm})^3 \approx 6.5$ (Fig. 4.22E).

We vary the length of the tube for a fixed inner diameter of 6.37 mm (width 10 mm) and thickness 0.15 mm. We observe that the frequency drops for increasing tube length, as more geometric volume of air is required for the kink to travel (Fig. 4.22F). The stroke increases with increasing tube length (Fig. 4.22G,J,K).

Finally, we vary the inner diameter of the tube by sealing tubes with widths from 7.5 mm to 15 mm, keeping the length fixed to 80 mm and thickness 0.15 mm. The frequency decreases for increasing inner diameter (Fig. 4.22H). In contrast to increasing the length, increasing the inner diameter results in nearly no change in the stroke (Fig. 4.22I,L,M).

In conclusion, with the overall information in Figure 4.22, a designer can determine tube parameters and inflow values that satisfy specific requirements in stroke and frequency. For example, given a requirement in stroke, we can determine the tube length that satisfies it (Fig. 4.22D). Then, for example, if we have a constraint in input flow that the pumps can provide, we check what frequency is reached by the tube of that length and width 10 mm (Fig. 4.22C). Given this result, if we require a higher (or lower) frequency, we design a tube with a lower (or higher) width (Fig. 4.22E) because the stroke will be unaffected (Fig. 4.22F).

Constrained actuation

The actuator undergoes the full-step actuation cycles even when constrained between two rigid walls. To study the behavior of the actuator when a rigid wall limits the workspace, we build the setup in Figure 4.23A. We mount the holder of the actuator on the bottom clamp of a tensile testing machine (details about the machine in Section 4.6.7) at a defined angle with the horizontal. We fix a 3D-printed flat PLA plate on the top clamp in series with the load cell. The plate displacement d is defined as a downward displacement of the top clamp. At zero displacement, the plate is not touching the oscillating actuator. Constant flow is provided with a proportional flow regulator, and the pressure in

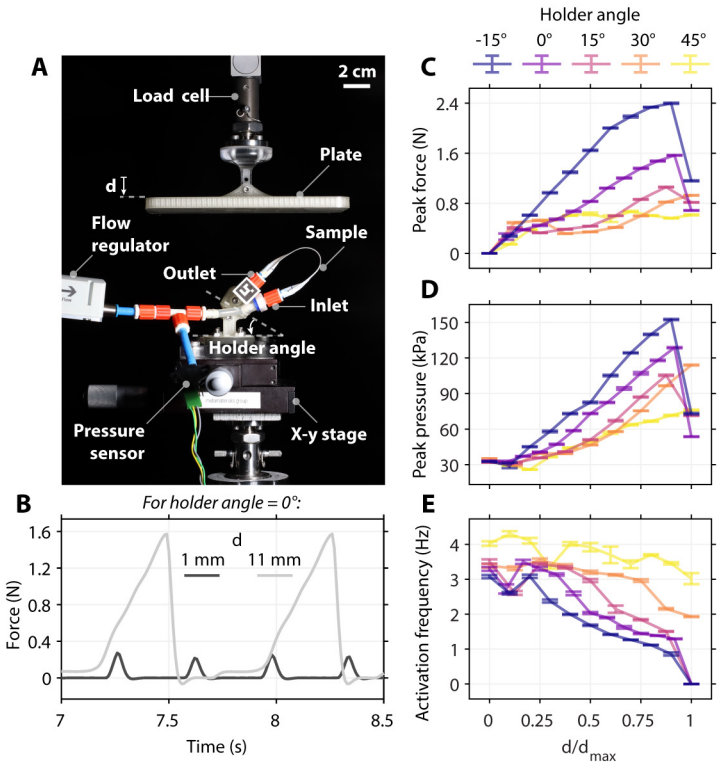

Figure 4.23
CONSTRAINED ACTUATION OF THE TPU POUCH ACTUATOR. (**A**) The experimental setup measures the force exerted by the actuator while oscillating against a fixed wall. (**B**) Example force profiles for a fixed holder angle (0°), for wall displacement d equal to 1 mm and 11 mm. (**C**) Peak force, (**D**) peak actuator pressure, and (**E**) oscillation frequency for five holder angle values, increasing the wall displacement.

the actuator is measured with a pressure sensor (Section 4.6.7) placed before the inlet of the actuator. An x-y stage is placed on the bottom clamp to align the actuator with the top plate.

When fixing the holder angle to 0° and the actuator in contact with the wall, we observe a tooth-shaped profile of the measured force in time; when the wall is closer to the actuator (for higher wall displacement d), amplitude of force increases and frequency decreases (Fig. 4.23B).

When scanning the entire domain of the wall displacement d, we observe an increase in peak force for increasing values of d, for five different values of the holder angle (Fig. 4.23C), with a maximum measured force of ~ 2.4 N. Likewise, the peak pressure inside the actuator increases with d (Fig. 4.23D), reaching ~ 150 kPa. This increase in peak force and

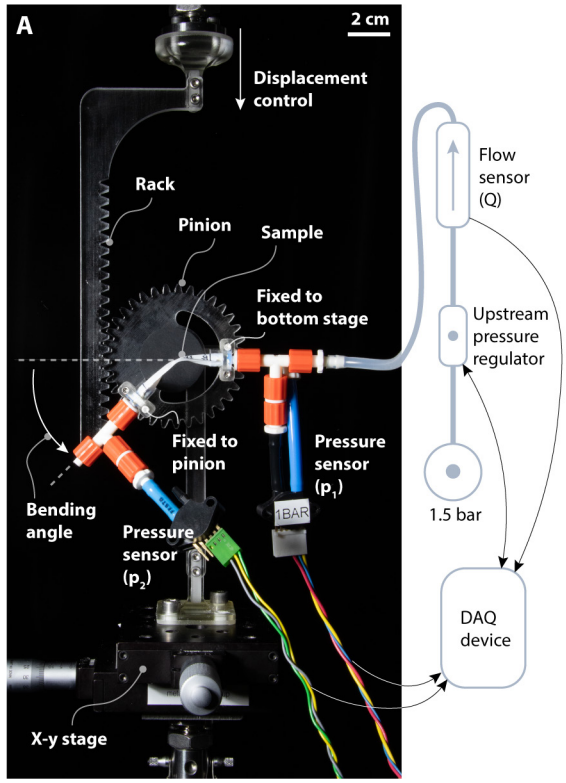

Figure 4.24
Continues to the right.
SETUP FOR EXPERIMENTS ON KINK BEHAVIOR UNDER BENDING AND PRESSURIZATION. (**A**) The experimental setup to control the bending angle and the upstream pressure of a tube while measuring the pressure drop over, and the flow through, the tube.

peak pressure is accompanied by a decrease in oscillation frequency (Fig. 4.23E). We do not observe oscillation (zero frequency) for holder angle −15°, 0°, and 15° at $d/d_{max} = 1$.

4.6.4 *Kink formation in thin tubes undergoing bending*

To investigate the behavior of the kink formation in thin tubes undergoing bending and pressurization and to understand the underlying differences between the specific tubes used throughout our study (silicone tubes and TPU pouches), we build a setup that involves two main parts (Fig. 4.24A).

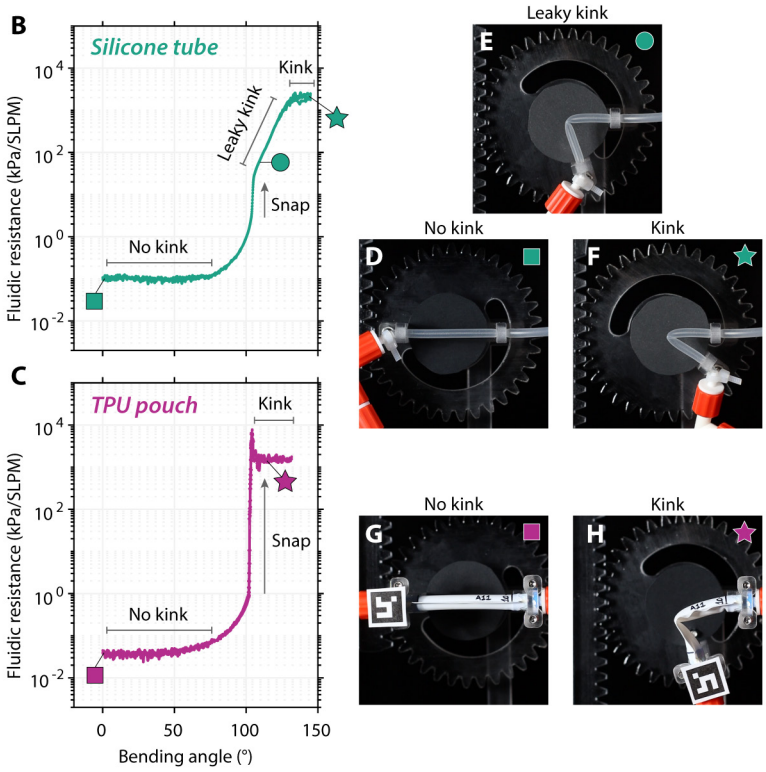

Figure 4.24
Continues from the left.
SETUP FOR EXPERIMENTS ON KINK BEHAVIOR UNDER BENDING AND PRESSURIZATION. Two example datasets for (**B**) the silicone tube sample and (**C**) the TPU pouch sample, where we fix the upstream pressure to 20 kPa, and we increase the bending angle in 1 minute. In both B and C, we overlay the results of three tests. In the case of the silicone tube, for increasing bending angle, after (**D**) an initial state with the absence of a kink, we observe (**E**) a snapping event to a leaky-link state, followed by (**F**) a fully-formed-kink state. In the case of the TPU pouch actuator, after (**G**) the no-kink state, the system directly snaps to (**H**) a fully-formed-kink state.

In the first part, to control the bending angle in a quasi-static fashion, we mount a 3D-printed rack on the top clamp of a tensile testing machine (details about the machine in Section 4.6.7), and a 3D-printed pinion on a bearing connected to the bottom clamp. In this way, controlling the displacement of the rack results in controlling the angle of the pinion. We place the sample on the setup, fixing the inlet side to the bottom stage, and the outlet side to the pinion, so that an imposed angle of the pinion results in an imposed angle between the inlet and the outlet. An

x-y stage mounted at the bottom guarantees alignment between the rack and the pinion. The setup is similar to the one used for the soft kink valves [48], although here we explicitly control the bending angle of the tube, instead of the linear distance between the inlet and the outlet.

In the second part, to control the upstream pressure in a quasi-static fashion, we connect the inlet of the sample to a proportional pressure regulator. The regulator is connected to a pressure supply of 1.5 bar. Note that, to guarantee that the desired upstream pressure is applied, we place a needle at the outlet of the tube (METCAL 918050-TE, 18GA 1/2"). The needle acts as a fluidic resistance, to impose the pressure drop needed for the regulator to set the upstream pressure. Between the pressure regulator and the inlet of the sample, we place a flow sensor to measure the airflow Q through the sample. Two pressure sensors are placed before and after the sample, to probe the upstream pressure p_1 and the downstream pressure p_2 (details on the sensors and regulators in Section 4.6.7).

We select a silicone tube sample with length 36 mm, inner diameter 2.5 mm, and thickness 0.4 mm, and a TPU pouch sample with length 36 mm and width 10 mm. This specific choice reflects the two kinds of tubes used throughout our study. We set the upstream pressure to 20 kPa, and we control the bending angle by linearly increasing the rack displacement from 0 mm to 88 mm for the silicone tube, and to 80 mm for the TPU pouch, in 1 minute. From the signals of p_1, p_2, and Q we extract the fluidic resistance as $(p_1 - p_2)/Q$.

In the case of the silicone tube (Fig. 4.24B), we observe low resistance (~ 0.1 kPa/SLPM) for low bending angle values, until ~ 80°, because no kink is present in the tube (Fig. 4.24D). At around 100°, the system snaps to a higher resistance state (~ 20 kPa/SLPM), because the kink suddenly forms (Fig. 4.24E). The kink is not fully closed, resulting in leakage through the kink; the resistance now increases exponentially with the bending angle ('leaky kink' regime in Figure 4.24B). Only for bending angles higher than ~ 130°, the kink is fully closed (Fig. 4.24F), with the output flow dropping to zero (plus sensor noise) ('kink' regime in Figure 4.24B).

For the case of the TPU pouch (Fig. 4.24C), we also observe an initial no-kink state (Fig. 4.24G). For increasing bending angle, the system shows a sudden snapping event at ~ 100°, with the kink fully forming (Fig. 4.24H). We don't observe an intermediate leaky-kink regime in this specific test on the TPU pouch.

We derive the phase spaces of both the silicone tube and the TPU pouch as the fluidic resistance function of upstream pressure and bending angle. We perform ten tests with the silicone tube, where we impose the upstream pressure (from 10 kPa to 100 kPa in increments of 10 kPa) and we sweep the bending angle (Fig. 4.25A). We reverse the loading

order by first imposing a bending angle and then sweeping the upstream pressure (Fig. 4.25B). These two experiments allow us to illustrate the phase space of the tube for both cases of loading order (Fig. 4.25C,D). We perform equivalent experiments for the TPU pouch but with a lower pressure limit since we observe the curves approaching asymptotes (Fig. 4.25E,F).

When we compare the phase spaces of the silicone tube (Fig. 4.25C,D) and of the TPU pouch (Fig. 4.25G,H), we notice some similarities. In both cases, increasing the upstream pressure leads to a reduction of the kink phase (Fig. 4.25C,G). This is due to the known effect of inhibition of the kink due to pressurization of the tube [48]. Moreover, increasing the imposed bending angle leads to kink formation in both cases (Fig. 4.25D,H).

Comparing the phase spaces, we also notice important differences. We observe a first difference at high upstream pressure values: the kink phase of the silicone tube disappears (Fig. 4.25C), while it is still present in the case of the TPU pouch (Fig. 4.25G). This difference also holds for low values of the imposed bending angle: the kink phase is not present in the case of the silicone tube (Fig. 4.25D), while it appears (for low pressures) in the case of the TPU pouch (Fig. 4.25H). Moreover, we see that in general, the silicone tube has a larger leaky kink phase compared to the TPU pouch. This is particularly evident at low pressure values, where it is practically absent for the TPU pouch, and it scans half of the angle domain for the silicone tube (Fig. 4.25C,G). In addition, for low pressure values, the kink of the TPU pouch appears at much lower values of bending angle than in the case of silicone tube (Fig. 4.25C,G). Finally, when the TPU pouch is first bent at high angle values and then pressurized, it cannot exit the kink phase when pressurized (Fig. 4.25H), while the silicone tube transitions to a leaky state (Fig. 4.25D).

Taken together, these observations lead us to the conclusion that the TPU pouch favors kink formation, and inhibits kink leakage, compared to the silicone tube, especially at low pressures. The ease of forming a kink and the reduced leakage directly result in the TPU pouch requiring dramatically lower input power than the silicone tube (approximately three orders of magnitude) to self-oscillate (Section 4.6.3).

4.6.5 *Robots analysis*

In this Section, we report additional results and calculations concerning our tethered and untethered robots. We report the analysis of *i)* the tethered robot stotting, *ii)* the untethered robot hopping, *iii)* the cost of transport of the untethered robot, *iv)* the untethered robot on irregular terrain, *v)* the tolerance of the implicit synchronization to imbalance

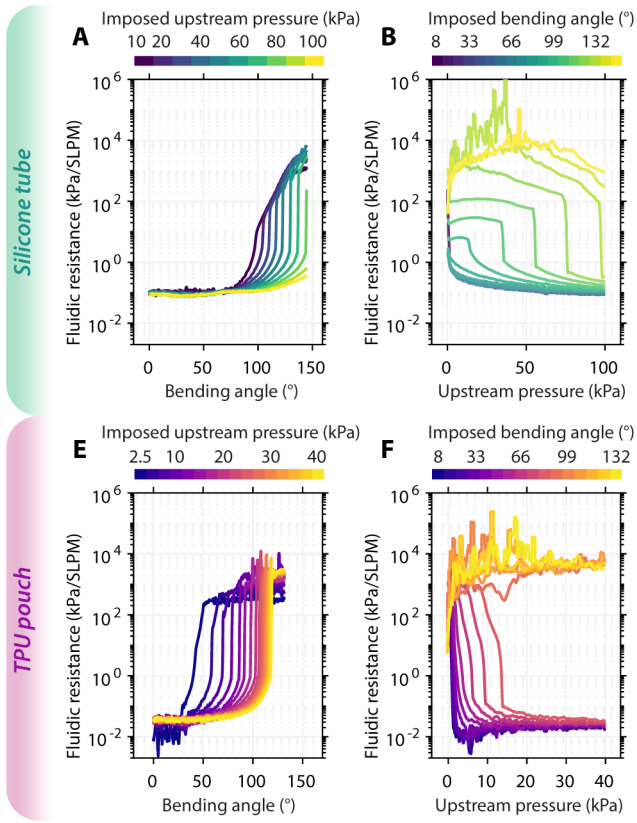

Figure 4.25
Continues to the right.
BEHAVIOR OF THE KINK UNDER BENDING AND PRESSURIZATION. (**A**, **E**) Fluidic resistance resulting from the quasi-static sweep of the bending angle, for different values of imposed upstream pressure (**A** silicone tube, **E** TPU pouch). (**B**, **F**) Fluidic resistance resulting from the quasi-static sweep of the upstream pressure for different values of imposed bending angle (**B** silicone tube, **F** TPU pouch).

between the inputs, and *vi)* the robots' speed performance compared with the state-of-the-art.

Tethered robot stotting

The tethered robot is connected to the pneumatic power source through a thin tube with inner diameter 2 mm, thickness 0.3 mm, and length 70 cm. When we apply a pressure $p_{in} = 1.7\,\text{bar} = 1.7 \times 10^5\,\text{Pa}$ at the tether alone, we measure a flow $Q_{in} \approx 28$ SLPM (Fig. 4.26A). We derive

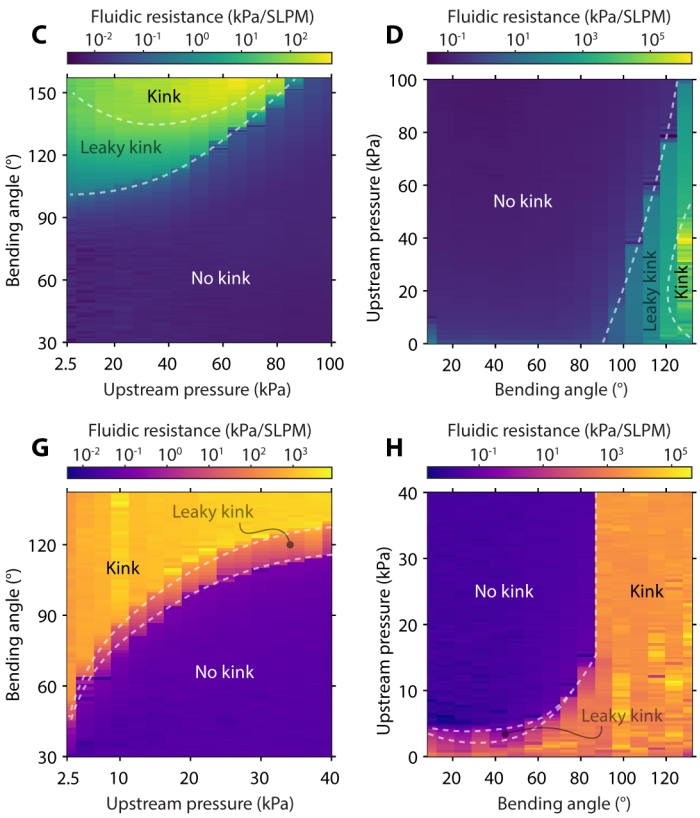

Figure 4.25
Continues from the left.
BEHAVIOR OF THE KINK UNDER BENDING AND PRESSURIZATION. (**C**, **G**) The resulting phase space when we fix the upstream pressure and sweep the bending angle (**C** silicone tube, **G** TPU pouch). (**D**, **H**) The resulting phase space when we fix the bending angle and sweep the upstream pressure (**D** silicone tube, **H** TPU pouch).

the flow in cubic meter per second by using Equation (4.33), obtaining $Q_{in} \approx 4.98 \times 10^{-4}\,m^3/s$.

We calculate the power provided to the robot via the tether:

$$P_{in} = p_{in} \cdot Q_{in}, \tag{4.26}$$

with $p_{in} = 1.7 \times 10^5$ Pa and $Q_{in} \approx 4.98 \times 10^{-4}\,m^3/s$, obtaining $P_{in} \approx 85\,W$. Each limb is therefore powered by ~ 21 W.

We perform six tests where we turn on the pressure at the tether, and we track the robot's location in time, observing repeatable behavior (Fig. 4.26B). We select the last 11 datapoints of the tracked location in time for each test, obtaining the steady-state speed for each test as the

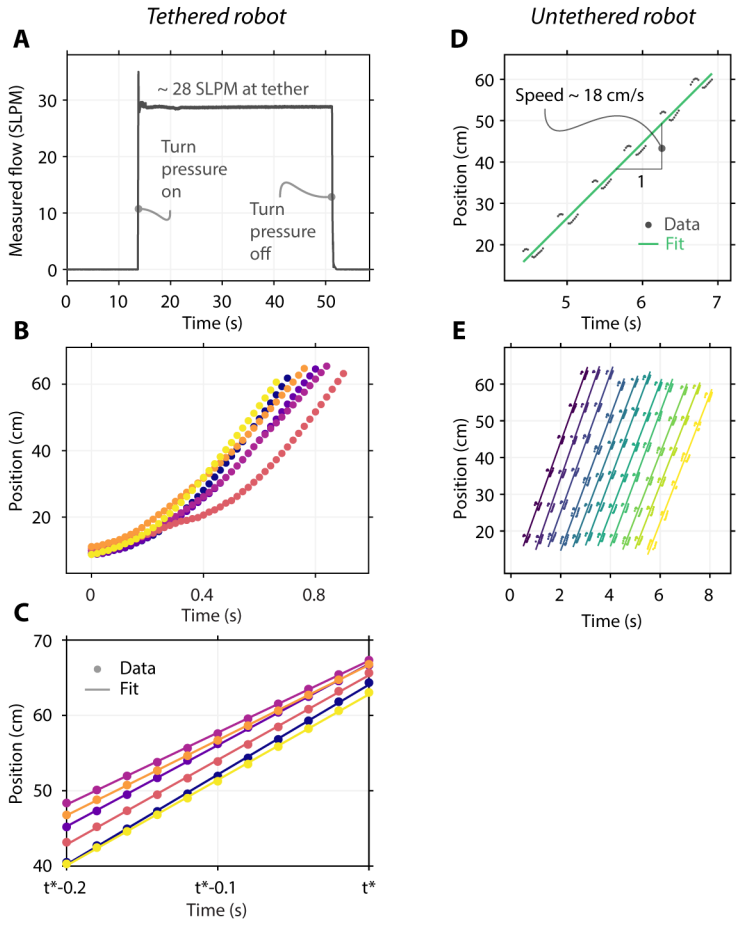

Figure 4.26
Continues to the right.
RUNNING ROBOTS. (**A**) We provide constant flow as input using a pressure source of 1.7 bar at the tether. (**B**) We let the robot run, measuring its location every 20 ms. (**C**) Last 11 datapoints of the location for each test (dots, each run with a different color), and linear fit (lines, each run with a different color). (**D**) One example dataset of the tracked position in time of the untethered robot (dots) and linear fit (line). (**E**) Eleven tests of the hopping untethered robot, offset by 0.5 s (each run with a different color).

slope of the linear fit (Fig. 4.26C). The average steady-state speed is 1.08 ± 0.09 m/s (30 ± 2.5 BL/s).

We calculated the Froude number FR of our robot according to:

$$\mathrm{FR} = \frac{v^2}{g \cdot h}, \tag{4.27}$$

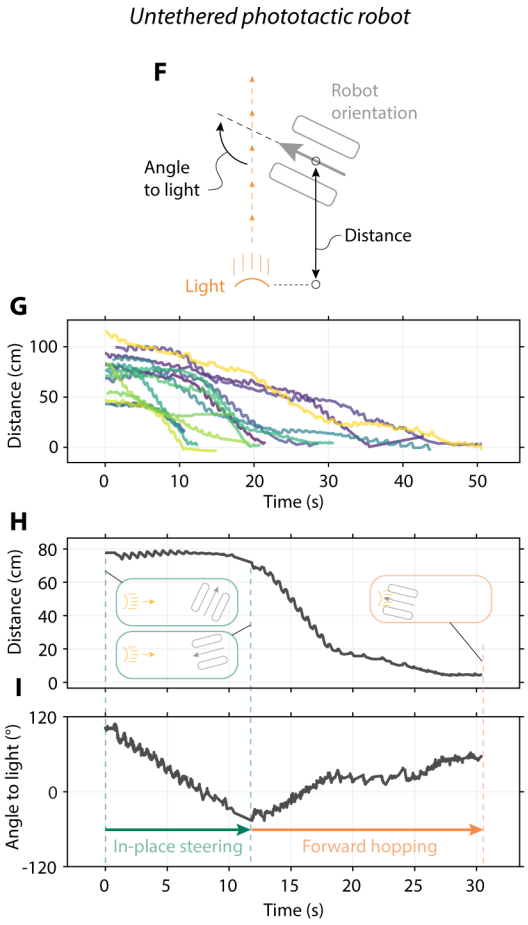

Figure 4.26
Continues from the left.
RUNNING ROBOTS. (**F**) Schematic showing the definitions used to describe the distance and orientation of the phototactic robot with respect to the light source. (**G**) The autonomous version of the untethered robot achieves phototaxis (87% success rate) among 15 runs (each run with a different color) as shown by the distance between the robot and the light decreasing in time. Detected (**H**) distance of the robot from the light and (**I**) its angle to the light during one example run.

with v the robot's speed, $g = 9.81\,\mathrm{m/s^2}$ gravity acceleration and h the hip joint height [168, 169]. The Froude number is useful when comparing locomoting gaits of robots or animals that widely differ in size, as it normalizes the speed in relation to the body size (hip joint height), similarly to the relative speed in body lengths per second. In our case,

the hip joint height is the distance between the rigid limb-connector and the ground, therefore, the height of the active soft limbs. This distance does vary in time as the limbs self-oscillate, so we consider the approximate average value throughout one oscillation cycle. In the case of the tethered robot, we have $v = 1.1\,\mathrm{m/s}$ and $h \approx 6\,\mathrm{mm} = 6 \times 10^{-3}\,\mathrm{m}$, obtaining FR ≈ 20.6.

We can predict the steady-state speed of the robot from the experimental results concerning an individual limb. Note that the following calculation is approximate, given the manufacturing differences between tubes and the approximate scaling factors. An individual limb with inner diameter 2.5 mm and asymmetry height 6 mm, when resonating, oscillates at ~ 155 Hz with a stroke of ~ 10 mm, resulting in an estimated single-limbed robot's speed of ~ 1.5 m/s (Fig. 4.14D-F). Note that the robot is equipped with actuators with inner diameter 2 mm, which are smaller than the 2.5 mm by a factor 0.8. We also designed the other parameters of the actuators on the robot (reference length and inlet-outlet distance) as scaled by a factor 0.8. Therefore we assume that the stroke in Figure 4.14E also scales by a factor 0.8. Importantly, in the final design we use shorter tubes on the robot, with length 18 mm (instead of the directly scaled length of ~ 28 mm), therefore we further scale the stroke by a factor 0.65. Moreover, the volume of air required for the kink to travel scales linearly with the length of the tube, as it approximates a cylinder with height being the distance covered by the kink along the tube. So, we estimate that the time required for the kink to travel also scales linearly with the length. Therefore, we scale the expected frequency by $1/0.65 = 1.54$, as we scaled the length of the tube by 0.65. Because we scaled the whole tube down by a factor 0.8, we scale the frequency by another factor 1.4 that we measured experimentally (Fig. 4.14A). This leads to an estimated speed (as stroke times frequency) of ~ 1.67 m/s, close to the measured speed of the real robot ($1.08\,\mathrm{m/s} \pm 0.09\,\mathrm{m/s}$). The difference might be due to losses in friction and overestimation of the effective stroke of the actuator when interacting with the ground.

Untethered robot hopping and swimming

One example dataset of the tracked position in time of the untethered robot shows that a linear fit captures the locomotion behavior (Fig. 4.26D). Among eleven runs, the robot locomotes in a repeatable fashion: to ease the visual understanding, in Figure 4.26E, we offset each dataset along the time-axis so that they are separated by 0.5 s. The robot hops with an average speed of $18.17 \pm 0.68\,\mathrm{cm/s}$ (1.93 ± 0.07 BL/s). We calculate the Froude number FR of the untethered robot using Eq. (4.27), with hip joint height $h \approx 20\,\mathrm{mm} = 2 \times 10^{-2}\,\mathrm{m}$, obtaining FR ≈ 0.16.

The phototactic version of the robot has two modifications. First, the on/off switch is removed. Second, each pump is connected to a transistor, which in turn is connected to a photoresistor (Section 4.6.6 and Fig. 4.37C for details on the connections). We place the robot with an initial angle and distance with respect to the light (Fig. 4.26F). With this relatively simple update involving the two photoresistors, the robot achieves phototaxis with 87% success rate among 15 runs (Fig. 4.26G). The robot steers in place because only one photoresistor detects light, as can be seen in Figure 4.26H,I by the distance not changing and the angle decreasing. The robot hops forward when both photoresistors detect light. Note that the forward hopping presents a slight drift, with the angle increasing while the distance from the light decreases (Fig. 4.26H,I). This might be due to differences between the two LDRs and the two transistors that, if large enough, result in different pressures in the actuators and, therefore, different forces exerted on the ground. Despite being synchronized in terms of phase, this asymmetry in the force amplitude might be the reason for the robot's drift. However, this drift is negligible in the forward-hopping behavior. Importantly, whenever the cumulative drift causes the robot to point in the 'wrong' direction, the robot autonomously compensates by steering in place, achieving successful phototaxis despite the manufacturing imperfections (Movie 4.7 for visual confirmation).

To quantify the phase shift between the two limbs in the swimming robot, we tether both limbs to two flow regulators set at 0.3 SLPM, and we measure pressure at the tethers with pressure sensors (Section 4.6.7). In addition to extrapolating the change in phase shift of the pressure signals due to the transition from ground to water (Fig. 4.7B), we also compute the average phase shift in steady-state conditions, for 50 oscillations of each limb, in both media. For the water case, we let the robot swim in the tank, and we consider pressure data of 50 oscillations of each limb when the robot is freely swimming, so we discard spurious data corresponding to the robot bumping against the walls of the tank. On the ground, we use pressure data of the robot hopping 50 times. We extrapolate the phase shift over these 50 limb oscillations, obtaining $0.6 \pm 4.2°$ for the ground case and $181.5 \pm 7.7°$ for the water case, confirming the stability of each gait in steady state.

Cost of transport of the untethered robot

We calculate the total cost of transport C_T of the untethered robot following:

$$C_T = \frac{E_{in}}{w \cdot d}, \tag{4.28}$$

with E_{in} the electrical input energy from the LiPo battery, w the weight of the robot, and d the distance traveled given the input energy [147]. We can rewrite equation (4.28) as function of input power P_{in} and robot's speed v:

$$C_T = \frac{P_{in}}{w \cdot v}. \tag{4.29}$$

The system operates with an electric power $P_{in} = 1.5\,W$. We calculate this value by visually measuring, with an ampere meter, the total current of $\sim 0.4\,A$ drawn by the hopping robot when connected to a $3.7\,V$ DC power supply. Considering $P_{in} = 2 \cdot P_{in}^{limb} \approx 1.5\,W$, robot's weight $w = 7.67 \times 10^{-2}\,kg \cdot 9.81\,m/s^2$, and speed $v = 1.817 \times 10^{-1}\,m/s$, we obtain:

$$C_T \approx 10.97. \tag{4.30}$$

Therefore, in terms of the total cost of transport, our robot is more efficient than a mouse and less efficient than a rat, according to the comprehensive list reported by Baines et al. [160].

We compare our tethered robot with the untethered robot in terms of speed and efficiency. The tethered robot moves fast with a high Froude number ~ 20.6, but inefficiently with high cost of transport ~ 1926. Our untethered robot, on the other hand, moves efficiently with a relatively low cost of transport ~ 11, but more slowly, with Froude number ~ 0.16.

Untethered robot locomoting on irregular terrain

To understand how the untethered robot negotiates irregular grounds, we started by placing a single bump in front of the untethered robot (Fig. 4.27). We ran multiple tests with bumps of width 200 mm, depth 16 mm and different heights ranging from 3 mm to 21 mm in increments of 3 mm.

We observed three distinct behaviors of the robot in response to the presence of the bump. The robot negotiates low bumps (up to around 9 mm) by hopping over it, as the soft limbs deform when interacting with the bump (Fig. 4.27A). The robot fails to overcome the bump for bump heights around 12 mm, as the front rigid limbs act as a pivot (Fig. 4.27B). Higher bumps act as an obstacle, and the robot avoids them as the limbs go out of synch, causing the robot to steer in place (Fig. 4.27C).

We ran five tests for each value of bump height for two cases of surface (flat metal and flat paper). For each test, we took note of the outcome of the negotiation. We observe that the success rate of negotiation drops as the bump height increases (Fig. 4.28A, purple). On a paper surface, the increase of friction between the limbs and the ground leads to higher success rates (Fig. 4.28B, purple). This is thanks to the front limbs

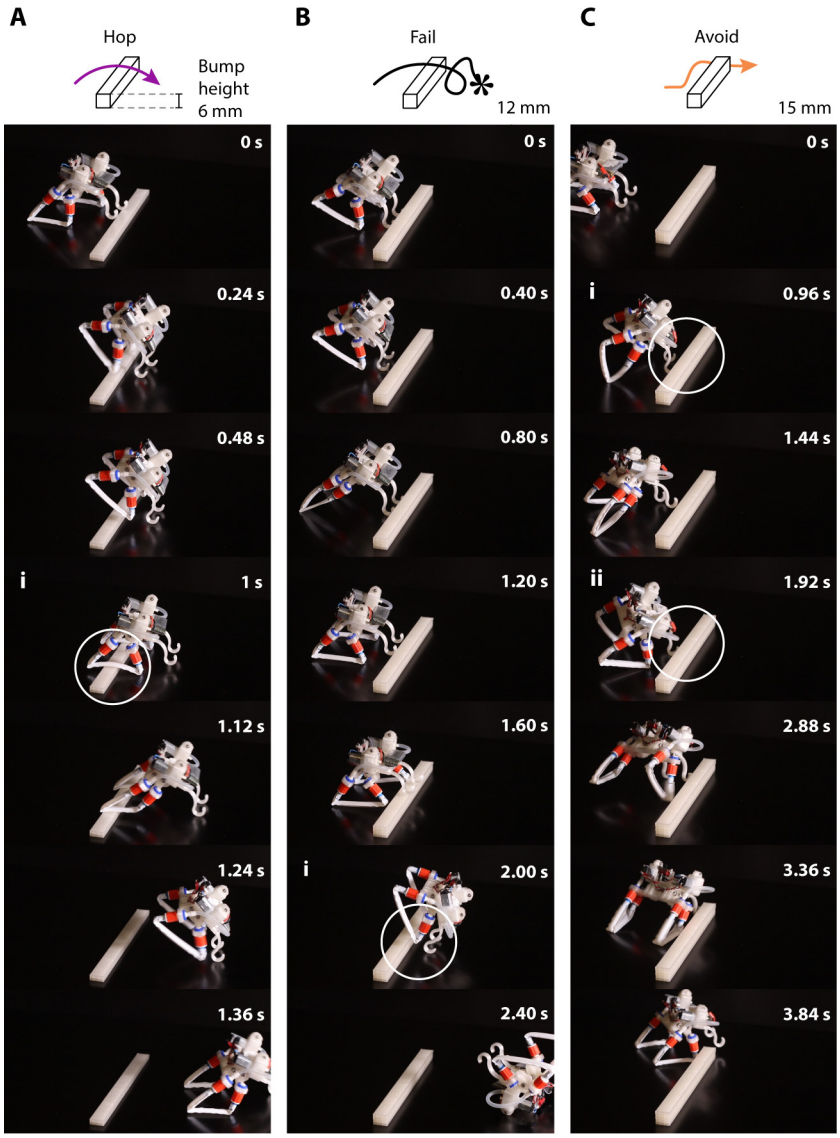

Figure 4.27
THE UNTETHERED ROBOT NEGOTIATING BUMPS. We observe three distinct reactions of the robot to a bump. (**A**) For bump height 6 mm, the robot hops over the bump, (i) with the limbs deforming when interacting with the bump. (**B**) For bump height 12 mm, the robot fails to negotiate the bump, (i) flipping around the front limbs. (**C**) For bump height 15 mm, the bump acts as an obstacle (experiment reported in Figure 4.7C). (i, ii) As the robot interacts with the obstacle, the limbs activate asynchronously, and the robot steers in place.

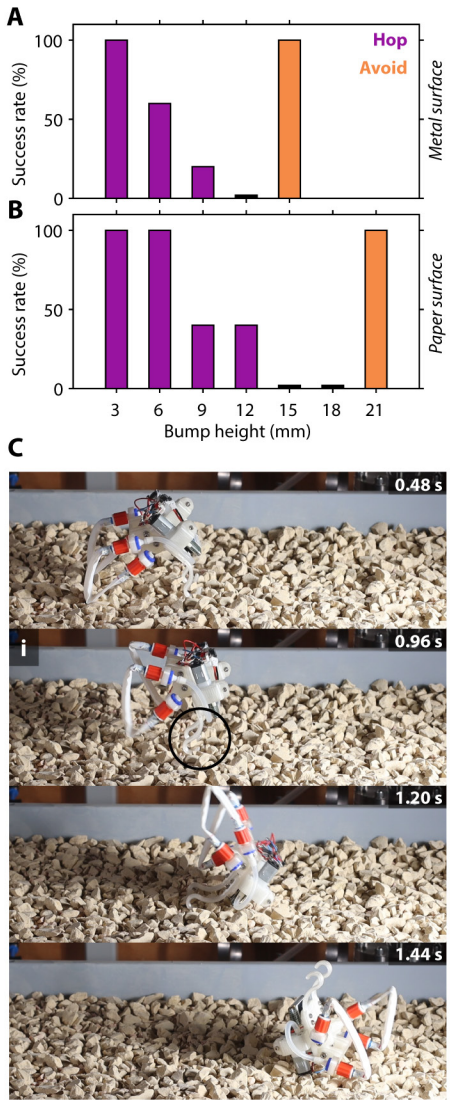

Figure 4.28
OUTCOME OF NEGOTIATION OF BUMPS AND INITIAL PERFORMANCE ON GRAVEL. (**A**) Success rate of bump negotiation on a flat metal surface, varying bump height (five tests for each value of bump height). (**B**) Success rate of negotiation on a paper surface. (**C**) When locomoting on granular terrain with granule size 8 mm-16 mm, the robot fails, (i) displaying the pivot-flipping behavior seen in Figure 4.27B.

elevating at larger heights, likely as a result of the higher forces exerted by the self-oscillating limbs due to the increased friction.

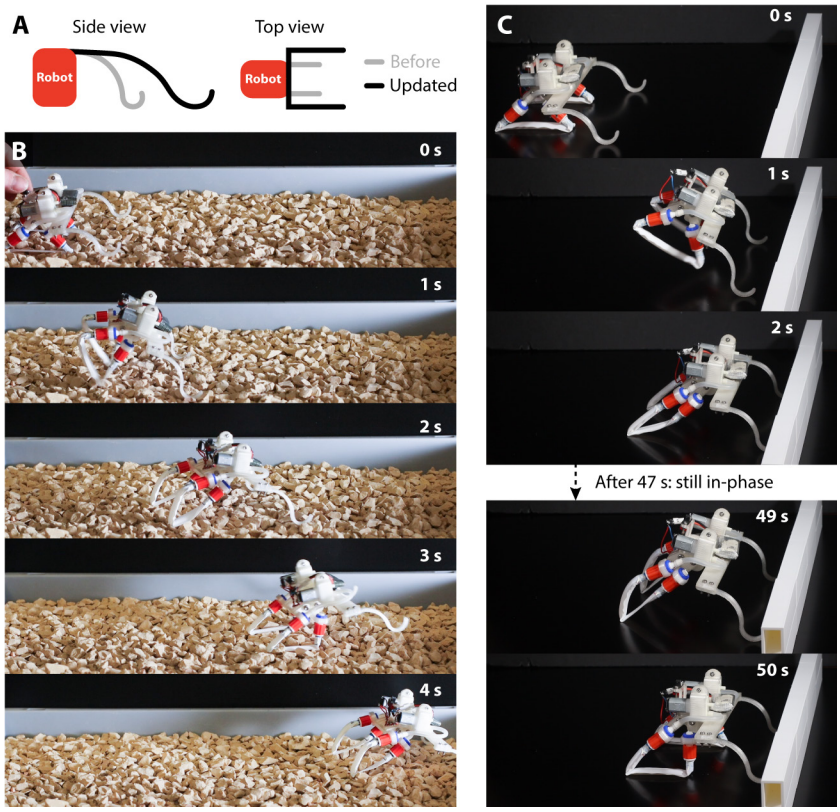

Figure 4.29
UPDATED DESIGN OF THE FRONT RIGID LIMBS RESULTS IN SUCCESSFUL LOCOMOTION ON GRANULAR TERRAIN. (**A**) Side view and top view of the robot (red) with the updated front rigid limbs (black) compared to the previous limbs (grey). The updated limbs are 15 mm longer and 105 mm wider. (**B**) The updated robot does not display the pivot-flipping issue seen in Figure 4.27 and successfully locomotes on a granular terrain with granule size 8 mm-16 mm. (**C**) The updated design diminishes the rotational motion of the robot, stabilizing the in-phase synchronization of the self-oscillating limbs and therefore preventing the obstacle avoidance behavior observed in Figure 4.27C.

With this understanding of how the robot deals with a single bump, we checked how it manages locomotion on an irregular, granular terrain with granules size between 8 mm and 16 mm (Stonewish Yellow 8-16mm, GAMMA). As shown in Figure 4.28C, the robot displays the same failure mode as in the single bump scenario, pivoting around the front rigid limbs. Considering that this whole-body flipping is the only failure mode we observed, we decided to re-design the front limbs to address the issue. We 3D-printed longer limbs (15 mm longer), and we placed them wider

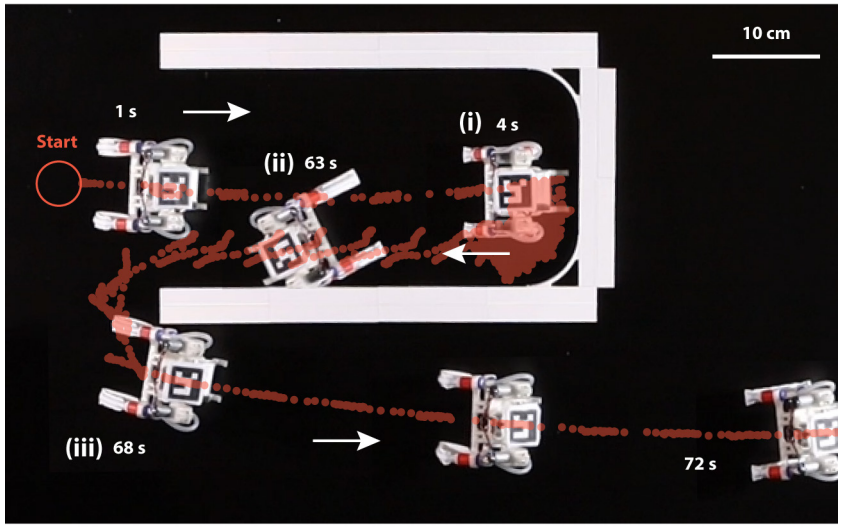

Figure 4.30
THE ROBOT AUTONOMOUSLY ESCAPES U-SHAPED OBSTRUCTIONS. When interacting with the walls, the robot randomly turns left or right, as shown in Figure 4.27C. (i) In this example test, the robot after 4 s interacts with the first wall. In the next ~ 60 s, the robot turns right and left multiple times, until it turns right twice in a row. (ii) The robot then hops straight. When the robot interacts with the bottom-left corner, the robot turns 180°. Note that this last interaction is particularly sensitive to the approach angle, as we observed the robot taking various random directions after interacting with corners (Movie 4.6).

on the body of the robot (105 mm wider) (Fig. 4.29A). The updated robot successfully locomotes on an uneven, granular terrain with granules size between 8 mm and 16 mm, with the limbs synchronizing in-phase (Fig. 4.29B). This updated design reduces the rotational motion of the robot, stabilizing the in-phase synchronization of the self-oscillating limbs. As seen in Figure 4.29C, this change in the body morphology removes the obstacle avoidance behavior that we previously observed in Figure 4.27C.

Tolerance of the implicit synchronization to imbalance between the inputs

To understand the tolerance of the synchronized behavior to differences in left and right inputs to the limbs, we focus on the untethered robot as the platform for the case study. To precisely control the variable inputs to each limb, we removed the pumps and battery, and we tethered each limb to a flow regulator (details on the fluidic setup in Section 4.6.7). We applied a constant input flow of 0.4 SLPM to the left limb, and we

varied the input flow to the right limb from 0.4 SLPM to 0.1 SLPM in intervals of 0.05 SLPM. For each of these cases, we measured the natural frequencies of the self-oscillating limbs when not interacting with the ground, and we then placed the robot in locomoting position on the ground.

In Figure 4.31A, we report the on-ground frequencies of the limbs as a function of the ratio of the two natural frequencies. We observe that up to natural frequencies ratio ~ 1.7, the two on-ground frequencies match (Fig. 4.31A), so their ratio is ~ 1 (Fig. 4.31B). Up to this value of the difference between the two inputs, the system is in a phase-lock state: the in-phase synchronization is stable (Fig. 4.31A,B, yellow highlight). For larger differences in inputs, the two limbs oscillate at different frequencies (Fig. 4.31A,B). We call this value the critical natural frequencies ratio (purple star in Figure 4.31B), as the synchronization tolerates a ratio of natural frequencies smaller than such value.

We repeated the same experiments while adding additional mass to the robot (Fig. 4.31C). We added weights of ~ 35 g and ~ 65 g. We discovered that, due to the added inertia, the critical ratio of natural frequencies increases (Fig. 4.31D). In other words, the system with mass ~ 98 g now synchronizes in-phase even if the natural frequency of the left limb is ~ 3.4 times the one of the right limb. This is because the two limbs are more strongly coupled, thanks to the increased downward force acting on them.

Robots' speed performance compared with the state-of-the-art

We frame the performance of our robots in the context of state-of-the-art soft robots. We gather data concerning the fastest tethered and untethered soft robots and classify them depending on their actuation and control mechanisms. We classify 'tethered' as any soft robot that is connected to the tether line, either for power or control. We call 'untethered' any soft robot that instead carries both power and control systems on board. Note that here, when we mention 'control', we slightly diverge from the classical mechatronics definition. We consider 'control' any mechanism that sequences the activation of robotic actuators so that a desired functionality, such as a walking gait, emerges. For example, classical control involves microcontrollers sending sequenced input signals to activate pumps or motors, and fluidic circuits generate these sequenced signals through the interaction of fluid flow or pressure and nonlinear mechanical elements, that imitate analog or digital electronic circuits [45].

Next, we divide the fast tethered robots into two categories. *i)* Soft robots that internally embody the actuation sequencing [44, 49, 50, 53,

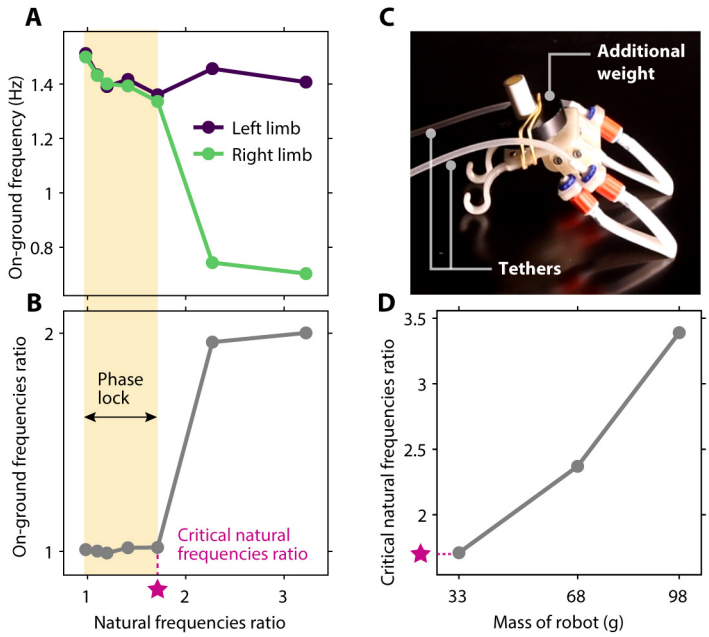

Figure 4.31

A LARGER BODY MASS INCREASES TOLERANCE TO IMBALANCE IN LEFT AND RIGHT INPUTS. We provide different values of inflow to the left and right limbs, and we measure both the two natural frequencies and the frequencies when the robot locomotes on the ground. (**A**) Frequencies of the left and right limbs when the robot locomotes on the ground as a function of the ratio of the natural frequencies of the two limbs. (**B**) Ratio of the on-ground frequencies of the limbs as a function of the ratio of the natural frequencies of the two limbs. The purple star indicates the critical natural frequencies ratio—higher values result in the limbs not activating in-phase, while lower values result in the phase lock of the limbs. (**C**) The robot has an additional weight placed on its back, and one tether connected to each limb. (**D**) The critical ratio of the natural frequencies increases for increasing mass of the robot.

55, 57, 58, 150] (blue dots in Figure 4.32 and in Figure 4.4I). *ii)* Soft robots that rely on external control apparatus for actuation sequencing (typically microcontrollers and software, or signal generators), spanning a wide range of physics underlying their actuation (among others, piezos, dielectric elastomers, shape-memory alloys, etc.) [157, 159, 170–182] (grey dots in Figure 4.32 and in Figure 4.4I).

By definition, the untethered robots carry their control systems on board. Therefore, technically, they all have internal actuation sequencing based either on microcontrollers or fluidic circuits. For this reason, we decide to classify them depending on the actuation technology: fluidic [39, 49, 55, 57, 58] (blue dots in Figure 4.33) compared to any other technol-

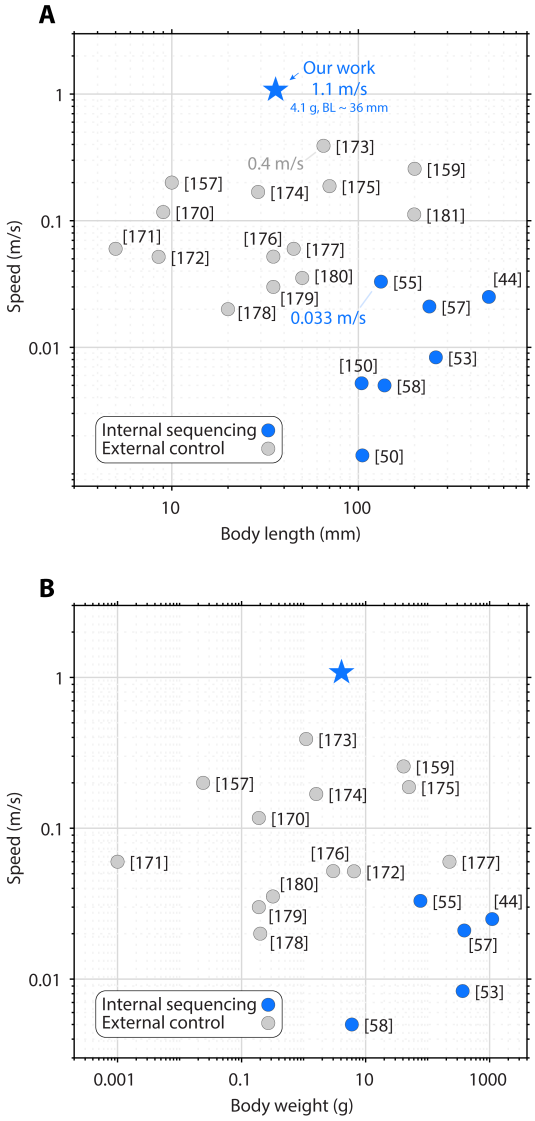

Figure 4.32

COMPARISON BETWEEN OUR TETHERED ROBOT AND COMPARABLE STATE-OF-THE-ART TETHERED SOFT ROBOTS. (**A**) Body length of some of the current fastest tethered soft robots versus their absolute speed. (**B**) Body weight of some of the current fastest tethered soft robots versus their absolute speed. The data points are reported in Table 4.1.

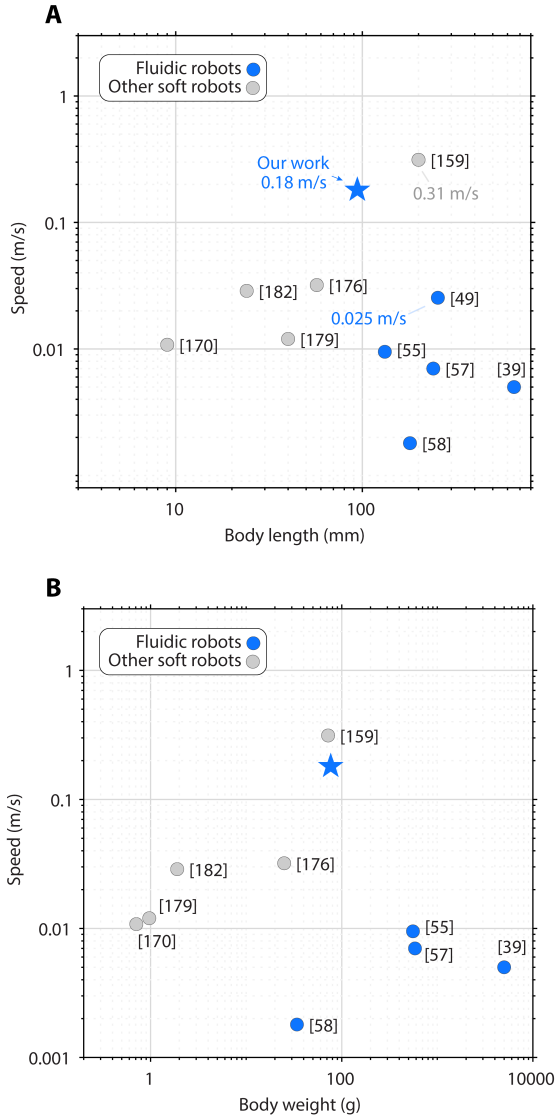

Figure 4.33
COMPARISON BETWEEN OUR UNTETHERED ROBOT AND COMPARABLE STATE-OF-THE-ART UNTETHERED SOFT ROBOTS. (**A**) Body length of some of the current fastest untethered soft robots versus their absolute speed. (**B**) Body weight of some of the current fastest untethered soft robots versus their absolute speed. The data points are reported in Table 4.2.

Table 4.1
STATE-OF-THE-ART TETHERED SOFT ROBOTS. Data of the tethered soft robots reported in Fig. 4.4I and in Figure 4.32 sorted for descending relative speed in body lengths per second (BL/s).

Reference	*Speed* (BL/s)	*Speed* (mm/s)	*Weight* (g)	*Length* (mm)
Our work	30	1080	4.09	36
[157]	20	200	0.024	10
[170]	13	117	0.19	9
[171]	12	60	0.001	5
[172]	6.1	51.83	6.5	8.5
[173]	6.01	390.5	1.1	65
[174]	5.82	168.6	1.6	29
[175]	2.68	187.5	50	70
[176]	1.5	52	3	35
[177]	1.33	60	225	45
[159]	1.28	257	41	200
[178]	1	20	0.2	20
[179]	0.85	30	0.19	35
[180]	0.7	35.3	0.32	50
[181]	0.56	112	n/a	199
[55]	0.25	33	76.5	132
[57]	0.09	21	390	240
[44]	0.05	25	1100	500
[150]	0.05	5.2	n/a	104
[53]	0.033	8.33	367	260
[58]	0.03	5	6	138
[50]	0.01	1.4	n/a	105

ogy (grey dots in Figure 4.33) [159, 170, 176, 179, 182]. The data gathered for this modest performance review are reported in Tables 4.1 and 4.2, sorted for descending relative speed (BL/s). Note that data strictly refers to robots that perform controlled, robust locomotion on a flat surface. We did not include robots locomoting on engineered surfaces or robots performing uncontrolled or unstable locomotion.

Table 4.2
STATE-OF-THE-ART UNTETHERED SOFT ROBOTS. Data of the untethered soft robots reported in Figure 4.33 sorted for descending relative speed (BL/s).

Reference	*Speed* (BL/s)	*Speed* (mm/s)	*Weight* (g)	*Length* (mm)
Our work	1.93	181	76.7	94
[159]	1.56	313	72	200
[170]	1.2	10.8	0.71	9
[182]	1.2	28.8	1.9	24
[176]	0.56	32	25	57
[179]	0.3	12	0.97	40
[49]	0.1	25.4	n/a	254
[55]	0.07	9.5	556	132
[57]	0.03	7	584	240
[58]	0.01	1.8	34	180
[39]	0.0076	5	5000	650

Our tethered robot is two orders of magnitude faster than state-of-the-art robots with internal actuation sequencing and runs at a speed comparable to other ultrafast soft robots that require external control signals to operate (Fig. 4.32 and Fig. 4.4I). Our untethered robot is one order of magnitude faster than state-of-the-art untethered fluidic robots and hops at a speed comparable to other untethered soft robots that implement any other soft technology (Fig. 4.33).

4.6.6 *Manufacturing*

The silicone tube actuator is composed of only two parts, a rigid holder and a soft tube, resulting in a three-step manufacturing procedure (Fig. 4.34). The thermoplastic polyurethane (TPU) pouch actuator, despite requiring more distinct parts than the silicone tube actuator, also follows a relatively straightforward manufacturing procedure (Fig. 4.35). The minimalistic design of the actuators results in a straightforward assembly of the tethered and untethered robots (Fig. 4.36). The STL files of all the 3D-printed components are available at our Zenodo repository [166] (DOI: 10.5281/zenodo.14055942).

Silicone tube actuator manufacturing

We 3D-print the rigid holder with the desired clamping distance d (Fig. 4.34A). Throughout our study, we chose the material VeroClear RGD810 (in combination with support material SUP705) using the Stratasys Eden260VS/VS PolyJet printer to achieve high precision. Similar results can be obtained with cheaper materials, e.g. PLA, using FDM 3D-printers such as the Ultimaker3. We press-fit the tube (internal diameter D_i and thickness t) in the left hole of the holder, and we mark the desired length l on the tube with a permanent marker (Fig. 4.34B). We press-fit the right side of the tube, making sure that the mark on the tube is aligned with the top surface of the holder (Fig. 4.34C). We estimate a total material cost of ~ 10 cents for an actuator with $l = 36\,mm$, $D_i = 2.5\,mm$, $t = 0.4\,mm$, and $d = 12\,mm$, with the holder printed in PLA (~ 2.7 cents) and the tube manufactured by Rubbermagazijn (~ 7.3 cents, since it is currently sold for 1.13 € per meter, and we require ~ 65 mm). A manufactured sample is shown in Figure 4.34D-F.

TPU pouch actuator manufacturing

We take two TPU sheets (Ecoseal™ Film T150 85A, Rivertex) with thickness 0.15 mm and two TPU Festo™ tubes (PUN-6X1-BL) with external diameter 6 mm and length 10 mm (Fig. 4.35A). We seal the two sheets along two parallel lines of length $L + 10\,mm$, with L the desired length of the actuator, placed at a distance W, which is the width of the actuator. Throughout our study, we used actuators with $L = 80\,mm$ and $W = 10\,mm$. To heat-seal the two sheets, we use the printer Felix Tec 4, with a custom-made head, previously used by our group for similar sealing purposes [91]. The head is equipped with a spherical nozzle that heats up and with an internal spring that allows for an even sealing of the sheets along the two lines. Note that we place a silicone mat between the bottom sheet and the print bed and oven paper between the top sheet and the hot head. The G-code sent to the printer is based on an Adobe Illustrator file containing the two parallel lines with desired length and distancing (red lines, Fig. 4.35B).

After sealing, we cut away the residual material using a scalpel. We insert the two TPU Festo™ tubes in the two open sides of the pouch, heat sealing the sheets to the tubes with a soldering iron at 300° so that the free length of the pouch tube is L (Fig. 4.35C). We insert Luer™ connectors (MLRL007-1 Male Luer to 500 Series Barb 3/32" 2.4 mm with Lock Ring FSLLR-3) in both Festo™ tubes to ease future connection in setups and robots (Fig. 4.35D). The actuator weights 0.88 g without the two Luer™ connectors, and 2.65 g with the connectors mounted. An

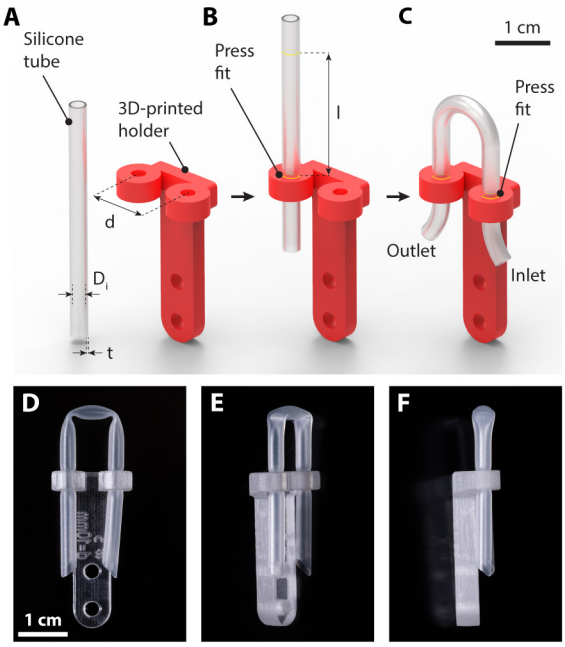

Figure 4.34
MANUFACTURING OF THE SILICONE TUBE ACTUATOR. The manufacturing of the silicone tube actuator follows a straightforward three-step procedure. After (**A**) printing the holder and marking the desired tube length, we (**B**) insert the tube in one end, sliding it until the first mark. (**C**) We then insert the other end. (**D**, **E**, **F**) Photographs of a manufactured sample.

example sample with L = 80 mm and W = 10 mm, when not pressurized, has low bending stiffness and doesn't display multistability (Fig. 4.35E). Finally, we connect the inlet to a holder that is fixed to a base with a 55° angle, and the outlet to a holder that is fixed in position on the base, but free to rotate (Fig. 4.35F).

Tethered robot manufacturing

The body of the tethered robot is monolithic, and it acts both as a structural element to keep the four limbs in place and as the fluidic circuit to couple the four limbs so that they synchronize in-phase. The top view of the body (Fig. 4.36A) displays the inner channels of diameter 3 mm and length ~ 15 mm that link the inlet to the four limbs connectors (Fig. 4.36B). We 3D-printed the body with the rigid material VeroClear RGD810, using the Stratasys Eden260VS/VS printer. We used the support material SUP705, which we then dissolved by placing the print in a 5%

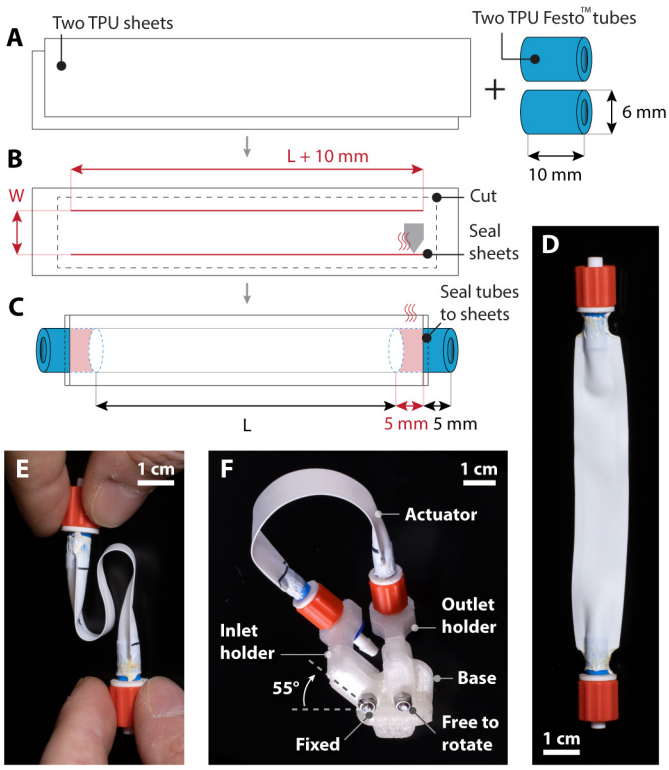

Figure 4.35
MANUFACTURING OF THE TPU POUCH ACTUATOR. The manufacturing of the TPU pouch actuator follows a three-step procedure. (**A**) We take two TPU sheets with thickness 0.15 mm and two TPU Festo™ with external diameter 6 mm and length 10 mm. (**B**) We heat-seal the two sheets along two lines of length L + 10 mm, at a distance *W* from each other (with L the desired length of the actuator and *W* the desired width) and we cut the residual material. (**C**) We insert the Festo™ tubes in both ends of the pouch (both entering 5 mm inside the pouch) and we seal the pouch to the tubes with a soldering iron. Photographs of a manufactured sample, (**D**, **E**) without and (**F**) with holder.

KOH solution in 20 L of water. However, one could 3D-print the robot's body with soft materials like TPU, given the monolithic design [52].

To reach the higher frequencies for the tethered robot, we implemented three design changes to the self-oscillating limb of Figure 4.1 and Figure 4.2. In Section 4.6.5, we explain in detail how such changes affect the frequency of the limbs and the speed of the robot. The three implemented changes are the following.

- We introduced an asymmetry in the design of the holder, placing the inlet higher than the outlet at a height h. We studied the influence of this parameter by testing samples with different asymmetry heights. In Figure 4.14D,E,F, we report the resulting frequency, stroke, and product between frequency and stroke for various heights. For the robot, we chose $h = 6\,\text{mm}$ as it maximizes the product of frequency and stroke of the limb and, therefore, the theoretical speed that the robot can reach.
- We scaled down the tube (including the inlet-outlet distance d and the asymmetry height h) by a factor ~ 0.8. The tube in Figure 4.1 and Figure 4.2 has inner diameter 2.5 mm and thickness 0.4 mm, while the updated tube has inner diameter 2 mm and thickness 0.3 mm. Scaling down the tube by a factor $k \approx 0.8$ decreases the volume of air required for the kink to travel forward in one cycle by a factor $k^3 \approx 0.512$. Therefore, in principle, this factor approximately doubles (1/0.512) the frequency of oscillation, as it halves the time required for the kink to travel, given the same inflow.
- In addition to adding asymmetry and scaling down the tube, we shortened it (so, shorter than the 0.8-scaled-down length) by another factor 0.65.

Each limb holder in the tethered robot is characterized by three parameters: the inclination α from the vertical, the distancing d, and the height h between the connector and the outlet holder (Fig. 4.36C). The holders of our robot are characterized by $\alpha = 30°$, $d = 7.8\,\text{mm}$, and $h = 3.9\,\text{mm}$. Each limb is mounted on the robot with a three-step process. The silicone tube (Rubbermagazijn) with inner diameter 2 mm and thickness 0.3 mm is fitted over the limb connector (Fig. 4.36D). A TPU Festo™ tube is fitted over the silicone tube to guarantee air-tightness (Fig. 4.36E). The silicone tube is press-fitted in the outlet holder, making sure that the actuator length is $l = 18\,\text{mm}$. The remaining part of the tube is inserted in the horizontal holder so that the output flow doesn't create horizontal thrust effects that would otherwise contribute to the locomoting behavior of the robot (Fig. 4.36F).

Untethered robot manufacturing

The design of the untethered robot is modular, as displayed by the exploded render in Figure 4.36G. Each module is 3D-printed in PLA (BASF Ultrafuse PLA filament, color neutral, 2.85 mm) with the Ultimaker3 printer. The main body (red) has a LEGO®-like design so that all the other modules can be inserted or screwed on it. We fix the pumps holder (orange) and the on/off switch holder (yellow) on top of the main body.

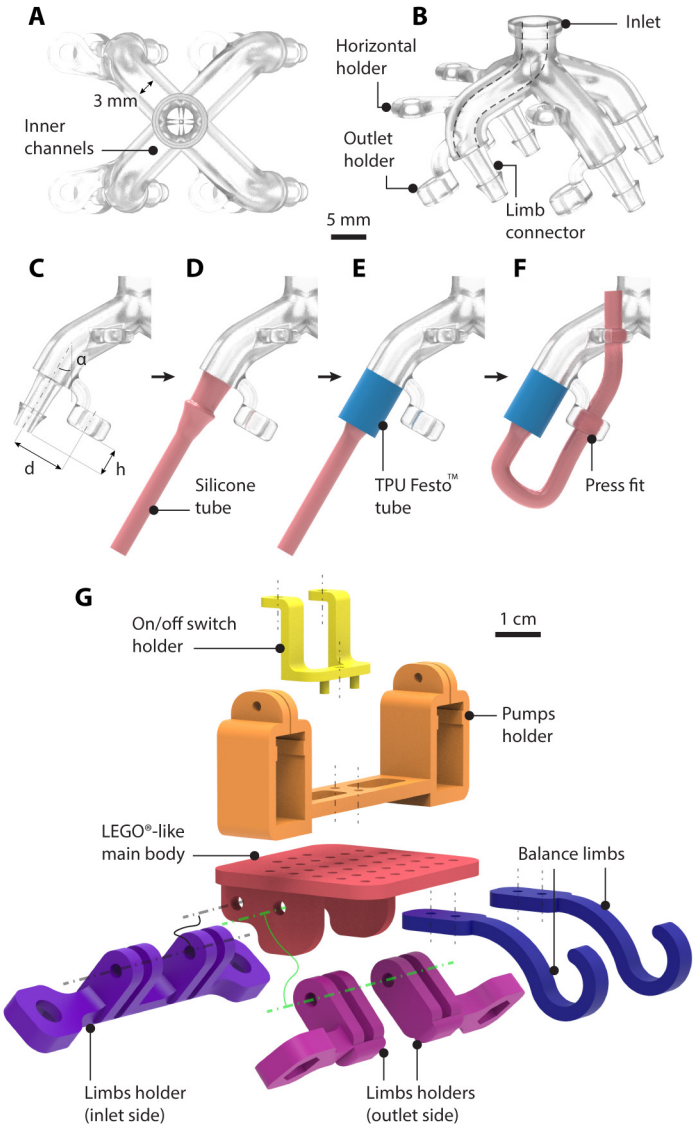

Figure 4.36
MANUFACTURING OF THE ROBOTS. (**A**, **B**) Renders of the body of the tethered robot. (**C**, **D**, **E**, **F**) The limbs are mounted on the robot with a three-step process. (**G**) Exploded render of the untethered robot.

On the bottom, we fix the limbs' inlets holder (purple) with a 55° angle to the main body surface, same as in the case of the single actuator in Figure 4.35F. We insert the outlet holders (pink) on the green axis without tightening the screws so they rotate freely. We insert the female

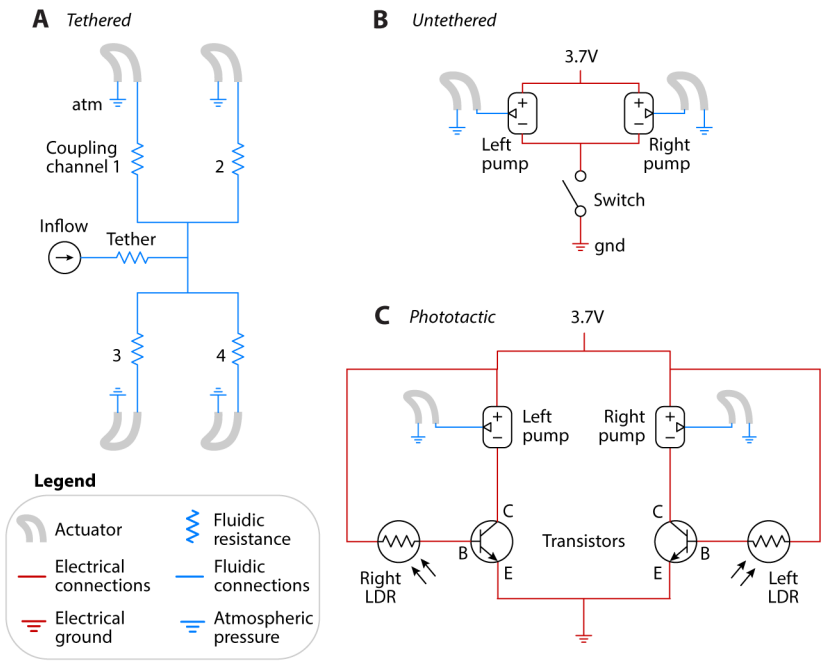

Figure 4.37
SCHEMATICS OF THE ROBOTS. (**A**) Schematic of the fluidic connections of the tethered robot. Schematic of the fluidic and electrical connections of (**B**) the untethered robot and of (**C**) the phototactic untethered robot.

Luer connector (FTLLB230-1 Thread Style Panel Mount 1/4-28 UNF to 200 series 1/8" 3.2 mm) on both inlet and outlet holders to interface with the actuator's male connector. Finally, the balance limbs (blue) are screwed into the front side of the robot.

We insert the two 3 V mini air pumps (YYPN20-3M) in the holder. Each pump is independently connected to a pouch actuator through a silicone tube (inner diameter 2 mm, length 80 mm). We place a LiPo battery (Carson 500608131 Lipo-Akku 3.7V 380mAh) using Velcro adhesives. The pumps are connected to the LiPo through an on/off switch. The phototactic version of the untethered robot is equipped with two photoresistors (GL5528 LDR) and two transistors (BC546A) to detect light and activate the associated pump.

The complete schematics of the fluidic and electrical connections for the tethered, untethered, and phototactic robots are reported in Figure 4.37, highlighting their minimalistic design.

4.6.7 *Experimental setups*

In this Section, we describe the setups that we use for our experimental campaigns. We use combinations of four setups, depending on the goal of each specific experiment. The *fluidic setup* is used wherever we need to control and acquire data of relevant fluidic quantities such as pressure and flow. The *high-speed recording setup* is used wherever imaging of the high-frequency oscillating actuator is needed. The *force-displacement setup* is used in the experiments where we constrain the actuator between fixed plates and where we control the bending angle of the tubes. The *torque-angle setup* is used in the experiments where we control the bending angle of the tubes while measuring the applied torque. The *ArUco tracking setup* is used whenever we are interested in the position and speed of the locomoting robots.

Fluidic setup

The fluidic setup, previously used by our group [53, 88] for similar acquisition purposes, is a custom-made acquisition setup based on the National Instruments IN USB-6212 input/output board and custom-made software. The setup has two analog output ports, which control the proportional pressure regulator (Festo^{TM} VEAB-L-26-D18-Q4-V1-1R1) and the proportional flow control valve (Festo^{TM} VEMD-L-6-14-20-D21-M5-1-R1-V4). Both regulators are connected to an upstream precision pressure regulator (Festo^{TM} LRP-1/4-10). The setup has multiple analog input ports, which read the voltage output of pressure and flow sensors. The pressure sensors used throughout our study are the NXP MPX5100DP to read up to 100 kPa, and the NXP MPX4250DP to read up to 250 kPa. To measure pressures in the actuators of the hopping untethered robot, we used more compact pressure sensors (Honeywell 015PDAA5). We used the airflow sensor Honeywell AWM5104 to measure mass flow up to 20 standard liter per minute (SLPM). The regulators and sensors are summarized in Table 4.3. To remove sensor noise, we filter all acquired raw data with the MATLAB function `smooth` with `loess` method. The connection between the various parts of the setup (regulators, sensors, and samples) is done using a combination of silicone tubes (Rubbermagazijn 2x4mm and 3x6mm), Festo^{TM} tubes (PUN-6X1-BL), and Luer^{TM} connectors (male-female, Luer-to-barb, and T connectors). The setup is equipped with digital output ports, used to trigger the high-speed recording setup and the force-displacement setup.

Table 4.3
COMPONENTS OF THE FLUIDIC DATA ACQUISITION SETUP. List of the components used to regulate and acquire the fluidic quantities (pressure and flow).

Part	*Model*
Input/output board	National Instruments IN USB-6212
Precision pressure regulator	Festo™ LRP-1/4-10
Pressure regulator	Festo™ VEAB-L-26-D18-Q4-V1-1R1
Proportional flow control valve	Festo™ VEMD-L-6-14-20-D21-M5-1-R1-V4
Pressure sensor 100 kPa	NXP MPX5100DP
Pressure sensor 250 kPa	NXP MPX4250DP
Pressure sensor 15	Honeywell 015PDAA5
Flowrate sensor 20 SLPM	Honeywell AWM5104

The airflow sensor that we used (Honeywell AWM5104) measures mass flowrate in Standard Liter Per Minute (SLPM). To obtain airflow values in SI units, we first convert to liters per minute [183]:

$$Q^{LPM} = Q^{SLPM} \cdot \frac{T_{gas}}{273.15} \cdot \frac{14.504}{p_{gas}}, \tag{4.31}$$

with the temperature of the gas $T_{gas} = 295.65\,K$ assumed to be equal to the temperature in our lab, and the pressure of the gas p_{gas} assumed atmospheric ($1.013\,25 \times 10^5$ Pa = 14.696), since in all our experiments the tubes vent to atmosphere. Therefore, we obtain the flow in liters per minute as:

$$Q^{LPM} = 1.068 \cdot Q^{SLPM}, \tag{4.32}$$

and we convert to cubic meters per second as:

$$Q^{m^3/s} = \frac{1.068}{6 \cdot 10^4} \cdot Q^{SLPM}. \tag{4.33}$$

Throughout the text, we reported flow rates in SLPM. In Table 4.4, we report the corresponding values in SI units obtained by applying Equation (4.33).

High-speed recording setup

The high-speed recording setup consists of the high-speed camera Phantom v4.2 with the lens Navitar f75mm / F1.8, together with the spotlight

Table 4.4
LOOKUP TABLE FOR THE CONVERSION OF UNITS OF FLOW RATE. Values of flow rate in standard liter per minute (SLPM), used throughout this Chapter, converted to cubic meter per second (m^3/s) using Eq. (4.33).

Flow rate (SLPM)	*Flow rate* (m^3/s)
0	0
0.05	8.9×10^{-7}
0.1	1.78×10^{-6}
0.3	5.34×10^{-6}
0.4	7.12×10^{-6}
3.8	6.76×10^{-5}
4	7.12×10^{-5}
6.5	1.16×10^{-4}
7.5	1.33×10^{-4}
11.4	2.03×10^{-4}
15	2.67×10^{-4}
16	2.85×10^{-4}
20	3.56×10^{-4}
28	4.98×10^{-4}

Nanlite FS-300B LED Bi-color. The camera is set to a 256x256 pixels resolution, acquisition rate of 4000 frames per second, and 10 µs shutter speed. The camera trigger is controlled through a digital signal sent by the fluidic setup to ensure synchronization of the acquisition of both setups. The camera continuously records frames and stores the ~ 0.5 s before the trigger instant.

Force-displacement setup

The force-displacement setup consists of the tensile-testing machine Instron 5965, equipped with a static load cell (Instron 2530-100N) with 100 N capacity. We used the machine in the displacement-control mode, storing force and displacement values. We trigger the starting of the test using a digital output from the fluidic setup, ensuring synchronization of the acquisition of both setups.

Torque-angle setup

The torque-angle setup consists of the microtorsion testing machine Instron MT1-E1 that controls the bending angle of the tube. At the same time, we measure the torque exerted on the tube with the load cell W-5510-T4 with torque capacity 0.225 N m.

ArUco tracking setup

To measure the speed of each of our robots, we place an ArUco marker vertically on top of the robot. We record the robot sideways at a rate of 50 fps with the camera Canon EOS 850D equipped with the lens Canon f50mm / F1.8. For each frame of the videos, we detect the pixels associated with the four corners of the ArUco marker. We define the position of the robot as the average of the four detected corners.

To detect the ArUco marker, we use the following algorithm. We begin by initializing the standard ArUco marker detection parameters (`cv2.aruco.DetectorParameters_create`) and accessing a predefined dictionary of ArUco markers that correspond to the printed ArUco on the robot (`aruco.DICT_4X4_100`). The script opens a video file using OpenCV's video capture capabilities (`cv2.VideoCapture`). This opens a VideoWriter object to save the processed output.

As the script processes the video, it iterates through each frame, cropping off the nonessential parts of the video. These are the areas that do not have an ArUco throughout the entire video. Note that this cropping procedure is important in the side view experiments as the robot sits on a wooden table. In fact, the table would interfere with the tracking since the texture of the wood can cause false positives in the ArUco detection. Each cropped frame is converted to the LAB color space to improve local contrast using Contrast-Limited Adaptive Histogram Equalization (`cv2.createCLAHE`). The script employs the `cv2.aruco.detectMarkers` function to detect the four corners of the ArUco markers in each frame. The script applies additional image processing methods if the initial detection attempt fails. For its second attempt, it uses a Gaussian blur (`cv2.GaussianBlur`) to soften the edges of the ArUco. For its third attempt, it employs a contrast and brightness adjustment to enhance the image using `cv2.convertScaleAbs`. In the rare cases where the four corners of the marker are not detected, the script is designed to use a fallback method, employing manual detection.

4.6.8 *Numerical analysis of the video recordings*

We develop an algorithm to extrapolate quantitative information from the high-speed videos of the actuator that self-oscillates at high frequency. The Python algorithm implements, for each frame `iFrame` of the recording, *detection* of the pixels associated with the edge of the tube and *clustering* of the outer and inner edges. Using MATLAB code, we extrapolate the *center line*, *local width*, *kink location along the center line*, *kink width*, *actuator's tip*, *kink distance*, and *kink velocity*.

Edge detection and clustering

SILICONE TUBE ACTUATOR. For each frame of the high-speed recordings, we increase the resolution using the command `cv.resize`. We convert to greyscale (`cv.cvtColor`) and apply Gaussian blur (`cv.gaussianBlur`). We perform Canny edge detection to identify pixels that separate bright areas from dark areas (`cv.Canny`). Note that an appropriate experimental setting of the lighting conditions, with the bright, illuminated tube on a dark background, is essential for successful edge detection.

For each frame, after edge detection, we have a matrix with `False` values, except for the `True` pixels associated with the edges. We cluster the inner and outer edges, obtaining two separate lists of points associated with the two edges. To do so, we visually define a vertical threshold `threshold_y` for the image to exclude pixels underneath it. We visually define a value `zero_x` representing a vertical line between the inlet and the outlet sides of the tube. We call the two sizes of the image `width` and `height`. We define the function `dfs` for a recursive depth-first search to find the connected pixels of the two clusters.

```
def dfs(x, y, visited, cluster):
    # Mark the pixel as visited and add it to the cluster
    visited.add((x, y))
    cluster.append((x, y))

    # Define the neighbors to visit
    neighbors = [(x-1, y), (x+1, y), (x, y-1), (x, y+1), (x-1, y-1), (x-1, y
     +1), (x+1, y-1), (x+1, y+1) ]

    # Visit each unvisited neighbor
    for nx, ny in neighbors:
        if (nx, ny) not in visited and 0 <= nx < width and 0 <= ny < height
     and ny <= start_y and table[ny, nx]:
            dfs(nx, ny, visited, cluster)
```

We find the starting index, and we run the recursive depth-first search.

```
# Find the starting y-coordinate for the outer edge
for y in range(0, height):
    for x in range(0, width):
```

```
        if table[y, x] > 0:
            start_y = y
            start_x = x

# Find the outer edge cluster
visited = set()
outer_edge = []
dfs(start_x, start_y, visited, outer_edge)
```

Note that, at this point, it is not ensured that the pixels associated with the edges are connected. Occasionally, we observe the pixels being disconnected at the kink, which is a challenging area of the image for the Canny detection algorithm. For this reason, we perform the recursive depth-first search twice, first starting from the left of the image, and then from the right. This ensures that the edges are complete. We then repeat this clustering process for the inner edge.

TPU POUCH ACTUATOR. The detection algorithm described so far proved challenging in the case of the TPU pouch actuator, given its sharper kinks. For this reason, we implemented a slightly different algorithm so that the edges of the TPU pouch actuator can reliably be detected for each frame. Similar to the previous algorithm, we open the video (`OpenCV`). With a loop, we process the data of the individual frames. For each frame, we perform a series of image-processing steps. We resize (using `cv.resize`) to enhance the number of pixels and therefore smooth the edges of the actuator. Second, we convert to grayscale (`cv.rgb2gray`) to highlight the difference between the black background and the white actuator. Third, we create a masking circle on the frame using `cv.circle`. This circle masks the actuator's holders, leaving only the TPU pouch tube visible. We combine this mask with the original image using `cv.bitwise_and` for selective focus on the TPU section of the actuator. Fourth, the script further processes each image by applying Gaussian blur (`cv.GaussianBlur`), smoothing the edges of the TPU and the background (specifically the kink, where the actuator folds onto itself). Fifth, we perform thresholding with `cv.threshold` to obtain a binary distinction between the TPU actuator and the background. Lastly, we use contour detection (`cv.findContours`) to extract the edge pixels between the TPU actuator and the background.

To cluster the inner and outer contours of the TPU pouch actuator, we employ the following custom algorithm to filter and connect the coordinates of the extracted contours. We start by identifying the start/end point of the outer contour as the coordinate with the maximum x and y positions. This is followed by a loop that sets the start as a reference and matches this with the closest coordinate in the list of all the contours. If the closest matching curve is within a set threshold (20 pixels), the algorithm connects the coordinates to form the curves, updates the newfound coordinate as a reference, and removes it from the initial list. Once

no connecting coordinate is found, the same is repeated for the inner contour. The end result is a set of two sequences of coordinates that represent the inner and outer edges of the TPU actuator in the image.

```
# Identify the initial reference point
ref_point_idx = np.argmax(np.sum(coords, axis=1))
ref_point = coords[ref_point_idx]

# Function to compute the distance between two points
def compute_distance(pt1, pt2):
    return np.sqrt(np.sum((pt1 - pt2)**2))

connected_coords_outer = [ref_point]
# Remove the reference point from the array
coords = np.delete(coords, ref_point_idx, axis=0)

while len(coords) > 0:
    # Compute distances from the current ref_point to all other points
    distances = np.array([compute_distance(ref_point, pt) for pt in coords])

    # Index of the closest point
    min_distance_idx = np.argmin(distances)

    # Check if the closest point is further than 20
    if distances[min_distance_idx] > 20:
        break

    # Append the new coordinate and update the reference point
    ref_point = coords[min_distance_idx]
    connected_coords_outer.append(ref_point)

    # Remove the selected coordinate from the array
    coords = np.delete(coords, min_distance_idx, axis=0)
    # select new reference point index
    ref_point_idx = np.argmax(np.sum(coords, axis=1))
```

Definition of quantities of interest

Through the edge detection and clustering process, we obtained the two lists of the outer and inner edges' history in time. Each element of the list is an array with the points associated with the edge at the instant of interest. For each of these arrays, we extrapolate the following quantities of interest, reported in Figure 4.38 for visual clarification.

- The *rearranged edges*, defined as the same points of the detected clusters, but rearranged using a single linkage hierarchical clustering with leaf order optimization.
- The cluster of the *closest points in the inner edge* to the outer edge, defined as the ensemble of points in the inner edge that minimize the Euclidean distance to each point in the outer edge.

- The *center line* cluster as the ensemble of the average values between each pair of points belonging to the ordered outer edge and their closest points in the inner edge.
- The *local width* of the tube, defined as the Euclidean distance between each pair of points, one belonging to the ordered outer edge and one to its closest point in the inner edge.
- The *center line reference frame*, defined as the cumulative sum of the distances between consecutive points belonging to the center line.
- The *actuator's tip*, defined as the point on the outer edge with the maximum y-coordinate in the x-y reference frame.
- The *kinks' location* along the center line, defined as the two local minima of the local width over the center line coordinate.
- The *kinks' position* in the x-y reference frame, defined as the points of the outer edge associated with the kinks' locations.
- The *kinks' width*, defined as the local width of the tube at the kinks' locations.

We then define the following, for each instant t_i.

- The *kink distance*, defined as the Euclidean distance between the kink position in the x-y plane at time t_i and the kink position in the x-y plane at the reference time t_{ref}, which is arbitrarily defined as the instant when the non-dominant kink changes role and becomes dominant.
- The *kink velocity*, defined as the finite difference of the kink distance. Note that the term *velocity* here is not used according to the classical meaning, since it expresses the rate of change of the distance of the kink and *not* the rate of change of its position.

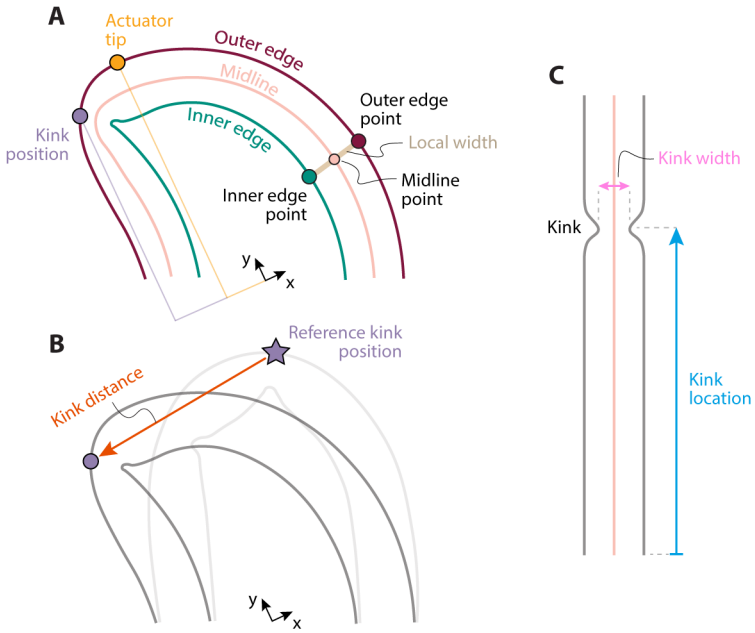

Figure 4.38
VISUAL REPRESENTATION OF THE DEFINED QUANTITIES. (**A**) Quantities that can be extrapolated from a single frame of the high-speed recordings. (**B**) Storing the kink position at an arbitrary reference instant allows us to define the kink distance. (**C**) Numerically unfolding the tube along the center line allows us to extrapolate the kink location and the kink width.

5

ACTIVE OSCILLATIONS OF ELASTIC MEMBRANES ARISING FROM THE COUPLING WITH A CATALYTIC REACTION

BASED ON: Comoretto, A., Gollob, S.D., Steur, E., Becker, K.P., Roche, E.T.*, and Overvelde, J.T.B.*, Active oscillations of elastic membranes arising from the coupling with a catalytic reaction, *in preparation*

ABSTRACT

Soft fluidic machines often rely on self-sustained oscillations to achieve tasks autonomously without the need for electronics or software. Typically, these oscillations arise from nonlinearity through complex mechanical geometries or from relatively involved fluidic circuitry, and are passive in that they require external power sources. Here we show that, by harnessing the coupling with a catalytic reaction, active oscillations can arise even in flat elastic membranes without the need for fluidic circuits or external power. We embed silver wire as the catalyst in a flat elastic membrane suspended over a pool filled with liquid hydrogen peroxide as fuel. When in contact with the catalyst, the fuel reacts, releasing gases. We observe an oscillation where the reaction activates and deactivates spontaneously, causing the membrane to cyclically inflate and deflate for hours consecutively. Using both experiments and a basic lumped-parameter model, we show that the oscillation arises from an interplay between capillarity of the catalyst, membrane stiffness, and venting resistance, which together give rise to negative feedback and separation of timescales. As such, we demonstrate an active oscillation in which the release of energy is directly coupled to internal states of the oscillation itself. By embodying energy within the oscillation dynamics, we expand the library of phenomena to achieve self-oscillation in autonomous soft fluidic machines.

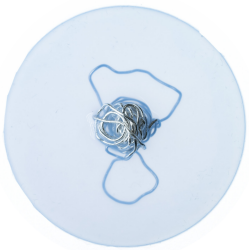

5.1 INTRODUCTION

Soft machines [26, 27] hold great promise for autonomous operation in real-world scenarios [63]. The intrinsic compliance of their body leads to features that distinguish them from rigid machines, including passive adaptability [64], safety when interacting with humans [30], and resilience to damage [31, 39].

Relatively recently, fluidic circuits [45] have been identified as a promising platform to increasingly move autonomy capabilities from a central electronic processor to the machine's soft body itself [184]. Fluidic circuits, consisting of networks of centimeter-scale tubings [46–48] and nonlinear inflatable elements [41, 85], allow for internal sequencing of complex motions given simple pneumatic inputs. For example, given a cyclic pressure drive, completely fluidic robots sequence leg movements to locomote [44], and even play Beethoven's Ninth Symphony [87].

To achieve such feats, these systems [44, 87] require an externally timed pressure signal. To increase the independence from external computers, fluidic circuits can generate their own timing signals internally, harnessing self-oscillation [185]. Given a constant input, self-oscillating fluidic circuits [50, 53–55, 58, 113, 131, 186] embedded in the machines' bodies generate oscillatory pressure signals, sequencing the actions of the machines. For example, fluidic relaxation oscillators obtain cyclic activation given a constant inflow of air through a single hysteretic valve that alternates between closed and open states [53, 131]. Fluidic ring oscillators [56], given constant input pressure, display a pressure wave that travels along a ring of three interconnected valves, sequentially inflating limbs of a locomoting robot [57]. In Chapter 4, self-oscillating limbs made of kinked elastic tubes display cyclic, asymmetric motions when connected to an external mini air pump, resulting in responsive, synchronized gaits across various environments [75].

In general, fluidic circuits rely on relatively complex mechanical designs to self-oscillate, where hysteretic behavior arises from microfluidic networks [125, 187] or macroscopic elements with highly nonlinear responses. For instance, as shown in Chapter 3, the relaxation oscillator [53, 131] relies on a shell with a non-monotonic pressure-volume curve and with a cut at its pole [88]; the ring oscillator [56] requires multiple bistable valves, each assembled from a bistable shell, an external soft capsule, and two kinking tubes [50]; the self-oscillating limb [75] in Chapter 4 leverages a thin elastic tube along which kink instabilities spontaneously form, travel, and disappear [153].

Moreover, these self-oscillations are passive, as they rely on an external pneumatic power supply, often in the form of a compressor. Even when untethered, the power supply is a separate component placed on board as bulky pumps and batteries [58, 75] or pressure canisters [57, 113].

To remove rigid parts associated with the power supply, researchers harnessed liquid fuels that rapidly decompose into gases when in contact with a catalyst [188, 189], directly inflating soft limbs [125]. However, even in this scenario, the energy system is external to the passive self-oscillating system, which still requires a relatively complex network of gates and microfluidic components [187] to generate cyclic activation.

Outside the realm of fluidics, self-shadowing effects are commonly used to obtain active oscillations. For instance, flat strips of photoactive polymers undergo self-oscillations when illuminated with constant light [190–192]. The stimulus-induced activation leads to shape changes that cause subsequent suppression of the stimulus, effectively resetting the system for the next cycle. Crucially, we observe that these systems are active, in that the access to the energy source is directly coupled to internal states of the oscillating dynamics, allowing relatively simple geometries (such as flat beams [156, 193]) to undergo out-of-equilibrium oscillations. This active oscillation architecture contrasts with typical fluidic self-oscillators, which instead require highly nonlinear mechanical elements, likely because of the passive oscillating system being decoupled from the active power-source system [57, 58, 75, 113, 125].

Here, we present a soft system to study active oscillations in the context of soft fluidic machines. We couple an elastic membrane with a catalytic chemical reaction of liquid hydrogen peroxide that decomposes into gases. We observe that this coupling alone leads to oscillations of the reaction, and thereby of the membrane, that self-sustain for hours consecutively. The pressure oscillation does not require membranes with complex, nonlinear responses, intricate fluidic circuits, or external power sources. Instead, we show with a lumped-parameter model that the dynamic inflation-deflation cycle arises from an interplay between the membrane stiffness, venting resistance, and capillarity of the catalyst. Importantly, in this system, the release of energy is directly coupled to internal states of the oscillation itself. Hence, we refer to this model system as an active fluidic oscillator that embodies energy [62].

5.2 AN ACTIVE FLUIDIC OSCILLATOR WITH EMBODIED ENERGY

To embody energy within a soft fluidic system, we look at liquid hydrogen peroxide due to its high energy density ~ 1.44 kJ/g, about one order of magnitude higher than common lithium-ion batteries [125]. When the fuel (concentration of 50 % hydrogen peroxide in water) comes into contact with a catalyst (99.9 % pure silver wire) (Fig. 5.1A), it rapidly decomposes the hydrogen peroxide into gas (water vapor and oxygen) and

residual liquid water (Fig. 5.1B), following the exothermic reaction [194]:

$$2\,H_2O_2\,(l) \longrightarrow 2\,H_2O\,(g,l) + O_2\,(g)\uparrow, \tag{5.1}$$

where we indicate the liquid phase (l), the gas phase (g), and the released heat ($\uparrow$). At atmospheric pressure, a small volume of liquid fuel decomposes into a large volume of gas, with a volume increase of ~ 250 times [195]. From just 6 mL of liquid fuel (Fig. 5.1A), we can obtain ~ 1.5 L of gas (Fig. 5.1B).

With the goal of coupling the reaction directly to a soft system, we embed the catalyst in an elastic silicone rubber membrane [Smooth-On Dragon Skin 10 (DS10)] (Fig. 5.1C). The catalyst is a silver wire with length 50 cm and diameter 0.5 mm, manually loosely packed in the shape of a sphere with a diameter of ~ 9 mm. The catalyst is only partially embedded in the membrane, with the majority of the surface area of the wire left exposed (Section 5.9). We then 3D-print a holder with a pool to contain 6 mL of fuel, with three ports to allow for the insertion of sensors (Fig. 5.1D). We clamp the membrane on top of this holder, with the catalyst facing the pool, obtaining a closed chamber between the membrane and the holder (Fig. 5.1E). Lastly, we seal the ports and connect a needle to one of them to have control over the amount of venting of the gases generated during the reaction (Fig. 5.1F). In Figure 5.2, we show a photograph of the complete experimental setup.

In an experiment where we fill the pool with fuel, we observe that this relatively simple system, composed of a flat membrane, a catalyst, fuel, and a needle (Fig. 5.1F), spontaneously self-sustains an active oscillation, visible from the membrane inflating and deflating cyclically (Fig. 5.1G).

5.3 THE ACTIVE OSCILLATION SELF-SUSTAINS FOR HOURS

To systematically study the active oscillation, we prepare the experiment by inflating the membrane so that the embedded catalyst is displaced away from the pool, as shown in Figure 5.2. This allows us to fill the pool with 6 mL of fuel without triggering the reaction. After this setup procedure, we start the experiment by venting the chamber to the atmosphere through the on/off valve (Fig. 5.2). We define the start of the experiment ($t = 0$ s) when the chamber reaches atmospheric pressure. After this initial manual interaction, we let the system evolve over time, without further external interactions.

In the first minutes of the experiment, we observe the start of an active oscillation of the membrane, which alternatively inflates and deflates between 10 kPa and 20 kPa at a frequency of ~ 0.06 Hz (Fig. 5.3A). Interestingly, after about 2 hours, the system is still oscillating, although

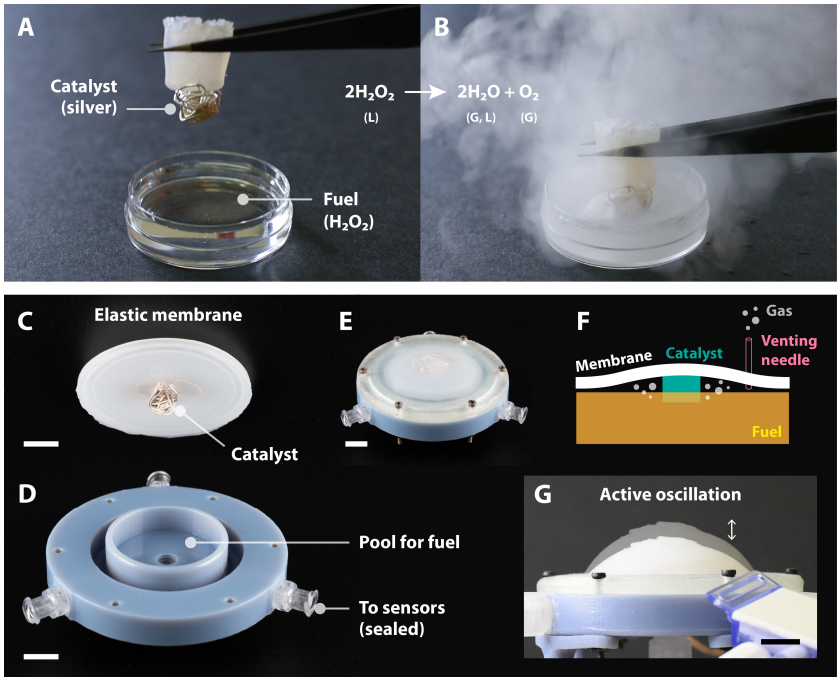

Figure 5.1
AN ACTIVE FLUIDIC OSCILLATOR WITH EMBODIED ENERGY. (**A**) When a catalyst (50 cm of silver wire with diameter 0.5 mm) enters in contact with fuel (liquid hydrogen peroxide, 50 % concentration in water), (**B**) the fuel rapidly decomposes releasing large amount of gas (water vapor and oxygen) and residual liquid water. The fuel stores large amount of energy (with energy density ~ 1.44 kJ/g, one order of magnitude higher than lithium-ion batteries [125]) which is released in gas, and hence can be directly used to power pneumatic systems. (**C**) We partially embed the silver wire catalyst in an elastic membrane, leaving the majority of the surface area of the wire exposed (Section 5.9). (**D**) The fuel (6 mL in volume) is contained in a 3D-printed rigid holder, with three ports for insertion of two temperature sensors and a pressure sensor. (**E**) The membrane is clamped on top of the fuel pool, with the catalyst facing the pool. (**F**) A needle is connected to one of the ports to vent the gases generated during the reaction. (**G**) The membrane exhibits an active oscillation, alternatively inflating and deflating as a consequence of the reaction activating and deactivating cyclically. Scale bars in C, D, E, and G are 1 cm.

at lower pressures (6-13 kPa) and with an order-of-magnitude lower frequency (~ 0.008 Hz) (Fig. 5.3B).

To better illustrate the active oscillation, we examine an individual oscillation cycle. In particular, we look at the evolution of pressure and catalyst temperature during the fourth cycle (Fig. 5.3C). We identify two

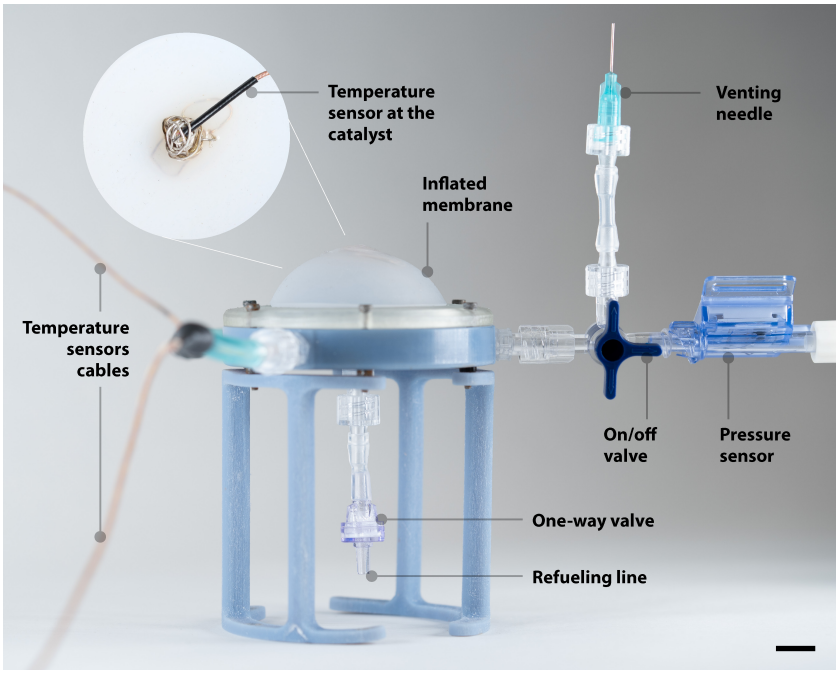

Figure 5.2
THE EXPERIMENTAL SETUP OF THE ACTIVE OSCILLATOR. We connect a one-way valve on the bottom of the chamber to allow initial injection of fuel into the pool. We insert two temperature sensors: one is attached directly to the catalyst, and the second measures the temperature of the air in the chamber. A needle allows for venting the reacted gases to atmosphere. A pressure sensor measures the pressure inside the chamber. We initially keep the membrane inflated (as shown in the photograph) using an on/off valve to prevent the catalyst from activating the reaction. Scale bar is 1 cm.

main phases within the period: a reaction phase followed by a discharge phase. At first, the catalyst temperature increases from 50 °C to 100 °C, indicating the activation of the catalytic reaction (Fig. 5.3C, orange line). This increase in temperature is accompanied by an increase in pressure to ~ 20 kPa (Fig. 5.3C, blue line), as a consequence of the gases generated during the reaction. Effectively, the system is transitioning from a state with cold catalyst and deflated membrane, and the catalyst dipped in the fuel (Fig. 5.3D(i)), to a state with hot catalyst and inflated membrane, and the catalyst displaced away from the fuel (Fig. 5.3D(ii)). While reacting, some of the generated gases leak into atmosphere through the venting needle. However, the faster timescale of the reaction dominates over the slower leakage, effectively causing an inflation of the membrane.

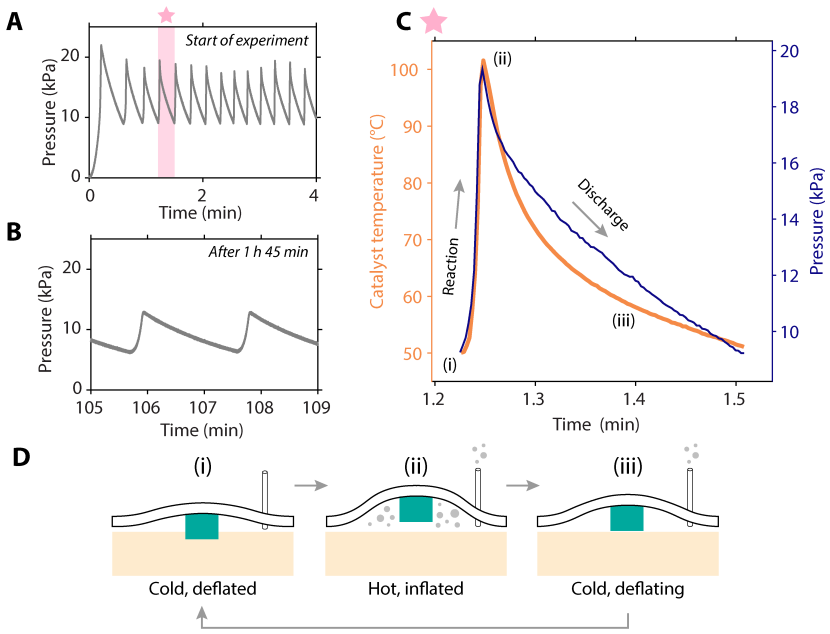

Figure 5.3
THE ACTIVE OSCILLATOR SPONTANEOUSLY INFLATES AND DEFLATES FOR HOURS. (**A**) Active oscillations occurring in the first 4 minutes of the experiment. (**B**) After 1 hour and 45 minutes, the active oscillation is still self-sustaining, with a lower frequency and at lower pressures. (**C**) The trends of the temperature at the catalyst and of the pressure during the fourth oscillation cycle highlight a reaction phase followed by a discharge phase. (**D**) Schematics of three stages of the oscillation cycle: (i) the catalyst is cold and dipped in the fuel, as the membrane is deflated, (ii) the catalyst is hot and the membrane is inflated as the reaction occurred, and (iii) the gases are venting to atmosphere, the membrane is deflating, and the catalyst is cooling down.

Eventually, when there is no more fuel attached to the catalyst, the reaction ends, and pressure stops increasing (Fig. 5.3C(ii)). This is the start of the discharge phase, in which the leakage through the venting needle takes over, causing pressure to drop (Fig. 5.3C, blue line). Simultaneously, the absence of contact with fuel allows the catalyst to cool down (Fig. 5.3C, orange line). As pressure decreases, the membrane deflates, causing the catalyst to displace toward the fuel (Fig. 5.3D(iii)). Once the catalyst comes into contact with the fuel, the reaction is activated again, and the cycle repeats.

In addition to this local profile of temperature and pressure within one cycle, the active oscillation also evolves globally over time. In the first ~ 13 min (Fig. 5.4, green star), the oscillation frequency increases

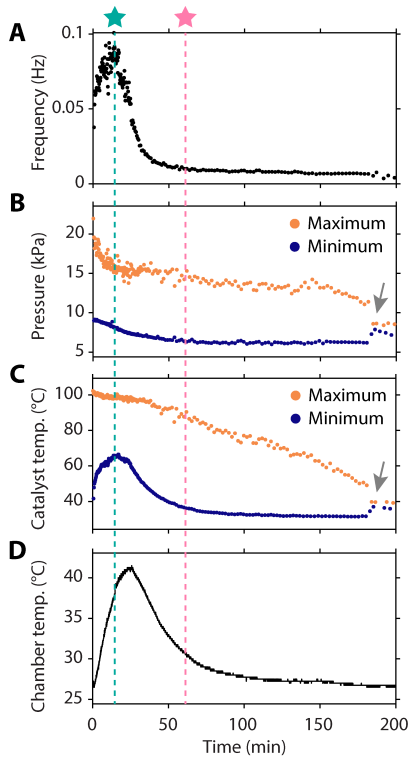

Figure 5.4
EVOLUTION IN TIME OF THE ACTIVE OSCILLATION. Evolution over more than 3 consecutive hours of (**A**) the oscillation frequency, (**B**) the maximum and minimum values of the oscillating pressure, (**C**) the maximum and minium values of the oscillating catalyst temperature, and (**D**) the temperature inside the chamber.

from 0.06 Hz to 0.1 Hz (Fig. 5.4A), with the maximum and minimum pressures marginally decreasing (Fig. 5.4B). Within this period, the maximum catalyst temperature stays at around 100 °C, the minimum catalyst temperature rises from 50 °C to 64 °C (Fig. 5.4C), and the chamber temperature goes from 26 °C to 37 °C (Fig. 5.4D).

After this initial phase, the frequency starts to drop. Approximately 1 h after the experiment started (Fig. 5.4, pink star), the frequency reaches a nearly steady-state[1] value of ~ 0.008 Hz (Fig. 5.4A). This is when the maximum and minimum values of the oscillating pressure and catalyst temperature reach a quasi-steady state as well (Fig. 5.4B,C). Excitingly, starting from 1 hour after the experiment begins, the system continues to

1 We refer to it as a nearly steady-state condition because the oscillation does not reach an actual steady state, as the fuel in the pool is being depleted in time.

oscillate in this nearly steady-state condition for 2 more hours. Eventually, at time 184 min, these large-amplitude oscillations cease to exist, and the system is attracted to a state with pressure ~ 8 kPa and catalyst temperature ~ 38 °C (Fig. 5.4B,C, gray arrows).

5.4 THE ACTIVE OSCILLATION IS AFFECTED BY PHYSICAL PARAMETERS

After observing these active oscillations that self-sustain for hours, we are interested in understanding the key factors that trigger and affect the active oscillation behavior. To start answering this question, we decide to vary two physical parameters that are relatively easy to tune experimentally: the membrane stiffness and the amount of venting resistance (Fig. 5.5).

When we equip the active oscillator with a stiffer membrane (DS20 with shore hardness 20 A instead of the previously used DS10 with shore hardness 10 A), we do not observe an oscillation anymore. Instead, we observe an initial increase in pressure (Fig. 5.5A, blue line), symptomatic of the reaction occurring. We then observe a gradual decrease in pressure, which converges within 15 min to a static condition with ~ 7.5 kPa. In contrast, the system with a softer membrane displays oscillations (Fig. 5.5A, orange line). From these observations, we learn that a stiffer membrane suppresses the active oscillation behavior and instead leads to a steady reaction that will occur until the hydrogen peroxide in contact with the catalyst is fully depleted.

Similarly to varying the membrane stiffness, we check how the system responds to variations in the venting resistance. We swap the 25 GA venting needle with a needle with larger diameter (16 GA), which offers lower resistance to airflow (Fig. 5.5B). We observe the membrane initially inflating to ~ 5 kPa, and then rapidly going back to atmospheric pressure (0 kPa). Although the reaction is occurring, the low venting resistance results in the generated gases venting to atmosphere without pressurizing the chamber. Since the membrane does not inflate, the catalyst stays dipped in the fuel, constantly inducing the reaction. Hence, the system stays at a state with zero pressure (Fig. 5.5B, blue line) and high catalyst temperature around 80°.

In general, we discovered that changes in two parameters (membrane stiffness and venting resistance) lead to substantially different output behaviors. These results suggest that the various parameters must be selected carefully to balance the competing influences of reaction rate, elastic forces, and leakage. In particular, a specific combination of low membrane stiffness and high venting resistance allows the active oscillation to self-sustain.

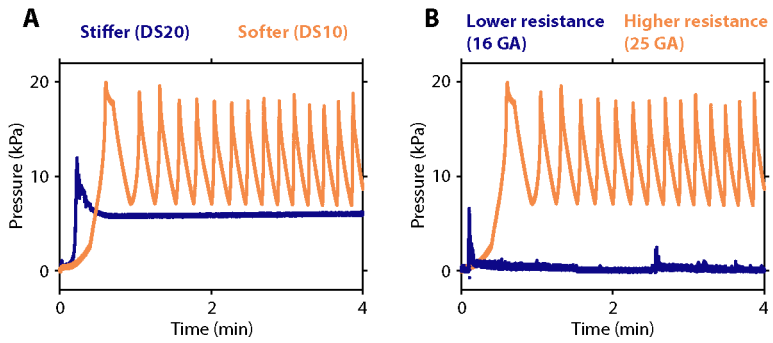

Figure 5.5
MEMBRANE STIFFNESS AND VENTING RESISTANCE CONTRIBUTE TO THE ACTIVE OSCILLATION. (**A**) Evolution in time of the pressure in the active oscillator with a stiffer membrane (Smooth-On DS20) (blue) and with a softer membrane (Smooth-On DS10) (orange), given the same venting resistance (25 GA needle). (**B**) Evolution in time of the pressure in the active oscillator with a lower venting resistance (16 GA needle) (blue) and with a higher venting resistance (25 GA needle) (orange), given the same membrane (Smooth-On DS10).

Now that we have learned that this combination of soft membrane and high resistance places the system in the oscillating regime, we still wonder what key principle is behind the active oscillation. In particular, we know that for an active oscillation to self-sustain, a form of negative feedback, switching nonlinearity, or delay within the internal states of the system is required [185]. What is the source of the active oscillation in our specific system?

5.5 A LUMPED-PARAMETER MODEL OF THE ACTIVE OSCILLATION

To understand the behavior of the active oscillation, and in particular to uncover the influence of various physical parameters, we develop a model that captures the physical contributions to the system (Fig. 5.6). The model aims to couple together the influence of the reaction kinetics, the effects of the catalyst temperature, the capillarity of the catalyst, the mechanics of deformation of the membrane, and the leakage through the venting resistor. The model, which lumps complex physical phenomena at play through relatively simple relationships, qualitatively captures the experimental results and offers insights into the key phenomena that enable the active oscillation to occur. Specifically, the model teaches us that the active oscillation arises from a time offset induced by the catalyst capillarity and negative feedback resulting from the catalyst being physically attached to the inflating membrane. Together, these

effects will also explain the reason why a stiffer membrane and a lower venting resistance suppress the active oscillation.

5.5.1 *Overview of the model*

In Figure 5.6A, we schematically represent the subsystems of the model related to both the catalytic reaction and the mechanics of the membrane. We model the main pool as a container with fuel, of which the mass is the sum of a reactable part $m^{R}_{f,p}$ (Fig. 5.6A, green) and an inert part $m^{I}_{f,p}$ (Fig. 5.6A, white). This distinction comes from using a fuel made of hydrogen peroxide diluted in water: when reacting, only the hydrogen peroxide will decompose, while water will not, being inert. Note that, although in Figure 5.6A we visually represent the fuel as two distinct mass parts, the fuel is a homogeneous mixture (a solution) of hydrogen peroxide and water.

We model the catalyst as another container of fuel, with a smaller fuel capacity compared to the larger pool (Fig. 5.6A, small rectangle). This assumption effectively implies that the catalyst can hold a certain amount of fuel through capillary forces. The mass of fuel in the catalyst is also modeled as the sum of a reactable part $m^{R}_{f,c}$ (Fig. 5.6A, purple) and an inert part $m^{I}_{f,c}$ (Fig. 5.6A, white). Through diffusion, fuel is allowed to be exchanged between the pool and the catalyst, with rate $\dot{m}_f$ (Fig. 5.6A, black arrows).

Crucially, we assume that only the reactable part of fuel *in the catalyst* decomposes into gases, with a reaction rate k_r (Fig. 5.6A, purple). We assume that the fuel in the pool does *not* react, motivated by the experimental observation that only hydrogen peroxide in close contact with the catalyst decomposes.

The inflating membrane does not operate in the snap-through [41] regime, that is, the pressure-displacement curve is fairly linear and does not present negative stiffness regions [196, 197] in the observed deformation range. Hence, we model the membrane as a linear spring with stiffness k_s attached to the catalyst, with a damper C_d in parallel (Fig. 5.6A, blue). The spring compresses vertically by a displacement u under the force F_p that originates from the pressurized gas inside the chamber.

The subsystem related to the internal gas is represented in Figure 5.6B. The reaction occurring at the catalyst generates gas products of mass m^{gen}_{g}, which increase the total mass of gas inside the chamber m_g, inducing pressurization p (Fig. 5.6B, purple). For simplicity, we assume that pressure does not affect the reaction rate. Intuitively, the gas that leaks through the venting needle (m^{leak}_{g}) decreases the mass of gas present in the chamber (Fig. 5.6B, black).

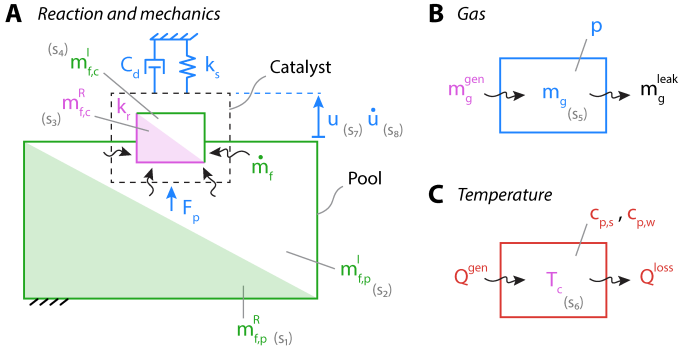

Figure 5.6
SCHEMATIC OF THE MODEL OF THE ACTIVE OSCILLATOR. (**A**) We model the pool as a volume of fuel with a reactable part $m_{f,p}^R$ (green) and an inert part $m_{f,p}^I$ (white). The catalyst is also modeled as a container of fuel, with a reactable part $m_{f,c}^R$ (purple) and an inert part $m_{f,c}^I$ (white). Through diffusion (black arrows), fuel exchanges between the pool and the catalyst, with rate $\dot{m}_f$. Only the reactable fuel in the catalyst is assumed to decompose into gases, with a reaction rate k_r. The catalyst is attached to a linear spring with stiffness k_s and a damper with damping coefficient C_d, and it moves upwards by a displacement u under the force F_p generated by the pressurized gas. (**B**) The mass of gas generated through the reaction m_g^{gen} increases the total mass of gas inside the chamber m_g, inducing pressurization p. The gas leaking through the venting needle m_g^{leak} reduces the mass of gas in the chamber. (**C**) The temperature of the catalyst T_c increases due to the heat Q^{gen} generated by the exothermic reaction, and decreases due to heat losses Q^{loss}, as a function of the catalyst mass m_c, the specific heat capacity of the silver catalyst $c_{p,s}$, the water mass $m_{f,c}^I$, and the specific heat capacity of water $c_{p,w}$. We denote the state variables as s_i, with $i = 1$ to 8.

The thermal subsystem of the model is shown in Figure 5.6C. Hydrogen peroxide decomposition is an exothermic reaction, which generates non-negligible heat [198]. We model this phenomenon by considering that the temperature of the catalyst T_c increases due to the heat Q^{gen} generated by the exothermic reaction. In addition, T_c decreases due to heat losses Q^{loss} as a function of the silver catalyst mass m_c, the silver specific heat capacity $c_{p,s}$, and the water specific heat capacity $c_{p,w}$. Importantly, we assume that the temperature of the catalyst affects the reaction rate $k_r = k_r(T_c)$, as the reaction is known to be temperature-dependent [199].

In total, our model represented in Figure 5.6 involves eight state variables: the mass of reactable fuel in the pool $m_{f,p}^R$, the mass of inert fuel in the pool $m_{f,p}^I$, the mass of reactable fuel in the catalyst $m_{f,c}^R$, the mass of inert fuel in the catalyst $m_{f,c}^I$, the mass of gas in the chamber m_g,

the temperature of the catalyst T_c, and the displacement u and velocity $\dot{u}$ of the membrane. The state vector becomes:

$$\mathbf{s}(t) = \begin{bmatrix} m^R_{f,p}(t) \\ m^I_{f,p}(t) \\ m^R_{f,c}(t) \\ m^I_{f,c}(t) \\ m_g(t) \\ T_c(t) \\ u(t) \\ \dot{u}(t) \end{bmatrix}. \tag{5.2}$$

In the following Sections, we introduce the key assumptions that lead to relationships between the state variables, resulting in a coupled system of eight ordinary differential equations (ODEs).

5.5.2 *Fuel mass balances*

In the pool, the total mass of fuel at time t is the sum of the reactable part and the inert part:

$$m_{f,p}(t) = m^R_{f,p}(t) + m^I_{f,p}(t). \tag{5.3}$$

Likewise, the total fuel mass attached to the catalyst through capillary forces is the sum of the reactable and inert parts:

$$m_{f,c}(t) = m^R_{f,c}(t) + m^I_{f,c}(t). \tag{5.4}$$

The reactable and inert mass of fuel in both the pool and the catalyst are state variables as in Eq. (5.2), so they can evolve in time. In later Sections, this will prove to be an important factor that drives the active oscillation behavior.

We define the concentration of reactable fuel in the pool $\alpha_p(t)$ as the ratio between the reactable mass and the total mass of fuel:

$$\alpha_p(t) = \frac{m^R_{f,p}(t)}{m_{f,p}(t)}. \tag{5.5}$$

At the beginning of the experiment, the concentration of reactable fuel in the pool[2] is $\alpha_{p_0} = 0.42$, and it will decrease over time as the reaction occurs.

2 We measure the actual value of the initial fuel concentration by weighing with a chemical mass balance (of 0.1 mg precision) a known volume of 1 mL of fuel measured with a precision pipette, and accounting for density of water ~ 1 g/mL and density of hydrogen peroxide ~ 1.4 g/mL. The value $\alpha_{p_0} = 0.42$ differs from the theoretical 0.5 of the manufactured 50% hydrogen peroxide, probably because of the spontaneous decomposition that occurred when storing the product in the lab between 2022 and 2024.

Likewise, we define the concentration of reactable fuel in the catalyst $\alpha_c(t)$ as the ratio between the reactable mass and the total mass (when the total mass is positive):

$$\alpha_c(t) = \begin{cases} 0 & \text{if } m_{f,c}(t) = 0, \\ \frac{m^R_{f,c}(t)}{m_{f,c}(t)} & \text{if } m_{f,c}(t) > 0. \end{cases} \tag{5.6}$$

5.5.3 *Surface area of contact between catalyst and fuel*

The contact between the moving catalyst and the fuel in the pool is a crucial element that affects the diffusion of fuel to the catalyst. During the experiment, the catalyst moves up and down, and at the same time, the height of the pool decreases as the reaction occurs: both affect the surface area of contact at time t.

We start by accounting for the total volume of fuel in the pool decreasing over time. The change in total volume of fuel in the pool since the start of the experiment $\Delta V_{f,p}(t)$ depends on the current concentration of fuel $\alpha_p(t)$ at time t, which affects the current fuel density:

$$\Delta V_{f,p}(t) = V_{f,p_0} - \frac{m_{f,p}(t)}{\rho_{H_2O_2} \cdot \alpha_p(t) + \rho_{H_2O} \cdot (1 - \alpha_p(t))}, \tag{5.7}$$

with $V_{f,p_0} = 6\,\text{mL}$ the initial volume of fuel in the pool, $\rho_{H_2O_2} = 1.45 \times 10^3\,\text{kg/m}^3$ the density of hydrogen peroxide, and $\rho_{H_2O} = 1 \times 10^3\,\text{kg/m}^3$ the density of water. This decrease in volume since the start of the experiment results in a reduced height of fuel in the pool $\Delta u_{f,p}(t)$. Knowing that the fuel pool is a cylindrical container, we get:

$$\Delta u_{f,p}(t) = \frac{\Delta V_{f,p}(t)}{r_p^2 \pi}, \tag{5.8}$$

with $r_p = 15.451\,\text{mm}$ the radius of the cylindrical pool.

To model the surface area of the contact between the catalyst and the fuel, we idealize the catalyst as a cylinder with radius r_c and height h_c. At $t = t_0$, the catalyst is at zero displacement u_0, and is assumed to be fully dipped in the pool. When the bottom of the catalyst is above the height of the pool ($u(t) > h_c - \Delta u_{f,p}(t)$), the contact area is zero. When the bottom of the catalyst is dipped underneath the pool surface, the portion of the cylinder underneath the pool surface contributes to the contact area:

$$A_s(t) = \begin{cases} 0 & \text{if } u(t) > h_c - \Delta u_{f,p}(t), \\ r_c^2\pi + 2\pi r_c \cdot \left(h_c - u(t) - \Delta u_{f,p}(t)\right) & \text{if } u(t) \le h_c - \Delta u_{f,p}(t), \end{cases}$$

(5.9)

in which we account for the decrease in the fuel height $\Delta u_{f,p}(t)$.

5.5.4 *Diffusion of fuel between catalyst and pool*

When the catalyst is in contact with the fuel in the pool, the fuel transfers from the pool onto the catalyst through capillary action, which we model in a simplified fashion as a diffusion process. We assume that the diffusion is a function of just the amount of fuel present in the catalyst, and not the amount of fuel in the pool, as the mass of fuel in the pool is much larger than the mass of fuel that can be present in the catalyst. The expected rate of fuel mass entering the catalyst through diffusion at time t is a function of the coefficient of diffusion C_f^{diff} and the contact surface area $A_s(t)$, and it is zero when the mass of fuel in the catalyst reaches the maximum mass value $m_{f,c}^{max}$ that can be held by the catalyst through capillary forces:

$$\dot{m}_{f,c}^{diff}(t) = C_f^{diff} \cdot A_s(t) \cdot (m_{f,c}^{max} - m_{f,c}(t)). \tag{5.10}$$

The maximum fuel mass in the catalyst $m_{f,c}^{max}$ is obtained from the assumed maximum fuel volume that can be held by the catalyst $V_{f,c}^{max}$ through capillary forces and the initial fuel concentration α_{p_0}:

$$m_{f,c}^{max} = V_{f,c}^{max} \cdot \left(\rho_{H_2O_2} \cdot \alpha_{p_0} + \rho_{H_2O} \cdot (1 - \alpha_{p_0})\right). \tag{5.11}$$

Of the total expected rate of fuel mass in Eq. (5.10), we distinguish between the diffusion of the reactable and inert parts. We model the reactable fuel flow rate from the pool entering the catalyst by accounting for the baseline capillary term, function of the pool concentration $\alpha_p(t)$, and for a factor that compensates for differences in concentration between the fuel present in the catalyst and in the pool:

$$\dot{m}_{f,c}^{R,diff}(t) = \dot{m}_{f,c}^{diff}(t) \cdot \alpha_p(t) + C_f^{diff} \cdot A_s(t) \cdot m_{f,c}^{max} \cdot (\alpha_p(t) - \alpha_c(t)). \tag{5.12}$$

To reach the expected total fuel flow rate, we define the inert fuel flow rate as the difference between the expected (Eq. (5.10)) and the reactable (Eq. (5.12)) rates:

$$\dot{m}_{f,c}^{I,diff}(t) = \dot{m}_{f,c}^{diff}(t) - \dot{m}_{f,c}^{R,diff}(t). \tag{5.13}$$

5.5.5 *Gas produced from the reaction*

We assume that the mass of hydrogen peroxide attached to the silver catalyst $m_{f,c}^{R}$ decomposes into only gas mass m_g^{gen} (water vapor and

oxygen gas) without any residual liquid water. In reality, only some of the generated water evaporates due to the high temperatures around 100 °C and some stays in liquid form; however, it is not obvious to quantify the amount of residual liquid water, so we neglect this contribution and we assume all water evaporates for simplicity. The hydrogen peroxide decomposition has been described as a first-order catalytic reaction [200]:

$$\dot{m}_g^{gen}(t) = k_r(T_c(t)) \cdot m_{f,c}^R(t). \tag{5.14}$$

This reaction is known to be temperature-dependent, where the rate k_r at which the reaction occurs is exponentially higher for higher temperatures T_c following the Arrhenius equation [199]. As we are aiming for a qualitative, yet informative, description of the overall coupled system, for simplicity, we assume the reaction rate to be linearly increasing with the catalyst temperature T_c:

$$k_r(T_c(t)) = k_{r_0} + C_r \cdot (T_c(t) - T_0), \tag{5.15}$$

with T_0 the ambient temperature, k_{r_0} the baseline reaction rate at ambient temperature, and C_r the reaction constant, that is the slope of the reaction rate function of catalyst temperature.

5.5.6 *Pressure and gas leakage*

While the reaction occurs and gases are being generated inside the chamber, at the same time, gas leaks through the venting needle, inducing a gas mass loss:

$$\dot{m}_g^{leak}(t) = \frac{p(t)}{R_l}, \tag{5.16}$$

with $p(t)$ the pressure inside the chamber and R_l a constant that represents the fluidic resistance of the venting needle. The pressure inside the chamber at time t is a function of the total mass of gas $m_g(t)$, under the assumption of ideal gas:

$$p(t) = \frac{m_g(t)}{M_g} \cdot \frac{R \cdot T_0}{V_{ch}}, \tag{5.17}$$

where M_g is the molar mass of the reacted gas, $R = 8.314\,\mathrm{J\,mol/K}$ is the gas constant, and $V_{ch} = 24 \times 10^{-6}\,\mathrm{m^3}$ is the volume of the chamber, which we assume to be constant for simplicity, despite it actually varying in the order of magnitude of 1 mL in experiments, as the membrane deforms when pressurized. We calculate $M_g = 0.022\,667\,\mathrm{kg/mol}$ as the molar mass of water vapor and oxygen mixture at a ratio of 2:1 moles,

based on the simplifying assumption that the product of the reaction is only gas (without liquid water), and based on the 2:1 molar ratio of the decomposition in Eq. (5.1). The gas mass balance (Fig. 5.6B) becomes:

$$\dot{m}_g(t) = \dot{m}_g^{gen}(t) - \dot{m}_g^{leak}(t). \tag{5.18}$$

5.5.7 *Thermal balance*

The catalytic reaction generates heat as a function of the heat of decomposition of the exothermic reaction $H_{dec} = 2884.5\,kJ/kg$ [198] and the rate of generation of gas:

$$\dot{Q}^{gen}(t) = H_{dec} \cdot \dot{m}_g^{gen}(t). \tag{5.19}$$

Simultaneously, the catalyst dissipates heat as a function of its temperature:

$$\dot{Q}^{loss}(t) = C_{loss} \cdot (T_c(t) - T_0), \tag{5.20}$$

with C_{loss} the heat loss coefficient.

The effective heat capacity of the catalyst $M_C(t)$ sees contributions from the silver mass m_c and the residual mass of water present on the catalyst $m_{f,c}^I(t)$:

$$M_C(t) = m_c \cdot c_{p,s} + m_{f,c}^I(t) \cdot c_{p,w}, \tag{5.21}$$

with $c_{p,s} = 235\,J/(kg\,°C)$ the specific heat capacity of silver and $c_{p,w} = 4200\,J/(kg\,°C)$ the specific heat capacity of water. The temperature dynamics (Fig. 5.6C) follow:

$$\dot{T}_c(t) = \frac{\dot{Q}^{gen}(t) - \dot{Q}^{loss}(t)}{M_C(t)}. \tag{5.22}$$

5.5.8 *Mechanics of the membrane*

We idealize the membrane as a vertical linear spring connected to the catalyst, with a damper in parallel to account for dissipative forces such as friction and other viscous effects (Fig. 5.6A, blue). We model the pressurization of the membrane as a force applied to the spring, which is proportional to the internal pressure in the chamber $p(t)$ and the surface area of the membrane A_m:

$$F_p(t) = A_m \cdot p(t). \tag{5.23}$$

The dynamics of the catalyst attached to the spring follow Newton's second law:

$$m_c \cdot \ddot{u}(t) = -k_s \cdot u(t) - C_d \cdot \dot{u}(t) + F_p(t), \tag{5.24}$$

with m_c the mass of the catalyst, k_s the spring stiffness, and C_d the damping coefficient[3].

5.5.9 *ODEs system*

Following the above relationships, we write the system of equations:

$$\begin{cases} \dot{m}^{R}_{f,p}(t) = -\dot{m}^{R,diff}_{f,c}(t) \\ \dot{m}^{I}_{f,p}(t) = -\dot{m}^{I,diff}_{f,c}(t) \\ \dot{m}^{R}_{f,c}(t) = \dot{m}^{R,diff}_{f,c}(t) - \dot{m}^{gen}_{g} \\ \dot{m}^{I}_{f,c}(t) = \dot{m}^{I,diff}_{f,c}(t) \\ \dot{m}_g(t) = \dot{m}^{gen}_{g}(t) - \dot{m}^{leak}_{g}(t) \\ \dot{T}_c(t) = \left[\dot{Q}^{gen}(t) - \dot{Q}^{loss}(t)\right]/M_C(t) \\ \dot{u}(t) = \dot{u}(t) \\ \ddot{u}(t) = \left[-k_s \cdot u(t) - C_d \cdot \dot{u}(t) + F_p(t)\right]/m_c \end{cases}, \tag{5.25}$$

in which we can plug in the relationships of Equations (5.12), (5.13), (5.14), (5.16), (5.19), (5.20), (5.21), (5.23), and consequently the rest of the required equations as described above, obtaining the set of 8 ODEs in Eq. 5.26 reported in Section 5.9.

5.6 THE MODEL EXPLAINS THE ACTIVE OSCILLATION

Having developed a model that takes into account the chemical reaction, the capillarity of the catalyst, the mechanics of the membrane, and gas and temperature balances, we first aim to confirm that the model captures the active oscillation observed in experiments. We assign physically plausible values to the parameters as summarized in Table 5.1, where we indicate for each parameter if it is either scientifically well established, or experimentally measured by us, or resulting from a qualitative fit so that the simulations qualitatively match the experiments in Figure 5.4. We integrate forward the set of ODEs in Eq. (5.26) with the MATLAB `ode23s` solver, which is effective in solving stiff ODEs through a modified Rosenbrock method [201, 202][4].

We observe that the model captures the active oscillation, with both the chamber pressure and the catalyst temperature oscillating at a frequency

3 We assign $m_c = 1.2\,g$ as measured, k_s so that the membrane lifts the catalyst past the fuel pool surface with 10 kPa of pressure, and $C_d = 0\,N\,s/m$ (Table 5.1).

4 Given the parameters in Table 5.1, the ODEs are stiff in that the timescale of diffusion is much faster than the timescale of reaction, which is faster than the timescale of the gases venting to atmosphere.

of ~ 0.011 Hz (Fig. 5.7A), qualitatively similar to the experiments (Fig. 5.3). The total mass of gas present in the chamber and the mass of reactable fuel in the catalyst also oscillate, with a time offset with respect to each other (Fig. 5.7B).

Importantly, we find that a key phenomenon enabling the active oscillation is this time offset between the catalyst gaining reactable fuel and the effective inflation of the membrane. This time offset can be better understood by looking closely at the third[5] inflation cycle (Fig. 5.7C,D). When the catalyst dips into the pool (green), it gains reactable fuel via diffusion (Fig. 5.7D, blue arrow). Pressure marginally rises because some of the gained fuel in the catalyst reacts, and importantly, it keeps rising (Fig. 5.7C, red arrow) even after the catalyst exits the pool (purple).

This delayed pressurization occurs because there is fuel present in the catalyst (which got transferred through diffusion and we assume it stays via capillary forces), which reacts and turns into gases (Fig. 5.7D, red arrow), even when the catalyst is no longer dipped in the pool. When this fuel is fully reacted ($m^R_{f,c} = 0$), pressure will decrease as the reacted gas vents to atmosphere through the venting needle (Fig. 5.7C, grey arrow). This causal sequence of diffusion-reaction-venting is not imposed a priori (as the ODEs hold at all times), but instead it arises from the separation of timescales of the three phenomena: diffusion occurs much faster than reaction, and reaction occurs much faster than venting.

This apparent time offset between the diffusion of reactable fuel into the catalyst and the reaction that generates gases results in a hysteretic behavior, noticeable when plotting pressure against reactable fuel in the catalyst $m^R_{f,c}$ (Fig. 5.7E). When dipped, $m^R_{f,c}$ increases while pressure drops (blue arrow). When pressure starts to increase (small red arrow), the catalyst has already gained $m^R_{f,c} \approx 12\,\text{mg}$. After exiting the pool, this gained fuel will react, hence pressure increases while $m^R_{f,c}$ decreases (red arrow), until $m^R_{f,c} = 0$ and the reacted gas vents to atmosphere (grey arrow).

Hence, this model teaches us that the active oscillation arises from two sources: 1) a time offset between fuel entering the catalyst in liquid form and leaving the catalyst in the form of gases, and 2) negative feedback between pressurization and reaction. The first contribution, the time offset, is a consequence of *i)* the catalyst being able to hold liquid on its surface through capillary forces, even when not dipped in the pool, and *ii)* the faster timescale of diffusion of fuel in the catalyst with respect to the timescale of the reaction, and the reaction faster than venting, which result in a causal sequence of events to arise, where first the

5 We focus on the third cycle to make sure we are not looking at the transient behavior of the first cycles.

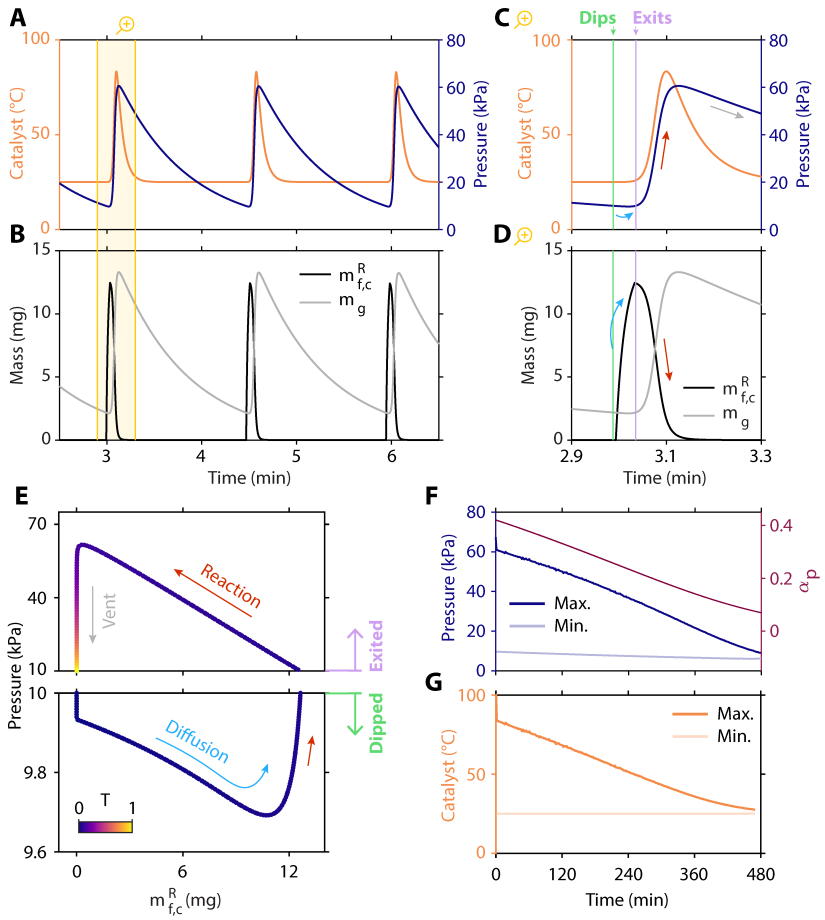

Figure 5.7

THE MODEL CAPTURES THE ACTIVE OSCILLATION. (**A**) Evolution in time of the catalyst temperature (orange) and the chamber pressure (blue) of the modeled system (third to fifth inflation cycles). (**B**) Evolution in time of the mass of reactable fuel in the catalyst (black) and the mass of gas in the chamber (gray) of the modeled system (third to fifth inflation cycles). (**C**, **D**) A zoomed view of the third inflation cycle highlights when the catalyst enters the pool (green) and when the catalyst exits the pool (purple). (**E**) Hysteresis highlighted by a period of oscillation displayed in the domain of reactable fuel in the catalyst $m^R_{f,c}$ vs. pressure. (**F**) The maximum and minimum pressure values (blue) and fuel concentration in the pool (dark red) decrease over 8 simulated hours. (**G**) The maximum catalyst temperature decreases over 8 hours, while the minimum catalyst temperature stays around ambient temperature. The parameters used in these simulations are listed in Table 5.1.

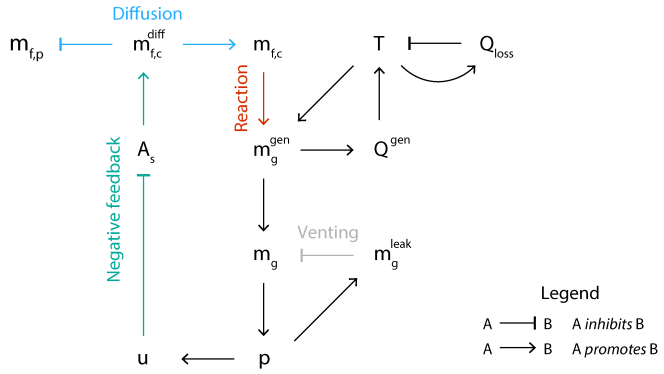

Figure 5.8
BLOCK DIAGRAM OF THE ACTIVE OSCILLATION. We represent how the key variables in the model qualitatively affect each other. Flat arrowheads from a variable A to a variable B indicate that A inhibits B, meaning that an increase in A causes a decrease in B. Pointy arrowheads from variable A to variable B indicate that A promotes B, meaning that an increase in A causes an increase in B. We highlight in blue the diffusion of fuel from the pool to the catalyst, causing an increase in the mass of fuel in the catalyst $m_{f,c}$. In red, we indicate the catalytic reaction that generates a mass of gas m_g^{gen} from the mass of fuel in the catalyst $m_{f,c}$. In grey, we indicate how the gas that vents to atmosphere reduces the mass of gas in the chamber. In green, we indicate the effect of negative feedback, for which an increase in displacement u causes a decrease in the surface area of contact A_s of the catalyst with the fuel in the pool, inhibiting diffusion of fuel to the catalyst.

diffusion occurs, then the reaction happens, then venting takes over. The second contribution, negative feedback, results from the catalyst being physically attached to the membrane, which displaces upwards when pressurized, hence distancing the catalyst from the pool of fuel.

The time offset between causally sequenced diffusion, reaction, and venting, and the negative feedback are apparent when we represent the model in a block diagram (Fig. 5.8) where the key variables either inhibit or promote each other, inspired by the representations in Ref. [203]. We notice how diffusion promotes the mass of fuel in the catalyst (Fig. 5.8, blue), which in turn promotes the generation of gases through the reaction (Fig. 5.8, red), which will cause pressurization and promote the catalyst displacement u to increase. In turn, the catalyst displacing upwards causes a decrease in the surface area of contact A_s of the catalyst with the fuel in the pool, inhibiting diffusion of fuel to the catalyst, thereby acting as a negative feedback mechanism (Fig. 5.8, green).

In addition to explaining the active oscillation behavior, the model also captures the long-term evolution in time of the oscillation. In particular, the model captures the decrease over time of the maximum and minimum oscillation pressures (Fig. 5.7F, blue). This is a consequence of the available reactable fuel in the pool being depleted, as indicated by the concentration of fuel in the pool dropping from $\alpha_p = 0.42$ to $\alpha_p = 0.07$ over the course of 8 simulated hours (Fig. 5.7F, dark red). The reduced amount of available reactable fuel effectively results in the system reacting less and less, as indicated by the maximum catalyst temperature dropping to ambient temperature (Fig. 5.7G). When this condition is reached after approximately 8 hours, the system stops oscillating.

5.7 INFLUENCE OF PARAMETERS ON THE ACTIVE OSCILLATION

Having learned that the separation of timescales and the negative feedback intrinsic to our system are the sources of the active oscillation, we wonder how the system responds to variations in key physical parameters. In particular, we will first vary parameters that can be tuned by design, such as membrane stiffness and venting resistance, to confirm that the model captures the change of behavior observed experimentally in Figure 5.5. Then, we will investigate how the behavior of the modeled system changes when we vary the parameters intrinsic to the reaction, such as catalyst capillary capacity and reaction constant. These two studies will inform us on whether there are other regimes that the system can be placed at (in addition to the already observed oscillation), on how sensitive to parameters the active oscillation phenomenon effectively is, and on whether we can tune specific parameters to obtain desired output behaviors, such as oscillation frequency and amplitude.

5.7.1 *Influence of design parameters*

Among the various parameters in Table 5.1, we focus on the membrane stiffness k_s and the venting resistance R_l as key design parameters, because they are relatively easy to tune by a designer. The former can be increased by casting the membrane with a stiffer silicone, while the latter can be tuned by swapping the venting needle with one with a different Gauge value, that is, with a different inner diameter, as we did in Figure 5.5.

When varying the membrane stiffness by four orders of magnitude, we visually identify three distinct regimes (Fig. 5.9A). The first regime shows that a soft membrane suppresses oscillations after an initial inflation (Fig. 5.9B(i)). In the second regime, the frequency of oscillation increases when the membrane is stiffer, while at the same time, the maximum

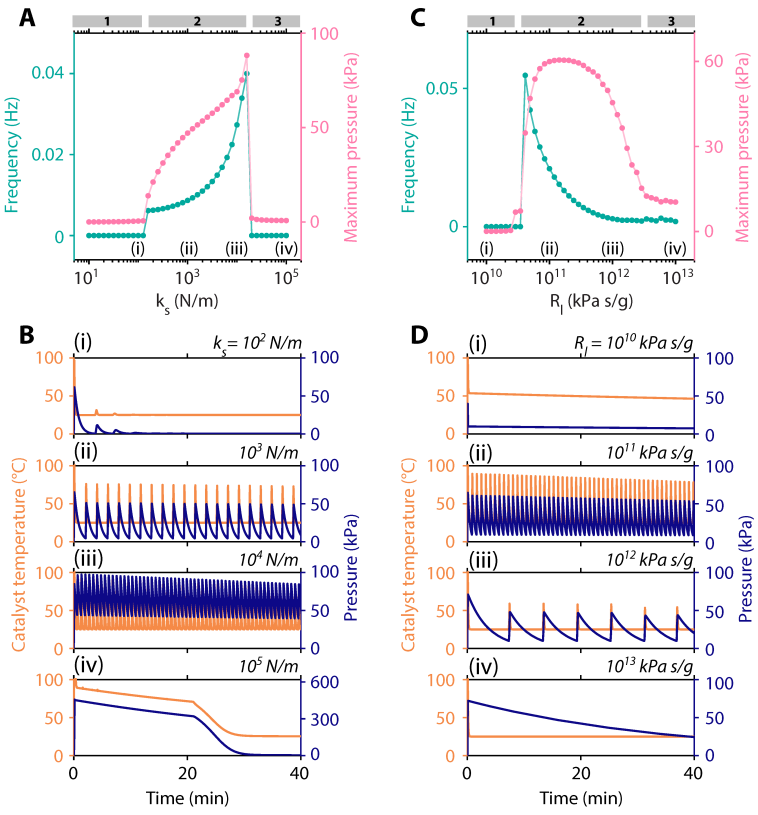

Figure 5.9
INFLUENCE OF MEMBRANE STIFFNESS AND VENTING RESISTANCE ON THE ACTIVE OSCILLATION. (**A**) Frequency (green) and maximum pressure (pink) of the active oscillation when varying the membrane stiffness k_s from 1×10^1 N/m to 1×10^5 N/m. The three regimes are highlighted with grey bars, with numbers 1, 2, and 3. (**B**) Catalyst temperature (orange) and pressure (blue) for the four key cases (i-iv) in A. (**C**) Frequency (green) and maximum pressure (pink) of the active oscillation when varying the venting resistance R_l from 1×10^{10} kPa s/g to 1×10^{13} kPa s/g. The three regimes are highlighted with grey bars, with numbers 1, 2, and 3. (**D**) Catalyst temperature (orange) and pressure (blue) for the four key cases (i-iv) in C. All simulation parameters (apart from the varied ones) are listed in Table 5.1. When frequency is zero, we define the maximum pressure as the pressure value at the end of the test, at time 40 min.

reached pressure increases as well (Fig. 5.9B(ii, iii)). The increase in frequency is a consequence of the discharge phase occurring within a short time period, as the stiffer membrane pushes the gases through the venting needle at a faster rate. The higher pressure is a direct result of the increased stiffness, as the displacement for which the catalyst lifts

past the pool occurs at a higher pressure. For even stiffer membranes, the system operates in the third regime, where the catalyst is dipped in the fuel and the reaction keeps occurring without oscillations, until the fuel in the pool completely depletes (Fig. 5.9B(iv)). The stiff-membrane regime in Figure 5.9B(iv) differs from the soft-membrane regime in Figure 5.9B(i), in that a stiffer membrane forces the catalyst to fully dip in the pool and induce a high-temperature, high-pressure reaction, while a softer membrane deforms considerably even at low pressure (at slow reaction rates), leading to a low-temperature, low-pressure reaction where the catalyst stays on the surface of the pool.

When varying the venting resistance, too, we observe three operational regimes (Fig. 5.9C). In the first regime, the resistance is so low that the reacted gases vent to atmosphere without inducing pressurization in the chamber (Fig. 5.9D(i)), as the venting timescale is in the same order of the reaction timescale. In the second regime, for low venting resistance, we observe relatively high oscillation frequencies, as the discharge phase occurs relatively rapidly (Fig. 5.9D(ii)). For higher venting resistance, the maximum reached pressure decreases (Fig. 5.9C, pink). This reduction is a result of the diminished losses of the reacted gases through venting: for each oscillation cycle, the reacted gases more effectively displace the membrane upward, stopping the reaction earlier. Simultaneously, for higher venting resistance, the frequency drops (Fig. 5.9C, green) because the discharge timescale lengthens (Fig. 5.9D(ii, iii)). Lastly, in the third regime, too high a venting resistance effectively suppresses the oscillation, as the membrane is attracted around the pool surface (~ 10 kPa) (Fig. 5.9D(iv)).

These results indicate that the membrane stiffness and the venting resistance, contextualized in the coupled system with intrinsic negative feedback and internal time offset, both enable the active oscillation to arise, and can be leveraged as design tools to tune the oscillation performance. Importantly, the results from the simulations in Figure 5.9 qualitatively match the experiments in Figure 5.5, where we observed that both a stiffer membrane and a lower resistance suppress oscillations.

5.7.2 *Influence of capillarity and reaction parameters*

Having confirmed that the model predicts changes in design parameters, we continue by studying how the system behaves when the capillarity of the catalyst has reduced or increased effect, that is, when the catalyst can hold more or less volume of fuel on its surface through capillary forces. We observe three main regimes when we vary the maximum volume of fuel that the catalyst can hold ($V_{t,c}^{max}$) by 3 orders of magnitude, between 3 µL and 3 mL (Fig. 5.10A).

The first regime appears at the very low volume of 3 µL (Fig. 5.10A, grey bar '1'), and is characterized by the absence of oscillation as indicated by the frequency being zero (Fig. 5.10A, green). In this regime, the catalyst holds so little volume of fuel that the fuel fully reacts before the catalyst lifts past the pool surface. While the low-temperature reaction occurs, this small amount of fuel in the catalyst is constantly being replenished through diffusion from the pool. Moreover, the small amount of generated gases vent to atmosphere, without inducing pressurization of the membrane. Hence, the system stabilizes at this steady-state slow-reaction condition, with pressure stabilizing at ~ 2.1 kPa and the catalyst temperature staying at ambient temperature (Fig. 5.10B(i)).

The second regime appears between 3 µL and 0.3 mL (Fig. 5.10A, grey bar '2'). In this regime, the maximum pressure increases (Fig. 5.10A, pink) and the frequency decreases (Fig. 5.10A, green) for larger capillary volumes. This trend is expected from the assumption that all the reactable fuel present on the catalyst must react. Hence, larger volumes of fuel on the catalyst will result in larger inflation, increasing the amplitude and lengthening the oscillation period (Fig. 5.10B(ii, iii)).

The third regime between 0.3 mL and 3 mL (Fig. 5.10A, grey bar '3') shows the maximum pressure dropping for increasing capillary volume, and the frequency even reaching zero for high enough volume values around 3 mL. In this regime, the catalyst can hold so much fuel that the first oscillation cycle substantially depletes the pool of fuel (which has an initial volume of 6 mL). This depletion in the first cycle results in the subsequent cycles reaching lower maximum pressures. If the fuel volume in the catalyst is large enough, the first cycle depletes the pool to a point that subsequent oscillations do not occur within the tested time frame (Fig. 5.10B(iv)).

Note that the regimes '1' and '3' are not physically relevant to our specific experiment, where the actual catalyst can hold around 0.2 mL of liquid through capillary forces[6]. However, looking at such extremes teaches us that *i)* enough capillary volume is required for a limit cycle to appear, otherwise the small amount of fuel held by the catalyst would react before displacing past the pool surface, and *ii)* too large a capillary volume would inhibit the oscillation after one initial inflation.

We then investigate the influence of the rate of the reaction on the active oscillation. When varying the reaction constant C_r (that is, the slope of the reaction rate function of temperature in Eq. (5.15)) by four

6 We measure the maximum volume of liquid that the catalyst can hold through capillary forces by dipping the catalyst in water and measuring the weight against its weight without water, obtaining 0.22 g, so 0.22 mL in volume.

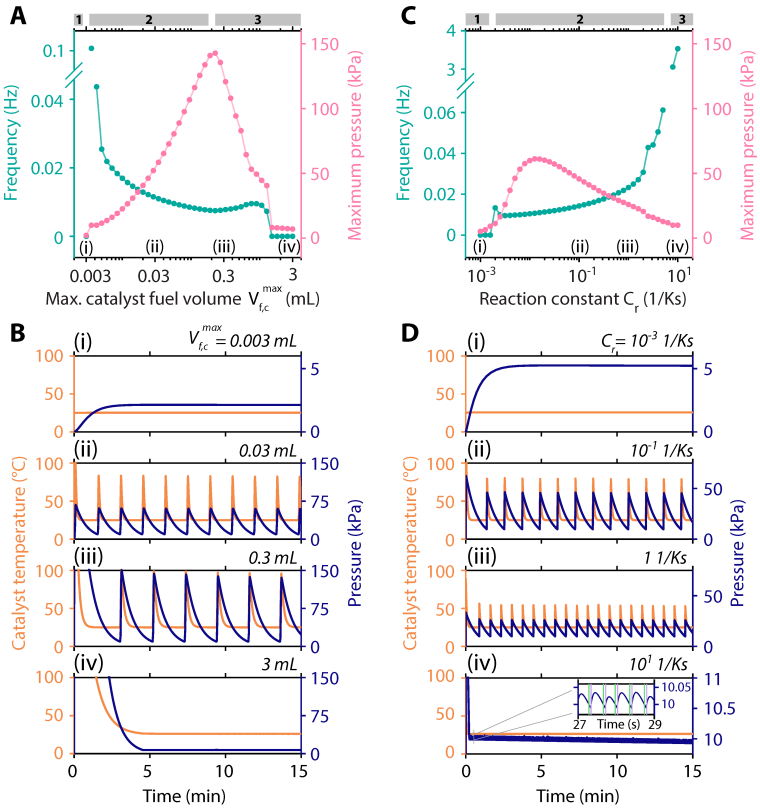

Figure 5.10

INFLUENCE OF CATALYST CAPILLARITY AND REACTION CONSTANT ON THE ACTIVE OSCILLATION. (**A**) Frequency (green) and maximum pressure (pink) of the active oscillation when varying the maximum volume of fuel in the catalyst $V_{f,c}^{max}$ from 3 µL to 3 mL. The three regimes are highlighted with grey bars, with numbers 1, 2, and 3. (**B**) Catalyst temperature (orange) and pressure (blue) for the four key cases (i-iv) in A. (**C**) Frequency (green) and maximum pressure (pink) of the active oscillation when varying the reaction constant R_c from 1×10^{-3} s/K to 1×10^{1} s/K. The three regimes are highlighted with grey bars, with numbers 1, 2, and 3. (**D**) Catalyst temperature (orange) and pressure (blue) for the four key cases (i-iv) in C. The inset in (iv) highlights the high-frequency oscillation occurring over 2 s, with the catalyst oscillating at low amplitude around the pool level, rapidly entering (green) and exiting (purple) the pool. All simulation parameters (apart from the varied ones) are listed in Table 5.1.

orders of magnitude[7], we visually identify three main regimes as well (Fig. 5.10C).

7 Note that, in principle, the reaction constant could be varied experimentally by using fuel with a lower or higher concentration of hydrogen peroxide, or by adding sodium hydroxide to the 50% concentrated fuel, to change the pH and obtain a more reactive fuel.

The first regime appears for very low values of the reaction constant around $C_r = 1 \times 10^{-3}$ s/K (Fig. 5.10C, grey bar '1'). This regime corresponds to a reaction rate so low that the reacted fuel is replenished through diffusion before the catalyst can lift past the pool surface, while the generated gases directly leak through the venting needle. In this regime, similar to regime '1' for low catalyst fuel volume in Figure 5.10A, the system stabilizes around 5 kPa of pressure and with the catalyst at ambient temperature (Fig. 5.10D(i)).

The second regime (Fig. 5.10C, grey bar '2') shows an increase in oscillation frequency (green) for higher values of the reaction constant. The maximum pressure (pink) first increases for reaction constant values up to 1×10^{-2} s/K. This is a consequence of a higher reaction rate, which in turn causes an increase in the catalyst temperature, which in turn affects the reaction rate itself. Overall, the fuel reacts more rapidly, thereby gas generation dominates over the gas losses through the venting needle. Beyond this reaction constant value around 1×10^{-2} s/K, we observe a decrease in the maximum pressure. This reduced maximum pressure for higher C_r is a consequence of the higher timescale of the reaction with respect to the diffusion, which implies that the catalyst does not have enough time to fully replenish its local fuel reservoir with reactable fuel. For instance, by increasing C_r from 1×10^{-1} s/K to 1 s/K (cases (ii) and (iii) in Fig. 5.10D), the resulting maximum reactable fuel mass in the catalyst lowers from ~ 8 mg to ~ 3.5 mg. As a consequence, the catalyst has a lower concentration of fuel, and hence the reaction will generate fewer gases, inducing less pressure inside the chamber.

The third regime (Fig. 5.10C, grey bar '3') occurs at relatively high values of reaction constant around 10 s/K. In these conditions, the reaction timescale is much higher than the diffusion timescale, and the system oscillates at higher frequencies above 3 Hz, at a pressure that stays around 10 kPa. The system is not undertaking the large-amplitude oscillations observed in the other regimes, and it rapidly exits and re-enters the pool of fuel (Fig. 5.10D(iv), inset), effectively being attracted to this partially inflated condition with the catalyst displacing around the contact point with the pool surface.

Hence, we learned that if the reaction is not fast enough, oscillations do not occur, and the catalyst stays fully dipped in the pool (Fig. 5.10D(i)). On the other hand, too fast a reaction results in the system oscillating with relatively small amplitude and high frequency around the surface of the pool (Fig. 5.10D(iv)), without undertaking large-amplitude oscillations that can be meaningfully harnessed for soft robotics applications.

5.8 DISCUSSION

We introduced a system that undergoes active oscillations by harnessing the coupling between the deformation of an elastic membrane and a catalytic reaction. We observe oscillations in which the access to and release of energy are directly coupled to internal states of the system, effectively embodying the energy source within the oscillator itself. Through a lumped-parameter model, we learned that the key phenomena underlying the oscillation are the negative feedback resulting from the catalyst being attached to the deforming membrane and the internal time offsets between diffusion, reaction, and venting, which arise from the three different timescales.

Despite its apparent simplicity, the model qualitatively captures the oscillation dynamics, and it reproduces the experimental results when varying parameters. Hence, the model both enables the understanding of the phenomena at play and can prove useful to provide design guidelines for oscillating soft robots. However, the current model follows a number of simplifications, which in future work can be extended to capture more details of the experiments. For instance, we model the reaction rate as linearly dependent on the catalyst temperature, while in reality, an exponential trend is expected [199]. Moreover, we assume that the chamber stays at ambient temperature, while experiments show that it can rise (Fig. 5.4D), and is likely the cause of the increase in frequency at the beginning of the experiment (Fig. 5.4A), which our model does not capture.

The current design of the active oscillator serves the purpose of an experimental testbed that operates under controlled conditions, so that we can effectively isolate the various contributions and understand the phenomena at play. For functional operation in practical real-world applications, we expect that the current prototype will require several changes. The device now relies on gravity to contain the fuel in the pool; other fuel storage solutions, such as soft porous materials like sponges [204, 205], would allow orientation-independent operation. Moreover, the manufacturing of the catalyst now follows a largely manual procedure (Section 5.9), hindering scalability and repeatability. Other manufacturing methods should be considered, such as casting or machining silver.

Despite embodying energy, the proposed approach to achieve active oscillations in soft robotic systems consumes fuel in the process. Although we showed that 6 mL of fuel is enough for the oscillations to sustain for more than 3 hours consecutively, considerably longer than the minutes typical of pressurized canisters [57], our approach opens the question of refueling. Refueling would involve transportation of hydrogen peroxide in bulk from the manufacturing plant, where it is currently manufac-

tured with energy-intensive and centralized processes [206], to the site of operation of the robot. Besides being an impractical solution to the goal of energy-autonomous robots, this transportation is often a hazardous process [207]. In a real-world scenario, where an untethered soft robot operates autonomously in the field, we envision a local approach to the synthesis of hydrogen peroxide directly from the water and air that are available in the surrounding environment. This approach has proven to be at reach, as researchers obtained concentrations of hydrogen peroxide up to 20% from water and oxygen through direct electrosynthesis [208]. However, considerable research effort is still required to obtain increased concentrations and to devise synthesis mechanisms that are embodied in the machine itself.

With this preliminary and explorative work, we show that relatively simple mechanical structures, such as flat elastic membranes, can undergo active oscillations when carefully coupled to other phenomena, such as capillary action and catalytic reactions. As such, we expand the library of phenomena that can be harnessed to achieve self-oscillations in soft fluidic machines, while at the same time embodying energy in the machine itself.

5.9 SUPPLEMENTARY INFORMATION

5.9.1 *Manufacturing the active oscillator*

To build the catalyst, we take a length of 50 cm of 99.9 % pure silver wire with diameter 0.5 mm (Sigma-Aldrich®, 327026). We manually deform the wire and coil it on itself, until it is loosely packed in the shape of a sphere with a diameter of ~ 9 mm. To avoid contamination of the catalyst, we manipulate the wire with clean tweezers. While coiling, we make sure not to tighten the wire, so that a great part of the wire surface area is exposed. During the coiling process, we create two loops external to the sphere (Fig. 5.11A), to ease embedding in the silicone membrane in the next step.

We attach the catalyst to a 3D-printed mold. The mold has the negative shape of the membrane, with a suspension block at the center. The catalyst is placed over the suspension block so that the two loops of the catalyst will be embedded in the poured silicone (Fig. 5.11B). A thin polypropylene thread (diameter ~ 0.1 mm) is looped around the catalyst and through two holes in the mold to keep the catalyst in place while pouring the silicone (Fig. 5.11B,C). We then pour silicone (pre-mixed part A and part B) into the open mold, and we let it cure (Fig. 5.11D). After curing, we cut the polypropylene thread and remove it.

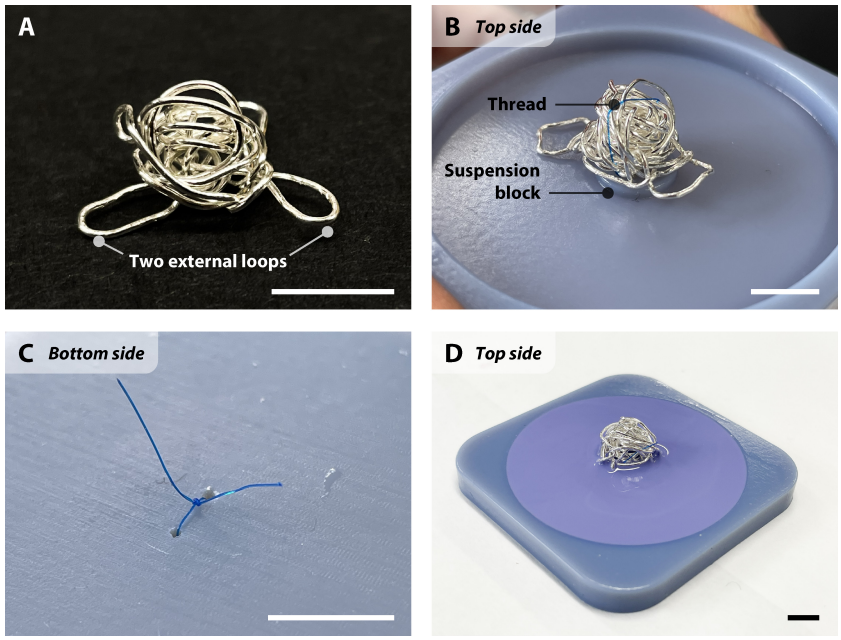

Figure 5.11
MANUFACTURING OF THE MEMBRANE WITH THE EMBEDDED CATALYST. (**A**) We build the catalyst by manipulating silver wire (0.5 mm diameter) in the shape of a sphere, with two external loops. (**B**) We connect the catalyst to the mold, over a suspension block, using a thin polypropylene thread. (**C**) The polypropylene thread is tied on the bottom side of the mold. (**D**) We pour silicone into the open mold. All scale bars are 1 cm.

The result is a silicone membrane with the catalyst partially embedded. The two external loops of the catalyst are fully embedded for a secure attachment to the membrane (Fig. 5.12A). Due to the presence of the suspension block in the mold, the membrane is not airtight on the bottom side (Fig. 5.12B). To seal the membrane, we deposit silicone adhesive (Sil-Poxy^{TM}, Smooth-On) over the hole left by the suspension block (Fig. 5.12C).

In Figure 5.13, we show the cross-section of the complete active oscillator introduced in Figure 5.1, with the membrane suspended over the 3D-printed pool that contains the fuel. The fuel is an aqueous solution of 50% hydrogen peroxide (Evonik Inc. PROPULSE HTP, 50% by weight). The pool (Fig. 5.13, bottom) is 3D-printed with a Stratasys Objet30 Prime, in the material VeroBlue (RGD840). The holder clamp (Fig. 5.13, top) is 3D-printed using a Formlabs Form 3B, in the material Clear Resin V4.

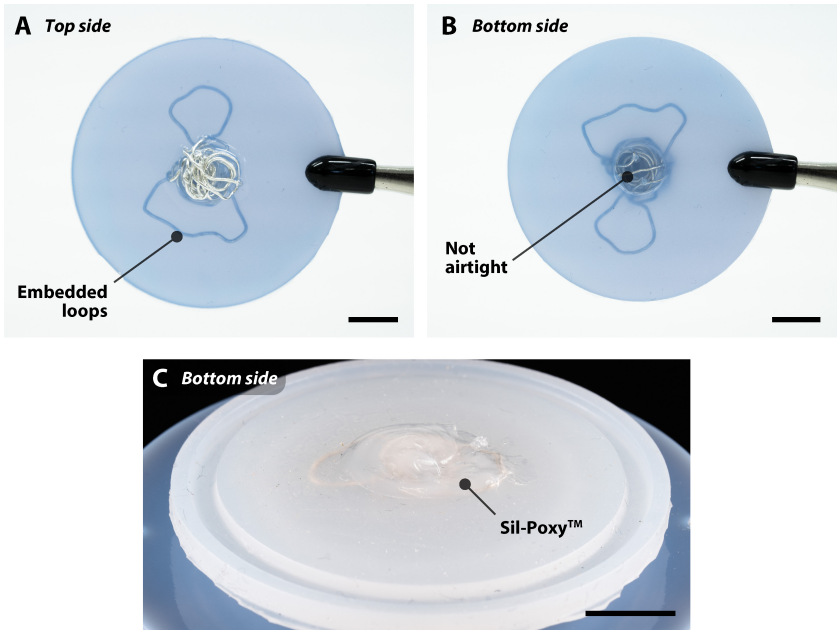

Figure 5.12
SEALING THE MEMBRANE. (**A**) Top view of the membrane with the catalyst. The embedded loops are visible inside the semi-transparent silicone. (**B**) The bottom view of the membrane after demolding highlights the area around the suspension block not being airtight. (**C**) We deposit Sil-Poxy™ over the hole left by the suspension block. Note that the bottom side of the membrane, as indicated here, will be the top side of the membrane when clamped in the final device. All scale bars are 1 cm.

5.9.2 *Experimental setup*

To acquire pressure, we use a Pendotech Luer single-use pressure sensor (PREPS-N-000), with the acquisition board PowerLab 16/35 (ADInstruments). To acquire temperature, we use a thermocouple (Type-K Glass Braid Insulated, Adafruit) with an amplifier board (MAX31855 breakout board, Adafruit) and a microcontroller (METRO 328, Adafruit).

Each experiment involves data acquisition of pressure inside the chamber and of temperature at the catalyst and inside the chamber, while the device oscillates. Each experiment is preceded by the following steps.

1. We place the on/off valve (Fig. 5.2) so that the chamber is not fluidically connected to the pressure sensor and the venting needle.

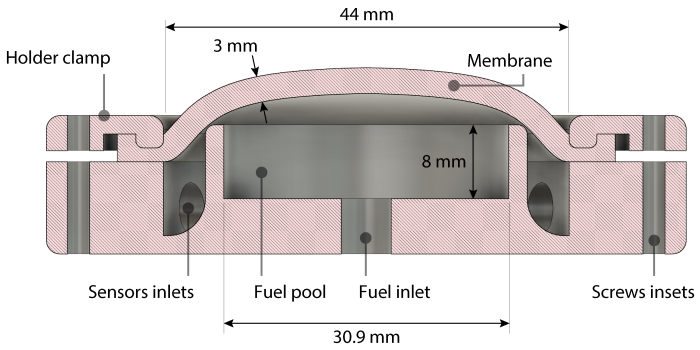

Figure 5.13
CROSS-SECTION OF THE DEVICE. A flat circular silicone membrane (thickness 3 mm, diameter after clamping 44 mm) is suspended over a cylindrical fuel pool (height 8 mm, internal diameter 30.9 mm) with a circular clamp. The membrane is clamped with its bottom side at a 4 mm lower height than the top of the pool, to ensure a pre-stretch. In the image, the membrane is depicted as pre-stretched, while it is flat in its rest state.

2. By using a syringe, we inflate the membrane via the one-way valve at the bottom of the holder, until the catalyst is above the surface of fuel in the pool.
3. We inject 6 mL of fuel through the same one-way valve.
4. We start acquiring temperature and pressure data.
5. We rotate the valve counterclockwise (in relation to Figure 5.2) to connect the chamber to both the pressure sensor and the venting needle. The membrane will deflate until the catalyst touches the fuel, and the experiment starts.

5.9.3 *The complete set of ODEs*

Starting from the set of Equations (5.25), we plug in the relationships in Equations (5.12), (5.13), (5.14), (5.16), (5.19), (5.20), (5.21), (5.23), and then the rest of the needed equations as described in Section 5.5, obtaining a set of 8 ODEs:

$$
\begin{cases}
\dot{s}_1 = -C_f^{diff} \cdot A_s(s_1, s_2, s_7) \cdot S_{react}^{diff}(s_1, s_2, s_3, s_4) \\
\dot{s}_2 = C_f^{diff} \cdot A_s(s_1, s_2, s_7) \cdot S_{inert}^{diff}(s_1, s_2, s_3, s_4) \\
\dot{s}_3 = C_f^{diff} \cdot A_s(s_1, s_2, s_7) \cdot S_{react}^{diff}(s_1, s_2, s_3, s_4) - s_3 \cdot \left[k_{r_0} + C_r \cdot (s_6 - T_0)\right] \\
\dot{s}_4 = -C_f^{diff} \cdot A_s(s_1, s_2, s_7) \cdot S_{inert}^{diff}(s_1, s_2, s_3, s_4) \\
\dot{s}_5 = s_3 \cdot \left[k_{r_0} + C_r \cdot (s_6 - T_0)\right] - \dfrac{R \cdot T_0}{R_l \cdot M_g \cdot V_{ch}} \cdot s_5 \\
\dot{s}_6 = \dfrac{H_{dec} \cdot s_3 \cdot \left[k_{r_0} + C_r \cdot (s_6 - T_0)\right] + C_{loss} \cdot (s_6 - T_0)}{m_c \cdot c_{p,s} + c_{p,w} \cdot s_4} \\
\dot{s}_7 = \dot{s}_7 \\
\dot{s}_8 = \dfrac{1}{m_c} \cdot \left(-k_s \cdot s_7 - C_d \cdot s_8 + \dfrac{A_m \cdot R \cdot T_0}{M_g \cdot V_{ch}} \cdot s_5\right)
\end{cases}
, \tag{5.26}
$$

with

$$
S_{react}^{diff}(s_1, s_2, s_3, s_4) = m_{f,c}^{max} \cdot \left(\frac{2s_1}{s_1 + s_2} - \frac{s_3}{s_3 + s_4}\right) - \frac{s_1 \cdot (s_3 + s_4)}{s_1 + s_2}, \tag{5.27}
$$

and

$$
S_{inert}^{diff}(s_1, s_2, s_3, s_4) = m_{f,c}^{max} \cdot \left(\frac{2s_1}{s_1 + s_2} - \frac{s_3}{s_3 + s_4} - 1\right) - \frac{s_1 \cdot (s_3 + s_4)}{s_1 + s_2} - s_3 - s_4, \tag{5.28}
$$

and $m_{f,c}^{max}$ as defined in Eq. (5.11), and

$$
A_s(s_1, s_2, s_7) = \begin{cases} 0 & \text{if } s_7 > h_c - \Delta u_{f,p}(t), \\ r_c^2 \pi + 2\pi r_c \cdot \left(h_c - s_7 - \Delta u_{f,p}(t)\right) & \text{if } s_7 \leq h_c - \Delta u_{f,p}(t), \end{cases} \tag{5.29}
$$

where

$$
\Delta u_{f,p}(t) = \frac{1}{r_p^2 \pi} \cdot \left(V_{f,p_0} - \frac{s_1 + s_2}{\rho_{H_2O_2} \cdot \frac{s_1}{s_1 + s_2} + \rho_{H_2O} \cdot \frac{s_2}{s_1 + s_2}}\right). \tag{5.30}
$$

In Eq. (5.11), (5.26), (5.27), (5.28), (5.29), and (5.30), only the state variables s_1, s_2, s_3, s_4, s_5, s_6, s_7, and s_8 depend on time, while the others are fixed parameters summarized in Table 5.1.

Table 5.1
PARAMETERS OF THE SIMULATIONS IN FIGURES 5.7, 5.9, 5.10. We refer to each parameter as 'known' when it is a scientifically established value, 'measured' when we experimentally measure it in the lab, or 'fitted' when we assign it to qualitatively fit the simulation to the experiment in Figure 5.3.

Param.	Value	Unit	Description	Motivation
T_0	298.15	K	Room temperature	Measured
R	8.314	J/(K mol)	Gas constant	Known
M_g	0.022667	kg/mol	Molar mass of gas	Known
ρ_{H_2O}	1×10^3	kg/m^3	Density of water	Known
$\rho_{H_2O_2}$	1.45×10^3	kg/m^3	Density of H_2O_2	Known
$c_{p,s}$	235	J/(kg °C)	Silver specific heat capacity	Known
$c_{p,w}$	4200	J/(kg °C)	Water specific heat capacity	Known
H_{dec}	2.8845×10^6	J/kg	H_2O_2 decomposition heat	Ref. [198]
C_{loss}	0.1	J/(K s)	Heat loss coefficient	Fitted
α_{p_0}	0.42	–	Initial fuel concentration	Measured
V_{ch}	24×10^{-6}	m^3	Initial chamber volume	Measured
V_{f,p_0}	6×10^{-6}	m^3	Initial fuel volume in pool	Measured
r_p	15.451×10^{-3}	m	Radius of pool	Measured
r_c	4.5×10^{-3}	m	Radius of catalyst	Measured
h_c	7×10^{-3}	m	Height of catalyst	Measured
m_c	1.2×10^{-3}	kg	Mass of catalyst	Measured
$V_{f,c}^{max}$	0.03×10^{-6}	m^3	Catalyst maximum fuel volume	Fitted
C_f^{diff}	1×10^4	s/m^2	Fuel diffusion constant	Fitted
C_r	0.02	1/(K s)	Reaction constant	Fitted
k_{r_0}	1×10^{-3}	1/s	Reaction rate at T_0	Fitted
R_l	0.2×10^{12}	Pa s/kg	Venting resistance	Fitted
k_s	1.7436×10^3	N/m	Spring stiffness	Measured
C_d	0	N s/m	Damping coefficient	Fitted

6 DISCUSSION

'Mens et manus'

MIT MOTTO

6.1 CONCLUSION

We started this research journey in Chapter 1, by asking ourselves: Can we embody autonomous capabilities, such as reflexes, environmental feedback, and switching of behaviors, in the physical structure of soft machines? The question arose from the observation that animals often delegate complex, autonomous behaviors to their body, especially when brain power is limited or entirely absent, as in the case of unicellular organisms. In such brainless beings, we noted how spontaneous and robust global behaviors, such as exploration for food, arise from local interactions of the organisms with the environment [24] and from the physics of the nonlinear response of their body [21, 22], without a center of command that controls them. This Thesis addresses the question with ingenuity, by leveraging the nonlinear responses intrinsic in seemingly simple mechanical structures such as elastic shells, soft hysteretic valves, and thin flexible tubes, which resemble everyday items such as Pop It! fidget toys [209], ketchup bottle valves [59], and wacky inflatable tube men [154].

In Chapter 2, we start by embodying mechano-fluidic memory in soft machines by exploiting the bistability of elastic shells to create discrete, stable operational states in a fluidic relaxation oscillator. Fluidic circuits built around the shells enable soft machines to program new behaviors upon interactions with the surroundings, such as steering to avoid obstacles. In Chapter 3, we provide a theoretical framework for understanding the dynamics of such nonlinear systems. Using a lumped-parameter model that couples the mechanical and the fluidic domain, we explain the coexistence of two modes, pressure regulation and oscillation, in the soft hysteretic valves inside the machines of Chapter 2.

Then, in Chapter 4 we depart from such internal control strategies, and instead we demonstrate how coordinated locomotion can emerge from the physical interactions between self-oscillating limbs and their environment. The limbs are made from kinked soft tubes and require only a constant airflow to synchronize their stepping motions, achieving fast and responsive locomotion without centralized control. Finally, in Chapter 5, we embody energy in these soft systems, eliminating the need for external power. We introduce and rationalize active oscillations that arise from the coupling of soft membranes with the catalytic reaction of a liquid fuel that cyclically decomposes into gases.

We find that there is a surprising amount of interesting physics at play in these devices, despite their apparent simplicity. By understanding and harnessing such rich physics, we can design functional, autonomous, and robust behaviors. From instilling memory in the body of soft machines to introducing a locomotion paradigm based on physical synchronization

of limbs, the contributions of this Thesis bring us a step closer to the embodied kind of autonomy often found in natural systems.

6.2 PERSPECTIVE

Building on the experimental research discussed in the previous chapters, we learn two general insights about embodying autonomy in soft machines. In the spirit of experimental physics, we should emphasize that these insights emerged thanks to a largely hands-on approach, through the careful handcrafting, playful exploration, and curious observation of the various centimeter-scale soft machines that we presented throughout this Thesis.

First, we learn that harnessing mechanisms with rich nonlinear responses enables multiple qualitatively distinct functions to be solved simultaneously by the same device. We define *co-localization* as the capability of localizing various different functionalities at the same time in one single device. Typically, multifunctional robots fulfill multiple functions only at separate moments in time through changes in the morphology or in the control inputs [160, 171, 210–216], or are constituted by multiple parts, each solving one specific function [217, 218]. Instead, in material science the concept of multifunctionality has been pushed further: a single material can co-localize various functionalities simultaneously [219], such as actuation, sensing, and communication [220], because of the capability of exhibiting various properties at once (for example, electrical or thermal conduction, stimulus-induced deformation, and structural support). This approach led to materials that walk [221], jump [222], dance [223], and even solve mazes [73]. This multifunctionality, while being widespread in material science, is often not adopted when designing robots and machines, where instead each individual part usually has one specific function.

To better illustrate this concept of co-localization, we can refer to practical examples from this Thesis. The self-oscillating limbs in Chapter 4 simultaneously function as fluidic clocks that oscillate given constant power, as actuators that perform work in the environment, as controllers that sequence the coordinated stepping motion, and as sensors that detect stimuli. In Chapter 2, the snapping of the shell expresses both the detection of the stimulus and the storage of this information as a memory element. In Chapter 5, the active oscillator is both a power source and a controller that regulates the cyclic energy release. Instead, although the hysteretic valves in Chapter 3 are multifunctional (they regulate pressure or oscillate), they do not co-localize these functions, as they can adopt the two behaviors only at separate times.

As a second insight, we learn that when a machine composed of highly nonlinear, multifunctional components interacts with its environment, robust and useful behaviors can spontaneously *emerge* from the coupled agent-environment system. This emergence of behaviors, such as autonomous locomotion, is a consequence of the tight integration of sensing, actuation, and control, which allows multifunctional systems to intrinsically close the action-reaction loop while operating in an environment. For instance, the short-term memory behavior in Chapter 2 arises from internal arrangements of nonlinear elastic shells and tubings that induce specific couplings between action and reaction, and the amphibious gait transitions in Chapter 4 arise from the synchronization eigenmodes being responsive to external stimuli, which are themselves induced by variations in the body-environment dynamics. Moreover, the nonlinear characteristics of the individual devices are responsible for facilitating rich couplings with the surroundings and leading to the global system being responsive. For example, the kinking instabilities in the limbs in Chapter 4 allow the coupled limbs to rapidly detect the presence of water or a substrate, as the kink will cause the internal pressure to decrease or increase, consequent to the interactions.

Internal nonlinearities facilitate the creation of multifunctional mechanisms that co-localize functionalities. This, in turn, allows for new behaviors to emerge from the interactions with the outside world, which then can lead to the emergence of autonomy, given that specific goals are met. We will now highlight how this vision carries several opportunities and associated challenges both in the engineering and the scientific domains.

6.2.1 *Engineering opportunities*

From the perspective of engineering robotic systems, our approach offers the main opportunity of simplifying the machines' design[1] for increased robustness, without sacrificing the complexity of the achievable functions. This uncompromising simplification is evident in the examples of memory units from elastic shells in Chapter 2, the robotic limbs made of just tubes in Chapter 4, and the active oscillations from flat membranes in Chapter 5. This advantage can prove particularly useful in applications where both reliability and richness in functionality are required, with machines that behave autonomously as if they carried a relatively delicate computer on board, without actually needing one.

For example, we envision that this approach will lead to the democratic adoption of cheap, yet functional devices, benefiting particularly the

1 The design of the machines is simplified. However, the design process is not straightforward, as we will highlight in Section 6.2.3.

biomedical field, where active implants, robotic pills, and functional devices in general should be low-cost and accessible [224]. As another example, space applications typically involve strong design constraints on size and weight, while maintaining high requirements in terms of robustness. In space exploration, simple yet capable [225] and cheap yet robust [226] machines could delegate the autonomous locomotion task to their soft mechanical body, avoiding breakdowns due to extreme weather or solar storms [111]. As a final example, we foresee that this approach will prove helpful in machines where computing power is severely limited, such as in the case of microscopic robots, in which physical internal interactions [227], multifunctional elements, and body-environment feedback [228] might play a dominant role compared to downstream signals from the limited on-board microelectronics [110].

In this engineering context, the approach presented in this Thesis also carries notable limitations. At the current stage, our systems prove to be largely task-specific, in that their functions are often pre-programmed. For instance, embodied memory through the elastic shells in Chapter 2 does not allow multiple goals beyond switching locomotion speeds, and the self-oscillating limbs in Chapter 4 do not solve tasks beyond responsive, coordinated locomotion. This limitation implies that each specific machine must be designed with the objective task known a priori, proving limiting for general-purpose applications. However, for practical applications, we could embrace this limitation and combine these task-specific, embodied, and distributed solutions with centralized, general-purpose processors to bring out the best from both worlds: robustness in the task-specific body, and versatility in the general-purpose brain.

To this end, we envision developing an extended library of fundamental multifunctional units, such as the shells in Chapter 2 and the limbs in Chapter 4, to create a modular framework. Such a framework would allow for the various co-localized functions of each unit to be combined to achieve rich global dynamical behaviors, and to be interfaced as desired with a central processor. This desire for modularity links to another limitation, that is, the current bottom-up nature of the design strategy to discover multifunctional devices with emergent behaviors. Currently, these phenomena lack rational design tools to obtain specific desired output functionalities. We will address this limitation in Section 6.2.3, together with other exciting challenges that are being opened by our approach.

6.2.2 *Scientific opportunities*

In addition to engineering applications, we envision opportunities for our mechano-fluidic devices in developing robophysical models [12, 144,

162, 163] to answer scientific questions about how animals locomote when they interact with their surroundings, across environments and scales.

Locomotion in vertebrates is often described as the effect of interplays between high-level control signals from the central nervous system, feed-forward central pattern generators in the spinal cord, and dynamic feedback loops between limbs and the environment [13, 229]. In this context, the coupled self-oscillating limbs in Chapter 4 could serve as a study platform for these low-level, embodied layers involving sensory feedback loops and body dynamics. In this direction, relatively recently, a rigid undulatory swimming robot equipped with force sensors confirmed the hypothesis that rhythmic motion in swimming vertebrates can emerge from local hydrodynamic force feedback alone, without requiring explicit signals from central pattern generators [230]. While rigid robots offer precise control over design parameters for testing these kinds of locomotion hypotheses, their rigidity risks overlooking critical dynamical contributions from the coupling between an animal's soft, deformable body and its environment. Because of their simultaneous functions of action, sensing, and reaction, our soft limbs exhibit a relatively vast richness of low-level behaviors while interacting with various environments, and hence are likely good candidates to test hypotheses about emergent locomotion in soft vertebrates coupled to their surroundings.

Besides the specific case of vertebrates, locomotion as a physical phenomenon is increasingly seen as an emergent property that arises from non-reciprocal [231] and local [232] interactions, without the necessary requirement for central controllers that orchestrate specific patterns [118]. Likely, this view will prove particularly useful when studying invertebrates [9, 68] and non-neuromuscular organisms, given that they do not possess a centralized brain, and yet they exhibit autonomous locomotion behaviors. Specifically, slime molds [24] and fungi [233] could be physically modeled as networks of active nonlinear soft channels, using experimental tools that stem from a combination of the tubes developed in Chapter 4 with the activity through fuels in Chapter 5. As another example, microscopic unicellular organisms that coordinate thousands of cilia [164] could be described with arrays of centimeter-scale active cilia that break symmetry and are coupled together for emergent behaviors, given that the mechanics underlying the limbs in Chapter 4 is likely scale-invariant.

From this perspective of harnessing mechano-fluidic nonlinearities as physical models of animal locomotion, the approach we propose in this Thesis also carries an important downside. By condensing multiple functions within a single device, we encounter the risk of oversimplifying the problem at hand. For instance, the asymmetric behavior of the soft tubes in Chapter 4 might represent too far an abstraction of the highly intricate

motions of living appendages. Moreover, the simultaneous occurrence of various functions in the devices, such as motion coordination, sensing, and oscillation, might become counterproductive when trying to isolate the contributions of individual parameters to the observed global behavior of the organism at hand. We foresee that striking a balance between an idealized physical simplification and an over-engineered design will be a grand challenge when modeling animal behaviors with mechano-fluidic robophysical experiments.

6.2.3 *Envisioned challenges*

Together with the opportunities mentioned above, the general approach proposed in this Thesis opens a series of associated challenges. Perhaps the most evident is the challenge of the inverse design. The nature of these multifunctional systems is of high integration, where internal mechano-fluidic networks and couplings with the external environment work together to generate emergent dynamic behaviors. This is a holistic view of an agent embedded in an environment, where the understanding of individual components alone does not guarantee the prediction of the outcome behavior when deployed in new environments, similar to how organisms behave from the perspective of integrative biology [119]. This feature makes the design particularly challenging, as it is not obvious to determine the right design criteria that lead to a given desired output behavior. This challenge is amplified by the fact that the typical engineering approach divides problems into isolated subproblems, which is likely ill-suited for such tightly coupled systems. In fact, in our integrated systems, even relatively small design changes can lead to highly different behaviors, as seen in Chapter 3 where a small modification to the valve suppresses the regulation mode. More generally, in this work we followed a bottom-up approach, where we first built the devices and then let them dynamically evolve in time, while observing their outcome behavior. The next challenge will be to rationalize a top-down design approach. Knowing the desired behavior, what is the design of highly-integrated, emergent devices that will enable it? Can the design be optimized for performance, robustness, or versatility? To this end, perhaps achieving such nature-inspired designs may require adopting design processes inspired by how nature itself designs, through evolution [161].

A second grand challenge concerns the scaling of the complexity of behaviors. In this work, we achieved autonomous behaviors mainly in terms of responsiveness to external stimuli. We implemented specific rules that allow the systems to dynamically tune their behavior based on internal and external conditions. Moving from such pre-programmed

responses to increasingly complex behaviors will prove challenging. One approach could consist of exploring the interactions between our decentralized mechano-fluidic processes and classical centralized computing, so that the machines could make decisions toward a high-level goal. Could centralized control handle the complexity of our nonlinear, dynamical systems? In the spirit of embodiment, another question arises: can mechano-fluidic soft machines learn through their body, without central control? Could the machines reprogram their own internal rules while operating in the field in real time? Relatively recently, physical learning [117, 234–236] proved promising in this direction. In physical learning, networks of springs can dynamically reprogram their parameters following learning rules that are strictly local, thereby not requiring global knowledge about the entire network. This implies that the learning is physical, in that the rules can be implemented in a distributed fashion within the structure the system is made of, without needing a centralized processor [234]. Given that in physical learning the heuristics are applied locally, similar to the examples in this Thesis, would it be possible to combine the two approaches, so that the rich interactions of the mechano-fluidic devices with the surroundings could be harnessed for learning?

Lastly, while in this work we focused on the *structure* of the machines by tuning elasticity and geometry, we recognize that the *materials* with which the structures are made can play a substantial role in achieving responsiveness [237]. Relatively recently, building biohybrid machines with organic living materials [238–241] has proven promising in this direction. Biohybrid machines are composed of living cells, which are the epitome of multifunctional systems. In fact, in nature, cells simultaneously solve disparate functions, ranging from energy storage to sensing and actuation: when multiple cells are combined, complex phenomena such as decision-making emerge spontaneously, including yourself now reading these words. In this sense, a grand challenge will be to build soft machines similar to the ones presented in this Thesis with such biohybrid materials, and to rationalize the complex physics that emerges when we do so. Perhaps, not so far in the future, artificial organisms [242, 243] will prove to be soft machines that embody even higher levels of autonomy.

BIBLIOGRAPHY

1. Braitenberg, V. *Vehicles: Experiments in Synthetic Psychology* ISBN: 9780262521123 (MIT Press, 1986).
2. Maes, P. *Designing autonomous agents: Theory and practice from biology to engineering and back* ISBN: 0262631350 (MIT Press, 1990).
3. Kelly, K. *Out of control: The new biology of machines, social systems, and the economic world* ISBN: 9780201483406 (Basic Books, 1994).
4. Herzog, L. & Weschler, L. *Strandbeest : the dream machines of Theo Jansen* ISBN: 9783836548496 (Taschen, 2014).
5. Putterill, J., Laurie, R. & Macknight, R. It's time to flower: the genetic control of flowering time. *BioEssays* **26,** 363–373 (2004).
6. Lentink, D., Dickson, W. B., van Leeuwen, J. L. & Dickinson, M. H. Leading-Edge Vortices Elevate Lift of Autorotating Plant Seeds. *Science* **324,** 1438–1440 (2009).
7. Marey, J. Photographs of a Tumbling Cat. *Nature* **51,** 80–81. ISSN: 1476-4687 (Nov. 1, 1894).
8. Kane, T. & Scher, M. A dynamical explanation of the falling cat phenomenon. *International Journal of Solids and Structures* **5,** 663–670. ISSN: 0020-7683 (1969).
9. Heydari, S., Johnson, A., Ellers, O., McHenry, M. J. & Kanso, E. Sea star inspired crawling and bouncing. *Journal of The Royal Society Interface* **17,** 20190700 (2020).
10. Alexander, R. M. Optimization and gaits in the locomotion of vertebrates. *Physiological Reviews* **69,** 1199–1227 (1989).
11. Klein, C. S., Marsh, G. D., Petrella, R. J. & Rice, C. L. Muscle fiber number in the biceps brachii muscle of young and old men. *Muscle & Nerve* **28,** 62–68 (2003).
12. Ramdya, P. & Ijspeert, A. J. The neuromechanics of animal locomotion: From biology to robotics and back. *Science Robotics* **8,** eadg0279 (2023).
13. Chiel, H. J. & Beer, R. D. The brain has a body: adaptive behavior emerges from interactions of nervous system, body and environment. *Trends in Neurosciences* **20,** 553–557. ISSN: 0166-2236 (1997).
14. Dickinson, M. H., Farley, C. T., Full, R. J., Koehl, M. A. R., Kram, R. & Lehman, S. How Animals Move: An Integrative View. *Science* **288,** 100–106 (2000).

15. Beal, D. N., Hover, F. S., Triantafyllou, M. S., Liao, J. C. & Lauder, G. V. Passive propulsion in vortex wakes. *J. Fluid Mech.* **549,** 385–402 (2006).

16. Orlovsky, G., Deliagina, T. G. & Grillner, S. *Neuronal Control of Locomotion: From Mollusc to Man* ISBN: 978-0-19-852405-2 (Oxford University Press, Sept. 1999).

17. Ijspeert, A. J. Central pattern generators for locomotion control in animals and robots: a review. *Neural networks* **21,** 642–653 (2008).

18. Cruse, H., Dürr, V. & Schmitz, J. Insect walking is based on a decentralized architecture revealing a simple and robust controller. *Philosophical Transactions of the Royal Society A: Mathematical, Physical and Engineering Sciences* **365,** 221–250 (2007).

19. Zehr, E. & Stein, R. B. What functions do reflexes serve during human locomotion? *Progress in Neurobiology* **58,** 185–205. ISSN: 0301-0082 (1999).

20. Seibel, B. A. & Drazen, J. C. The rate of metabolism in marine animals: environmental constraints, ecological demands and energetic opportunities. *Philosophical Transactions of the Royal Society B: Biological Sciences* **362,** 2061–2078 (2007).

21. Flaum, E. & Prakash, M. Curved crease origami and topological singularities enable hyperextensibility of *L. olor*. *Science* **384,** eadk5511 (2024).

22. Krishnamurthy, D. & Prakash, M. Emergent programmable behavior and chaos in dynamically driven active filaments. *Proceedings of the National Academy of Sciences* **120,** e2304981120 (2023).

23. Nakagaki, T., Yamada, H. & Hara, M. Smart network solutions in an amoeboid organism. *Biophysical chemistry* **107,** 1–5 (2004).

24. Tero, A., Takagi, S., Saigusa, T., Ito, K., Bebber, D. P., Fricker, M. D., Yumiki, K., Kobayashi, R. & Nakagaki, T. Rules for Biologically Inspired Adaptive Network Design. *Science* **327,** 439–442 (2010).

25. Suzumori, K., Iikura, S. & Tanaka, H. Applying a flexible microactuator to robotic mechanisms. *IEEE Control Systems Magazine* **12,** 21–27 (1992).

26. Ilievski, F., Mazzeo, A. D., Shepherd, R. F., Chen, X. & Whitesides, G. M. Soft robotics for chemists. *Angew. Chemie - Int. Ed.* **50,** 1890–1895 (2011).

27. Trimmer, B. Soft robots. *Current Biology* **23,** R639–R641. ISSN: 0960-9822 (2013).

28. Kim, S., Laschi, C. & Trimmer, B. Soft robotics: a bioinspired evolution in robotics. *Trends in Biotechnology* **31,** 287–294. ISSN: 0167-7799. (2025) (May 2013).

29. Rus, D. & Tolley, M. T. Design, fabrication and control of soft robots. *Nature* **521,** 467–475 (2015).

30. Laschi, C., Mazzolai, B. & Cianchetti, M. Soft robotics: Technologies and systems pushing the boundaries of robot abilities. *Sci. Robot.* **1,** 1–12 (2016).

31. Aygül, C., Güven, C., Frunzi, S. A., Katz, B. J. & Nemitz, M. P. A framework for soft mechanism driven robots. *Nature Communications* **16,** 1426 (2025).

32. Shintake, J., Cacucciolo, V., Floreano, D. & Shea, H. Soft robotic grippers. *Advanced materials* **30,** 1707035 (2018).

33. Hirose, S. & Umetani, Y. The development of soft gripper for the versatile robot hand. *Mechanism and Machine Theory* **13,** 351–359. ISSN: 0094-114X (1978).

34. Wang, Z., Freris, N. M. & Wei, X. SpiRobs: Logarithmic spiral-shaped robots for versatile grasping across scales. *Device.* ISSN: 2666-9994. (2025) (2024).

35. Shepherd, R. F., Ilievski, F., Choi, W., Morin, S. A., Stokes, A. A., Mazzeo, A. D., Chen, X., Wang, M. & Whitesides, G. M. Multigait soft robot. *Proceedings of the National Academy of Sciences* **108,** 20400–20403 (2011).

36. Hawkes, E. W., Blumenschein, L. H., Greer, J. D. & Okamura, A. M. A soft robot that navigates its environment through growth. *Science Robotics* **2,** eaan3028 (2017).

37. Hawkes, E. W., Majidi, C. & Tolley, M. T. Hard questions for soft robotics. *Sci. Robot.* **6** (2021).

38. Pfeifer, R. & Bongard, J. *How the Body Shapes the Way We Think: A New View of Intelligence* ISBN: 9780262281553 (MIT Press, Oct. 2006).

39. Tolley, M. T., Shepherd, R. F., Mosadegh, B., Galloway, K. C., Wehner, M., Karpelson, M., Wood, R. J. & Whitesides, G. M. A Resilient, Untethered Soft Robot. *Soft Robotics* **1,** 213–223 (2014).

40. Kumar, S., Tiwari, I., Ortega-Jimenez, V. M., Dillman, A. R., He, D., Hu, Y. & Bhamla, S. Reversible kink instability drives ultrafast jumping in nematodes and soft robots. *Science Robotics* **10,** eadq3121 (2025).

41. Overvelde, J. T. B., Kloek, T., D'haen, J. J. A. & Bertoldi, K. Amplifying the response of soft actuators by harnessing snap-through instabilities. *Proceedings of the National Academy of Sciences* **112,** 10863–10868 (2015).

42. Patek, S. N., Korff, W. & Caldwell, R. L. Deadly strike mechanism of a mantis shrimp. *Nature* **428,** 819–820 (2004).

43. Steinhardt, E., seung P. Hyun, N., sung Koh, J., Freeburn, G., Rosen, M. H., Temel, F. Z., Patek, S. N. & Wood, R. J. A physical model of mantis shrimp for exploring the dynamics of ultrafast systems. *Proceedings of the National Academy of Sciences* **118,** e2026833118 (2021).

44. Gorissen, B., Milana, E., Baeyens, A., Broeders, E., Christiaens, J., Collin, K., Reynaerts, D. & De Volder, M. Hardware Sequencing of Inflatable Nonlinear Actuators for Autonomous Soft Robots. *Advanced Materials* **31,** 1804598 (2019).

45. McDonald, K. & Ranzani, T. Hardware Methods for Onboard Control of Fluidically Actuated Soft Robots. *Frontiers in Robotics and AI* **8.** ISSN: 2296-9144 (2021).

46. Vasios, N., Gross, A. J., Soifer, S., Overvelde, J. T. B. & Bertoldi, K. Harnessing Viscous Flow to Simplify the Actuation of Fluidic Soft Robots. *Soft Robotics* **7,** 1–9 (2020).

47. Matia, Y., Kaiser, G. H., Shepherd, R. F., Gat, A. D., Lazarus, N. & Petersen, K. H. Harnessing Nonuniform Pressure Distributions in Soft Robotic Actuators. *Advanced Intelligent Systems* **5,** 2200330 (2023).

48. Luo, K., Rothemund, P., Whitesides, G. M. & Suo, Z. Soft kink valves. *Journal of the Mechanics and Physics of Solids* **131,** 230–239. ISSN: 0022-5096 (2019).

49. Decker, C. J., Jiang, H. J., Nemitz, M. P., Root, S. E., Rajappan, A., Alvarez, J. T., Tracz, J., Wille, L., Preston, D. J. & Whitesides, G. M. Programmable soft valves for digital and analog control. *Proceedings of the National Academy of Sciences* **119,** e2205922119 (2022).

50. Rothemund, P., Ainla, A., Belding, L., Preston, D. J., Kurihara, S., Suo, Z. & Whitesides, G. M. A soft, bistable valve for autonomous control of soft actuators. *Science Robotics* **3,** eaar7986 (2018).

51. Preston, D. J., Rothemund, P., Jiang, H. J., Nemitz, M. P., Rawson, J., Suo, Z. & Whitesides, G. M. Digital logic for soft devices. *Proceedings of the National Academy of Sciences* **116,** 7750–7759 (2019).

52. Zhai, Y., Boer, A. D., Yan, J., Shih, B., Faber, M., Speros, J., Gupta, R. & Tolley, M. T. Desktop fabrication of monolithic soft robotic devices with embedded fluidic control circuits. *Science Robotics* **8,** eadg3792 (2023).

53. van Laake, L. C., de Vries, J., Malek Kani, S. & Overvelde, J. T. B. A fluidic relaxation oscillator for reprogrammable sequential actuation in soft robots. *Matter* **5,** 2898–2917. ISSN: 2590-2385 (2022).

54. Mousa, M., Rezanejad, A., Gorissen, B. & Forte, A. E. Frequency-Controlled Fluidic Oscillators for Soft Robots (Adv. Sci. 43/2024). *Advanced Science* **11,** 2470264 (2024).

55. Conrad, S., Teichmann, J., Auth, P., Knorr, N., Ulrich, K., Bellin, D., Speck, T. & Tauber, F. J. 3D-printed digital pneumatic logic for the control of soft robotic actuators. *Science Robotics* **9,** eadh4060 (2024).

56. Preston, D. J., Jiang, H. J., Sanchez, V., Rothemund, P., Rawson, J., Nemitz, M. P., Lee, W.-K., Suo, Z., Walsh, C. J. & Whitesides, G. M. A soft ring oscillator. *Science Robotics* **4,** eaaw5496 (2019).

57. Drotman, D., Jadhav, S., Sharp, D., Chan, C. & Tolley, M. T. Electronics-free pneumatic circuits for controlling soft-legged robots. *Science Robotics* **6,** eaay2627 (2021).

58. Lee, W.-K., Preston, D. J., Nemitz, M. P., Nagarkar, A., MacKeith, A. K., Gorissen, B., Vasios, N., Sanchez, V., Bertoldi, K., Mahadevan, L. & Whitesides, G. M. A buckling-sheet ring oscillator for electronics-free, multimodal locomotion. *Science Robotics* **7,** eabg5812 (2022).

59. Brown, P. E. *United States Patent : 5861366 DISPENSING VALVE FOR PACKAGING* 1995.

60. Xi, Y., Marzin, T., Huang, R. B., Jones, T. J. & Brun, P.-T. Emergent behaviors of buckling-driven elasto-active structures. *Proceedings of the National Academy of Sciences* **121,** e2410654121 (2024).

61. Guan, J. H., Tamim, S. I., Magoon, C. W., Stone, H. A. & Sáenz, P. J. Galloping Bubbles. *Nature Communications* **16,** 1572. ISSN: 2041-1723 (Feb. 2025).

62. Aubin, C. A., Gorissen, B., Milana, E., Buskohl, P. R., Lazarus, N., Slipher, G. A., Keplinger, C., Bongard, J., Iida, F., Lewis, J. A. & Shepherd, R. F. Towards enduring autonomous robots via embodied energy. *Nature* **602,** 393–402 (2022).

63. Rus, D. & Tolley, M. T. Design, fabrication and control of soft robots. *Nature* **521,** 467–475 (2015).

64. Whitesides, G. M. Soft Robotics. *Angewandte Chemie International Edition* **57,** 4258–4273 (2018).

65. Brown, E., Rodenberg, N., Amend, J., Mozeika, A., Steltz, E., Zakin, M. R., Lipson, H. & Jaeger, H. M. Universal robotic gripper based on the jamming of granular material. *Proceedings of the National Academy of Sciences* **107,** 18809–18814 (2010).

66. Drotman, D., Jadhav, S., Karimi, M., de Zonia, P. & Tolley, M. T. *3D printed soft actuators for a legged robot capable of navigating unstructured terrain* in *2017 IEEE International Conference on Robotics and Automation (ICRA)* (2017), 5532–5538.

67. Bai, H., Kim, Y. S. & Shepherd, R. F. Autonomous self-healing optical sensors for damage intelligent soft-bodied systems. *Science Advances* **8,** eabq2104 (2022).

68. Po, T., Kanso, E. & McHenry, M. J. Cooperative transport in sea star locomotion. *Current Biology* **34,** 2551–2557.e4. ISSN: 0960-9822 (2024).

69. Delvolvé, I., Bem, T. & Cabelguen, J.-M. Epaxial and Limb Muscle Activity During Swimming and Terrestrial Stepping in the Adult Newt, Pleurodeles waltl. *Journal of Neurophysiology* **78,** 638–650 (1997).

70. Ijspeert, A. J., Crespi, A., Ryczko, D. & Cabelguen, J.-M. From Swimming to Walking with a Salamander Robot Driven by a Spinal Cord Model. *Science* **315,** 1416–1420 (2007).

71. Flavell, S. W., Raizen, D. M. & You, Y.-J. Behavioral States. *Genetics* **216,** 315–332. ISSN: 1943-2631 (Oct. 2020).

72. Kamp, L. M., Zanaty, M., Zareei, A., Gorissen, B., Wood, R. J. & Bertoldi, K. Reprogrammable sequencing for physically intelligent under-actuated robots. *arXiv preprint arXiv:2409.03737* (2024).

73. Zhao, Y., Chi, Y., Hong, Y., Li, Y., Yang, S. & Yin, J. Twisting for soft intelligent autonomous robot in unstructured environments. *Proceedings of the National Academy of Sciences* **119,** e2200265119 (2022).

74. He, Q., Yin, R., Hua, Y., Jiao, W., Mo, C., Shu, H. & Raney, J. R. A modular strategy for distributed, embodied control of electronics-free soft robots. *Science Advances* **9,** eade9247 (2023).

75. Comoretto, A., Schomaker, H. A. H. & Overvelde, J. T. B. Physical synchronization of soft self-oscillating limbs for fast and autonomous locomotion. *Science* **388,** 610–615 (2025).

76. Kaspar, C., Ravoo, B. J., van der Wiel, W. G., Wegner, S. V. & Pernice, W. H. The rise of intelligent matter. *Nature* **594,** 345–355 (2021).

77. Chen, T., Pauly, M. & Reis, P. M. A reprogrammable mechanical metamaterial with stable memory. *Nature* **589,** 386–390. ISSN: 1476-4687 (Jan. 2021).

78. Yasuda, H., Buskohl, P. R., Gillman, A., Murphey, T. D., Stepney, S., Vaia, R. A. & Raney, J. R. Mechanical computing. *Nature* **598,** 39–48 (2021).

79. Kwakernaak, L. J. & van Hecke, M. Counting and Sequential Information Processing in Mechanical Metamaterials. *Phys. Rev. Lett.* **130,** 268204 (26 2023).

80. Jules, T., Reid, A., Daniels, K. E., Mungan, M. & Lechenault, F. Delicate memory structure of origami switches. *Physical Review Research* **4,** 013128 (2022).

81. Bense, H. & van Hecke, M. Complex pathways and memory in compressed corrugated sheets. *Proceedings of the National Academy of Sciences* **118,** e2111436118 (2021).

82. Shohat, D., Hexner, D. & Lahini, Y. Memory from coupled instabilities in unfolded crumpled sheets. *Proceedings of the National Academy of Sciences* **119,** e2200028119 (2022).

83. Guo, X., Guzmán, M., Carpentier, D., Bartolo, D. & Coulais, C. Non-orientable order and non-commutative response in frustrated metamaterials. *Nature* **618,** 506–512 (2023).

84. Yasuda, H., Tachi, T., Lee, M. & Yang, J. Origami-based tunable truss structures for non-volatile mechanical memory operation. *Nature Communications* **8,** 962 (2017).

85. Bell, M. A., Cattani, L., Gorissen, B., Bertoldi, K., Weaver, J. C. & Wood, R. J. A soft, modular, and bi-stable dome actuator for programmable multi-modal locomotion. *IEEE Int. Conf. Intell. Robot. Syst.*, 6529–6535 (2020).

86. Park, T., Choi, E., Kim, C. S., Park, J. O. & Hong, A. A Multi-Segmented Soft Finger Using Snap-Through Instability of a Soft Valve With a Slit. *IEEE Robot. Autom. Lett.* **7,** 6990–6997 (2022).

87. Van Raemdonck, B., Milana, E., De Volder, M., Reynaerts, D. & Gorissen, B. Nonlinear Inflatable Actuators for Distributed Control in Soft Robots. *Advanced Materials* **35,** 2301487 (2023).

88. van Laake, L. C., Comoretto, A. & Overvelde, J. T. B. On the coexistence of pressure regulation and oscillation modes in soft hysteretic valves. *Journal of Fluids and Structures* **126,** 104090. ISSN: 0889-9746 (2024).

89. Picella, S., van Riet, C. M. & Overvelde, J. T. B. Pneumatic coding blocks enable programmability of electronics-free fluidic soft robots. *Science Advances* **10,** eadr2433 (2024).

90. Taffetani, M., Jiang, X., Holmes, D. P. & Vella, D. Static bistability of spherical Caps. *Proc. R. Soc. A Math. Phys. Eng. Sci.* **474** (2018).

91. Arfaee, M., Kluin, J. & Overvelde, J. T. B. *Modeling the behavior of elastic pouch motors* in *2023 IEEE International Conference on Soft Robotics (RoboSoft)* (2023), 1–6.

92. Zou, S., Picella, S., de Vries, J., Kortman, V. G., Sakes, A. & Overvelde, J. T. B. A retrofit sensing strategy for soft fluidic robots. *Nature Communications* **15,** 539 (2024).

93. Liu, T., Chen, Y., Hutchinson, J. W. & Jin, L. Buckling of viscoelastic spherical shells. *J. Mech. Phys. Solids* **169,** 105084 (2022).

94. Pandey, A., Moulton, D. E., Vella, D. & Holmes, D. P. Dynamics of snapping beams and jumping poppers. *EPL (Europhysics Lett.* **105,** 24001 (2014).

95. Gorissen, B., Melancon, D., Vasios, N., Torbati, M. & Bertoldi, K. Inflatable soft jumper inspired by shell snapping. *Science Robotics* **5,** eabb1967 (2020).

96. Abbasi, A., Yan, D. & Reis, P. M. Probing the buckling of pressurized spherical shells. *J. Mech. Phys. Solids* **155,** 104545 (2021).

97. Lee, A., Jiménez, F. L., Marthelot, J., Hutchinson, J. W. & Reis, P. M. The Geometric Role of Precisely Engineered Imperfections on the Critical Buckling Load of Spherical Elastic Shells. *J. Appl. Mech. Trans. ASME* **83,** 1–11 (2016).

98. Sobota, P. M. & Seffen, K. A. Bistable polar-orthotropic shallow shells. *Royal Society Open Science* **6,** 190888 (2019).

99. Morash, V. S., Pensky, A. E. C. & Miele, J. A. Effects of Using Multiple Hands and Fingers on Haptic Performance. *Perception* **42,** 759–777 (2013).

100. Cowan, N. in *Essence of Memory* (eds Sossin, W. S., Lacaille, J.-C., Castellucci, V. F. & Belleville, S.) 323–338 (Elsevier, 2008).

101. Martin, G., Carlson, N. & Buskist, W. *Psychology* 2010.

102. Staudacher, E. M., Gebhardt, M. & Dürr, V. in (ed Simpson, S.) 49–205 (Academic Press, 2005).

103. Saager, F. & Gewecke, M. Antennal Reflexes in the Desert Locust Schistocerca Gregaria. *Journal of Experimental Biology* **147,** 519–532. ISSN: 0022-0949 (Nov. 1989).

104. GEWECKE, M. Antennae: Another Wind-sensitive Receptor in Locusts. *Nature* **225,** 1263–1264 (1970).

105. Lundstrom, M. Moore's Law Forever? *Science* **299,** 210–211 (2003).

106. Sitti, M. Physical intelligence as a new paradigm. *Extreme Mechanics Letters* **46,** 101340. ISSN: 2352-4316 (2021).

107. Sitti, M., Ceylan, H., Hu, W., Giltinan, J., Turan, M., Yim, S. & Diller, E. Biomedical Applications of Untethered Mobile Milli/Microrobots. *Proceedings of the IEEE* **103,** 205–224. ISSN: 0018-9219 (2015).

108. Furube, T., Nakashima, D., Matsuda, S., Mikami, K., Hatakeyama, T., Takeuchi, M., Fukuda, K., Ueno, A., Okita, H., Kawakubo, H., Nakamura, M., Nagura, T. & Kitagawa, Y. Evaluating stiffness of gastric wall using laser resonance frequency analysis for gastric cancer. *Cancer Science* **116,** 143–151. ISSN: 1349-7006 (2025).

109. Kim, K., Edwards, S., Fuxa, K., Lin, H., Shrestha, S., Fan, H., Diaz, N., Berinstein, J., Naik, R., Zhou, Y. & Dong, X. Mucosa-Interfacing Capsule for In Situ Sensing the Elasticity of Biological Tissues. *Advanced Materials Technologies* **n/a,** 2401487.

110. Miskin, M. Z., Cortese, A. J., Dorsey, K., Esposito, E. P., Reynolds, M. F., Liu, Q., Cao, M., Muller, D. A., McEuen, P. L. & Cohen, I. Electronically integrated, mass-manufactured, microscopic robots. *Nature* **584,** 557–561 (2020).

111. Klesh, A. T., Cutler, J. W. & Atkins, E. M. *Cyber-Physical Challenges for Space Systems* in *2012 IEEE/ACM Third International Conference on Cyber-Physical Systems* (2012), 45–52.

112. Dunbabin, M. & Marques, L. Robots for Environmental Monitoring: Significant Advancements and Applications. *IEEE Robotics Automation Magazine* **19,** 24–39 (2012).

113. Zhai, Y., Yan, J., De Boer, A., Faber, M., Gupta, R. & Tolley, M. T. Monolithic Desktop Digital Fabrication of Autonomous Walking Robots. *Advanced Intelligent Systems* **n/a,** 2400876 (2025).

114. Luo, D., Maheshwari, A., Danielescu, A., Li, J., Yang, Y., Tao, Y., Sun, L., Patel, D. K., Wang, G., Yang, S., *et al.* Autonomous self-burying seed carriers for aerial seeding. *Nature* **614,** 463–470 (2023).

115. Miyaki, Y. & Tsukagoshi, H. Self-Excited Vibration Valve That Induces Traveling Waves in Pneumatic Soft Mobile Robots. *IEEE Robotics and Automation Letters* **5,** 4133–4139 (2020).

116. Van Laake, L. C. & Overvelde, J. T. B. Bio-inspired autonomy in soft robots. *Communications Materials* **5,** 198 (2024).

117. Patil, V. P., Ho, I. & Prakash, M. Self-learning mechanical circuits. *arXiv preprint arXiv:2304.08711* (2023).

118. Schomaker, H. A. H., Picella, S., Küng Garcia, A., van Laake, L. C. & Overvelde, J. T. B. Robust Phototaxis by Harnessing Implicit Communication in Modular Soft Robotic Systems. *Advanced Functional Materials* **34,** 2310932 (2024).

119. Tavassoly, I., Goldfarb, J. & Iyengar, R. Systems biology primer: the basic methods and approaches. *Essays in biochemistry* **62,** 487–500 (2018).

120. Comoretto, A., Koppen, S., Mandke, T. & Overvelde, J. T. B. Embodying mechano-fluidic memory in soft machines to program behavior upon interactions: replication package. *Zenodo* (2025).

121. Robin, A. C. Paper bag problem. *Mathematics today* **40,** 104–107 (June 2004).

122. Oh, K. W., Lee, K., Ahn, B. & Furlani, E. P. Design of pressure-driven microfluidic networks using electric circuit analogy. *Lab Chip* **12,** 515–545 (2012).

123. Gorissen, B., Reynaerts, D., Konishi, S., Yoshida, K., Kim, J. W. & De Volder, M. Elastic Inflatable Actuators for Soft Robotic Applications. *Adv. Mater.* **29,** 1–14 (2017).

124. Rich, S. I., Wood, R. J. & Majidi, C. Untethered soft robotics. *Nat. Electron.* **1,** 102–112 (2018).

125. Wehner, M., Truby, R. L., Fitzgerald, D. J., Mosadegh, B., Whitesides, G. M., Lewis, J. A. & Wood, R. J. An integrated design and fabrication strategy for entirely soft, autonomous robots. *Nature* **536,** 451–455 (2016).

126. Mahon, S. T., Buchoux, A., Sayed, M. E., Teng, L. & Stokes, A. A. Soft Robots for Extreme Environments: Removing Electronic Control. *CoRR* **abs/1903.10779** (2019).

127. Hubbard, J. D., Acevedo, R., Edwards, K. M., Alsharhan, A. T., Wen, Z., Landry, J., Wang, K., Schaffer, S. & Sochol, R. D. Fully 3D-printed soft robots with integrated fluidic circuitry. *Science Advances* **7,** eabe5257 (2021).

128. Song, S., Joshi, S. & Paik, J. CMOS-Inspired Complementary Fluidic Circuits for Soft Robots. *Adv. Sci.* **2100924,** 2100924 (2021).

129. Hoang, S., Karydis, K., Brisk, P. & Grover, W. H. A pneumatic random-access memory for controlling soft robots. *PLoS One* **16,** 1–25 (2021).

130. Napp, N., Araki, B., Tolley, M. T., Nagpal, R. & Wood, R. J. *Simple passive valves for addressable pneumatic actuation* in *2014 IEEE Int. Conf. Robot. Autom.* (IEEE, 2014), 1440–1445. ISBN: 978-1-4799-3685-4.

131. Comoretto, A., Koppen, S., Mandke, T. & Overvelde, J. T. Embodying mechano-fluidic memory in soft machines to program behaviors upon interactions. *Device* **3,** 100863 (2025).

132. Arfaee, M., Vis, A. & Kluin, J. Future technologies in total artificial heart development: can a robot become as good as a donor heart? *Eur. Heart J.,* 1–3 (2022).

133. Arfaee, M., Vis, A., Bartels, P. A., van Laake, L. C., Lorenzon, L., Ibrahim, D. M., Zrinscak, D., Smits, A. I., Henseler, A., Cianchetti, M., *et al.* A soft robotic total artificial hybrid heart. *Nature Communications* **16,** 1–14 (2025).

134. Reis, P. M. A Perspective on the Revival of Structural (In) Stability With Novel Opportunities for Function: From Buckliphobia to Buckliphilia. *J. Appl. Mech. Trans. ASME* **82,** 111001 (2015).

135. Champneys, A. R., Dodwell, T. J., Groh, R. M., Hunt, G. W., Neville, R. M., Pirrera, A., Sakhaei, A. H., Schenk, M. & Wadee, M. A. Happy Catastrophe: Recent Progress in Analysis and Exploitation of Elastic Instability. *Front. Appl. Math. Stat.* **5,** 1–30 (2019).

136. Marthelot, J., Jiménez, F. L., Lee, A., Hutchinson, J. W. & Reis, P. M. Buckling of a Pressurized Hemispherical Shell Subjected to a Probing Force. *J. Appl. Mech. Trans. ASME* **84** (2017).

137. Evkin, A. Y. & Lykhachova, O. V. Design buckling pressure for thin spherical shells: Development and validation. *Int. J. Solids Struct.* **156-157,** 61–72 (2019).

138. Gomez, M., Moulton, D. E. & Vella, D. Critical slowing down in purely elastic 'snap-through' instabilities. *Nat. Phys.* **13,** 142–145 (2017).

139. Gomez, M., Moulton, D. E. & Vella, D. Dynamics of viscoelastic snap-through. *J. Mech. Phys. Solids* **124,** 781–813 (2019).

140. Brinkmeyer, A., Santer, M., Pirrera, A. & Weaver, P. M. Pseudo-bistable self-actuated domes for morphing applications. *Int. J. Solids Struct.* **49,** 1077–1087 (2012).

141. Welty, J., Wicks, C., Wilson, R., Rorrer, G. *Fundamentals of Momentum, Heat, and Mass transfer* ISBN: 9780470128688 (Wiley, 2007).

142. Strogatz, S. H. *Nonlinear dynamics and chaos: with applications to physics, biology, chemistry, and engineering* (Chapman and Hall/CRC, 2024).

143. Khalil, H. *Nonlinear Systems* ISBN: 9780130673893 (Prentice Hall, 2002).

144. Ijspeert, A. J. Biorobotics: Using robots to emulate and investigate agile locomotion. *Science* **346,** 196–203 (2014).

145. Clark, E. G., Kanauchi, D., Kano, T., Aonuma, H., Briggs, D. E. G. & Ishiguro, A. The function of the ophiuroid nerve ring: how a decentralized nervous system controls coordinated locomotion. *Journal of Experimental Biology* **222,** jeb192104. ISSN: 0022-0949 (Jan. 2019).

146. Pfeifer, R., Lungarella, M. & Iida, F. Self-Organization, Embodiment, and Biologically Inspired Robotics. *Science* **318,** 1088–1093 (2007).

147. Collins, S., Ruina, A., Tedrake, R. & Wisse, M. Efficient Bipedal Robots Based on Passive-Dynamic Walkers. *Science* **307,** 1082–1085 (2005).

148. Stella, F., Achkar, M. M., Della Santina, C. & Hughes, J. Synergy-based robotic quadruped leveraging passivity for natural intelligence and behavioural diversity. *Nature Machine Intelligence,* 1–14 (2025).

149. Raibert, M. H. *Legged robots that balance* (MIT Press, 1986).

150. Nabae, H. & Kitamura, E. Self-excited valve using a flat ring tube: Application to robotics. *Frontiers in Robotics and AI* **9.** ISSN: 2296-9144 (2022).

151. Yirmibeşoğlu, O. D., Oshiro, T., Olson, G., Palmer, C. & Mengüç, Y. Evaluation of 3D Printed Soft Robots in Radiation Environments and Comparison With Molded Counterparts. *Frontiers in Robotics and AI* **6.** ISSN: 2296-9144 (2019).

152. Casper, J. L., Micire, M. & Murphy, R. R. *Issues in intelligent robots for search and rescue* in *Unmanned Ground Vehicle Technology II* (eds Gerhart, G. R., Gunderson, R. W. & Shoemaker, C. M.) **4024** (SPIE, 2000), 292 –302.

153. Tsukagoshi, H., Kitagawa, A., Tambo, K. & Chiba, H. *A Fluid Self-excited Oscillation Peculiar to Flat Ring Tube and its Application to Wearable Robots* in *Proceedings 2007 IEEE International Conference on Robotics and Automation* (2007), 3138–3139.

154. Gazit, D. & Dranger, A. L. *Apparatus and method for providing inflated undulating figures* (US6186857B1 Patent, 2001).

155. Pikovsky, A., Rosenblum, M. & Kurths, J. *Synchronization: A Universal Concept in Nonlinear Sciences* (Cambridge University Press, 2001).

156. Vantomme, G., Elands, L. C. M., Gelebart, A. H., Meijer, E. W., Pogromsky, A. Y., Nijmeijer, H. & Broer, D. J. Coupled liquid crystalline oscillators in Huygens' synchrony. *Nature Materials* **20,** 1702–1706 (2021).

157. Wu, Y., Yim, J. K., Liang, J., Shao, Z., Qi, M., Zhong, J., Luo, Z., Yan, X., Zhang, M., Wang, X., Fearing, R. S., Full, R. J. & Lin, L. Insect-scale fast moving and ultrarobust soft robot. *Science Robotics* **4,** eaax1594 (2019).

158. Walther, F. R. Flight Behaviour and Avoidance of Predators in Thomson's Gazelle (Gazella Thomsoni Guenther 1884). *Behaviour* **34,** 184–221. ISSN: 00057959. (2023) (1969).

159. Xiong, Z., Su, Y. & Lipson, H. *Fast Untethered Soft Robotic Crawler with Elastic Instability* in *2023 IEEE International Conference on Robotics and Automation (ICRA)* (2023), 2606–2612.

160. Baines, R., Patiballa, S. K., Booth, J., Ramirez, L., Sipple, T., Garcia, A., Fish, F. & Kramer-Bottiglio, R. Multi-environment robotic transitions through adaptive morphogenesis. *Nature* **610,** 283–289 (2022).

161. Bhatia, J. S., Jackson, H., Tian, Y., Xu, J. & Matusik, W. *Evolution gym: a large-scale benchmark for evolving soft robots* in *Proceedings of the 35th International Conference on Neural Information Processing Systems* (Curran Associates Inc., Red Hook, NY, USA, 2024). ISBN: 9781713845393.

162. Aguilar, J., Zhang, T., Qian, F., Kingsbury, M., McInroe, B., Mazouchova, N., Li, C., Maladen, R., Gong, C., Travers, M., Hatton, R. L., Choset, H., Umbanhowar, P. B. & Goldman, D. I. A review on locomotion robophysics: the study of movement at the intersection of robotics, soft matter and dynamical systems. *Reports on Progress in Physics* **79,** 110001 (2016).

163. Aydin, Y. O., Rieser, J. M., Hubicki, C. M., Savoie, W. & Goldman, D. I. in *Robotic Systems and Autonomous Platforms* (eds Walsh, S. M. & Strano, M. S.) 109–127 (Woodhead Publishing, 2019). ISBN: 978-0-08-102260-3.

164. Bull, M. S., Prakash, V. N. & Prakash, M. Ciliary flocking and emergent instabilities enable collective agility in a non-neuromuscular animal. *arXiv preprint arXiv:2107.02934* (2021).

165. Usevitch, N. S., Hammond, Z. M., Schwager, M., Okamura, A. M., Hawkes, E. W. & Follmer, S. An untethered isoperimetric soft robot. *Science Robotics* **5,** eaaz0492 (2020).

166. Comoretto, A., Schomaker, H. A. H. & Overvelde, J. T. B. Physical synchronization of soft self-oscillating limbs for fast and autonomous locomotion: replication package. *Zenodo* (2025).

167. Van Raemdonck, B., Milana, E., De Volder, M., Reynaerts, D. & Gorissen, B. Nonlinear Inflatable Actuators for Distributed Control in Soft Robots. *Advanced Materials* **35,** 2301487 (2023).

168. Alexander, R. M. Optimization and gaits in the locomotion of vertebrates. *Physiological Reviews* **69,** 1199–1227 (1989).

169. Alexander, R. M. Walking and running. *The Mathematical Gazette* **80,** 262–266 (1996).

170. Mao, G., Schiller, D., Danninger, D., Hailegnaw, B., Hartmann, F., Stockinger, T., Drack, M., Arnold, N. & Kaltenbrunner, M. Ultrafast small-scale soft electromagnetic robots. *Nature Communications* **13,** 4456 (2022).

171. Hu, W., Lum, G. Z., Mastrangeli, M. & Sitti, M. Small-scale soft-bodied robot with multimodal locomotion. *Nature* **554,** 81–85 (2018).

172. Zhao, J., Zhang, J., McCoul, D., Hao, Z., Wang, S., Wang, X., Huang, B. & Sun, L. Soft and Fast Hopping–Running Robot with Speed of Six Times Its Body Length Per Second. *Soft Robotics* **6,** 713–721 (2019).

173. Chen, R., Yuan, Z., Guo, J., Bai, L., Zhu, X., Liu, F., Pu, H., Xin, L., Peng, Y., Luo, J., Wen, L. & Sun, Y. Legless soft robots capable of rapid, continuous, and steered jumping. *Nature Communications* **12,** 7028 (2021).

174. Aubin, C. A., Heisser, R. H., Peretz, O., Timko, J., Lo, J., Helbling, E. F., Sobhani, S., Gat, A. D. & Shepherd, R. F. Powerful, soft combustion actuators for insect-scale robots. *Science* **381,** 1212–1217 (2023).

175. Tang, Y., Chi, Y., Sun, J., Huang, T.-H., Maghsoudi, O. H., Spence, A., Zhao, J., Su, H. & Yin, J. Leveraging elastic instabilities for amplified performance: Spine-inspired high-speed and high-force soft robots. *Science Advances* **6,** eaaz6912 (2020).

176. Huang, X., Kumar, K., Jawed, M. K., Nasab, A. M., Ye, Z., Shan, W. & Majidi, C. Chasing biomimetic locomotion speeds: Creating untethered soft robots with shape memory alloy actuators. *Science Robotics* **3,** eaau7557 (2018).

177. Robertson, M. A. & Paik, J. New soft robots really suck: Vacuum-powered systems empower diverse capabilities. *Science Robotics* **2,** eaan6357 (2017).

178. Duduta, M., Clarke, D. R. & Wood, R. J. *A high speed soft robot based on dielectric elastomer actuators* in *2017 IEEE International Conference on Robotics and Automation (ICRA)* (2017), 4346–4351.

179. Ji, X., Liu, X., Cacucciolo, V., Imboden, M., Civet, Y., Haitami, A. E., Cantin, S., Perriard, Y. & Shea, H. An autonomous untethered fast soft robotic insect driven by low-voltage dielectric elastomer actuators. *Science Robotics* **4,** eaaz6451 (2019).

180. Park, T. & Cha, Y. Soft mobile robot inspired by animal-like running motion. *Scientific Reports* **9,** 14700 (2019).

181. Umedachi, T, Vikas, V & Trimmer, B. A. Softworms: the design and control of non-pneumatic, 3D-printed, deformable robots. *Bioinspiration Biomimetics* **11,** 025001 (2016).

182. Liang, J., Wu, Y., Yim, J. K., Chen, H., Miao, Z., Liu, H., Liu, Y., Liu, Y., Wang, D., Qiu, W., Shao, Z., Zhang, M., Wang, X., Zhong, J. & Lin, L. Electrostatic footpads enable agile insect-scale soft robots with trajectory control. *Science Robotics* **6,** eabe7906 (2021).

183. Wikipedia contributors. *Standard litre per minute — Wikipedia, The Free Encyclopedia* 2023.

184. Milana, E., Santina, C. D., Gorissen, B. & Rothemund, P. Physical control: A new avenue to achieve intelligence in soft robotics. *Science Robotics* **10,** eadw7660 (2025).

185. Jenkins, A. Self-oscillation. *Physics Reports* **525,** 167–222. ISSN: 0370-1573 (2013).

186. Tanaka, S., Nabae, H. & Suzumori, K. Serially Coupled Self-Excited Pneumatic Actuator for Environment-Adaptive Steering Robot. *IEEE Robotics and Automation Letters* **9,** 10479–10486 (2024).

187. Mosadegh, B., Kuo, C. H., Tung, Y. C., Torisawa, Y. S., Bersano-Begey, T., Tavana, H. & Takayama, S. Integrated elastomeric components for autonomous regulation of sequential and oscillatory flow switching in microfluidic devices. *Nat. Phys.* **6,** 433–437 (2010).

188. Onal, C. D., Chen, X., Whitesides, G. M. & Rus, D. *Soft mobile robots with on-board chemical pressure generation* in *Robotics Research: The 15th International Symposium ISRR* (2017), 525–540.

189. Gollob, S. D., Comoretto, A., Yu, Q., Fernandez, M., Adebajo, K., Overvelde, J. T. B., Becker, K. & Roche, E. T. *A Pressure-Amplifying Monopropellant Engine for Actuator-Localized Pneumatic Power* in *2025 IEEE 8th International Conference on Soft Robotics (RoboSoft)* (2025), 1–8.

190. Gelebart, A. H., Jan Mulder, D., Varga, M., Konya, A., Vantomme, G., Meijer, E., Selinger, R. L. & Broer, D. J. Making waves in a photoactive polymer film. *Nature* **546,** 632–636 (2017).

191. Gelebart, A. H., Vantomme, G., Meijer, E. & Broer, D. J. Mastering the photothermal effect in liquid crystal networks: a general approach for self-sustained mechanical oscillators. *Advanced Materials* **29,** 1606712 (2017).

192. Zhao, Y., Xuan, C., Qian, X., Alsaid, Y., Hua, M., Jin, L. & He, X. Soft phototactic swimmer based on self-sustained hydrogel oscillator. *Science Robotics* **4,** eaax7112 (2019).

193. Zhao, Y., Li, Q., Liu, Z., Alsaid, Y., Shi, P., Khalid Jawed, M. & He, X. Sunlight-powered self-excited oscillators for sustainable autonomous soft robotics. *Science Robotics* **8,** eadf4753 (2023).

194. Zumdahl, S. S. & Zumdahl, S. A. *Chemistry* 9th ed. (Cengage Learning, 2014).

195. Wehner, M., Tolley, M. T., Mengüç, Y., Park, Y.-L., Mozeika, A., Ding, Y., Onal, C., Shepherd, R. F., Whitesides, G. M. & Wood, R. J. Pneumatic energy sources for autonomous and wearable soft robotics. *Soft Robotics* **1,** 263–274 (2014).

196. Hart-Smith, L. & Crisp, J. Large elastic deformations of thin rubber membranes. *International Journal of Engineering Science* **5,** 1–24 (1967).

197. Selvadurai, A. & Shi, M. Fluid pressure loading of a hyperelastic membrane. *International Journal of Non-Linear Mechanics* **47,** 228–239 (2012).

198. Mok, J., Helms, W., Sisco, J. & Anderson, W. Thermal decomposition of hydrogen peroxide, part i: Experimental results. *Journal of propulsion and power* **21,** 942–953 (2005).

199. Corpening, J., Heister, S., Anderson, W. & Austin, B. *A model for thermal decomposition of hydrogen peroxide* in *40th AIAA/ASME/SAE/ASEE Joint Propulsion Conference and Exhibit* (2004), 3373.

200. Pirault-Roy, L., Kappenstein, C., Guerin, M., Eloirdi, R. & Pillet, N. Hydrogen peroxide decomposition on various supported catalysts effect of stabilizers. *Journal of Propulsion and Power* **18,** 1235–1241 (2002).

201. Shampine, L. F. & Reichelt, M. W. The MATLAB ODE Suite. *SIAM journal on scientific computing* **18,** 1–22 (1997).

202. Press, W. H. *Numerical recipes 3rd edition: The art of scientific computing* (Cambridge University Press, 2007).

203. Meijer, L. H., Joesaar, A., Steur, E., Engelen, W., van Santen, R. A., Merkx, M. & de Greef, T. F. Hierarchical control of enzymatic actuators using DNA-based switchable memories. *Nature Communications* **8,** 1117 (2017).

204. Siddique, J., Anderson, D. & Bondarev, A. Capillary rise of a liquid into a deformable porous material. *Physics of fluids* **21** (2009).

205. Ha, J., Kim, J., Jung, Y., Yun, G., Kim, D.-N. & Kim, H.-Y. Poroelasto-capillary wicking of cellulose sponges. *Science Advances* **4,** eaao7051 (2018).

206. Hans-Joachim, R. & Georg, P. *Production of hydrogen peroxide* 1939.

207. Edwards, J. K. & Hutchings, G. J. Palladium and gold–palladium catalysts for the direct synthesis of hydrogen peroxide. *Angewandte Chemie International Edition* **47,** 9192–9198 (2008).

208. Xia, C., Xia, Y., Zhu, P., Fan, L. & Wang, H. Direct electrosynthesis of pure aqueous H2O2 solutions up to 20% by weight using a solid electrolyte. *Science* **366,** 226–231 (2019).

209. Grose, J. *How the Pop It! Invaded Your Home* (The New York Times, 2021).

210. Sîrbu, I.-D., Moretti, G., Bortolotti, G, Bolignari, M., Dirè, S., Fambri, L., Vertechy, R. & Fontana, M. Electrostatic bellow muscle actuators and energy harvesters that stack up. *Science Robotics* **6,** eaaz5796 (2021).

211. Rogatinsky, J., Recco, D., Feichtmeier, J., Kang, Y., Kneier, N., Hammer, P., O'Leary, E., Mah, D., Hoganson, D., Vasilyev, N. V., *et al.* A multifunctional soft robot for cardiac interventions. *Science Advances* **9,** eadi5559 (2023).

212. Joyee, E. B., Szmelter, A., Eddington, D. & Pan, Y. 3D printed biomimetic soft robot with multimodal locomotion and multifunctionality. *Soft Robotics* **9,** 1–13 (2022).

213. Shah, D. S., Powers, J. P., Tilton, L. G., Kriegman, S., Bongard, J. & Kramer-Bottiglio, R. A soft robot that adapts to environments through shape change. *Nature Machine Intelligence* **3,** 51–59 (2021).

214. Seong, M., Sun, K., Kim, S., Kwon, H., Lee, S.-W., Veerla, S. C., Kang, D. K., Kim, J., Kondaveeti, S., Tawfik, S. M., *et al.* Multifunctional magnetic muscles for soft robotics. *Nature Communications* **15,** 7929 (2024).

215. Mintchev, S. & Floreano, D. Adaptive morphology: A design principle for multimodal and multifunctional robots. *IEEE Robotics & Automation Magazine* **23,** 42–54 (2016).

216. Daler, L., Mintchev, S., Stefanini, C. & Floreano, D. A bioinspired multi-modal flying and walking robot. *Bioinspiration & biomimetics* **10,** 016005 (2015).

217. Dong, Y., Wang, L., Xia, N., Yang, Z., Zhang, C., Pan, C., Jin, D., Zhang, J., Majidi, C. & Zhang, L. Untethered small-scale magnetic soft robot with programmable magnetization and integrated multifunctional modules. *Science Advances* **8,** eabn8932 (2022).

218. Mundaca-Uribe, R., Askarinam, N., Fang, R. H., Zhang, L. & Wang, J. Towards multifunctional robotic pills. *Nature Biomedical Engineering* **8,** 1334–1346 (2024).

219. Ferreira, A. D. B., Nóvoa, P. R. & Marques, A. T. Multifunctional Material Systems: A state-of-the-art review. *Composite Structures* **151,** 3–35 (2016).

220. McEvoy, M. A. & Correll, N. Materials that couple sensing, actuation, computation, and communication. *Science* **347,** 1261689 (2015).

221. Maeda, S., Hara, Y., Sakai, T., Yoshida, R. & Hashimoto, S. Self-walking gel. *Advanced Materials* **19,** 3480–3484 (2007).

222. Kim, Y., van den Berg, J. & Crosby, A. J. Autonomous snapping and jumping polymer gels. *Nature Materials* **20,** 1695–1701 (2021).

223. Zhao, Y., Hong, Y., Qi, F., Chi, Y., Su, H. & Yin, J. Self-sustained snapping drives autonomous dancing and motion in free-standing wavy rings. *Advanced Materials* **35,** 2207372 (2023).

224. Bhamla, M. S., Benson, B., Chai, C., Katsikis, G., Johri, A. & Prakash, M. Hand-powered ultralow-cost paper centrifuge. *Nature Biomedical Engineering* **1,** 0009 (2017).

225. Farhadi, D., Pernigoni, L., Melancon, D. & Bertoldi, K. Origami crawlers: exploring a single origami vertex for complex path navigation. *Advanced Materials,* 2502293 (2025).

226. Brooks, R. A. & Flynn, A. M. *Fast, cheap and out of control* 1989.

227. Taghavi, M., Wang, W., Shim, K., Zhang, J., Cohen, I. & Apsel, A. Coordinated behavior of autonomous microscopic machines through local electronic pulse coupling. *Science Robotics* **9,** eadn8067 (2024).

228. Yasa, I. C., Ceylan, H., Bozuyuk, U., Wild, A.-M. & Sitti, M. Elucidating the interaction dynamics between microswimmer body and immune system for medical microrobots. *Science Robotics* **5,** eaaz3867 (2020).

229. Ijspeert, A. J. & Daley, M. A. Integration of feedforward and feedback control in the neuromechanics of vertebrate locomotion: a review of experimental, simulation and robotic studies. *Journal of Experimental Biology* **226,** jeb245784 (2023).

230. Thandiackal, R., Melo, K., Paez, L., Herault, J., Kano, T., Akiyama, K., Boyer, F., Ryczko, D., Ishiguro, A. & Ijspeert, A. J. Emergence of robust self-organized undulatory swimming based on local hydrodynamic force sensing. *Science Robotics* **6,** eabf6354 (2021).

231. Veenstra, J., Scheibner, C., Brandenbourger, M., Binysh, J., Souslov, A., Vitelli, V. & Coulais, C. Adaptive locomotion of active solids. *Nature,* 1–7 (2025).

232. Ishiguro, A., Shimizu, M. & Kawakatsu, T. A modular robot that exhibits amoebic locomotion. *Robotics and Autonomous Systems* **54,** 641–650 (2006).

233. Oyarte Galvez, L., Bisot, C., Bourrianne, P., Cargill, R., Klein, M., van Son, M., van Krugten, J., Caldas, V., Clerc, T., Lin, K.-K., *et al.* A travelling-wave strategy for plant–fungal trade. *Nature,* 1–9 (2025).

234. Stern, M., Hexner, D., Rocks, J. W. & Liu, A. J. Supervised learning in physical networks: From machine learning to learning machines. *Physical Review X* **11,** 021045 (2021).

235. Stern, M. & Murugan, A. Learning without neurons in physical systems. *Annual Review of Condensed Matter Physics* **14,** 417–441 (2023).

236. Du, Y., Veenstra, J., van Mastrigt, R. & Coulais, C. Metamaterials that learn to change shape. *arXiv preprint arXiv:2501.11958* (2025).

237. Zhang, X., Chen, L., Lim, K. H., Gonuguntla, S., Lim, K. W., Pranantyo, D., Yong, W. P., Yam, W. J. T., Low, Z., Teo, W. J., *et al.* The pathway to intelligence: using stimuli-responsive materials as building blocks for constructing smart and functional systems. *Advanced Materials* **31,** 1804540 (2019).

238. Raman, R., Cvetkovic, C., Uzel, S. G., Platt, R. J., Sengupta, P., Kamm, R. D. & Bashir, R. Optogenetic skeletal muscle-powered adaptive biological machines. *Proceedings of the National Academy of Sciences* **113,** 3497–3502 (2016).

239. Ricotti, L., Trimmer, B., Feinberg, A. W., Raman, R., Parker, K. K., Bashir, R., Sitti, M., Martel, S., Dario, P. & Menciassi, A. Biohybrid actuators for robotics: A review of devices actuated by living cells. *Science Robotics* **2,** eaaq0495 (2017).

240. Morimoto, Y., Onoe, H. & Takeuchi, S. Biohybrid robot powered by an antagonistic pair of skeletal muscle tissues. *Science Robotics* **3,** eaat4440 (2018).

241. Raman, R. *Biofabrication* (MIT Press, 2021).

242. Kriegman, S., Blackiston, D., Levin, M. & Bongard, J. A scalable pipeline for designing reconfigurable organisms. *Proceedings of the National Academy of Sciences* **117,** 1853–1859 (2020).

243. Blackiston, D., Lederer, E., Kriegman, S., Garnier, S., Bongard, J. & Levin, M. A cellular platform for the development of synthetic living machines. *Science Robotics* **6,** eabf1571 (2021).

AUTHOR'S PUBLICATIONS

1. Comoretto, A., Koppen, S., Mandke, T. & Overvelde, J. T. B. Embodying mechano-fluidic memory in soft machines to program behaviors upon interactions. ☆ *Device* **3,** 100863 (2025).
2. Comoretto, A., Schomaker, H. A. H. & Overvelde, J. T. B. Physical synchronization of soft self-oscillating limbs for fast and autonomous locomotion. *Science* **388,** 610–615 (2025).
3. van Laake, L.C.*, Comoretto, A.* & Overvelde, J. T. B. On the coexistence of pressure regulation and oscillation modes in soft hysteretic valves. *Journal of Fluids and Structures* **126,** 104090 (2024).
4. Comoretto, A., Gollob, S. D., Steur, E., Becker, K. P., Roche, E. T.† & Overvelde, J. T. B†. Active oscillations of elastic membranes arising from the coupling with a catalytic reaction. *In preparation.*
5. Gollob, S. D., Comoretto, A., Yu, Q., Fernandez, M., Adebajo, K., Overvelde, J. T. B., Becker, K. P. & Roche, E. T. A pressure-amplifying monopropellant engine for actuator-localized pneumatic power. *2025 IEEE 8th International Conference on Soft Robotics (RoboSoft),* 1–8 (2025).
6. Mousa, M., Comoretto, A., Overvelde, J. T. B. & Forte, A. E. Multifunctional fluidic units for emergent, responsive robotic behaviors. *Submitted.*
7. Picella, S., Comoretto, A., Vaarkamp, O. & Overvelde, J. T. B. Harvesting environmental circadian oscillations for energy autonomy in soft robots. *Submitted.*
8. Gollob, S. D., Comoretto, A., Yu, Q., Fernandez, M., Merton, H., Overvelde, J. T. B., Becker, K. P. & Roche, E. T. Hydrogen peroxide-powered pneumatic engine architecture for untethered soft robots with embodied energy. *In preparation.*
9. Galassi, L., Lorenzon, L., Comoretto, A., Cianchetti, M.† & Overvelde, J. T. B†. Coupling torsional instabilities with inverted artificial muscles for a soft artificial heart ventricle. *In preparation.*
10. Mohanty, S., Baconnier, P., Schomaker, H. A. H., Comoretto, A., van Hecke, M. & Overvelde, J. T. B. Autonomous switching of locomotion behaviors in ciliary walkers. *In preparation.*

(☆ Journal cover, * Equal contribution, † Co-corresponding)

ACKNOWLEDGMENTS

This thesis condenses four years of creation, research, and obsession. It has been a journey that I could not have embarked on alone. Thank you to all the pirates of the crew: I will thank you in pseudo-random order. Forgive me if you are not in these lines of text: my heart thanks you, and you know it.

First and foremost, thank you, Bas. As the maverick captain of this exploration ship, you never imparted orders, but strong recommendations based on educated intuition. Even when land is nowhere to be seen, you somehow feel in which direction to sail toward, no matter where the wind blows. I will forever be grateful for the kind of PhD you enabled me to pursue. Allowing me to follow my creative expression, while guiding it and shaping it into rigorous science, is the best gift you could give me. I thank you for being the mentor who shaped the way I now see the world: without you, I wouldn't be the scientist and person I am today. Indeed, many of your lessons go beyond science: strive for beauty, look at the glass as always fully full, question everything, dig deep, and move on.

Erik, as co-promotor, thank you for your helpful feedback and the support in the final, yet crucial, steps of the journey. I want to extend my gratitude to the other committee members: thank you René van de Molengraft, Auke Ijspeert, Marleen Kamperman, Danquing Lio, and Vito Cacucciolo, for dedicating the time to read this thesis. Your appreciation for the work made me proud of the effort.

This is the kind of enterprise that doesn't happen just inside the walls of a research institute. Outside of the academic bubble, I had invaluable support that I'm grateful for. Thank you, Mom, Dad, and Sister. Who I am, is thanks to you. Since the very beginning, you taught me to enjoy learning and creating. Thank you for instilling in me an appreciation for the balance of having fun while being serious about it. Thank you for the foundation you built, which I will always rely on, way beyond these PhD years. You are the safe port where the ship can always come back when the treasure hunt needs a break. Thank you Davide: your unlimited passion for music would inspire anyone to be passionate about anything. Thank you, Sofia, for always making me smile: maybe in about a decade or two, you will read these words, and I will surely be thankful for all the experiences we will have had together. Thank you, zio Gian and zia Francesca: you inspired me to pursue excitement, both at work and in life. Thank you, zia Kety, for cheering for me every step of the way.

Thank you, Devanshi: partner, motivator, mirror, fan of weird, supporter of my obsessive interests. You are a constant source of inspiration: I look at you, and I see who I want to be. Thank you for your near infinite patience. It's hard to live next to an academic: thank you for smiling and making me smile, no matter how spiky the times are. Your encouragement and support have virtually no end: thank you for keeping up with the difficulties that come with pursuing exciting science, including my relocations in the US and now in Belgium. I am impossibly lucky to have you in my life, hand in hand, walking *our* happy road. Thank you also for bringing an extended family into my life: Prerna, Ravi, Neeru ma'am, thank you for the joyful moments we had.

There are crew members who joined the ship long before it found the PhD waters. Thank you, Giampo, Peter, and Max. When I first told you that I would do a PhD on robots that could be intelligent while being made of just balloons, you didn't blink. That was great. Also, thank you for not allowing the connecting rope to break: your travels to come find me have been one of the most precious events of the past years. You fill me with joy. Thank you Giampo, for never giving up on telling me to go out there and fuel my passion for taking photographs: when I forget my own self, you make me remember. Thank you Peter, for inspiring me to try to find the creativity within me, looking at the way you do it all the time. Thank you Max, for truly being there for me every day as if we saw each other yesterday, even when it's actually been months.

Erasmus friends, thank you: you shaped the way I think and see the world, and even if indirectly, you had a strong influence on how my PhD developed. Thank you, Freddi, Roxie, Lore, Mar, Carli, Katja, Eiko, Anto, Niccolò, Stefano, Giacomo, Mattia, Vanessa, Andreas, Kasper, Eva, Stef, Federico, and all: each of you played an essential role during one of the most influential years that shaped my person.

To my Amsterdam crew, you are the best adventure companions one can wish for. Thank you for always loving me the way I am, and for supporting my PhD journey with lots of laughs, endless conversations, and unforgettable moments. You are a strong foundation, with you it's always a joyful time. Thank you, María, for constantly showing me what really matters in life: the people around us. Thank you, Dion, brother, for being there, always ready to listen, and for giving me the confidence to believe in myself. Thank you, Killian, for constantly fueling me with so much energy. Thank you all, Elisa, Johanna, Felix, Andrea: we had a great time. Thank you, Hui, Datta, and Ravi: you made my first year in Amsterdam just great, despite the pandemic.

Soft Robotic Matter members, past and present: you are immensely inspiring individuals—colleagues who inevitably became friends, one coffee break after the other. Mannus, office mate and partner in crime during our first conferences. Thank you for your wisdom and humor,

for reminding me of life outside of research, for transmitting creativity via osmosis. We did this together! Thank you, Paul, for showing me that there is virtually no end to the deep obsession with seemingly simple ideas. Niels, hero with no cape, thank you for keeping the ship afloat, one screw at a time. Without your sharp skills, none of the strange ideas in this Thesis could have seen the light of day. Thank you for your friendly, ever-present patience and support. Luuk, reliable guidance during my first shy steps, thank you for teaching me the skill of precision and the strength of wondering with your '*Oh, that's interesting!*'. Thank you, Sergio, for showing me how to look at phenomena with a physics eye: '*Nature doesn't care about us!*'. Thank you for listening when I needed it. Thank you, Katrien: with your sharp mind, positivity, and excitement, you remind me that work-life balance is not needed, when it's all life. Shibo! Since the first day you joined AMOLF, you have been inspirational with the elegance of your scientific approach, and your deeply human presence has been a gift I will always be thankful for. Maziar, thanks for your quiet wisdom: you might not remember it, but you once told me not to acquire more data than I could find time to look at within the PhD time. It's a valuable tip that I will always carry with me. Lio, thanks for bringing fresh and exciting ideas to the group during the last months of my PhD, when it's time to wrap up more and think less. Sumit! What a ride! Thanks for being there when I needed experienced advice. Thank you for bringing ciliary walkers to life: it would be an emptier world without them. Nienke, thanks for showing the meaning of persistence in building something: I cheer for your soft robotic heart to be super durable. Stijn, adopted office mate: thank you for reminding me that life is out there, and that the unexpected is to be cherished. Bob, mysterious man, every time with one more card in your deck, whether a Pokémon or not: thank you for the constant reminder that what matters is what we are interested in, and that we should give our passions the space they deserve. Jelle, thanks for the fun during our months as interns: good times, good laughs. Elif, thanks for bringing materials knowledge and smiling moments to AMOLF. Paul Baconnier, thanks for the depth of our conversations about science, you are a rock. Jack: thanks for the support, the cheering, the good laughs. And Dhawal: if only I could remember all the jokes, I would have guaranteed laughing for the next decade–damn it. Thank you Petra and Rob: it was fun to work together on the press release. Thank you Oana for helping in providing access to many papers, they were essential reads for this thesis. Thank you Remco for patiently solving all my problems with computers, and thank you Clyde for making sure we all have a nice office to work in. Thank you Florian, Agustin, Giorgio, Becca, Charlotte, Luca, Erwin, Tess, Astrid, Ze, Manon, Kun, Yorick, Milo, Maddy, Arno, Parisa, Finn, Sima, Theo, Colin, Bernat, Margot, Pascal, and all: every interaction we had left a mark.

And of course, I want to thank the students I supervised: an old and predictable (yet true) saying says that students teach you stuff, while you try to teach them something. Thank you, Laura, Olivier, Matt, and Tanaya: I know you have been patient when I was going on my tangents. It was fun to work together.

Thank you also to the principal investigators at AMOLF who influenced my scientific approach: Martin van Hecke, Said Rodriguez, Marc Serra-Garcia, Nachi Stern, Sander Tans, Kristina Ganzinger, Wim Noorduin, Bruno Ehrler, Ewold Verhagen. I extend my gratitude to some of the academics I encountered around, as our interactions shaped the way I look at science: thank you Corentin Coulais, Ali Sadeghi, Daan Haver, Benjamin Gorissen, Tianyu Wang, Katia Bertoldi, Davood Farhadi, Adel Djellouli, Aniket Pal, David Mélançon, Marquise Bell, Perla Maiolino, Edoardo Milana, Marco Fontana, Giacomo Moretti, Florian Hartmann, Ellen Roels, Leon Kamp, Giovanni Bordiga, Hiroyuki Nabae, Shoma Tanaka, Nana Obayashi, Bert Van Raemdonck, Cosimo Della Santina, Kam Bielawski, Ellen Rumley. Thank you to the RAD collaborators Antonio Forte and Mostafa Mousa: guys, you rock! Thank you to my new supervisor at KU Leuven, PT Brun, for believing in me and hiring me as postdoc: it will be fun to build the new lab and to work together.

In these years, I have been lucky to travel and do research in the dynamic and energetic institution that MIT is (thanks for making it happen, Bas and Ellen). This has been intellectually fulfilling, but most importantly, it allowed me to meet and collaborate with smart, compassionate, and creative individuals that otherwise would never have entered my life. Ellen Roche and Kait Becker, thank you for mentoring me and welcoming me to your labs, even if for just a few months: I came back home a different person, both scientifically and personally, also thanks to your influence. Thank you, Sam, for welcoming me wholeheartedly in Boston. Our collaboration quickly turned into a friendship: I hope both will stay for years to come. I learned a lot from you, but you know that already. Thank you, Hews Street crew: Diego, Chava, José, Margot, you made me feel at home away from home. Thanks to all the students and researchers at TTDD Lab and FIDL, you all contributed to the wonderful times inside and outside the lab: thank you Andreas, Markus, Manisha, Yiling, Keegan, Connor, Tom, Qiyun, Carly, Rose, Eve, Lauren, Brian, Kore, Eddy, Carlos, Alix, Jane, Vishnu, Emmanuel, Charlotte, Qifan, Cat, Daniel, Nina, Annie, Olivia, and Evan. Boston also gifted me with friendships outside of the lab that are there to stay. Thank you, Niccolò, for the long and beautiful conversations. Thank you, Maxi and Fra, you ensured laughs and excitement in a foreign land. Thank you Jackson, for welcoming me to the city and making me feel Amsterdam was not that far away, after all.

Lastly, I want to thank the vibrant institution/community/phenomenon that is AMOLF: a magical place to pursue meaningful science, while having fun doing it.

ABOUT THE AUTHOR

Alberto Comoretto was born on January 3rd, 1996, in Brescia, Italy. After the scientific high school, in 2015, he moved to the mountains in Trentino to earn his Bachelor of Science in Industrial Engineering at the University of Trento. In 2018, he carried out his Bachelor's Thesis on highly stretchable sensors for soft robotics based on dielectric elastomers with professor Marco Fontana.

He then enrolled in the Master of Science in Mechanics and Mechatronics Engineering. During the studies, he spent one year as an exchange student at Chalmers University of Technology in Gothenburg, Sweden. There, he learned bioinspired algorithms, computational mechanics, and to enjoy climbing.

In 2020, looking for exotic research on modern mechanics, he moved to Amsterdam, where he conducted his Master's Thesis research as a Scientific Intern in the Soft Robotic Matter Group at AMOLF, under the supervision of professor Bas Overvelde and, at the time, PhD student Luuk van Laake. More a revelation than a job, this fulfilling experience made Alberto realize that fundamental and experimental research on soft matter was his drive. In 2021, his thesis earned him the Master of Science with full marks *cum laude*.

Healthily obsessed about the mechanics of soft objects, he started his PhD in the same group that same year. During the next four years, he will spend countless hours playing with tubes, shells, and other mechanical toys in the lab, drink too many coffees at the AMOLF coffee corner, happily supervise Master students, and give talks at multiple international and national conferences. In 2024, he worked as a Visiting Researcher at MIT in the TTDD Lab with professor Ellen T. Roche. There, he carried out research on harnessing chemical fuels for untethered soft devices. This Thesis is the result of his four years of doctoral research.

Excited about what's next to discover, Alberto is now a postdoc at KU Leuven with professor P.-T. Brun in the SMaRT Lab (Soft Matter, Rheology and Technology), where he studies, among other topics, the physics of instabilities in solidifying fluids and soft matter.